THE UNIVERSITY
of ADELAIDE

Reaction Control Jet Actuators for Air-Breathing Hypersonic Vehicles

Warrick Miller

The University of Adelaide
Faculty of Engineering, Computer and Mathematical Sciences
School of Mechanical Engineering

A thesis submitted in fulfilment of the requirements for the degree of Doctor of Philosophy in engineering.

January 2019

Supervisors:
Associate Professor Paul Medwell
Associate Professor Con Doolan
Dr. Minkwan Kim

Submission Date: 7 November 2018
Amendment Date: 22 January 2019

School of Mechanical Engineering
The University of Adelaide, 5005
SA, Australia

Typeset by the author using LaTeX.
Printed in Australia.

Contents

List of Figures

List of Tables

Abstract

Air-breathing hypersonic vehicles have an engine which is tightly integrated with the airframe. This integration leads to complex dynamic characteristics, such as propulsion-pitch coupling. As a result, air-breathing hypersonic vehicles tend to be unstable and high frequency control is required to maintain steady flight. To provide high frequency control, aerodynamic control surfaces may need to be supplemented or replaced by high frequency actuators.

Reaction control (RC) jets are an attractive solution, as they are commonly used to supplement aerodynamic control surfaces for exo-atmospheric control of hypersonic vehicles, and can operate at high frequency. If RC jets are operated within the atmosphere, an interaction force is generated in addition to the jet thrust. Understanding this interaction force is important in the design of a control system that implements RC jet actuators for use within the atmosphere. This thesis studies the unsteady interaction between an RC jet, and a hypersonic crossflow.

A generic hypersonic vehicle model was used to investigate flight conditions where supplementary control may be required. Due to the instability caused by propulsion-pitch coupling, aerodynamic control surfaces alone are unable to control the vehicle's rigid-body modes at several flight conditions.

To analyse RC jet flow physics, an implicit large-eddy simulation (ILES) methodology was developed, verified and validated using a number of canonical supersonic flow problems, and experimental data for a steady jet in hypersonic crossflow.

The steady and pulsed operation of a sonic, round jet issuing from a flat plate into a hypersonic (Mach 5.0) crossflow with a laminar in-flow boundary layer was investigated numerically. The pressure distribution induced on the plate is unsteady, and is influenced by shock and vortex structures that form around the jet. The unsteady and time-averaged behaviour of these structures has been described, leading to an improved understanding of the jet interaction flow physics.

When the jet was pulsed, flow structures were influenced by the presence of shocks in the flow, allowing penetration per unit jet mass flow to increase by a maximum of 68% compared with the steady jet. Pulsing also provides a higher jet interaction force per unit jet mass flow compared with a steady jet, with a 52% increase recorded at a 33% duty-cycle.

The start-up process for both steady and pulsed jets was also considered. The interaction force during start-up acts as a lightly damped second-order system. An

overshoot is observed in the control force, corresponding to expansion of the jet flow behind the initial lead shock, before the flow settles to a quasi-steady state on a time-scale related to the time taken for the jet fluid to reach the trailing edge of the flat plate.

To assess the effectiveness of RC jets as a supplement to aerodynamic control, jet control was implemented on the generic air-breathing hypersonic vehicle, showing a significant improvement at all supersonic flight conditions.

This thesis provides an increased understanding of the unsteady interaction between steady and pulsed sonic jets in hypersonic crossflow, which has applications in reaction jet control of air-breathing hypersonic vehicles.

Declarations

I certify that this work contains no material which has been accepted for the award of any other degree or diploma in my name in any university or other tertiary institution and, to the best of my knowledge and belief, contains no material previously published or written by another person, except where due reference has been made in the text. In addition, I certify that no part of this work will, in the future, be used in a submission in my name for any other degree or diploma in any university or other tertiary institution without prior approval of the University of Adelaide.

I give permission for the digital version of my thesis to be made available on the web, via the University's digital research repository, the Library Search and also through web search engines, unless permission has been granted by the University to restrict access for a period of time.

I acknowledge the support I have received for my research through the provision of an Australian Government Research Training Program Scholarship.

Warrick Miller

Acknowledgements

First and foremost, I would like to thank my wife, Ashleigh, who has supported me throughout this journey. Without her support and understanding, I would never have completed this thesis.

I would also like to thank my family, for their support and encouragement throughout my education.

I am grateful to my colleagues at the Air Warfare Centre and DST Group, specifically Mr Graham Akroyd, who has supported this endeavour and provided time and assistance throughout.

Finally, I would like to thank my academic supervisors, whose support and patience have been invaluable and has made this an enjoyable academic experience. Also, I would like to thank the School of Mechanical Engineering for providing resources, support and other assistance. The use of supercomputer facilities provided by eResearchSA is also appreciated.

Chapter 1

Introduction

Air-breathing hypersonic flight has many potential applications, both civilian and military. In the military context, air-breathing hypersonic flight provides the key to the "prompt global strike" capability (Woolf, 2013), which would allow targets anywhere on Earth to be reached from a single location within as little as one hour. Air-breathing vehicles operate within the atmosphere, which reduces the risk of a conventional strike being misinterpreted as a nuclear intercontinental missile launch. Another military application of air-breathing hypersonic flight is the "operationally responsive space" capability (Hank et al., 2008) to rapidly put payloads into orbit, support and maintain them, and return them to Earth. The same properties that make air-breathing hypersonic vehicles attractive for military applications also provide significant advantages to civilian applications, by reducing intercontinental flight times and providing cheap, reliable access to space.

The hypersonic flow regime is characterised by several phenomena, including viscous interaction and high temperature effects, which progressively begin to influence the flow physics at high speeds, typically above Mach 5 (Anderson, 2001). As a result, hypersonic flight is generally defined as flight within the atmosphere, at speeds above Mach 5.

Hypersonic flight has been achieved in many applications using rocket propulsion, or glide vehicles. Examples include the Space Shuttle, the North American X-15, and Inter-Continental Ballistic Missiles (ICBMs). As shown in Figure 1.1, the potential efficiency of air-breathing (scramjet) propulsion systems is much greater than rockets, due to the fact that air-breathing vehicles only carry fuel and not oxidiser (Smart, 2008).

One of the limitations to the development of an operational air-breathing hypersonic vehicle is the control system. The typical contemporary design of air-breathing hypersonic vehicles has the propulsion system tightly integrated with the airframe. This integration causes unique dynamic characteristics, including dynamic coupling (Bolender and Doman, 2007), and as a result air-breathing hypersonic vehicles tend to be unstable. These unique dynamics are an active field of research, as outlined in Section 2.1 of this thesis. The implication for the control system is that high

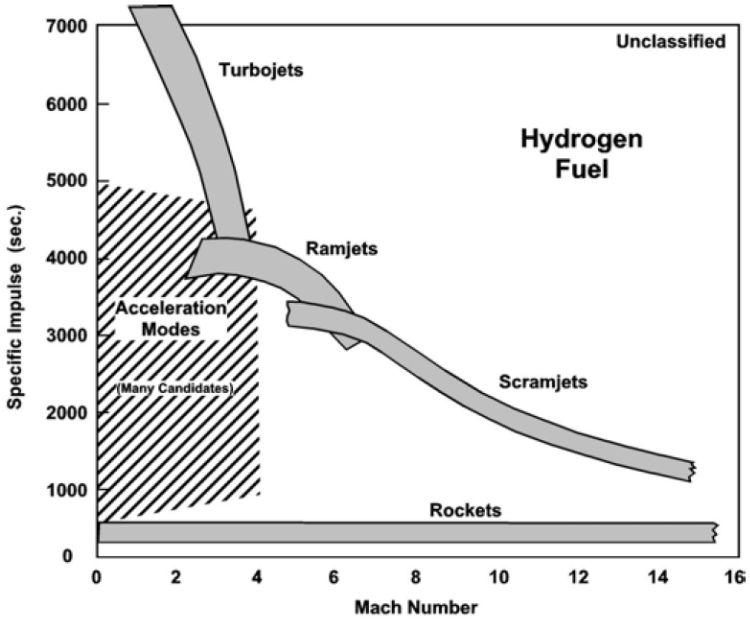

Figure 1.1: Specific impulse available from various methods of propulsion (Smart, 2008).

frequency control, beyond that which is achievable with conventional aerodynamic control surfaces, may be required to maintain steady flight. Current estimates of the required control frequencies are limited to the consideration of longitudinal dynamics of simplified vehicles at a single trimmed flight condition. An aim of this thesis is to provide a more complete description of integrated air-breathing hypersonic vehicle dynamics and control requirements across a wide range of flight conditions.

Reaction control jets are widely used as a supplement to aerodynamic control surfaces, to provide exo-atmospheric control on hypersonic vehicles. For example, reaction control was implemented on the Space Shuttle Orbiter to provide pitch, roll, and yaw control, both in orbit and during early re-entry, where dynamic pressure and aerodynamic control authority is low. The ability of reaction control systems to operate at higher frequencies than is achievable using aerodynamic control surfaces makes reaction control jets an attractive option to provide the requisite high frequency control within the atmosphere. Reaction control has been applied to endo-atmospheric missile systems, including the US Patriot PAC-3 theatre missile defence system and the US Terminal High Altitude Area Defense (THAAD) system, for high frequency control.

When operated within the atmosphere, the interaction between the jet and the hypersonic free-stream flow across the jet orifice, i.e. the crossflow, generates a complex system of shocks and vortices. This poses a major challenge when designing the control system, as thruster performance depends on these shock and vortex structures, which induce a complex, unsteady pressure distribution on the surface of the vehicle. This induced pressure modifies the control force caused by the jet. The time-averaged interaction between a steady jet and crossflow is well understood (refer to Section 2.4

of this thesis); several in-depth reviews have been compiled, summarising hundreds of publications over sixty years of research (Margason, 1993; Mahesh, 2013). However, the unsteady aspects of the interaction are not well characterised in the hypersonic regime. Increased understanding of the unsteady interaction between a reaction control jet and hypersonic crossflow is of practical interest – a well designed injection system requires detailed knowledge of the flow-field.

When the jet is operated at high frequency, the flow-field is analogous to that of a pulsed jet in crossflow. Pulsed jets have been studied in subsonic crossflow, and have been shown to significantly increase penetration and mixing compared with steady jets. Despite the potential applications for increased penetration and mixing in supersonic and hypersonic crossflow, the pulsed jet in crossflow interaction is also not well characterised in this regime. The penetration and mixing behaviour of pulsed jets in hypersonic crossflow is of interest to reaction control systems, and other applications including fuel injection for scramjet engines.

1.1 Thesis Outline

A review of relevant literature is provided in Chapter 2. The unique dynamic properties of air-breathing hypersonic vehicles are described, with a focus on the implications for control actuator design. The ability of different actuator types to meet these requirements is summarised, leading to the selection of reaction control jets as an appropriate supplement for aerodynamic control. The physics of the interaction between a jet and hypersonic crossflow is also reviewed. The review highlights the gaps in understanding of the transient interaction between reaction control jets and hypersonic crossflow. Finally, these gaps are are distilled into aims for this thesis.

Chapter 3 uses a generic air-breathing hypersonic vehicle model to estimate the control requirements over a range of flight conditions. The stability of rigid-body modes, the control authority, control bandwidth, and response to atmospheric turbulence are all considered. The influence of dynamic coupling is estimated through comparison to an un-coupled vehicle.

Chapter 4 describes the numerical methodology used in this thesis to investigate the unsteady interaction between a reaction control jet and hypersonic crossflow. The governing equations are outlined, and the discretization, solution methods, and turbulence models are described.

Verification and validation of the numerical methodology is described in Chapter 5. A build-up approach is used to ensure the simulations are able to accurately and reliably predict the relevant flow features. The focus is on reproducing relevant experimental data and ensuring that mesh resolution is adequate to resolve the flow. Test cases considered are simple unit problems, and a jet issuing into a quiescent atmosphere.

Chapter 6 provides additional verification and validation data for a steady jet in hypersonic crossflow. Simulation data is compared with experiments conducted by Erdem (2011). Chapter 6 also provides an in-depth analysis of the unsteady interaction

between a steady jet and hypersonic crossflow; the individual vortex and shock features are described. These structures induce a surface pressure distribution, which generates a control force. These aspects are analysed, and traced back to the causative flow features.

The operation of an unsteady jet in hypersonic crossflow is considered in Chapter 7. Square-wave pulsing is considered for a range of frequencies and duty-cycles. The influence of pulsing on the flow structures, jet penetration, and interaction force is described.

The start-up behaviour of both steady and pulsed jets into hypersonic crossflow is described in Chapter 8. The development of shock and vortex structures are described, and their affect on jet penetration and control force are quantified.

The relevance of the transient flow physics to vehicle control is shown via implementation of reaction jet control, as a supplement to conventional aerodynamic control, in the generic air-breathing hypersonic vehicle model. This is considered in Chapter 9.

Finally, Chapter 10 contains conclusions and proposals for future work.

1.2 Publications Arising from this Thesis

Sections of the work presented in this thesis have been previously published. The numerical verification and validation in Chapter 5 is based on the publication:

Miller, W., P. Medwell, M. Kim and C. Doolan. "Computational Methodology for Investigating the Transient Interaction between an Reaction Control Jet and a Hypersonic Crossflow". In *Aerospace Sciences Meeting*, AIAA, San Diego, CA, (2016).

The specific jet in quiescent atmosphere analysis presented in Section 5.3 is based on the publication:

Miller, W., C. Doolan, Z. Prime and M. Kim (2014). "Simulation of a Transient Supersonic Jet", *Australasian Fluid Mechanics Conference*, AFMS, Melbourne, Australia.

The steady jet in hypersonic crossflow study presented in Chapter 6 is based on the publication:

Miller, W., P. Medwell, C. Doolan, and M. Kim. "Transient interaction between a reaction control jet and a hypersonic crossflow". *Physics of Fluids* Vol. 30, 046102 (2018).

The unsteady jet in hypersonic crossflow study in Chapter 7 is based on the publication:

Miller, W., P. Medwell, C. Doolan, and M. Kim. "Numerical investigation of a pulsed reaction control jet in hypersonic crossflow". *Physics of Fluids* Vol. 30, 106108 (2018).

Finally, the jet steady start-up behaviour described in Section 8.1 is based on the publication:

Miller, W., C. Doolan, P. Medwell and M. Kim (2018). "Transient Start-up of a Sonic Jet in Hypersonic Crossflow", *Australasian Fluid Mechanics Conference*, AFMS, Adelaide, Australia.

Chapter 2

Literature Review

This chapter reviews the design and unique dynamic properties of air-breathing hypersonic vehicles, and the flow physics of a Reaction Control (RC) jet when operated in a hypersonic crossflow.

This chapter is structured in five sections. Section 2.1 summarises the design of air-breathing hypersonic vehicles, and their dynamic properties. A summary of air-breathing hypersonic vehicle control actuator requirements has been compiled from available literature in Section 2.2, and a brief review of actuator types and their ability to meet these requirements is provided in Section 2.3, leading to a justification for the choice of RC jets as a suitable supplement to aerodynamic control surfaces. The flow physics of both the steady and transient interaction between a jet and crossflow is detailed in Section 2.4. A summary of the review and identification of gaps in the literature that are addressed in this thesis are outlined in Section 2.5.

2.1 Air-breathing Hypersonic Vehicles

Air-breathing propulsion is recognised as the most efficient means of propulsion at hypersonic speed because it can utilise oxygen from the atmosphere to burn fuel (Urzay, 2018). Air-breathing hypersonic vehicles are typically designed with an integrated scramjet engine to maximise efficiency. A simplified example of such a vehicle is provided in Figure 2.1 (Bolender and Doman, 2007). The integrated design is such that the fore- and aft-body contribute to the lift and pitching moments, as well as contributing to the compression and expansion functions for the propulsion system. Such vehicles are highly unstable and exhibit unique dynamic characteristics, including unprecedented coupling between the aerodynamic and propulsive forces (Rodriguez et al., 2008; Anderson, 2006).

The coupling manifests because the fore-body creates a bow shock that forms part of the compression system for the engine (Bolender and Doman, 2007). The pressure rise on the forward fuselage due to compression also produces lift, and a nose-up pitching moment. The rearward fuselage is shaped to facilitate external expansion of the exhaust gases, forming the upper half of an expansion nozzle. As a result, the

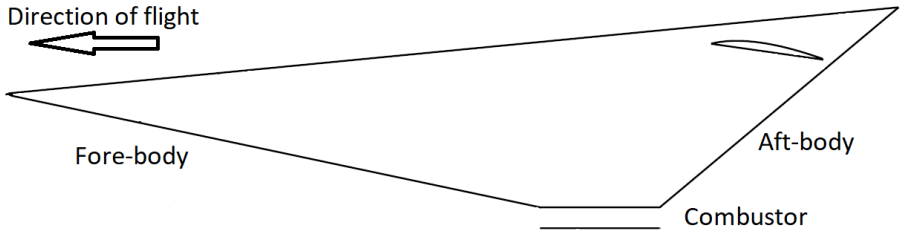

Figure 2.1: Simplified example of an air-breathing hypersonic vehicle, adapted from Bolender and Doman (2007).

pressure distribution on the rearward fuselage also generates lift, and a nose-down pitching moment. If the engine is mounted below the vehicle's centre of gravity, the propulsive force will also generate a nose-up pitching moment. Thus, the propulsion system, including the fore- and aft-body, contributes to the lift and pitching moments, which depend on Mach number, angle-of-attack, and the engine power setting (Doman et al., 2006). This creates a propulsion-pitch coupling phenomena. With the engine mounted below the centre of gravity, additional thrust will create a nose-up pitching moment and increase the angle-of-attack. This increased angle-of-attack changes the pressure distribution over the fore- and aft-body, which changes the engine inlet and outlet conditions, thus changing the thrust. The net result of this feedback is high frequency perturbations to thrust, lift, angle-of-attack, airspeed, and pitching moment. The changes to fore- and aft-body pressure distributions may also cause structural bending and aero-elastic modes to be included in the coupling.

Early work to investigate this dynamic propulsion-pitch coupling was performed by Walton (1989), who considered thrust performance sensitivity to variations in free-stream dynamic pressure and angle-of-attack. Chan et al. (1991) considered the effect of vehicle elasticity on longitudinal flight dynamics for the NASA National Aerospace Plane (NASP) project, and vonEggers Rudd and Pines (2000) applied piston theory to a caret wing waverider model flying at Mach 10 to identify both the longitudinal instability and the benefit of including the propulsion system in controller design. In addition, Heeg et al. (1993) considered active control of aero-elastic interactions on a vehicle with coupled rigid-body and aero-elastic interactions. This work identified that including flexibility in the model had a destabilising effect, as did aerodynamic heating and increased free-stream Mach number.

To allow users to study trajectory and control solutions for realistic air-breathing hypersonic vehicles in the open literature, as part of NASP program, White et al. (1992) generated a generic hypersonic aerodynamics model example (GHAME). The GHAME is a realistic, yet generic, model of a single-stage-to-orbit (SSTO) air-breathing hypersonic vehicle without propulsion-pitch coupling. This model was further developed by Zipfel (2007) and includes six degree-of-freedom rigid-body dynamics, an aerodynamic heating model, and a propulsion model.

The first attempts to generate a comprehensive analytical model to study longitudinal dynamics and flight controls for air-breathing hypersonic vehicles with propulsion-

pitch coupling were by Chavez and Schmidt (1994a) and Raney et al. (1993). Chavez and Schmidt (1994a) identified that these aircraft exhibit strong aero-elastic and aero-propulsive dynamic interactions – integrated flight and propulsion control systems are necessary. Dynamic modes of the vehicle, which set the requirements for the control system, were quantified by Chavez and Schmidt (1994a) for trimmed level flight at Mach 8, at an altitude of 30.48 km (100 000 ft). Raney et al. (1993) developed a model to assess interactions between longitudinal rigid-body flight dynamics, propulsion systems, and elastic modes, and considered flight at two conditions: Mach 6, 22.8 km altitude, and Mach 10, 29 km altitude. This study found that a 4° bend in the fuselage structure can double the total lift at the Mach 6 flight condition. Moment perturbations induced by elastic deflections were large, and significant control activity is likely required to maintain stable, trimmed flight.

Bolender and Doman (2007) extended the work of Chavez and Schmidt (1994a), creating a detailed structural model of a vehicle with geometry similar to Figure 2.1, flying at Mach 8, 25.9 km (85 000 ft) altitude. Bolender and Doman (2007) included the effects of the oscillating bow shock on the propulsion system's performance, and the presence of coupling between longitudinal rigid-body accelerations and flexible-body dynamics. This work highlighted the propulsion-pitch, structural, and aero-elastic coupling present in these vehicles, produced a representative model of the longitudinal coupled dynamics, and showed that air-breathing hypersonic vehicles are typically unstable, with high frequency rigid-body, structural, and aero-elastic modes. Bolender and Doman (2007) also highlighted that air-breathing hypersonic vehicles that utilise aerodynamic control surfaces exhibit non-minimum phase behaviour.

Colgren et al. (2009) extended this work to include lateral modes, using a 10 degree-of-freedom model based on the NASA generic winged-cone hypersonic vehicle configuration (Shaughnessy et al., 1990), with aerodynamics calculated using wind tunnel and Computational Fluid Dynamics (CFD) methods. Colgren et al. (2009) considered an entire flight trajectory, rather than a single reference flight condition, although vehicle dynamics were only published for a steady-state pull-up manoeuvre at a Mach 5, 18.3 km (60 000 ft) altitude flight condition.

The summary of vehicle dynamic modes for a range of propulsion-pitch coupled air-breathing hypersonic vehicle models, provided in Table 2.1, shows that air-breathing hypersonic vehicles tend to be unstable in pitch, and the magnitude of the predicted pitch instability varies between models.

Further studies have extended these models by including the effects of additional flow phenomena specific to the hypersonic regime. Echols et al. (2015) showed that the inclusion of a more detailed propulsion model on the vehicle of Bolender and Doman (2007) increased the open-loop instability by approximately 33 %. Oppenheimer et al. (2007) incorporated unsteady aerodynamics into the same model through the use of a combination of Prandtl-Meyer flow, oblique shock theory, and piston theory, and found that the unsteady aerodynamics increased the frequency of the unstable modes by up to 50%. Rodriguez et al. (2008) showed that the vehicle of Bolender and Doman (2007)

Table 2.1: A summary of eigenvalues, natural frequency, and damping ratio of dynamic modes for propulsion-pitch coupled air-breathing hypersonic vehicle models.

Eigenvalue	**Frequency (Hz)**	**Damping Ratio**	**Mode**
Chavez and Schmidt (1994a) model			
-0.55 ± 16.46i	2.6	0.033	Body Flex
-2.5	0.40	1.00	Short-period
2.31	0.37	-1.00	Short-period
1.14×10^{-6}	1.8×10^{-7}	1.00	Altitude
-0.002 ± 0.057i	0.009	0.035	Phugoid
vonEggers Rudd and Pines (2000) model			
-1.78	0.28	1.00	Short-period
1.75	0.28	-1.00	Short-period
-0.048 ± 0.174i	0.03	0.27	Phugoid
Bolender and Doman (2007) model			
-2.72 ± 49.3i	7.9	0.055	Aero-elastic
-0.376 ± 16.2i	2.9	0.0196	Body Flex
-1.42	0.23	1.00	Short-period
1.35	0.21	-1.00	Short-period
-5.79×10^{-4}	9.2×10^{-5}	1.00	Altitude
$-1.68 \times 10^{-5} \pm 0.0266$i	0.004	-6.31×10^{-4}	Phugoid
Colgren et al. (2009) model			
-0.10 ± 3.53i	0.56	0.03	Short-period
$-5.69 \times 10^{-4} \pm 1.3 \times 10^{-3}$i	8.25×10^{-3}	0.07	Phugoid
$-0.02 \pm 6.81 \times 10^{-3}$i	0.003	0.94	Roll / Spiral
0.058 ± 0.77i	0.12	0.075	Dutch Roll

becomes less stable at lower altitudes, and at higher Mach numbers, in agreement with Heeg et al. (1993). Fidan et al. (2003) showed that real-gas effects not included in the previously published models can also affect the control characteristics. This was experienced in the early period of operation of the Space Shuttle, where predicted control deflections required to longitudinally trim the vehicle during re-entry were under-estimated by a factor of two, primarily due to real-gas effects (Maughmer et al., 1993). Several additional studies (Skujins et al., 2008; Falkiewicz et al., 2009; Falkiewicz and Cesnik, 2009; Falkiewicz et al., 2010; Skujins et al., 2010; Falkiewicz et al., 2011) further highlight the uncertainty surrounding the effectiveness of control systems to deal with unstable hypersonic vehicles in the presence of propulsion-pitch, structural, and aero-elastic coupling. Finally, Zhang et al. (2016) found that the inclusion of gravity and centrifugal force in their model reduced the frequency of the altitude mode by 20%, but did not affect other rigid-body modes.

Using these air-breathing hypersonic vehicle models, several authors have developed and tested control strategies for air-breathing hypersonic vehicles in the open literature, with vary levels of complexity, for example Prime et al. (2012); Echols et al. (2015); Wang et al. (2016). To be successful, these control strategies must be robust to account for the significant uncertainty in vehicle dynamics and coupling behaviour.

Other hypersonic aerodynamic phenomena have been studied over many years, which are yet to be included in published air-breathing hypersonic vehicle models. For example, Orlik-Ruckeman (1966) investigated hypersonic viscous interaction for a 3° wedge at Mach 17, which changed the pitching moment by 50% – 200%. Other hypersonic phenomena, including boundary layer transition and separation are active fields of research (Kimmel et al., 2013; Gosse et al., 2014; Balakumar and Chou, 2018). Dedicated research programs relating to hypersonic vehicle controls strategies (Bahm et al., 2005; Smith et al., 2011; Dauby et al., 2015) and propulsion (Jackson et al., 2015) are also ongoing.

From this summary it is apparent that air-breathing hypersonic vehicle dynamics are characterised by the presence of dynamic propulsion-pitch coupling. This has significant implications for vehicle control. It has been recommended that the propulsion system be integrated with the overall control system, and that active control of high-frequency elastic deformations may be required to maintain stable, trimmed flight. There have been several studies into the impact of various physical phenomena on vehicle dynamics, and detailed vehicle models have been developed. While these models contain a significant level of fidelity in one or more specific aspects of the dynamics, the complexity of the modelling techniques required to gain that fidelity means these methods do not lend themselves to consideration of a broad range of vehicle configurations and flight conditions. As a result, the literature lacks a comprehensive study of a generic propulsion-pitch coupled air-breathing hypersonic vehicle flying at a wide range of representative flight conditions. For example, the dynamics of a coupled air-breathing hypersonic vehicle may be quite different at subsonic and supersonic velocity than at hypersonic velocity. Vehicle dynamics, and the requirements

they impose on control actuators, are not known for an entire mission profile for a representative coupled air-breathing hypersonic vehicle.

2.2 Control System Requirements

The requirements of the control system are driven by the dynamic modes of the vehicle, which were summarised in Table 2.1. Sensitivity analyses have shown that vehicle dynamics vary significantly with small changes to flight conditions (i.e. Mach number and altitude) in the hypersonic regime (Rodriguez et al., 2008). As described in the previous section, accurate estimation of vehicle dynamics is hampered by dynamic coupling, sensitivity to free-stream conditions, and uncertainty in hypersonic flow phenomena such as boundary layer transition.

For a vehicle controlled by a closed-loop to be stable, the control system bandwidth must be greater than the frequency of the unstable poles (Doman et al., 2006). Stein (2003) provided a rule-of-thumb that, to be robust, the control system bandwidth should exceed the frequency of the most unstable pole by a factor of 10.

From the data in Table 2.1, the frequency of the most unstable longitudinal rigid-body pole of a coupled air-breathing hypersonic vehicles has been estimated at approximately 0.4 Hz at a single, trimmed, hypersonic flight condition. As mentioned previously, the coupled dynamics across the full range of potential flight conditions have not been quantified in the open literature.

It has also been shown that unsteady aerodynamics can increase this frequency by up to 50% (Oppenheimer et al., 2007), and that the frequency is sensitive to flight conditions (Rodriguez et al., 2008). For example, a decrease in cruise altitude from 33.5 km to 24.4 km at Mach 8 increases the frequency of the unstable short-period mode in a flexible, propulsion-pitch coupled vehicle by 85% (Rodriguez et al., 2008). Accounting for these factors, the rule-of-thumb requires a control bandwidth of approximately 10 Hz to control longitudinal rigid-body modes in a typical trimmed hypersonic cruise condition. Structural and aero-elastic modes introduced by propulsion-pitch coupling can further increase the control requirements by introducing unstable modes at high frequencies, beyond 30 Hz (Chavez and Schmidt, 1994b), thus pushing the required bandwidth up to approximately 300 Hz if active control of these modes is required, as suggested by Heeg et al. (1993). Manoeuvre requirements may further increase the required bandwidth beyond 300 Hz.

In addition to instability problems, Bolender and Doman (2007) identified non-minimum phase behaviour between the elevator and flight path angle. To command an increase in flight path angle using conventional aerodynamic control, the elevator lift is reduced to create a nose-up pitching moment. This reduction of lift momentarily reduces the overall lift on the vehicle, causing an initial decrease in altitude. This phenomena will limit the bandwidth of an aerodynamic control system, as the closed-loop bandwidth must be less than the frequency of the smallest non-minimum phase zero (Doman et al., 2006), ideally by a factor of two (Echols et al., 2015). Doman et al.

(2006) suggested adding a canard, which operates in conjunction with the elevator, to overcome this difficulty. However, such a solution introduces issues with heating and structural strength, therefore reducing reliability of the control system (Dickeson et al., 2010). Further limitations are placed on the maximum control system bandwidth, in that the control system should not excite the flexible modes of the vehicle, unless these modes are also actively controlled (Echols et al., 2015).

In summary, high frequency, unstable dynamic modes are a feature of air-breathing hypersonic vehicles. High-bandwidth control is required for these vehicles, with estimated frequencies up to 30 Hz, based on a rule-of-thumb to control the rigid-body modes of coupled vehicles at a single, hypersonic flight condition. If active control is required for structural and aero-elastic modes, the control bandwidth increases to 300 Hz. Even without the rule-of-thumb for a robust control system, the minimum requirement to maintain stability is approximately 3 Hz for rigid-body modes and 30 Hz for structural and aero-elastic modes.

2.3 Actuator Properties

The previous sections show that the control actuator requirements of air-breathing hypersonic vehicles are demanding. Specifically, the control actuator bandwidth requirements far exceed those of a conventional subsonic or supersonic aircraft, due to the unique propulsion-pitch coupling effects. This section reviews the properties of common control actuators, to assess their ability to meet these bandwidth requirements, while maintaining the required control authority. Several actuator types have been considered, and their strengths and weaknesses will be briefly summarised in this section.

Aerodynamic control surfaces are the primary method of control actuation for conventional aircraft, due to their simple layout and precise force and moment application. There is no need to store additional fuel to operate the actuators, and their performance in terms of both control authority and bandwidth is adequate for most subsonic and supersonic aircraft (FAA, 2004). However, aerodynamic control surfaces have limitations at low dynamic pressure (Anderson, 2006); can become ineffective at high angle-of-attack (Kaufman et al., 1965); and add weight and drag when used to control an unstable vehicle (Shaughnessy and Gregory, 1991). Further, vehicles with aerodynamic control surfaces may exhibit non-minimum phase behaviour, which is important for integrated air-breathing vehicle configurations (Doman et al., 2006).

The maximum deflection rate of aerodynamic control surfaces is limited to approximately 150 deg/s, (Davidson et al., 2001; Ryu and Andrisani, 2003), or approximately 10 – 12 Hz, depending on deflection limits (Stein, 2003; Anderson and Knight, 2012). At higher rates, valve dynamics, hydraulic fluid compressibility, and structural dynamics begin to take effect. More complex control surfaces, such as stabilators, can have much lower deflection rate limits, around 24 deg/s for a high performance aircraft, according to Brumbaugh (1994). With these limits imposed, aerodynamic control is not sufficient

to ensure stability of an air-breathing hypersonic vehicle, where control bandwidth greater than 30 Hz is required.

To reduce instability and allow controlled flight with aerodynamic control surfaces, current hypersonic vehicle designs, including the NASA X-43A (Peebles, 2008) and Australian Defence Science and Technology (DST) Group / US Air Force Research Laboratory (AFRL) Hypersonic International Flight Research Experimentation (HIFiRE) 4 (Smith et al., 2011) vehicles are required to use ballast. This is undesirable, as it reduces or constrains the payload capacity of the vehicle. Even with ballast and without propulsion, and therefore without propulsion-pitch coupling, the HIFiRE 4 vehicle is unstable over a significant portion of the flight envelope, and is limited to high angle-of-attack and low dynamic pressure flight conditions to maintain controllability (Smith et al., 2011). In the case of the X-43A, the ballast was sufficient to ensure longitudinal static stability, but constituted approximately 30% of the total vehicle mass (Peebles, 2008). Other vehicles, such as the Space Shuttle (Chazen and Sanscrainte, 1974; Kanipe, 1983), the US Army Terminal High Altitude Area Defense (THAAD) missile (Chamberlain et al., 2000), and other modern re-entry vehicle designs (Alkandry, 2012; Pezzella and Viviani, 2016), use reaction control jets or body flaps to supplement conventional aerodynamic control, primarily in low dynamic pressure environments.

The control authority of aerodynamic control surfaces is limited only by their size, deflection limits, and the free-stream dynamic pressure. However, large control surfaces are heavy and cause more drag. At high dynamic pressure, where aerodynamic control surfaces are most effective, aerodynamic heating limits the maximum deflection at hypersonic Mach numbers.

Reaction control jets are an attractive alternative, or supplement, to aerodynamic control surfaces, especially for operation in the upper atmosphere, due to their ability to operate in a low dynamic pressure environment. RC jets also have the advantage of producing near-zero drag when not in operation, but add weight if fuel must be carried.

The effectiveness of RC jets operating in the atmosphere is complicated by the interaction between the jet and crossflow. This interaction can increase or decrease the force applied by the actuator, and can also change the effective location where the force acts, therefore changing control moments. This complexity makes RC jets an infrequent design choice for endo-atmospheric operation. RC jets are, however, often installed on hypersonic vehicles for exo-atmospheric operation, as mentioned previously.

The bandwidth limit of RC jets depends on the mechanism through which the jet fluid is supplied. Cutler and Drummond (2008) demonstrated a pulsed jet operating up to 1400 Hz. However, when operated in a crossflow, the time taken for the steady interaction force to establish, and the transient start-up behaviour, is highly uncertain, and depends on many variables. Ebrahimi (2000) showed that the steady interaction force takes approximately 6 ms to establish, and another 5 ms to shut down in a Mach 5 crossflow, corresponding to a maximum usable bandwidth of around 100 Hz. Further analysis of the interaction between RC jets and crossflow is provided in Section 2.4.

Similar to aerodynamic control, the control authority that can be provided by RC

jets is high; limited only by the thrust that can be produced by the jet, which depends on fuel capacity, fuel supply pressure, fuel type, and nozzle design.

External burning can increase the control force provided by RC jets by increasing the pressure in the interaction region (Cassel, 2003). However, this comes at a cost of increased local heating and requires an ignition source and reactive fuel (Cattafesta and Sheplak, 2011). This increases actuator complexity and further complicates the crossflow interaction. Further, the difficulties associated with external combustion at supersonic and hypersonic speeds mean external burning actuators at not yet feasible for hypersonic vehicles.

There are other actuator types that may be used to supplement aerodynamic control. Plasma actuation is a popular method of flow control and several different types of plasma actuator have been developed for this purpose. Plasma actuators may also be used to generate a fuel source for RC jets. However, plasma actuators such as dielectric-barrier-discharge (DBD) actuators have low efficiency, primarily due to the high voltage power source required (Seifert, 2007), and rely on augmentation of the control force by flow phenomena such as boundary layer instabilities (Corke et al., 2010). The control authority available from plasma actuators with current technologies was shown by Ferry and Rovey (2010) to be insufficient to control a vehicle.

Thrust vectoring is another commonly used means of increasing manoeuvrability, especially at low dynamic pressure (Doman et al., 2006), and has proven to be an effective control actuator to supplement aerodynamic control for rocket and jet-turbine powered vehicles. However, low thrust margins available with a scramjet engine, and the difficulties associated with dynamic propulsive-pitch coupling, makes thrust vectoring unattractive for an integrated air-breathing hypersonic vehicle.

Other means of control, such as electro-magnetic and magneto-hydro-dynamic actuators, are generally intended for specialised applications (Cattafesta and Sheplak, 2011), and are not sufficiently developed to be suitable for manoeuvring and control of an air-breathing hypersonic vehicle.

In summary, while aerodynamic control remains the prevalent method applied to air-breathing hypersonic vehicles, significant design trade-offs including ballast, trajectory modifications, and complex controller designs are required to accommodate the bandwidth limits imposed by propulsion-pitch coupling, non-minimum phase behaviour, and high frequency structural and aero-elastic modes. RC jets are an attractive alternative, or supplement, as they provide high bandwidth and authority and may already be fitted to the vehicle for exo-atmospheric operation. This study will consider the application of RC jets to provide high bandwidth control to replace or supplement aerodynamic control surfaces on air-breathing hypersonic vehicles.

2.4 Reaction Control Jet Interaction

When operated in the atmosphere, force is generated by a reaction control jet via two mechanisms: the thrust of the jet, and the interaction between the jet and crossflow,

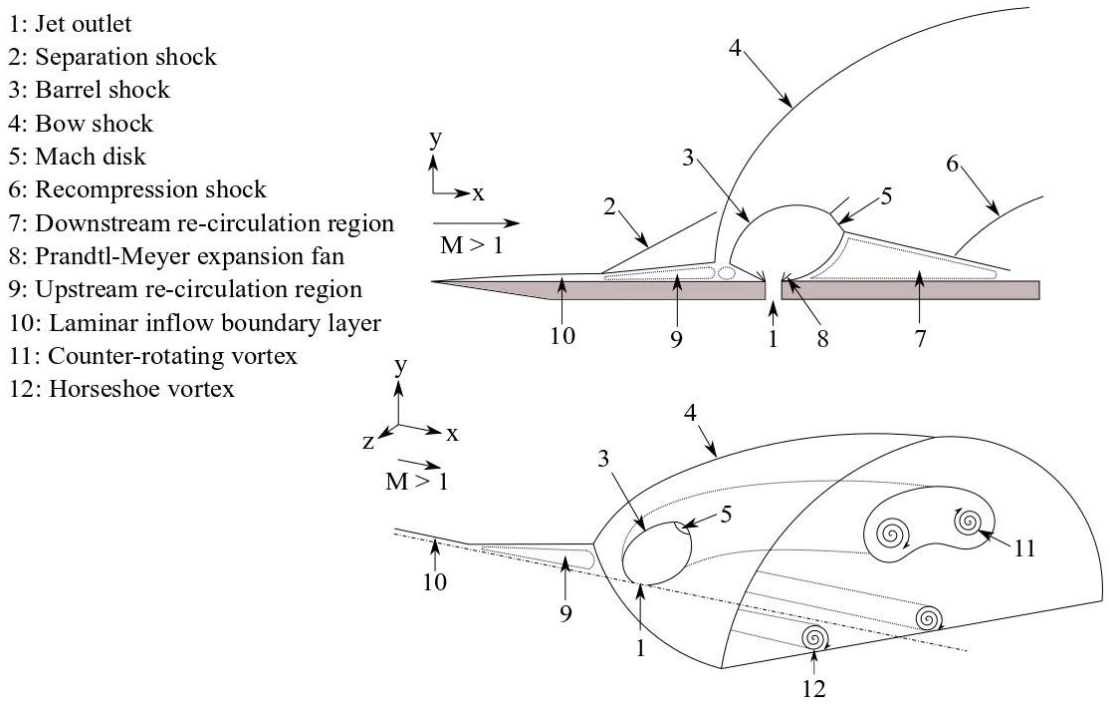

Figure 2.2: Schematic of the two- and three-dimensional time-averaged interaction flow-field of a reaction control jet in supersonic crossflow.

caused by the induced pressure distribution on the surface of the vehicle. Thrust can be determined through the general thrust equation (Anderson, 2001):

$$T = \dot{m}_j U_j + A_j \left(p_j - p_a\right) \tag{2.1}$$

where T is the jet thrust, $\dot{m}_j$, U_j, A_j and p_j are the mass flow rate, velocity, area and pressure at the jet exit respectively, and p_a is the atmospheric pressure in the jet region.

The jet-in-crossflow interaction is complex, unsteady, and can significantly affect the total control force. The physics controlling the interaction force between a sonic, under-expanded jet and supersonic crossflow has been the subject of a large body of research, comprehensive reviews have been provided by Margason (1993) and Mahesh (2013). Early experimental studies determined various aspects of the flow structure, including shock shape and location, jet concentration profiles, geometry of separated flow regions, and pressure fields (Spaid and Zukoski, 1968; Mahaffey et al., 1968; Rogers, 1971).

A schematic of a typical time-averaged shock and vortex structure is shown in Figure 2.2. The obstruction caused by the jet generates a bow shock (4) in the free-stream. The velocity of the free-stream flow, outside the boundary layer, increases in the transverse direction, due to the curvature of the bow shock. The approaching crossflow is turned upward as the boundary layer grows directly upstream of the jet, forming a re-circulation region (9) within the separated boundary layer. The internal structure of the jet is initially similar to that of a jet in quiescent atmosphere (Adamson and Nicholls, 1959). The under-expanded jet initially expands through a Prandtl-Meyer

expansion fan (8), centred at the edge of the jet nozzle, and expands rapidly before being compressed through the barrel shocks (3) and a Mach disk (5). In the near-field, the jet fluid flows vertically for approximately one jet diameter, depending on crossflow boundary layer thickness, before it is influenced by the crossflow (Schetz et al., 1967). The jet fluid passing through the Mach disk loses momentum and is quickly turned downstream by the crossflow. However, much of the jet fluid passes through the weaker oblique barrel shocks, maintaining its momentum (Santiago and Dutton, 1997). The greatest jet penetration is achieved by high momentum flow passing through the windward side of the barrel shock. Papamoschou et al. (1991) performed a parametric experimental study to confirm that jet penetration depends primarily on jet-to-crossflow momentum ratio J, defined by Schetz and Billig (1966) as follows:

$$J \equiv \frac{\rho_j U_j^2}{\rho_\infty U_\infty^2} = \frac{\gamma_j p_j M_j^2}{\gamma_\infty p_\infty M_\infty^2} \tag{2.2}$$

where ρ is density, M is Mach number, γ is the ratio of specific heats, and subscripts j and ∞ refer to the jet and free-stream respectively. Empirical relations for estimating jet penetration were derived by Papamoschou and Hubbard (1993) using this definition, and many similar relationships have been developed for various jet and crossflow conditions, for example: Keffer and Baines (1963); Smith and Mungal (1998); Hasselbrink and Mungal (2001); Muppidi and Mahesh (2005); Portz and Segal (2006).

The Mach disk is a normal shock that creates a region of subsonic flow. This forms a slip surface with the supersonic crossflow, and these two streams form a mixing layer at the top edge of the jet trajectory, at up to three times the height of the Mach disk (van Lerberghe et al., 2000). A single horseshoe vortex (12) is present near the plate and wraps around the base of the jet (Rana et al., 2011), while a counter-rotating vortex pair (11) dominates the far-field (Beresh et al., 2005), although smaller vortices exist, including upper and lower trailing vortices (Viti et al., 2009; Sun and Hu, 2018). The single counter-rotating vortex pair emerges in the time-averaged flow-field from the merging of these smaller vortices into a single coherent longitudinal vortex pair. Downstream, a reflected shock extends from the triple point, where the barrel shock intersects the Mach disk, and impinges on the plate. This impingement causes the boundary layer to suddenly thicken, creating a weak shock (6). The reflected shock from the upstream triple point is often indistinguishable as a result of the strong interference created by the bow shock and crossflow. The downstream re-circulation region (7) is smaller in a supersonic crossflow than that observed for jets in subsonic crossflow, due to a reduction in entrainment of crossflow (Santiago and Dutton, 1997). In a supersonic crossflow, the flow downstream of the barrel shock accelerates rapidly due to crossflow fluid that has moved laterally around the barrel shock and impinges on itself in the plane of symmetry.

A triangular concave region of the barrel shock was identified by Viti et al. (2009) immediately downstream of the jet outlet, caused by reflection of the barrel shock from the plate. This forms a channel on the leeward side of the barrel shock, creating a

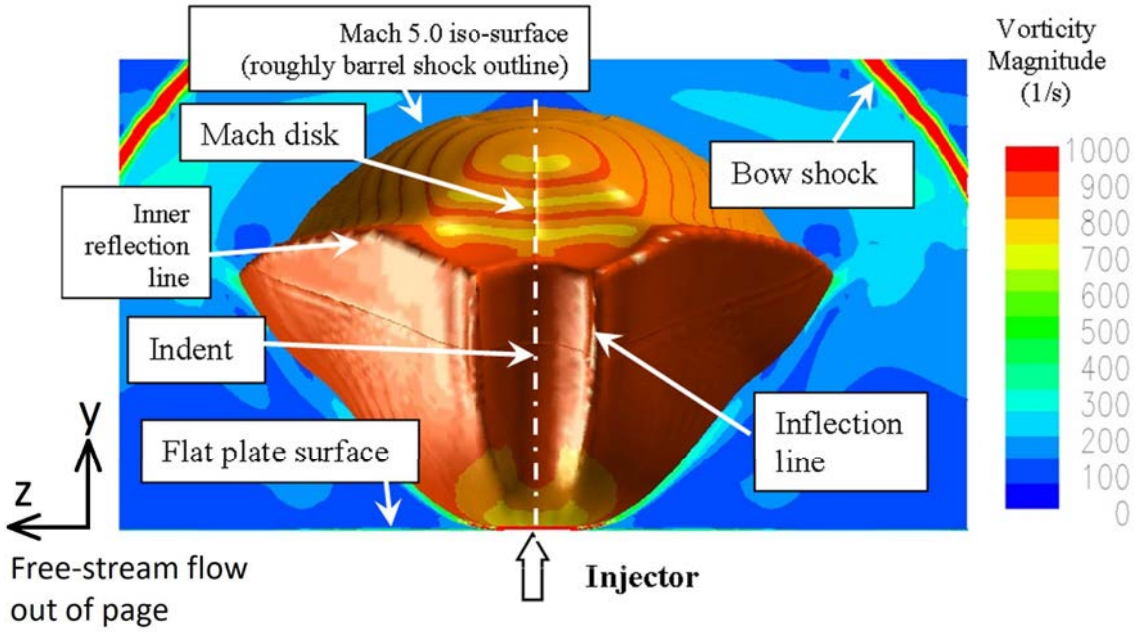

Figure 2.3: Mach 5 iso-surface (approximate location of barrel shocks) of a sonic, perfect air jet in Mach 4 crossflow, coloured by contours of vorticity magnitude, showing concave region and internal reflection line on the barrel shock (Viti et al., 2009).

region of low pressure, which is counterproductive for reaction control jet applications. An internal reflection line is also created by folding of the barrel shock. These appear as fin-like structures that extend along the barrel shock (Viti et al., 2009). These structures are shown in Figure 2.3.

All the aforementioned flow structures combine to induce a pressure distribution on the body, resulting in the interaction force. There are two main features of the interaction force. High pressures in the upstream re-circulation region augment the force produced by the jet thrust (Brandeis and Gill, 1996), while a large low pressure region downstream of the injector decreases the force (Spaid and Zukoski, 1968). The low pressure region downstream couples with the high pressure upstream to form a pitching moment around the injector. A well designed injection system requires detailed knowledge of the flow-field and the flow structures responsible for these high and low pressure regions. Once these structures are understood, they can be altered to improve the performance of the injection system (Viti et al., 2009).

While the time-averaged flow-field described above is well documented, these structures exhibit significant temporal variations. If the RC jet is operated at high frequency, the time-dependent aspects of the interaction become important to the overall control force applied by the jet. Previous work has focused on time-averaged or instantaneous flow-fields, but has not identified the dynamic nature of the flow, or provided a detailed explanation of the wall pressure distribution and interaction force. Additionally, previous studies into detailed physics of jets in crossflow have been limited to subsonic and supersonic ($M_\infty < 5$) crossflows. High fidelity numerical methods, such as large-eddy simulation (LES), have not been applied to the jet in hypersonic crossflow.

In the unsteady flow, horseshoe vortices form upstream of the jet leading edge in the re-circulation region. In a subsonic crossflow, Kelso et al. (1996) observed that the downstream structure of the horseshoe vortex depends on the sign of vorticity. Horseshoe vortices with vorticity the same sign as the wall boundary layer extend downstream along the flat plate and are incorporated into the wake. Horseshoe vortices with the opposite sign to the boundary layer are lifted from the wall. Kelso et al. (1996) also observed that horseshoe vortices in subsonic crossflow fall into one of three regimes: steady, oscillating, or coalescing. The specific regime determines whether two or three distinct vortices are present. Oscillations and periodicity were observed by Krothapalli et al. (1990) at certain jet-to-crossflow velocity ratios, while several other studies have shown a steady horseshoe vortex (Ruiz et al., 2015). The horseshoe vortex regimes influence the unsteady surface pressure upstream of the jet outlet, and therefore will influence the control force.

In a supersonic crossflow, Viti et al. (2009) used a Reynolds Averaged Navier Stokes (RANS) approach to observe time-averaged horseshoe vortex behaviour similar to that of a subsonic crossflow. Fluid from the upstream re-circulation region with vorticity the opposite sign to the wall boundary layer was transported from the wall and deposited behind the jet to form part of the counter-rotating vortex pair, while fluid from vortices with the same sign as the wall boundary layer travelled downstream along the plate. Additional vortices within the re-circulation region have been reported in other studies (Chenault and Beran, 1998), which behave in a similar manner, depending on the sign of vorticity. Although it is critical to the formation of the high pressure region upstream of the jet outlet that augments the control force, investigations into the structure of the horseshoe vortices for supersonic crossflows with a laminar in-flow boundary layer have not been reported.

There is another large re-circulation region downstream of the jet outlet, where the flow remains separated from the plate. In this region, the time-averaged velocity field is dominated by a single streamwise-oriented counter-rotating vortex pair (Beresh et al., 2005). The single counter-rotating vortex pair observed in the time-averaged flow emerges from the merging of three smaller, longitudinal trailing vortices (Viti et al., 2009); two vortices are developed by interaction between the slow jet fluid downstream of the Mach disk and the fast free-stream, the other originates on the windward side of the barrel shock. These three vortices rotate with respect to each other around a common longitudinal axis, as shown in Figure 2.4, and combine to form a single counter-rotating pair in the time-averaged flow-field. While the existence and origin of these vortices has been reported (Viti et al., 2009; Sun and Hu, 2018), their unsteady motion has not been detailed. As these vortices dominate the far-field, their unsteady motion is likely to have a significant influence on the interaction force.

Other longitudinal vortices have been identified (Viti et al., 2009; Kawai and Lele, 2009; Rana et al., 2011), the structure of which depends on free-stream Mach number. Kawai and Lele (2009) used LES to investigate the jet in supersonic crossflow at Mach 1.6, using a rescaling-reintroducing method to generate inflow turbulence. Kawai

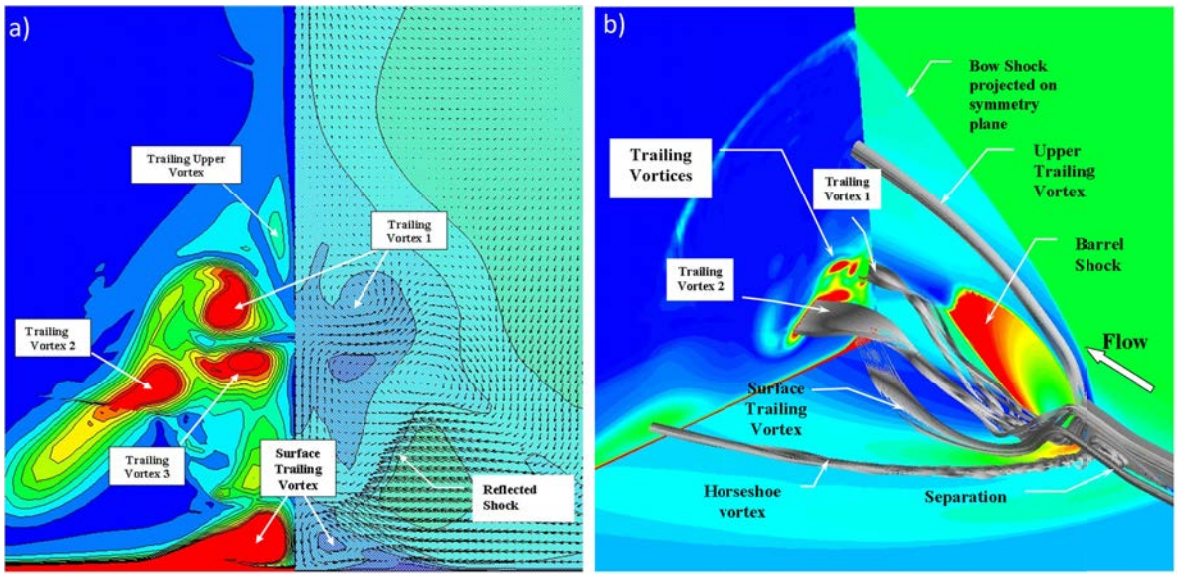

Figure 2.4: Sonic, perfect air jet in Mach 4 crossflow, adapted from Viti et al. (2009). (a) Cross-plane mappings of vorticity magnitude (left) and Mach number (right) with velocity vectors superimposed, at 15 jet diameters downstream of the jet outlet, and (b) Isometric view of the flow around the injector, highlighting the main vortical structures.

and Lele (2009) identified a set of counter-rotating vortices inside the boundary layer in the wake region, and proposed that these were induced by suction from the counter-rotating vortex pair. Viti et al. (2009) contend that these vortices originate in the re-circulation region immediately upstream of the jet outlet, which is supported by the Direct Numerical Simulations (DNS) of Sun and Hu (2018). Viti et al. (2009) also found that, in the time-averaged flow-field of a jet in a Mach 4 crossflow, there is an upper set of counter-rotating vortices, that follow the leading edge of the bow shock away from the plate. These were not observed by Rana et al. (2011) using implicit LES at Mach 1.6 with a digital filter based turbulent inflow data generation method, but were observed by Kawai and Lele (2010) in the same Mach 1.6 flow, using a finer mesh. Sun and Hu (2018) investigated upper trailing vortices in detail at a Mach 2.7 flow condition. They found that upper trailing vortices are weak, are more prominent at high momentum ratio, and rotate in the opposite direction to the primary counter-rotating vortices. These vortices are generated by baroclinic production due to shear between flow through the Mach disk, and high-speed flow around the barrel shock.

Several structures are present in the unsteady jet-in-crossflow interaction that are not observed in the time-averaged flow-field. Jet shear-layer vortices form at the upstream barrel shock, and are shed periodically due to Kelvin-Helmholtz instability in the shear-layer. The behaviour of these vortices depends on jet-to-crossflow velocity ratio, $R = U_j/U_\infty$; jet pressure, p_j; jet Reynolds number, $Re_{dj} = U_j d_j/\nu_j$; and jet pipe geometry (Fric and Roshko, 1994).

Several authors have proposed different mechanisms for the development and evolution of jet shear-layer vortices in a subsonic crossflow. Broadwell and Breidenthal (1984) initially described the vortices as being formed due to the jet normal force,

or "lift" force analogous to tip vortices on finite wings. Kelso et al. (1996) detailed a proposed mechanism of jet shear-layer evolution from a round jet with high Reynolds number injected flush into a subsonic crossflow. The proposed shear-layer development consists of a periodic vortex roll-up and separation caused by Kelvin-Helmholtz instability similar to a free jet, superimposed with a re-orientation imposed by the crossflow. This results in a "tilting-and-folding" process that aligns the vortex rings with the direction of the jet, thus contributing to the formation of the counter-rotating vortex pair. This interpretation of vortex development is supported by the numerical simulations of Cortelezzi and Karagozian (2001); however, Lim et al. (2001) provide an alternate explanation, that the cylindrical jet shear-layer rolls up to form two independent rows of vortex loops, one upstream (windward) and one downstream (leeward). These arms contribute to the vorticity of the counter-rotating vortex pair, but folding and bending of individual coherent vortex rings is not required. Rather, individual shear-layer segments roll up on either the windward or leeward side of the jet, but not on both. This interpretation is supported by Marzouk and Ghoniem (2007). Yet another mechanism is proposed by Yuan et al. (1999), where LES showed that quasi-steady hanging vortices formed in mixing layers at the edge of the jet coincide with lateral roll-ups of the shear-layer and an adverse pressure gradient causes them to break down into the counter-rotating vortex pair. The direction of the shear-layer vorticity depends on the local velocity ratio between the jet and crossflow.

Smith and Mungal (1998) observed that the formation of the jet shear-layer vortices is delayed in a subsonic crossflow with increased velocity ratios, $R > 5$. Recent work in subsonic crossflows shows that this delayed formation is not related to velocity ratio, but rather to shear-layer instabilities (Getsinger et al., 2014; Karagozian, 2014; Gevorkyan et al., 2016). There are two distinct mechanisms for jet shear-layer roll-up in subsonic crossflow. For jets with "absolutely unstable" shear-layers, there is a rapid, or immediate shear-layer vorticity roll-up. This corresponds to formation of a clear, symmetric counter-rotating vortex pair (Gevorkyan et al., 2016). This behaviour is observed for jets with low jet-to-crossflow momentum ratio (J) and low velocity ratio (R). If the shear-layer is "convectively unstable", the shear-layer vorticity roll-up is delayed. This can result in an asymmetric, or non-existent longitudinal vortex-pair in the mean jet cross-section, which has been observed in high J, high R cases. At lower jet-to-crossflow momentum ratio, the location of shear-layer roll-up moves closer to the jet exit and the spacing between individual vortices is reduced (Gevorkyan et al., 2016). This information allows significant increases in penetration and mixing to be achieved through tailored pulsing schemes (Karagozian, 2014). Figure 2.5 shows the relationship between the shear layer vortices and the longitudinal counter-rotating vortex pair. Different roll-up mechanisms in the shear-layer result in different vortex structures.

The evolution of shear-layer vortices in supersonic crossflow is more complex than subsonic crossflow, although the structures are qualitatively similar (Chai et al., 2015). In a supersonic crossflow, when jet velocity is low compared to free-stream velocity (i.e.

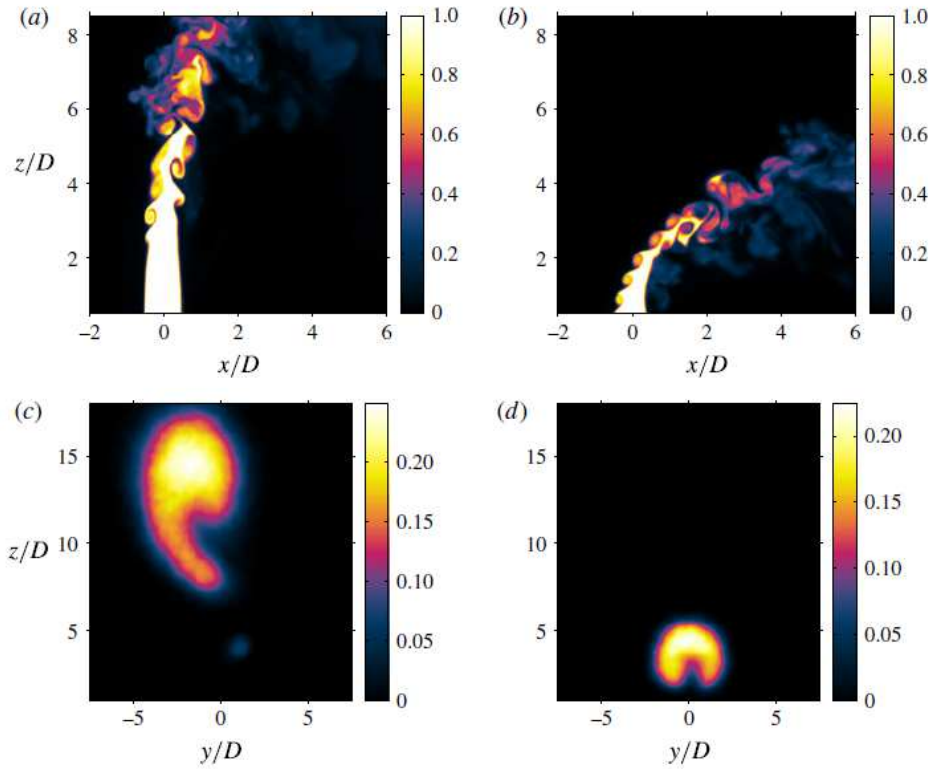

Figure 2.5: Instantaneous centreplane images and time-averaged cross-sectional slices at $x/d = 5.5$ of flush nozzle-generated jet in subsonic crossflow, adapted from Gevorkyan et al. (2016). (a) $J = 41$, (b) $J = 5$, (c) $J = 41$, and (d) $J = 5$.

$R \lesssim 2$), shear-layer vortices take the form of hair-pin vortices, rather than vortex rings (Sau and Mahesh, 2010). As a result, the shear-layer vortices are sometimes referred to as hair-pin vortices in this regime (Andre et al., 2017).

Large variations in size, shape, symmetry and periodicity of shear-layer vortices in supersonic crossflow were observed experimentally by van Lerberghe et al. (2000). Kawai and Lele (2009) reported periodic shear-layer vortex shedding at Strouhal Numbers, $St_\infty = 0.4 - 0.6$, based on jet diameter and free-stream velocity, $St_\infty = f \times d_j/U_\infty$, in a Mach 1.6 crossflow, with a jet-to-crossflow momentum ratio, $J = 1.7$ and a turbulent in-flow boundary layer. Chai et al. (2015) reported a dominant global mode at $St_\infty = 0.3$ at the same conditions, based on an explicit LES using the dynamic Smagorinsky sub-grid model, with turbulent inflow data generated from a separate simulation of boundary layer transition. Ben-Yakar (2000) reported a shedding frequency of $St_j = 1$, based on jet diameter and jet outlet velocity, $St_j = f \times d_j/U_j$, for a higher free-stream Mach number flow with higher jet-to-crossflow momentum ratio ($M_\infty = 3.4$, $J = 4.1$); while Andre et al. (2017) investigated the development of shear-layer vortices using implicit LES for a range of pressure ratios in a Mach 4.2 crossflow. Based on a detached-eddy simulation (DES) of hydrogen injection into Mach 3.38 crossflow with a finite-rate chemistry model, Won et al. (2010) claimed that the shear-layer vortices form in counter-rotating pairs, although this has not been supported by other studies.

Jet shear-layer vortices are convected downstream at a velocity approaching the free-stream velocity. Gruber et al. (1997) tracked the development and convection of jet shear-layer vortices for circular and elliptical jets, using both air and helium, in a Mach 2 crossflow, at $J = 1.9$. Similar studies have been conducted (Ben-Yakar et al., 2006; Takahashi et al., 2010; Watanabe et al., 2012, 2013) to track shear-layer vortex convection, stretching, and tilting. Differences in convective and mixing properties have been observed for different injectant species. Shear-layer vortices were found to persist long distances for hydrogen jets, while ethylene jets tended to break down nearer the jet exit. Ben-Yakar (2000) concluded that the different behaviour was due to the lower jet exit velocity of ethylene (315 m/s) compared with hydrogen (1205 m/s) for a given jet-to-crossflow momentum ratio. Therefore, ethylene eddies are exposed to larger velocity gradients across the shear-layer when exposed to a hypersonic (Mach 3.38, 2360 m/s) crossflow.

Wake vortices are unsteady, upright, tornado-like vortices present immediately downstream of the jet exit. Fric and Roshko (1994) suggest that, in subsonic crossflow, wake vortices originate in the boundary layer and terminate in the counter-rotating vortex pair. However, jet fluid has also been observed to flow into the boundary layer in subsonic crossflow, for velocity ratios $5 < R < 32$ (Mahesh, 2013). In subsonic crossflows, at high Reynolds numbers, with $R < 3$, these upright vortices are shed irregularly. When $R > 3$ the upright vortices become more periodic and larger in scale (Kelso et al., 1996). Two mechanisms for the arrangement of wake vortices was identified by Kelso et al. (1996), corresponding to either alternating signs of eddy circulation, or to pairs of eddies forming mushroom-like structures.

In comparison to subsonic crossflow, wake vortices formed in a supersonic crossflow tend not to be organised, and are much less distinct than the shear-layer vortices (van Lerberghe et al., 2000). Organised upright wake vortices are most prominent once the jet has completed most of its turning, and are absent nearer the injector, where the jet is turning considerably. van Lerberghe et al. (2000) observed these vortices for $J = 1.7$, while Smith and Mungal (1998) only observed jet fluid in the wake when $J > 100$ for a subsonic incompressible jet-in-crossflow.

Ruiz et al. (2015) observed additional v-shaped vortices on the windward side of the jet shear-layer in subsonic crossflow, using LES. These vortices grow from azimuthal instability of the ring vortices, which produces small counter-rotating vortex pairs with a rotational axis parallel to the jet axis. These v-shaped vortices are thought to be responsible for the observed deposition of jet fluid in the upstream crossflow, but have not been reported in supersonic crossflows.

The shock structure also contains a number of unsteady features. Santiago and Dutton (1997); van Lerberghe et al. (2000) observed unsteadiness in the barrel shock region, most visible as a periodic flattening of the windward barrel shock into two or more straight segments that join at sharp corners. At other times, indentations or rippling was also observed in the bow shock, with little or no shock movement. Kawai and Lele (2009) identified the source of both the periodic flattening of the barrel shock

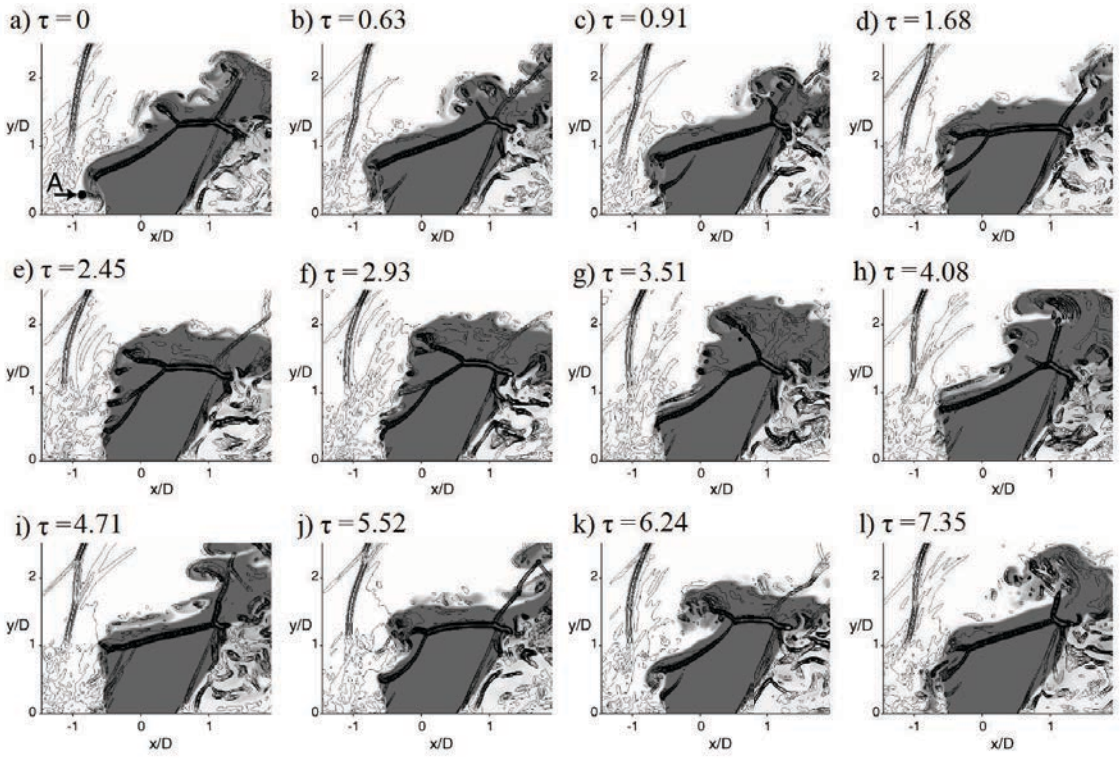

Figure 2.6: Instantaneous flow through the jet centreline showing the interaction between a fully established sonic air jet with a supersonic ($M_\infty = 1.6$) crossflow, with $J = 1.7$, adapted from Kawai and Lele (2010).

and deformation of the bow shock as pressure fluctuations inside the upstream re-circulation region. The instantaneous shock structure for an under-expanded jet in supersonic crossflow is depicted in Figure 2.6, from the LES of Kawai and Lele (2010), showing barrel shock deformation at non-dimensional times, $\tau = t \times U_\infty / d_j$.

Although it is critical to the formation of the high pressure region upstream of the jet outlet that augments the control force, investigations into the unsteady shear-layer vortex structure for hypersonic ($M_\infty > 5$) crossflows with a laminar in-flow boundary layer have not been reported. Chai et al. (2015); Kawai and Lele (2010) considered a laminar in-flow boundary layer at the same flow conditions as Santiago and Dutton (1997) ($M_\infty = 1.6$, $J = 1.7$). With the boundary layer thickness matched to the experimental (turbulent) boundary layer, the shear-layer vortex shedding is reduced from $St_\infty = 0.4 - 0.6$ to $St_\infty = 0.2$, and the upstream and downstream re-circulation regions are larger, driving significant differences in wall pressure distributions. The influence of the thicker laminar in-flow boundary layer expected at higher free-stream Mach number has not been reported.

In addition, while significant attention has been paid to the shear-layer vortices, the unsteady motion of horseshoe vortices in the upstream re-circulation region and the longitudinal trailing vortices downstream has not been detailed in a supersonic or hypersonic crossflow with a laminar in-flow boundary layer.

2.4.1 Pulsed Jet in Crossflow

This thesis is focused on the application of reaction control jets to supplement aerodynamic control surfaces and provide high frequency control. High frequency control requires the jet to be switched on and off on-demand. This is akin to operating in a pulsed mode.

Operating in a pulsed mode adds complexity to the flow. Increased jet penetration has been the focus of pulsed jet research to date, as deeper penetration is desirable in many jet-in-crossflow applications. For example, increasing jet penetration increases mixing rate, which is critical in scramjet engines with a short residence time (Murugappan et al., 2005).

There have been extensive studies of pulsed jets in subsonic crossflows (Chang and Vakili, 1995; Hermanson et al., 1998; Johari et al., 1999; Eroglu and Breidenthal, 2001; M'Closkey et al., 2002; Shapiro et al., 2006; Sau and Mahesh, 2008, 2010). Previous studies have shown that penetration and spread of a pulsed jet is significantly higher than a steady jet, and can be maximised in certain conditions. The effects of Strouhal number, stroke ratio, L/D, where a column of fluid with length L is ejected through a nozzle with exit diameter D, injection type, and momentum flux on penetration were considered in subsonic crossflow. M'Closkey et al. (2002) showed that square-wave excitation is more effective than sinusoidal forcing at increasing jet penetration. Low frequency forcing yields significant increases in penetration depth, while high frequency forcing, at frequencies near the natural shear-layer instability, does not cause appreciable change in jet penetration over a steady jet (Eroglu and Breidenthal, 2001; Narayanan et al., 2003). In addition, long injection times yield moderate enhancement over a steady jet, while short injection times and a small duty-cycle (defined as the ratio of pulse width to the pulsing time period) yields significant enhancement (Johari et al., 1999). Sau and Mahesh (2008, 2010) described variation in vortex structure and penetration depth of a pulsed jet in subsonic crossflow, which strongly depends on L/D and velocity ratio, and identified three regimes: low velocity ratio, where hairpin-type shear-layer vortices form rather than ring-type; high velocity ratio at high stroke ratio where ring-type vortices are accompanied by a trailing column of vorticity, as observed in a quiescent atmosphere (Gharib et al., 1998); and high velocity ratio at low stroke ratio, where ring-type vortices are not accompanied by a trailing column of vorticity. At high velocity ratio, optimal penetration is observed at the transition from distinct ring-type vortices to ring-type vortices with trailing vorticity sheets.

Further studies of pulsed jets in subsonic crossflow have been performed in the context of improving jet penetration and mixing (Getsinger et al., 2014; Karagozian, 2014; Gevorkyan et al., 2016). These studies found that optimisation of jet penetration depth depends on shear-layer stability. This allows penetration to be increased for both high velocity ratio and low velocity ratio jets. These studies also show that shear-layer stability is closely related to the formation and symmetry of the longitudinal counter-rotating vortex pair in the mean flow-field, as described previously. At high momentum

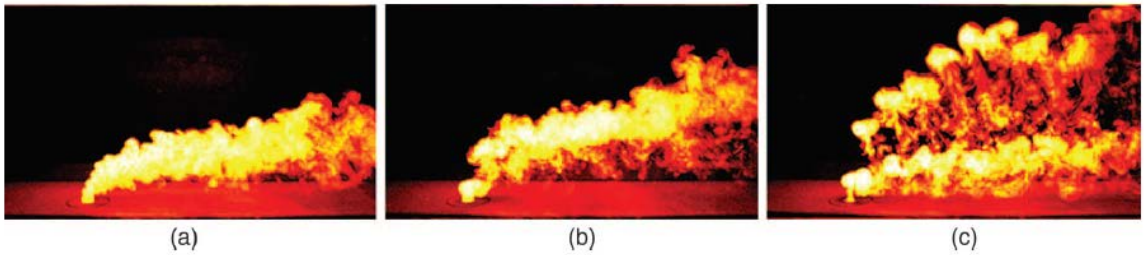

Figure 2.7: Smoke visualisation of a jet injected into a subsonic ($U_\infty = 1.2$ m/s) crossflow from a flush nozzle at an average velocity ratio of $R = 2.58$. (a) Un-forced jet, (b) Pulsed jet, with sine-wave pulsing at one-third of the natural shear-layer vortex shedding frequency, (c) Pulsed jet, with square-wave pulsing at one-third of the natural shear-layer vortex shedding frequency with a 22% duty cycle. Adapted from M'Closkey et al. (2002).

ratio and high velocity ratio, the shear-layer is convectively unstable, resulting in delayed shear-layer vortex roll-up and no symmetric counter-rotating vortex pair (see Figure 2.5 (a)). For this flow, optimal penetration is achieved with a sinusoidal temporal jet inlet velocity profile. At low momentum ratio and low velocity ratio, the shear-layer is absolutely unstable (see Figure 2.5 (b)). Optimal penetration in this regime requires a square-wave temporal jet inlet velocity profile. An example of a high momentum ratio jet, subjected to steady, sinusoidal, and square-wave excitation is provided in Figure 2.7.

In the case of a sonic jet in supersonic crossflow, the ratio of jet to free-stream velocity is low and therefore the low velocity ratio regime (defined as $R \lesssim 2$ by Bidan and Nikitopoulos (2011); Sau and Mahesh (2010)) is of primary interest. As stated previously, for steady injection in this regime, shear-layer vortices appear as hair-pin structures which naturally form and shed periodically. Based on observations for pulsed jets in subsonic crossflow, it is expected that for long pulses (at frequencies much lower than the natural shedding frequency), this shedding will occur regardless of Strouhal number or stroke ratio, so penetration depth will be independent of these parameters, while for short pulses (frequencies above the natural shedding frequency) the shedding will occur over a shorter time than the natural time scale, resulting in smaller and weaker vortices (Sau and Mahesh, 2010). The low velocity ratio regime with a subsonic crossflow was further elaborated by Bidan and Nikitopoulos (2011, 2013), where an additional transitional regime was identified between the high and low stroke ratio cases.

Despite the potential for increased penetration and mixing identified in subsonic crossflow, there is a smaller body of literature in relation to pulsed jets in supersonic crossflow. The shedding of shear-layer vortices and barrel shock deformation was simulated by Shi et al. (2016) for a sinusoidal pulsed jet, with pulsing period N, in a Mach 1.6 crossflow. The results, shown in Figure 2.8, show that the process is analogous to the naturally shed shear-layer vortices for steady jet injection. Shear-layer vortices

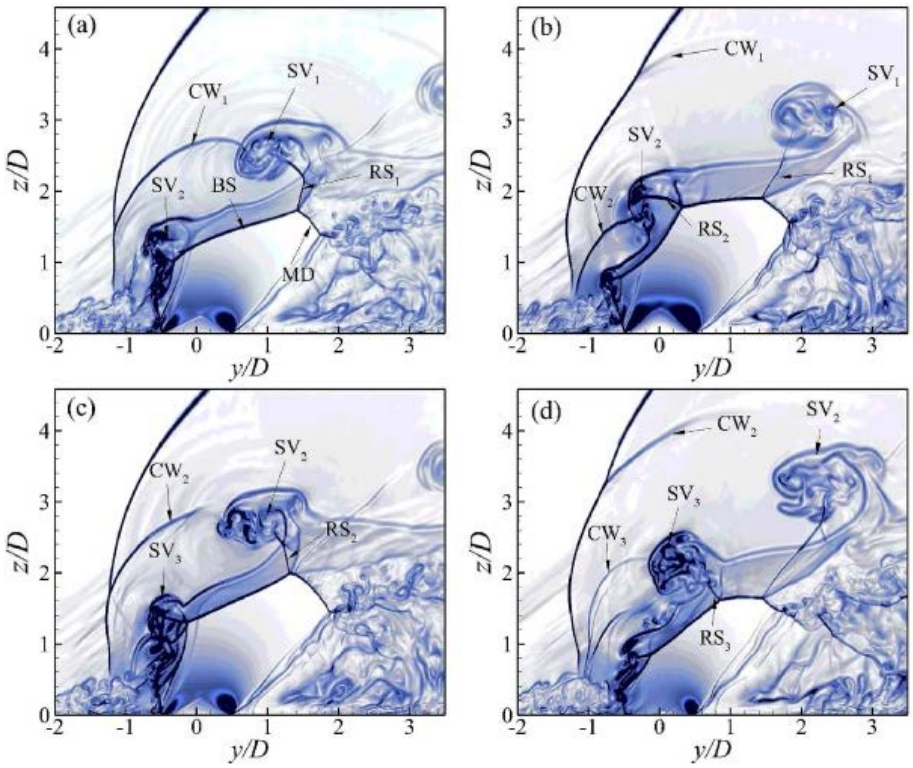

Figure 2.8: Contours of density gradient in the jet centreline, for a sinusoidally pulsed sonic jet in supersonic ($M_\infty = 1.6$) crossflow, with $J = 2.2$, at times: (a) $\tau = 0N/4$, (b) $\tau = N/4$, (c) $\tau = N/2$, and (d) $\tau = 3N/4$. Adapted from Shi et al. (2016).

(labelled SV) periodically shed, and are accompanied by reflected shocks (labelled RS) and deformation of the windward barrel shock. Compression waves (labelled CW) also emanate radially out from the jet, which are not observed for steady injection. Only a small increase in penetration was observed, which is consistent with observations in subsonic crossflow.

Bogdanoff (1994) also identified that pulsing can increase penetration and mixing in a supersonic crossflow, and suggested a Hartmann-Sprenger tube as a possible mechanism by which to pulse fuel injected into a scramjet. Randolph et al. (1994) used low frequency square-wave pulses from a sonic jet into a supersonic (Mach 2.5) crossflow to increase penetration by 12% over a steady jet with equal momentum flux. Significant increases in penetration have also been observed using other excitation methods (Murugappan and Gutmark, 2005; Murugappan et al., 2006). Recent preliminary studies have considered more complex geometries and have identified that fuel penetration depth decreases with increasing pulsing frequency, consistent with observations in subsonic crossflow (Chen and Zhao, 2017; Ni et al., 2017).

Cutler et al. (2013) showed that a sonic pulsed jet in a Mach 2 crossflow resulted in increased penetration over steady jet injection with the same mass flow and supply total pressure, and observed no coherent longitudinal counter-rotating vortex pair, when using a low frequency (1 Hz) pulse; while Williams and Moeller (2016) showed that sinusoidally pulsing a sonic jet at higher frequency ($St_\infty = 0.089$) in a supersonic (Mach 2.3) crossflow improved penetration by 20% to 35%. These results conflict with

results from subsonic crossflow (Karagozian, 2014; Gevorkyan et al., 2016), and the results of Shi et al. (2016), where at low velocity ratio, a clear vortex pair should be observed, and square-wave pulsing is required to significantly affect penetration.

Randolph et al. (1994) suggest that there are two reasons why pulsing may increase penetration depth in supersonic crossflow. First, when the jet is pulsed, there is a finite time interval within each pulsing period before the Mach disk forms, allowing the jet to penetrate further without total pressure loss from the shock, resulting in deeper penetration. The second mechanism is the inertial force created by the acceleration of the jet flow over a finite time interval. These mechanisms are different to a subsonic crossflow, where increased penetration is linked to the formation of distinct shear-layer vortex rings. However, detailed studies regarding the physics of increased penetration in supersonic crossflow are lacking. Wind tunnel experiments (Kouchi et al., 2010) with a sonic jet in a Mach 2 crossflow with a sinusoidal pulse indicated that penetration height reaches a maximum before pressure reaches a maximum in each pulse. Once the jet pressure reaches a maximum, the penetration returns to the steady value. This result was independent of jet peak pressure, and indicates that the rate of change of pressure may be driving the increased penetration, which supports the mechanisms for increased penetration identified by Randolph et al. (1994). However, the effect of a high frequency square-wave pulse on a supersonic crossflow is yet to be studied.

A number of studies have been conducted into single pulses at higher stroke ratios. This is relevant to reaction control jet applications, where a jet may be used in a single pulse. These studies have focused on the interaction force generated during the jet start-up and shut-down processes.

York et al. (1992) investigated the transient start-up of a supersonic jet in a supersonic crossflow using a parabolised Navier-Stokes CFD code and a RANS turbulence model. As the jet starts-up, the high pressure that originated at the jet orifice was seen to move downstream with the crossflow, however, the impact on the control force was not published. A number of papers have been published by Naumann et al. (1993a,b, 1996, 1998) investigating the unsteady nature of the jet start-up flow-field via wind tunnel experiments. Force data published for transient jet start-up in an established crossflow is unreliable due to measurement difficulties in the experiment, where oscillations of the model in the crossflow prevented accurate measurement of the control force.

The transient start-up was also studied by Chamberlain et al. (2000) and Dash et al. (2000) and applied to the US Army THAAD missile. The flight conditions of interest were Mach 3 – 7, at altitudes around 15 – 30 km. Chamberlain et al. (2000) found that if chamber pressure is increased linearly from 30% to 100% on the vehicle at Mach 3 with a zero degree angle-of-attack, the shock structure is developed very quickly, while the development of the wake structure behind the jet takes place over a longer time-period. Insufficient data was published to allow specific time-periods to be deduced in a non-dimensional form. The rapid development of the shock structure caused an initial overshoot in the control force. Soon afterwards, the jet shock wrapped around

the vehicle, creating a high pressure region underneath the vehicle that counteracts the control force. As the wake structure establishes, the low pressure wake completes the aerodynamic force balance resulting in a steady control force. Chamberlain et al. (2000) concluded that, while the initial control force overshoot is significant in magnitude, the time-scales are low enough to have a negligible impact on the THAAD control system.

Dash et al. (2000) studied the THAAD missile at a Mach 8, 45 km altitude flight condition and found that while a separated flow region was quickly established upstream of the jet outlet, significant changes in the flow structure caused by diffusive processes persist for longer time-periods. Again, insufficient data was published to allow a specific time-period to be deduced in a non-dimensional form.

From these studies it can be deduced that, with a linearly increasing jet pressure, there are two aspects that affect the control force: the shock structure and the turbulent wake structure, which are established on different time-scales; the shock structure establishes much faster than the turbulent wake.

Ebrahimi (2000) simulated the start-up and shut-down of a supersonic jet in a hypersonic ($M_\infty = 5$) free-stream at altitudes of 19 – 35 km. The transient start-up and shut-down force coefficients (C_F) are provided in Figure 2.9. Ebrahimi (2000) predicts a large overshoot, a settling time corresponding to non-dimensional time, $\tau \approx 100$ and a shut-down time corresponding to $\tau \approx 130$. The large magnitude of the steady interaction force is caused by the finned missile geometry trapping the high pressure jet fluid. The magnitude of the overshoot depends on the jet-to-crossflow pressure ratio, but the settling time and shut-down time does not. The use of a RANS turbulence model prevents detailed analysis of flow structures to identify the cause of the overshoot and the settling time, as RANS simulations are unable to resolve the unsteady, turbulent flow features. Although the jet start-up used by Ebrahimi (2000) is instantaneous (i.e. square-wave) and Chamberlain et al. (2000) assumed a linear build-up, the results are generally in agreement, with a large overshoot in control force and the flow structure established on a similar time-scale.

Further studies of the transient jet start-up and shut-down in hypersonic crossflow were conducted by Zhang et al. (2008), who focused on a missile geometry at Mach 3 and 6 at an altitude of 10 km, with a 20° angle-of-attack. In this case, no overshoot was observed, and the interaction force closely follows the jet thrust. As this data was obtained at a high angle-of-attack, with the jet on the leeward side of the body, the crossflow pressure differs considerably from the other studies, making direct comparison difficult. The use of RANS turbulence models once again prevented resolution of the important unsteady flow structures.

Recent work by DeSpirito (2012) focused on transient forces on a generic missile in supersonic flow during jet start-up and shut-down. For a jet pulse with a 10% rise and fall time, the transonic and supersonic flow conditions show significant differences, as shown in Figure 2.10. In a supersonic crossflow at sea-level, the maximum jet force is reached after $\tau \approx 160$, while in transonic crossflow at sea-level, it takes $\tau \approx 220$ with a much larger overshoot. Presumably the major difference is the shock structure

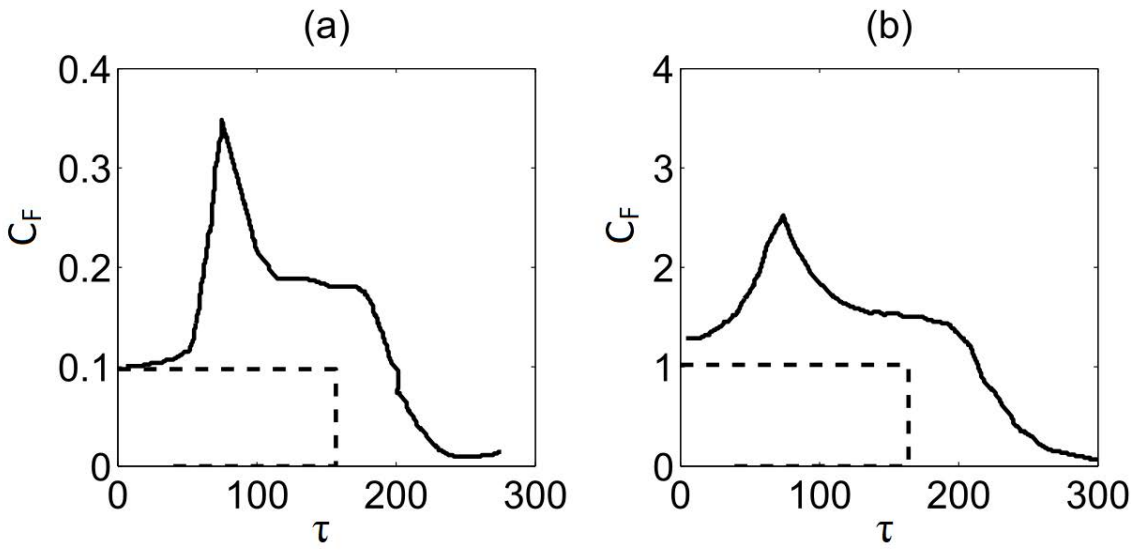

Figure 2.9: Jet interaction force coefficients for a supersonic (Mach 3) jet issuing from a slender missile body into a Mach 5 crossflow, at (a) 19.7 km altitude ($J = 60$), and (b) 35.1 km altitude ($J = 631$). Solid line: jet interaction force, Dash line: jet thrust. Data from Ebrahimi (2000).

developed in a supersonic crossflow. As DeSpirito (2012) also used a RANS turbulence model, the source of discrepancy cannot be identified. However, it is clear that free-stream Mach number has a significant influence on the transient interaction.

Each of the studies that investigate the transient start-up and shut-down process have used a cylindrical, finned missile geometry. This complicated geometry, combined with the use of RANS turbulence models, means that detailed understanding of the jet start-up and shut-down processes has not been achieved.

2.5 Summary and Gaps

Current air-breathing hypersonic vehicle designs use an integrated configuration, with the fore- and aft-body of the vehicle forming part of the propulsion system. Studies have shown that these vehicles tend to be unstable, and are subject to unprecedented coupling caused by interaction between the aerodynamics, propulsion, and structure. This coupling necessitates an integrated control system with a high bandwidth. While many models have been developed to study the coupling phenomena, these existing models are complex, and are not amenable to consideration of a broad range of flight conditions. As a result, the rigid-body motion of an unstable, propulsion-pitch coupled air-breathing hypersonic vehicle has not been previously quantified over a representative flight trajectory.

Control bandwidth is driven by the need to control the unstable modes of the vehicle. A survey of air-breathing hypersonic vehicles from the literature allows the minimum control system bandwidth to be estimated at approximately 10 Hz for a typical, trimmed hypersonic cruise condition. This bandwidth can increase to above

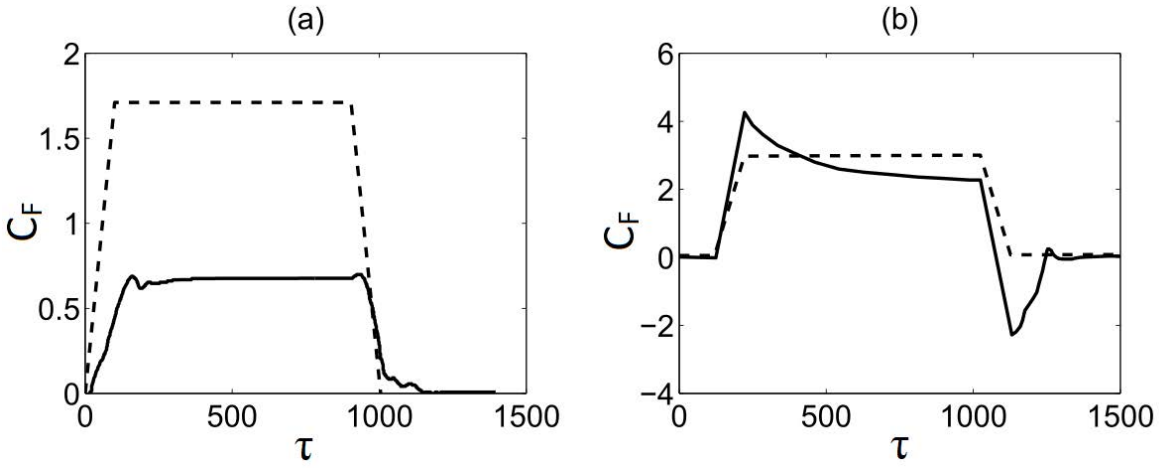

Figure 2.10: Jet interaction force coefficients, for a sonic jet issuing from a slender missile body into (a) Supersonic ($M_\infty = 1.5$) crossflow at sea-level with $J = 151$, and (b) Transonic ($M_\infty = 0.95$) crossflow at sea-level with $J = 377$. Data from DeSpirito (2012).

300 Hz if active control of structural and aero-elastic modes is required. If manoeuvre requirements and multiple flight conditions are considered, this could increase further. Aerodynamic control surfaces are unable to operate at these bandwidths. Reaction control jets are an attractive alternate, or supplement, control actuator, due to their ability to operate at high bandwidth. However, as vehicle dynamics have not been quanitified over a broad range of conditions, the control bandwidth required to complete an entire mission profile is not known.

A well designed reaction control system requires detailed knowledge of the flow-field and the flow structures responsible for the interaction force generated when the jet is operated in the atmosphere. Many studies have been conducted to characterise the steady interaction between jets and supersonic and hypersonic crossflows. However, investigation of the time-dependent interaction force, and the development and motion of shock and turbulent structures that influence the interaction force, has been focused on supersonic ($M_\infty < 5$) crossflows with turbulent in-flow boundary layers. Unsteady flow structures and interaction force for jets in hypersonic crossflow, with a laminar in-flow boundary layer, have not been investigated in detail using high fidelity numerical methods, such as LES. A limited number of studies with a laminar in-flow boundary layer in supersonic crossflow have shown important differences in shear-layer vortex shedding and in the upstream and downstream re-circulation regions, but do not describe the unsteady flowfield. Therefore, the influence of the laminar in-flow boundary layer and hypersonic crossflow on the unsteady jet interaction force remains unclear.

When operated at high frequency, the reaction control jet operates as a pulsed jet. While pulsed jets have been extensively studied in subsonic crossflow, consideration of pulsed jets in supersonic and hypersonic crossflows has been limited. Studies have focused on jet penetration and mixing, with significant improvements observed over steady jets. Trends from subsonic flow research indicate that square-wave pulsing is

likely to further increase jet penetration and mixing in supersonic crossflow, but square-wave jet pulsing is yet to be investigated in supersonic or hypersonic crossflow. The effect of pulsing on the jet interaction force has also not been considered in supersonic or hypersonic crossflow.

The interaction force developed during the jet start-up process has been investigated, but previous work is limited to RANS studies related to specific supersonic missile designs. The results show that the shock and vortex structures evolve on different time-scales, and that jet outflow conditions, Mach number, and pressure ratio all affect the interaction force. However, these effects are specific to the individual missile geometries. The application of LES to simulate the start-up of a sonic jet in hypersonic crossflow over a flat plate allows the unsteady interaction force during start-up to be explained more generally, with reference to jet interaction flow structures.

2.6 Thesis Aims

The gaps identified in Section 2.5 may be condensed into the following aims:

1. To investigate the rigid-body dynamics of a generic, representative, propulsion-pitch coupled air-breathing hypersonic vehicle, across a broad range of flight conditions, and determine the unstable rigid-body mode frequencies and the required control bandwidth.

2. To develop and validate a numerical large-eddy simulation (LES) methodology for simulating the transient interaction between a reaction control jet and a hypersonic crossflow.

3. To use the developed numerical methodology to investigate the unsteady interaction between steady and pulsed reaction control jets and hypersonic crossflow, with a laminar in-flow boundary layer, focusing on the shock and vortex structures and their influence on the interaction force.

4. To compare the actuator force characteristics of reaction control jets and aerodynamic control surfaces on the generic, representative, propulsion-pitch coupled air-breathing hypersonic vehicle model, to assess the impact on the flight characteristics.

Chapter 3

Dynamics and Control

This chapter addresses the first aim of the thesis, which is to investigate the rigid-body dynamics of a generic, representative, propulsion-pitch coupled air-breathing hypersonic vehicle, across a broad range of flight conditions, and determine the unstable rigid-body mode frequencies and the required control bandwidth. This will allow an estimate of the frequencies at which control actuators must operate to fly the vehicle, and will define the frequency range over which reaction control jets will be required to replace or supplement aerodynamic control surfaces.

A rigid-body model is developed using small-disturbance theory, with modifications to incorporate the characteristic propulsion-pitch coupling mechanism of airframe-integrated air-breathing hypersonic vehicles described in Chapter 2. The vehicle and single-stage-to-orbit flight trajectory are described in Section 3.1. Vehicle rigid-body dynamics are investigated at several discrete flight conditions in Section 3.2. Control authority and bandwidth requirements are assessed in Sections 3.3 and 3.4, respectively. The dynamics are modified using closed-loop control to provide acceptable stability and control characteristics, defined by military flying qualities standards for piloted aircraft in MIL-F-8785C (USDoD, 1980), with results provided in Section 3.5. The ability of the control actuators to maintain stability in the presence of atmospheric turbulence is assessed in Section 3.6. Section 3.7 provides a comparison between a coupled and uncoupled vehicle, to highlight the impact of propulsion-pitch coupling on the longitudinal dynamics and control requirements. Conclusions regarding the implications for the control of air-breathing hypersonic vehicles are provided in Section 3.8.

3.1 The Generic Air-Breathing Hypersonic Vehicle Model

The Generic Hypersonic Aerodynamics Model Example (GHAME) vehicle described in Chapter 2 is used to analyse the stability and control characteristics of a generic air-breathing hypersonic vehicle. The GHAME vehicle is a conceptual single-stage-to-orbit airframe-integrated air-breathing hypersonic vehicle, with control actuation via twin

Table 3.1: Mass and geometric properties of the two generic air-breathing hypersonic vehicles.

	Full-size Vehicle (Zipfel, 2007)		Missile-size Vehicle	
	Take-off	Land	Take-off	Land
Mass m, kg	136 000	54 400	2 041	820
Inertia I_{xx}, kg·m^2	1.6×10^6	1.2×10^6	1 400	1 100
Inertia I_{yy}, kg·m^2	31.6×10^6	19.3×10^6	28 800	17 600
Inertia I_{zz}, kg·m^2	32.5×10^6	20.2×10^6	29 700	18 400
Area S, m^2	557.4		33.9	
Wing span b, m	24.4		6.0	
Aerodynamic chord c, m	22.9		5.6	

elevons and a single rudder (White et al., 1992). Two variations of the GHAME vehicle have been considered in this work: the original vehicle configuration described by Zipfel (2007), which represents a large transport aircraft with a take-off mass of 136 000 kg, and a smaller, missile-size vehicle where mass was scaled at 1.5% of the full-size vehicle, to give a representative missile mass of 2 040 kg. Volume, area, and length of the missile-size vehicle were scaled geometrically at 1.5%, 6%, and 25%, respectively. Mass and geometric properties of the two vehicles are summarised in Table 3.1.

A schematic of the vehicle is shown in Figure 3.1 (White et al., 1992). Wings and vertical tail are thin triangular plates with no dihedral. The engine is wrapped around the lower fuselage in an integrated configuration. For the missile-size vehicle, the flight profile and aerodynamic coefficients were kept identical to the full-size vehicle. While highly simplified, this configuration has been widely used as a generic, yet representative, air-breathing hypersonic vehicle, for example Sachs (2005); Banerjee et al. (2016).

3.1.1 Aerodynamics

The GHAME aerodynamic database was developed by Zipfel (2007), with aerodynamic derivatives expressed as tabular functions of Mach number and angle-of-attack (AOA). The model consists of realistic aerodynamic data developed using the Aerodynamic Preliminary Analysis System (APAS), which uses panel methods to estimate aerodynamic coefficients for arbitrary bodies. A detailed description of APAS is provided by Maughmer et al. (1993), who concluded that, with the exception of the lateral control moments at supersonic Mach numbers, all predictions are acceptable for use at the conceptual design stage. Within APAS, low Mach number data ($M < 3$) was generated using the Unified Distribution Panel (UDP) methodology, while high Mach number aerodynamics were derived using the Supersonic/Hypersonic Arbitrary Body

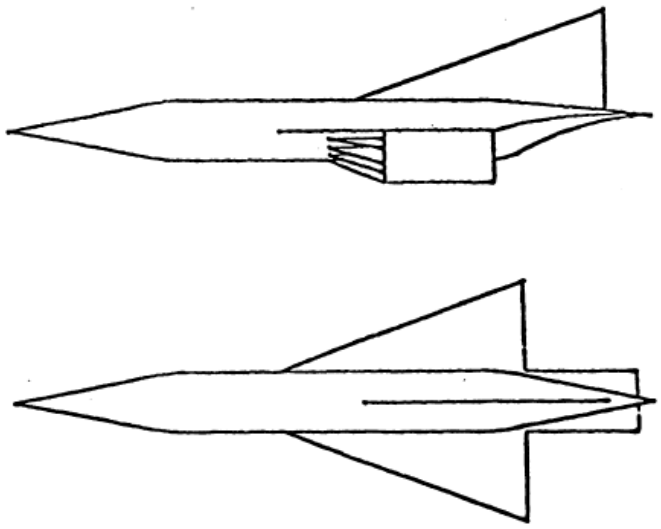

Figure 3.1: Schematic of the GHAME vehicle (White et al., 1992).

Program (S/HABP) code, and from experimental data obtained from the Space Shuttle and X-24B/C (White et al., 1992). The UDP is a first-order panel method based on linear potential flow theory, including edge effects and semi-empirical techniques for the calculation of skin friction drag (Maughmer et al., 1993). The S/HABP uses Modified Newtonian impact theory and Prandtl-Meyer expansion theory, with empirical data for boundary layer conditions and viscous effects (White et al., 1992). As a highly accurate aerodynamic model is not required, this method provides a suitable aerodynamic database for a representative air-breathing hypersonic vehicle. The method developed in this work can be applied to any aerodynamic database.

Forces and moments were provided in stability axes, with lift, L, and drag, D, replacing the Z and X body axis force components respectively. Moments (pitch, m, roll, l, and yaw, n) were in body axes. The vehicle is controlled by a rudder and two elevons. The elevons function as ailerons using differential movement, and elevators using coordinated movement, according to the following relationships (Zipfel, 2007):

$$\delta_a = \frac{\delta v_l - \delta v_r}{2}; \delta_e = \frac{\delta v_l + \delta v_r}{2} \tag{3.1}$$

where δ_a and δ_e refer to the effective elevator and aileron deflections respectively, and δv_l and δv_r refer to the left and right elevon deflections.

The force and moment equations were developed based on a modification to the equations developed using small-disturbance theory, as follows:

$$C_L = C_{L0}(M,\alpha) + C_{L\alpha}(M,\alpha)\alpha + C_{L\delta_e}(M,\alpha)\delta_e + C_{Lq}(M,\alpha)q\frac{c}{2V} \tag{3.2}$$

$$C_D = C_{D0}(M,\alpha) + C_{D\alpha}(M,\alpha)\alpha \tag{3.3}$$

$$C_m = C_{m0}(M,\alpha) + C_{m\alpha}(M,\alpha)\alpha + C_{m\delta_e}(M,\alpha)\delta_e + C_{mq}(M,\alpha)q\frac{c}{2V} + C_{mT} \tag{3.4}$$

$$\begin{aligned} C_Y = {} & C_{Y0}(M,\alpha) + C_{Y\beta}(M,\alpha)\beta + C_{Y\delta_a}(M,\alpha)\delta_a + C_{Y\delta_r}(M,\alpha)\delta_r \\ & + C_{Yp}(M,\alpha)p\frac{b}{2V} + C_{Yr}(M,\alpha)r\frac{b}{2V} \end{aligned} \tag{3.5}$$

$$\begin{aligned} C_l = {} & C_{l0}(M,\alpha) + C_{l\beta}(M,\alpha)\beta + C_{l\delta_a}(M,\alpha)\delta_a + C_{l\delta_r}(M,\alpha)\delta_r \\ & + C_{lp}(M,\alpha)p\frac{b}{2V} + C_{lr}(M,\alpha)r\frac{b}{2V} \end{aligned} \tag{3.6}$$

$$\begin{aligned} C_n = {} & C_{n0}(M,\alpha) + C_{n\beta}(M,\alpha)\beta + C_{n\delta_a}(M,\alpha)\delta_a + C_{n\delta_r}(M,\alpha)\delta_r \\ & + C_{np}(M,\alpha)p\frac{b}{2V} + C_{nr}(M,\alpha)r\frac{b}{2V} \end{aligned} \tag{3.7}$$

where C is a force or moment coefficient, M is Mach number, α is angle-of-attack, β is angle-of-side-slip, p, q, and r are roll, pitch, and yaw rates, c is chord length, b is wing span, and V is airspeed. Force and moment coefficients (for example, C_L) are expressed as a sum of the trimmed coefficient (e.g. C_{L0}) and perturbations caused by small perturbations in body rates (e.g. C_{Lq}), angle-of-attack or side-slip (e.g. $C_{L\alpha}$, $C_{Y\beta}$), or control inputs (e.g. $C_{L\delta_e}$).

As recommended by Zipfel (2007), the effect of body rates on the lift and side forces (i.e. C_{Lq}, C_{Yp} and C_{Yr}) are neglected, and side forces (C_Y) and rolling and yawing moment coefficients (C_l and C_n) are assumed to have negligible trim coefficients (i.e. C_{Y0}, C_{l0} and $C_{n0} = 0$).

The dynamic propulsion-pitch coupling is included by the C_{mT} term in Equation 3.4. C_{mT} represents the pitching moment caused by thrust, which is offset from the centre of gravity due to the mounting of the engine beneath the fuselage. The propulsion system is modelled as a lumped system; pitching moment is the only interaction between the propulsion and aerodynamics. Other aerodynamic coefficients, such as drag, lift, and lateral forces and moments, do not depend on thrust.

To provide thrust over a wide range of Mach numbers, necessary for a single-stage-to-orbit flight profile, the GHAME assumes a turbojet-ramjet-scramjet propulsion model, where thrust, T, depends on specific impulse, I_{sp}, and capture area, CA, which depend only on Mach number, angle-of-attack, and throttle setting, as follows (Zipfel, 2007):

$$T = 29\rho g V \left(A_{cowl} \times CA(M,\alpha)\right)\left(\delta_T \times I_{sp}(M,\delta_T)\right) \tag{3.8}$$

where ρ is air density, g is gravitational acceleration, CA is capture area, δ_T is the throttle setting, and A_{cowl} is the fixed geometric area of the intake. Therefore, the pitching moment depends on both AOA and Mach number as well as engine throttle setting. For the full-size vehicle, $A_{cowl} = 27.87$ m^2 (Zipfel, 2007). This is scaled to $A_{cowl} = 1.69$ m^2 for the missile-size vehicle.

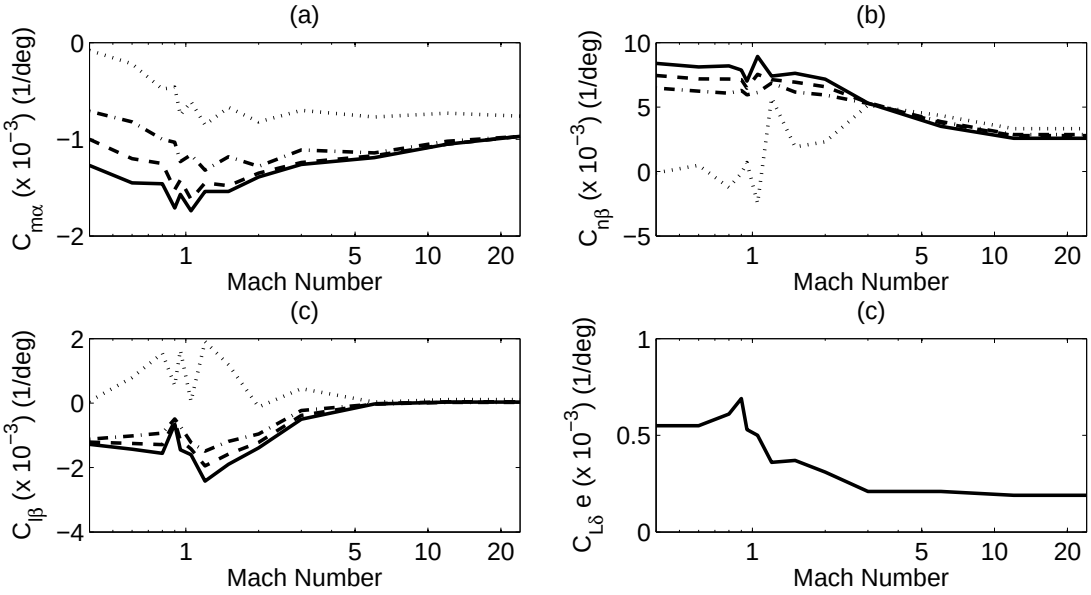

Figure 3.2: Selected GHAME aerodynamic coefficients. (a) Pitch ($C_{m\alpha}$), (b) Yaw ($C_{n\beta}$), (c) Roll ($C_{l\beta}$), and (d) Elevator ($C_{L\delta e}$). Solid line: $\alpha = -3°$, Dash line: $\alpha = 0°$, Dot-Dash Line: $\alpha = +3°$, Dotted Line: $\alpha = +21°$

Trim thrust is calculated using the GHAME propulsion model, and C_{mT} is calculated based on the trim thrust being applied at a fixed moment arm, set at 10% of the wing span, i.e.:

$$C_{mT} = \frac{T \times 0.1 \times b}{QSc} \tag{3.9}$$

where Q is dynamic pressure, and S is reference area ($S = c \times b$).

All other terms are included in the GHAME aerodynamic database. Selected aerodynamic coefficients are provided in Figure 3.2. Figure 3.2 (a) shows that without propulsion-pitch coupling, the GHAME vehicle is longitudinally statically stable throughout the flight envelope ($C_{m\alpha} < 0$). With the exception of the transonic regime at high AOA, the GHAME is also directionally stable ($C_{n\beta} > 0$, see Figure 3.2 (b)). Roll stability depends on $C_{l\beta}$ and varies depending on both Mach number and AOA (see Figure 3.2 (c)). Figure 3.2 also highlights the highly variable aerodynamics in the transonic regime. Aerodynamics are nearly independent of Mach number for $M > 10$. Elevator effectiveness ($C_{L\delta e}$) is independent of AOA, and is shown in Figure 3.2 (d). This is also highly variable in the transonic regime and decreases with increasing Mach number.

3.1.2 Flight Conditions

Vehicle dynamics were analysed at 11 discrete conditions along a generic single-stage-to-orbit trajectory. The trajectory consists of an ascent phase, a level flight phase, and a descent phase; and is based on the trajectory described by Colgren et al. (2009) for a similar generic hypersonic vehicle. Modifications were made to suit the GHAME and

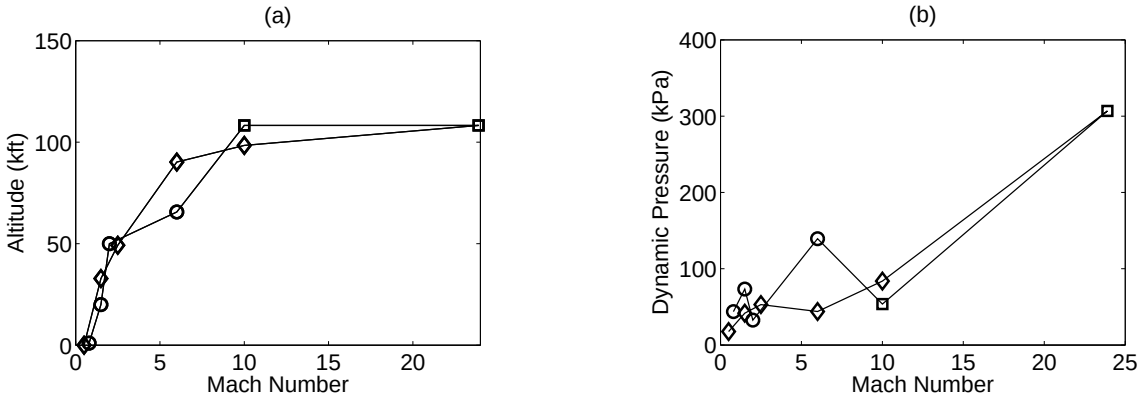

Figure 3.3: (a) Flight profile, and (b) Dynamic pressure along the reference flight profile. ∘: Ascent; □: Cruise; ♢: Descent.

to extend the flight envelope to include all available Mach numbers in the aerodynamic database. The flight profile is shown in Figure 3.3 (a). In the ascent phase, the vehicle begins at a trimmed condition at $M = 0.8$ at an altitude of 305 m (1 000 ft). Subsonic flight is maintained to an altitude of approximately 3 km (10 000 ft). The vehicle then accelerates through Mach 2 at 15.2 km (50 000 ft) to Mach 6 at approximately 20 km (65 000 ft). An additional acceleration brings the vehicle to cruise at Mach 10, 33 km (108 000 ft). An alternate cruise velocity of Mach 24 at 33 km is also considered. This represents the upper limit of the aerodynamic database, and is somewhat similar to a ballistic re-entry flight condition. The descent follows a different path, with the vehicle reaching Mach 6 at 27.4 km (90 000 ft), Mach 2.5 at 15.2 km (50 000 ft), and Mach 1.5 at 10 km (33 000 ft) before landing at Mach 0.5. The analysis considers the vehicle dynamics for both vehicles at these 11 discrete trimmed conditions. Figure 3.3 (b) shows the dynamic pressure at each flight condition.

3.1.3 Validation

To confirm that the GHAME model was implemented correctly, a plot of the calculated elevator deflection required to trim the vehicle in the longitudinal axes, ignoring propulsion-pitch coupling, across a range of Mach numbers and AOA, was generated in Figure 3.4. The results compare well with previously published data (White et al., 1992). This provides some confidence that the model has been implemented correctly, and correct elevator deflections are calculated at all Mach numbers and angles-of-attack.

3.2 Rigid-Body Dynamics

To achieve trim, the calculation of lift must take into account the centripetal acceleration, as follows (Bilimoria and Schmidt, 1995):

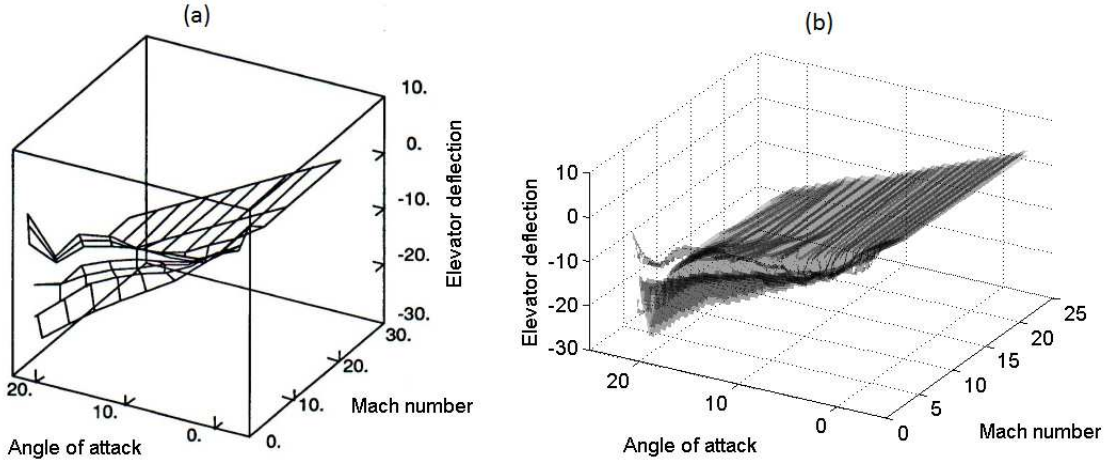

Figure 3.4: Contours of trim elevator deflection (δ_e). (a) Data from White et al. (1992); (b) Data from current study.

$$L = W - \frac{mV^2}{\mathrm{h} + R_E} \tag{3.10}$$

where L is lift, W is weight, m is mass, V is airspeed, h is altitude, and R_E is Earth's radius.

Using this, and noting that Thrust = Drag, $C_m = 0$, and $q = 0$ for level trimmed flight, Equations 3.2, 3.3, and 3.4 can be rearranged as follows:

$$C_{L0}(M,\alpha) + C_{L\alpha}(M,\alpha)\alpha + C_{L\delta_e}(M,\alpha)\delta_e - C_L = 0 \tag{3.11}$$

$$C_{D0}(M,\alpha) + C_{D\alpha}(M,\alpha)\alpha - C_T = 0 \tag{3.12}$$

$$C_{m0}(M,\alpha) + C_{m\alpha}(M,\alpha)\alpha + C_{m\delta e}(M,\alpha)\delta_e + C_{mT} = 0 \tag{3.13}$$

where $C_L = L/\left(\frac{1}{2}\rho V^2 S\right)$ and $C_T = T/\left(\frac{1}{2}\rho V^2 S\right)$. Lift is calculated from Equation 3.10.

Equations $3.11 - 3.13$ were solved simultaneously for α, C_T, and δ_e, with an initial guess of $\alpha = 0$, $C_T = 0$, and $\delta_e = 0$, using a least-squares algorithm, subject to the constraints: $-3° < \alpha < 21°$, $-30° < \delta_e < 30°$, and $C_T \geq 0$. These represent the limits of the GHAME database for α, and assumed maximum control deflections for δ_e. The maximum elevator deflection corresponds to either a physical deflection limit, or a reduced effectiveness due to stall.

The analysis uses the 1976 U.S. Committee on Extension to the Standard Atmosphere (COESA) standard atmospheric model for ideal, dry air to estimate velocity for a given altitude and Mach number, and assumes constant gravitational acceleration and constant R_E.

Once the trim state was found, thrust was calculated from C_T, and throttle setting, δ_T, was determined using Equation 3.8. The solution is valid for $0 < \delta_T < 2$.

The trim values of δ_e, α, and T at each flight condition are shown in Figure 3.5. Once a suitable trim solution for M, α, δ_T, and δ_e was obtained, the remaining aerodynamic coefficients were interpolated from the GHAME aerodynamic and propulsion databases.

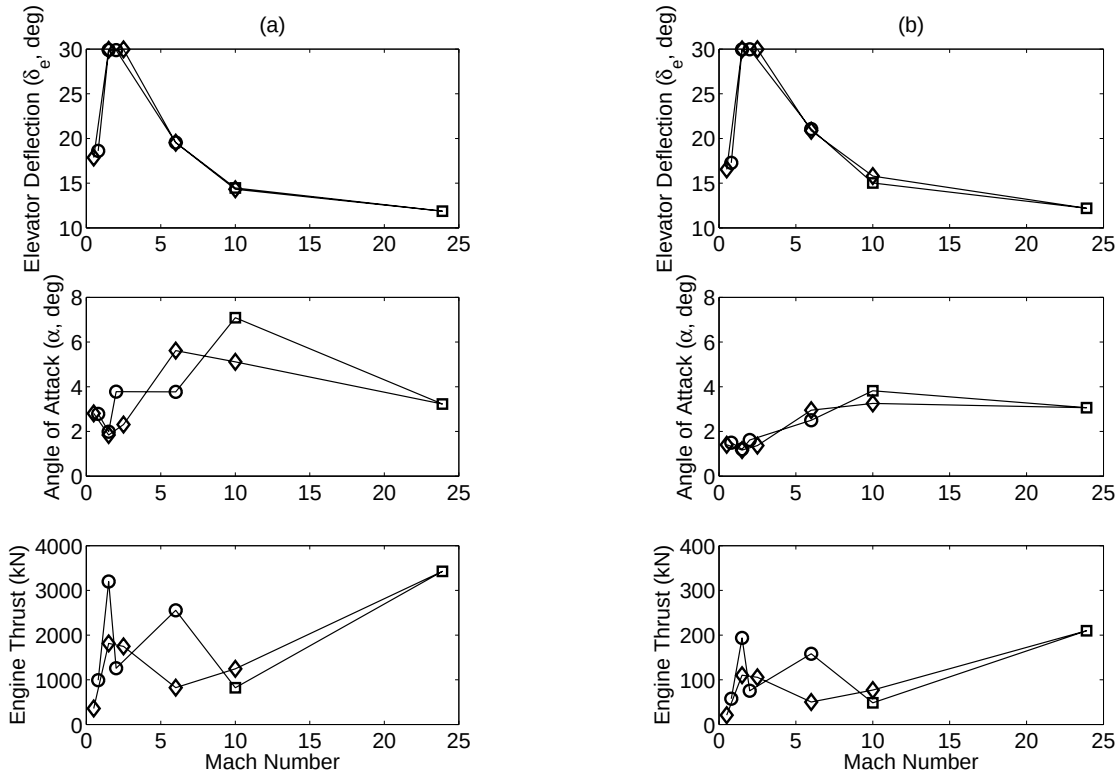

Figure 3.5: Trim elevator deflection, δ_e, AOA, α, and T for (a) Full-size vehicle, and (b) Missile-size vehicle. ○: Ascent; □: Cruise; ◊: Descent.

Figure 3.5 shows that trim requires large elevator deflections in the transonic regime for both vehicles. This is caused by higher drag in this region, which requires higher thrust. The thrust causes a large pitching moment which must be countered by the elevator. At higher Mach numbers, a combination of lower drag coefficient and higher control authority reduce the trimmed elevator deflection. Much higher thrust is required for the full-size vehicle due to the larger mass, drag, and wetted area (note the different y-axis scales for thrust between Figure 3.5 (a) and (b)). As a result, slightly higher angles-of-attack are required to balance the propulsive pitching moment. This is most pronounced in the supersonic regime. In addition, the control actuators saturate in the transonic regime, with $\delta_e = 30°$. In these cases, trim is achieved by increased angle-of-attack and engine thrust, resulting in an inefficient cruise condition.

3.3 Control Authority

Control authority is the amount of force that can be exerted by the actuator to achieve a desired response. There are two parameters of interest: actuator force required to trim the vehicle, and maximum force available to perturb the vehicle from the trimmed state, or to manoeuvre the vehicle.

The actuator force required to trim the vehicle is calculated as:

$$L_e = C_{Le} \times \frac{1}{2}\rho V^2 S = C_{L\delta e}(M, \alpha)\delta_{e,trim} \times \frac{1}{2}\rho V^2 S \tag{3.14}$$

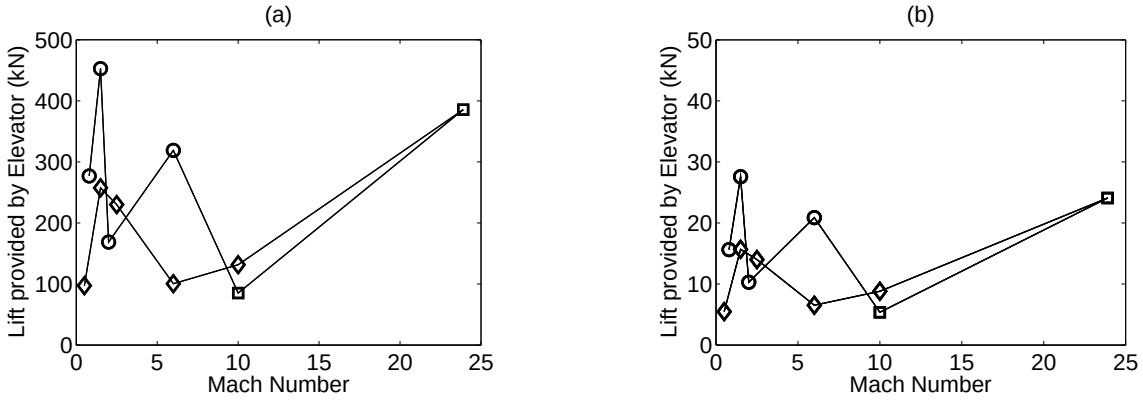

Figure 3.6: Lift provided by the elevator at trim for (a) Full-size vehcile, and (b) Missile-size vehicle. ∘: Ascent; □: Cruise; ♢: Descent.

where L_e is the lift generated by the elevator, C_{Le} is the elevator lift coefficient ($C_{Le} = C_{L\delta e} \times \delta_e$), S is the GHAME vehicle's reference area, and δ_e is elevator deflection. The actuator force at trim calculated using these areas is provided in Figure 3.6.

As the aerodynamic model is linear, the maximum control force available to perturb the vehicle from the trimmed state occurs at maximum control surface deflection. The available force is measured by load factor, defined as Lift / Weight ($n = L/W$). Maximum load factor available from the trimmed state is determined by rearranging Equations 3.2 and 3.4, and by noting that $C_L = nC_W$, and that $n = 1$, $q = 0$, and $C_m = 0$ for trimmed level flight. Solving for n gives the following:

$$n = \left(\frac{1}{C_W}\right)\left(C_{L0} - \left(\frac{C_{L\alpha}}{C_{m\alpha}}\right)(C_{m0} + C_{mT}) + \delta_e\left(C_{L\delta e} - \left(\frac{C_{L\alpha}}{C_{m\alpha}}\right)C_{m\delta e}\right)\right) \tag{3.15}$$

Load factor gives an indication of the control authority. If $n \approx 1$, the vehicle has little control authority. When n is large, the vehicle is able to produce significantly more lift than is required for trim, making the vehicle manoeuvrable. There are two possible ways to generate load factor, using the elevator to increase lift and pitching moment, or the throttle to increase thrust and pitching moment. As this work is focused on the control authority of aerodynamic control surfaces, the contribution of the propulsion system to the load factor is ignored, i.e. $C_{mT} = 0$. Maximum load factor is provided in Figure 3.7, assuming a maximum elevator deflection of 30°.

The manoeuvrability of each vehicle is highly dependent on the specific flight condition. Both vehicles have low manoeuvrability in the transonic region, where the elevators are saturated at trim. For the full-size vehicle, the available load factor has a minimum value of 0.1 g at Mach 1.5, while the missile-size vehicle has a minimum of 0.27 g at Mach 2. In the subsonic and supersonic regions, both vehicles have better manoeuvrability, between 0.3 g and 2.5 g for the full-size vehicle and between 2.8 g and 12.5 g for the missile-size vehicle. These values are reasonable for these classes of vehicle. At Mach 24, the elevator effectiveness is very high, due to the high dynamic pressure, making the vehicle extremely manoeuvrable. Up to 30 g is achievable for the full-size vehicle, and over 100 g is achievable for the missile-size vehicle. However, there

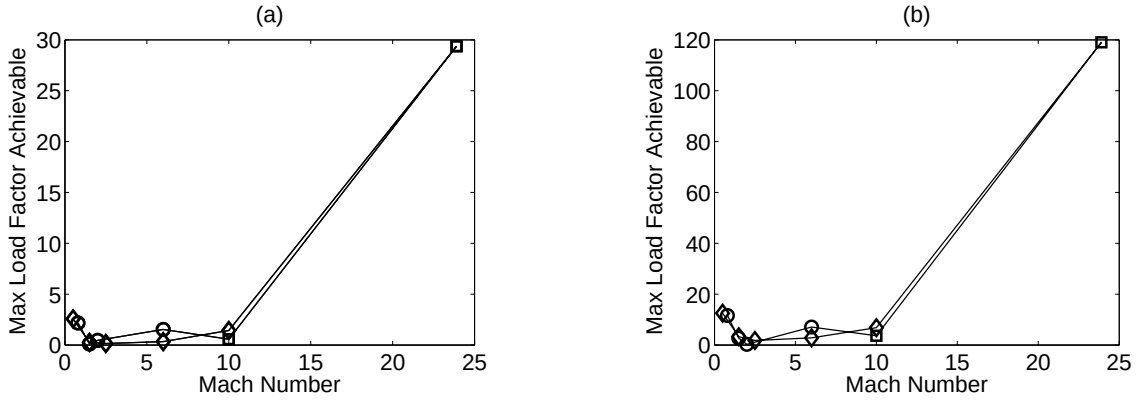

Figure 3.7: Maximum achievable load factor, assuming $\delta_{e,max} = 30°$, for (a) Full-size vehicle, and (b) Missile-size vehicle. ∘: Ascent; □: Cruise; ♢: Descent

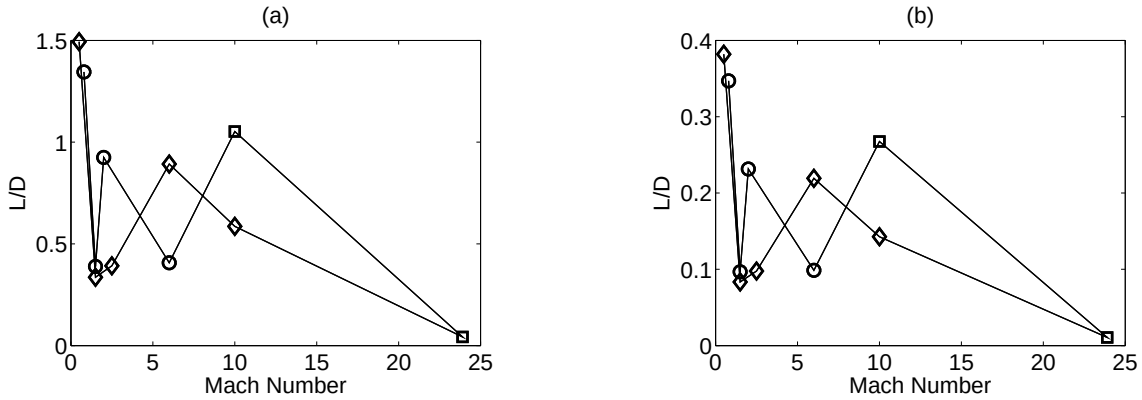

Figure 3.8: Trim lift-to-drag ratio (L/D) for (a) Full-size vehicle, and (b) Missile-size vehicle. ∘: Ascent; □: Cruise; ♢: Descent

are other limitations, for example structural loads and aerodynamic heating, which would limit the performance at such a high dynamic pressure. Further, this analysis only considers the initial response of the vehicle to elevator deflection. In a manoeuvre, the angle-of-attack will change in response to the initial elevator input, which changes the trim state and aerodynamic coefficients.

The amount of force available from the aerodynamic control surfaces must be compared to the drag they produce. The vehicle's lift-to-drag ratio (L/D) at each trim condition is provided in Figure 3.8. L/D is poor for both vehicles when compared to a conventional subsonic aircraft, but is comparable to a missile in the supersonic regime, where L/D varies between $0.2-1.5$ depending on angle-of-attack (Ahmad et al., 2016). Notably, L/D is almost zero at the Mach 24 flight condition. This means high levels of thrust are required to overcome drag and maintain trim at high Mach number, resulting in an inefficient cruise condition. However, as stated previously, Mach 24 more closely resembles a ballistic re-entry flight condition, where lower L/D is expected.

The L/D values in Figure 3.8 are a reflection of the vehicle's aerodynamics, and may not be highly dependent on the actuators. Therefore, it is useful to consider the drag caused by the elevator in isolation. The GHAME drag model (Equation 3.3) does not contain an elevator drag term, so this cannot be directly calculated from the GHAME

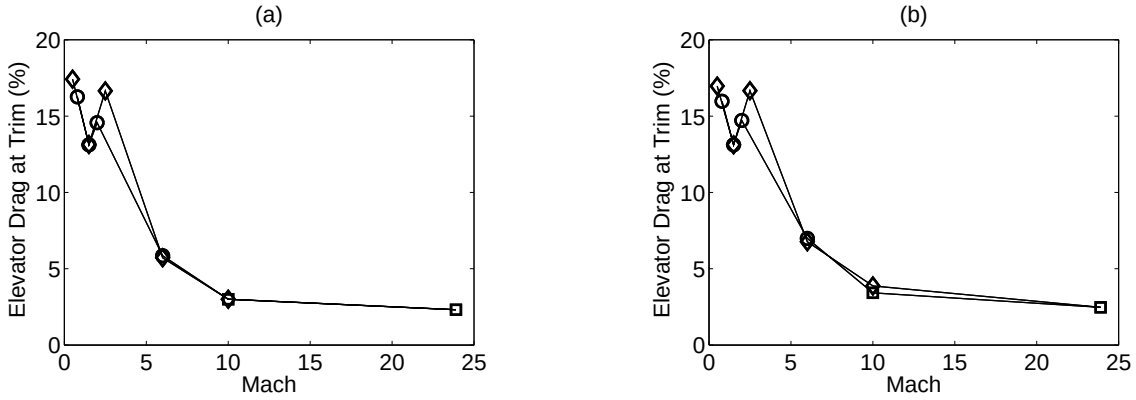

Figure 3.9: Drag caused by elevator at trim for (a) Full-size vehicle, and (b) Missile-size vehicle. ○: Ascent; □: Cruise; ◇: Descent

aerodynamic database. Newtonian theory (Anderson, 2006) can be used to provide an approximation, as follows:

$$D_e = \frac{1}{2}\rho V^2 S_e \times 2\sin^2(\delta_e) \times \sin(\delta_e) \tag{3.16}$$

This requires an estimate of elevator area, S_e. Newtonian theory can again be used to approximate elevator lift, as follows:

$$L_e = \frac{1}{2}\rho V^2 S_e \times 2\sin^2(\delta_e) \times \cos(\delta_e) \tag{3.17}$$

Using Equations 3.14 and 3.17, elevator area can be calculated as:

$$\frac{S_e}{S} = \frac{C_{L\delta e}(M,\alpha) \times \delta_{e,trim}}{2\sin^2(\delta_{e,trim}) \times \cos(\delta_{e,trim})} \tag{3.18}$$

Newtonian theory provides a reasonable estimate of lift at high Mach number, with errors of 19% and 5% reported for 15° wedge and cone shapes, respectively, at Mach 20 (Anderson, 2006). Therefore, S_e was calculated at the Mach 24 flight condition for the full-size vehicle. This results in an elevator area of 15.2 m^2 for the full-size vehicle, or approximately 3% of the total vehicle area. The drag caused by the elevator at trim is plotted in Figure 3.9, as a percentage of overall drag at trim. This shows that the elevator contributes a large portion of the overall drag at the trim conditions, due to the large trim elevator deflections. It should be noted that Newtonian theory is only accurate at hypersonic Mach numbers. For $M < 5$, elevator drag was estimated based on experimental drag coefficient data for a rectangular flat plate in subsonic flow, at various angles of attack (Ortiz et al., 2012).

The high manoeuvrability at high dynamic pressure is an advantage of using of aerodynamic control surfaces on the GHAME vehicle, provided the propulsion system can overcome the associated drag. In practice, aerodynamic control effectiveness at high dynamic pressure is limited by external constraints, such as structural loads and aerodynamic heating. At lower dynamic pressures, manoeuvrability is acceptable using aerodynamic control, except in the transonic regime, where the elevators are saturated to maintain trim.

Elevator drag is high at the trim conditions, as the propulsive moments must be balanced, resulting in large elevator deflections. This significantly increases drag, resulting in poor lift-to-drag ratios and inefficient flight. Therefore, while an alternative actuator configuration is not required to improve control authority, it may be beneficial to improve efficiency.

3.4 Bandwidth

The required control actuator bandwidth is related to the vehicle's dynamic modes. In this section, rigid-body dynamics are quantified and used to provide an estimate of required actuator bandwidth. Longitudinal and lateral motion are considered separately.

3.4.1 Longitudinal Motion

A state-space model of the longitudinal dynamics was developed using linearised equations of motion. The small-disturbance theory of Nelson (1989) was used, with modifications as required to incorporate dynamic propulsion-pitch coupling. The state-space model and associated derivatives are as follows:

$$\dot{\mathbf{x}} = \mathbf{A}\mathbf{x} + \mathbf{B}\mathbf{u} \tag{3.19}$$

where $\mathbf{x}$ is the state vector, $\mathbf{u}$ is the input vector, $\mathbf{A}$ is the state matrix, and $\mathbf{B}$ is the input matrix.

$$\underbrace{\begin{bmatrix} \Delta\dot{u} \\ \Delta\dot{w} \\ \Delta\dot{q} \\ \Delta\dot{\theta} \end{bmatrix}}_{\dot{\mathbf{x}}} = \underbrace{\begin{bmatrix} X_u & X_w & 0 & -g \\ Z_u & Z_w & u_0 & 0 \\ M_u + M_{\dot{w}}Z_u & M_w + M_{\dot{w}}Z_w & M_q + M_{\dot{w}}u_0 & 0 \\ 0 & 0 & 1 & 0 \end{bmatrix}}_{\mathbf{A}} \underbrace{\begin{bmatrix} \Delta u \\ \Delta w \\ \Delta q \\ \Delta\theta \end{bmatrix}}_{\mathbf{x}} + \underbrace{\begin{bmatrix} X_{\delta e} & X_{\delta T} \\ Z_{\delta e} & Z_{\delta T} \\ M_{\delta e} + M_{\dot{w}}Z_{\delta e} & M_{\delta T} + M_{\dot{w}}Z_{\delta T} \\ 0 & 0 \end{bmatrix}}_{\mathbf{B}} \underbrace{\begin{bmatrix} \Delta\delta_e \\ \Delta\delta_T \end{bmatrix}}_{\mathbf{u}} \tag{3.20}$$

The formulae for each of these derivatives are:

$$X_u = \frac{(-C_{Du} + C_{Tu})QS}{mu_0} \qquad M_u = C_{mu}\frac{QSc}{u_0 I_y}$$
$$X_w = \frac{(-C_{D\alpha} + C_{T\alpha})QS}{mu_0} \qquad M_{\dot{w}} = C_{m\dot{\alpha}}\frac{QSc}{u_0 I_y}\frac{c}{2u_0}$$
$$Z_u = \frac{-(C_{Lu} + 2C_{L0})QS}{mu_0} \qquad M_w = (C_{m\alpha} + C_{mT\alpha})\frac{QSc}{u_0 I_y}$$
$$Z_w = \frac{-(C_{L\alpha} + C_{D0})QS}{mu_0} \qquad M_q = C_{mq}\frac{c}{2u_0}\frac{QSc}{I_y}$$
$$Z_{\delta e} = \frac{C_{L\delta e}QS}{m} \qquad M_{\delta e} = C_{m_{\delta e}}\frac{QSc}{I_y}$$
$$X_{\delta T} = \frac{C_{XT}QS}{m} \qquad M_{\delta T} = C_{mT}\frac{QSc}{I_y}$$

States u, w, q, and θ are the forward velocity, vertical velocity, pitch rate, and flight path angle, respectively. Q is the dynamic pressure, and I_y is the moment of inertia about the y-axis, i.e. the pitch moment of inertia. The subscript 0 refers to the reference, or trimmed, flight condition.

For a typical uncoupled vehicle, drag and pitching moment are assumed to be constant with respect to airspeed (i.e. $C_{Du} = C_{mu} = 0$, Nelson (1989)). The introduction of propulsion-pitch coupling means that both drag and pitching moment depend on airspeed. The derivatives C_{Du} and C_{mu} are calculated by the local gradient of the aerodynamic database, as follows:

$$\begin{aligned} C_{Du} &= \frac{\partial}{\partial u}(C_{D0}(M,\alpha) + \alpha C_{D\alpha}(M,\alpha)) \\ &= M\left(\frac{\partial C_{D0}(M,\alpha)}{\partial M} + \alpha\frac{\partial C_{D\alpha}(M,\alpha)}{\partial M}\right) \end{aligned} \tag{3.21}$$

$$\begin{aligned} C_{mu} &= \frac{\partial}{\partial u}\Bigg(C_{m0}(M,\alpha) + \alpha C_{m\alpha}(M,\alpha) + \delta_e C_{m\delta_e}(M,\alpha) \\ &\quad + C_{mq}(M,\alpha)q\frac{c}{2V} + C_{mT}\Bigg) \\ &= M\Bigg(\frac{\partial C_{m0}(M,\alpha)}{\partial M} + \alpha\frac{\partial C_{m\alpha}(M,\alpha)}{\partial M} + \delta_e\frac{\partial C_{m\delta e}(M,\alpha)}{\partial M} \\ &\quad + \frac{\partial C_{mq}(M,\alpha)}{\partial M}q\frac{c}{2V} + \frac{\partial C_{mT}}{\partial M}\Bigg) \end{aligned} \tag{3.22}$$

where $\partial C_{mT}/\partial M$ depends on both $CA(M,\alpha)$ and $I_{sp}(M,\delta_T)$ from Equation 3.8. The derivatives with respect to Mach number are simply calculated from the gradients of the GHAME aerodynamic and propulsion databases. C_{Lu} is calculated using Prandtl-Glauert theory at all flight conditions (Anderson, 2001).

The propulsion-pitch coupling also requires evaluation of thrust terms, C_{Tu}, $C_{T\alpha}$, and $C_{mT\alpha}$ not typically considered for an uncoupled vehicle. These are calculated by the local gradient of the GHAME propulsion database, as follows:

$$C_{Tu} = \frac{\partial}{\partial u}\left(29\rho g V\left(A_{cowl} \times CA(M,\alpha)\right)\left(\delta_T \times I_{sp}(M,\delta_T)\right)\right)$$
$$= M \times 29\rho g V \delta_T A_{cowl}\left[\left(\frac{\partial I_{sp}(M,\delta_T)}{\partial M} \times CA\right) + \left(\frac{\partial CA(M,\alpha)}{\partial M} \times I_{sp}(M,\delta_T)\right)\right] \tag{3.23}$$

$$C_{T\alpha} = \frac{\partial}{\partial \alpha}\left(29\rho g V\left(A_{cowl} \times CA(M,\alpha)\right)\left(\delta_T \times I_{sp}(M,\delta_T)\right)\right)$$
$$= 29\rho g V \delta_T A_{cowl} I_{sp}(M,\delta_T)\frac{\partial CA(M,\alpha)}{\partial \alpha} \tag{3.24}$$

$$C_{mT\alpha} = C_{T\alpha} \times \frac{0.1b}{c} \tag{3.25}$$

It was assumed that there is no lag in down-wash at the tail (i.e. $C_{m\dot{\alpha}} = 0$).

The propulsive control derivatives $X_{\delta T}$ and $M_{\delta T}$ are calculated from their coefficients, which are defined as follows:

$$C_{XT} = \frac{\partial}{\partial \delta_T}\left(29\rho g V\left(A_{cowl} \times CA(M,\alpha)\right)\left(\delta_T \times I_{sp}(M,\delta_T)\right)\right)$$
$$= 29\rho g V\left(A_{cowl} \times CA(M,\alpha)\right)\left[I_{sp}(M,\delta_T) + \left(\delta_T \times \frac{\partial I_{sp}(M,\delta_T)}{\partial \delta_T}\right)\right] \tag{3.26}$$

$$C_{mT} = C_{XT} \times \frac{0.1b}{c} \tag{3.27}$$

It was assumed the thrust vector is parallel to the body axis, so the effect of propulsion in the normal plane is zero (i.e. $Z_{\delta T} = 0$). The effect of elevator deflection on airspeed is also neglected (i.e. $X_{\delta e} = 0$).

The state-space model was used to approximate the natural frequency and damping ratio of the open-loop system. For a conventional (uncoupled) aircraft, the linearised longitudinal open-loop system consists of two pairs of complex conjugate poles, which represent the short-period and phugoid motion. The short-period motion is characterised by high frequency oscillations in angle-of-attack, at constant airspeed, while the phugoid motion generally corresponds to low frequency changes in flight path angle and altitude, with corresponding variations in airspeed. The longitudinal poles for the two vehicles at each flight condition are provided in Table 3.2. This shows that both vehicles have unstable longitudinal rigid-body modes at several flight conditions. In this case, the poles are not always complex conjugate pairs, there are several poles with no imaginary part, corresponding to over-damped motion. The natural frequency, ω_n, and damping ratio, ζ, of over-damped motion can be calculated as follows (Karnopp and Fischer, 1990):

$$\omega_n = \sqrt{\omega_1 \omega_2} \tag{3.28}$$

$$\zeta = \frac{\omega_1 + \omega_2}{\sqrt{2\omega_1\omega_2}} \tag{3.29}$$

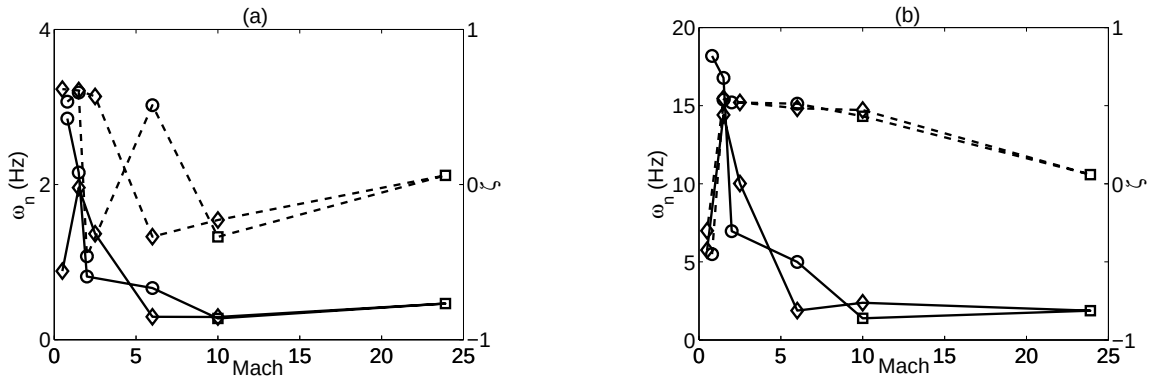

Figure 3.10: Short-period natural frequency and damping ratio, for (a) Full-size vehicle, and (b) Missile-size vehicle. Solid Line: Natural frequency (Hz); Dash Line: Damping ratio. ○: Ascent; □: Cruise; ◊: Descent

The maximum frequency of the unstable poles is quite high, at 2.7 Hz (16.7 rad/s) for the full-size vehicle, and 18 Hz (115 rad/s) for the missile-size vehicle. This represents the minimum control bandwidth required to maintain stability (Doman et al., 2006). Further, the rule-of-thumb for a robust control system is that the control bandwidth should exceed the frequency of the most unstable pole by a factor of 10 (Stein, 2003). This would require a control bandwidth of 27 Hz for the full-size vehicle, and 180 Hz for the missile-size vehicle, which exceeds the $10 - 12$ Hz upper limit for electromechanical actuators (Anderson and Knight, 2012) and is far in excess of typical aerodynamic control surfaces, which are rate limited to around $25 - 150$ deg/s, corresponding to approximately $0.5 - 5$ Hz peak-to-peak (Brumbaugh, 1994; Davidson et al., 2001; Ryu and Andrisani, 2003). The high-frequency instability occurs primarily in the transonic region, where drag and therefore thrust is high, leading to the largest impact from the propulsion-pitch coupling. At high Mach number, the real part of the poles is small, but there is a large imaginary part, corresponding to high frequency oscillatory motion with low damping. The increase in stability at high Mach number agrees with observations of Schmidt et al. (1991).

Short-period motion is characterised by rapid angle-of-attack variations at constant speed. Short-period characteristics (natural frequency and damping ratio) are shown in Figure 3.10. Both vehicles exhibit high frequency short-period modes in the transonic regime. Frequencies range from $0 - 3$ Hz for the full-size vehicle, and $0 - 20$ Hz for the missile-size vehicle. For both vehicles in the transonic regime, damping ratio magnitudes range between 0.1 and 0.6, while damping is very low in the hypersonic regime. For an uncoupled vehicle, short-period frequency generally follows dynamic pressure variations. This behaviour is not observed when propulsion-pitch coupling is introduced. Short-period frequency is low at high Mach number, where dynamic pressure is high. Both vehicles exhibit similar behaviour due to their aerodynamic similarity. Due to its lower mass and inertia, the missile-size vehicle has higher frequency (note the different y-axis scales between Figure 3.10 (a) and (b)), with similar damping.

For an uncoupled vehicle, phugoid motion involves a change in pitch angle and

Table 3.2: Poles for longitudinal rigid-body modes.

Mach number	Altitude (m)	Mode	Full-size (rad/s)	Missile-size (rad/s)
0.8	305	short-period	-9.57 ± 15.1i	51.5 ± 102i
		phugoid	-2.24, 16.7	-125, 0.105
1.5	6,096	short-period	-8.03 ± 10.9i	-56.8 ± 88.8i
		phugoid	10.7, 0.836	97.2, 0.025
2.0	15,240	short-period	2.37 ± 4.53i	-22.8 ± 37.4i
		phugoid	-5.32, -0.73	41.7, 0.02
6.0	20,000	short-period	-2.14 ± 3.59i	-16.1 ± 26.9i
		phugoid	3.02, 0.216	28.5, 0.007
10.0	33,000	short-period	0.58 ± 1.62i	-3.76 ± 7.85i
		phugoid	-1.33, -0.003	6.76, 0.04
24.0	33,000	short-period	-0.172 ± 2.92i	-0.69 ± 11.8i
		phugoid	-0.0004 ± 0.0006i	-0.057, 0.00005
10.0	30,000	short-period	0.42 ± 1.79i	-7.05 ± 13.2i
		phugoid	-0.97, -2.08	12.8, 0.004
6.0	27,500	short-period	0.63 ± 1.74i	-5.7 ± 10.3i
		phugoid	-1.57, -0.107	9.94, 0.007
2.5	15,000	short-period	-4.87 ± 7.06i	-32.8 ± 53.7i
		phugoid	7.09, 0.477	60.1, 0.017
1.5	10,000	short-period	-7.47 ± 9.79i	-49.5 ± 75.8i
		phugoid	0.76, 9.36	82, 0.03
0.5	0	short-period	-3.42 ± 4.38i	10.9 ± 34.8i
		phugoid	-3.3, 4.4	-49.1, 0.21

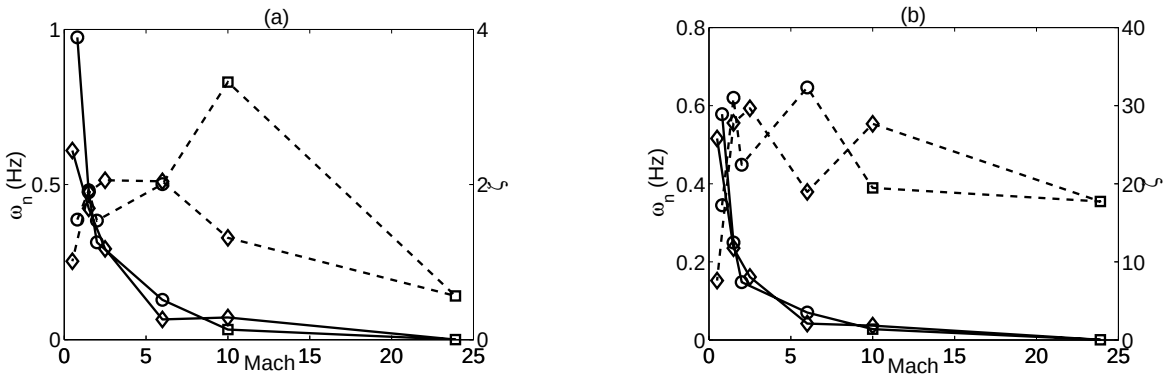

Figure 3.11: Phugoid natural frequency and damping ratio, for (a) Full-size vehicle, and (b) Missile-size vehicle. Solid Line: Natural frequency (Hz); Dash Line: Damping ratio. ○: Ascent; □: Cruise; ♢: Descent

velocity, and occurs over longer time periods, at constant angle-of-attack (Nelson, 1989). The phugoid mode generally follows the trends expected from incompressible flow for an uncoupled vehicle, where inverse relationships are observed between natural frequency and airspeed, and between damping ratio and L/D (Nelson, 1989). Phugoid frequencies range from $0-1$ Hz for the full-size vehicle, and $0-0.7$ Hz for the missile-size vehicle (see Figure 3.11). The small L/D values mean the phugoid motion is heavily damped, with damping ratios greater than 1 at several trim conditions, resulting in the over-damped motion described previously. Maximum damping occurs in the supersonic regime for the full-size vehicle, with a maximum damping ratio of 3.3. The smaller vehicle has higher damping, with a maximum damping ratio of approximately 32 in the Mach 6 (ascent) flight condition. The overall behaviour and trends are similar between vehicles, and correspond with previous studies (Sachs, 2005).

The maximum short-period frequency for the full-sized, coupled GHAME vehicle is around 3 Hz, which occurs in the transonic regime. At hypersonic Mach numbers ($M \approx 6$), short-period frequency is around $0.3-0.7$ Hz, depending on dynamic pressure, which is similar to other coupled hypersonic vehicles with similar mass (Bolender and Doman, 2007; Chavez and Schmidt, 1994b). This frequency increases to over 20 Hz for the missile-size vehicle. Clearly, mass properties have a significant impact on short-period frequency, and smaller vehicles will require a higher control bandwidth. Further, it is clear that the hypersonic regime is not the critical regime for control bandwidth, vehicle dynamics are faster in the transonic regime for this vehicle. Operation of air-breathing hypersonic vehicles in this regime has not been previously addressed in the literature.

Phugoid frequency is more varied between vehicles in the literature. The full-size vehicle results are slightly higher than other vehicles with similar aerodynamic and mass properties.

In the case of damping ratio, short-period matches similar vehicles, while phugoid does not. In this work, both vehicles have highly damped or over-damped phugoid modes. This is related to the low L/D of the GHAME vehicle, which is in-turn driven

by the inefficient trim conditions and high elevator deflections caused by propulsive-pitch coupling.

3.4.2 Lateral Motion

For lateral rigid-body modes, the procedure follows that of the longitudinal modes. A state-space model was developed for the the lateral dynamics using linearised equations of motion. The model is simplified by assuming the product of inertia $I_{xz} = 0$, which removes any inertial coupling between longitudinal and lateral motion. Therefore, the propulsion system has no effect on the lateral motion, so the analysis follows Nelson (1989).

The state-space model was used to approximate the open-loop system, which consists of three modes: a spiral mode, corresponding to rotation about the z axis, a roll mode, corresponding to rotation about the x axis, and a dutch roll mode, which consists of both side-slip and yaw (Nelson, 1989).

Spiral and roll modes are first-order, and consist of only a single pole on the real axis. These modes are either convergent or divergent, depending on stability. Both spiral and roll modes exhibit instability at certain flight conditions. Therefore, it is informative to consider the poles of the spiral and roll modes to determine their stability. This data is provided in Table 3.3.

Although both spiral and roll modes show some instability, the time constant is very long, especially for the full-size vehicle. The shortest time constant occurs for the roll mode on the missile-size vehicle, and is approximately 3.6 s, corresponding to an unstable pole at 0.275 rad/s. Therefore, while the behaviour is divergent, it diverges very slowly.

The dutch roll mode is a second-order mode and therefore consists of complex conjugate poles. Dutch roll motion is stable at each trim condition (see Table 3.3). The natural frequencies and damping ratios of the dutch roll mode compare well with the limited data available in the literature, where low dutch roll frequency and damping was reported (Colgren et al., 2009). Here, frequencies are in the $0.3 - 0.8$ Hz range for the full-size vehicle, and $1.5 - 3.5$ Hz for the missile-size vehicle (see Figure 3.12). Damping ratios are below 0.3 for both vehicles. Dutch roll poles are complex conjugates, as expected for a conventional aircraft, as propulsion-pitch coupling does not affect the lateral modes.

The most unstable lateral rigid-body pole for the full-size vehicle corresponds to the roll mode at subsonic speed (Mach 0.8) and is located at 0.005 Hz (0.029 rad/s). Therefore, the control system bandwidth required is 0.05 Hz, using the rule-of-thumb. The missile-size vehicle has an unstable roll mode with a pole at 0.04 Hz (0.275 rad/s) at the Mach 2 flight condition, requiring a control bandwidth of 0.4 Hz, according to the rule-of-thumb.

In this case, the lateral modes can be controlled using aerodynamic control surfaces.

Table 3.3: Poles for lateral rigid-body modes.

Mach number	Altitude (m)	Mode	Full-size (rad/s)	Missile-size (rad/s)
0.8	305	spiral	-0.914	0.03
		roll	0.029	-3.11
		dutch roll	-0.853 ± 2.33i	-3.8 ± 9.8i
1.5	6,096	spiral	-0.511	0.001
		roll	0.002	-1.1
		dutch roll	-1.11 ± 3.27i	-5.08 ± 13.6i
2.0	15,240	spiral	-0.137	-0.003
		roll	0.005	0.275
		dutch roll	-0.398 ± 2.19i	-2.04 ± 9.29i
6.0	20,000	spiral	0.001	0.001
		roll	-0.526	-2.09
		dutch roll	-0.091 ± 3.83i	-0.38 ± 15.4i
10.0	33,000	spiral	0.0008	0.0008
		roll	-0.107	-0.416
		dutch roll	-0.02 ± 2.24i	-0.08 ± 8.97i
24.0	33,000	spiral	0.0004	0.0004
		roll	-0.224	-0.9
		dutch roll	-0.05 ± 5.1i	-0.2 ± 20.7i
10.0	30,000	spiral	0.0008	0.0008
		roll	-0.17	-0.7
		dutch roll	-0.034 ± 2.91i	-0.15 ± 11.7i
6.0	27,500	spiral	0.001	0.001
		roll	-0.19	-0.73
		dutch roll	-0.035 ± 2.38i	-0.155 ± 9.53i
2.5	15,000	spiral	0.0025	0.0025
		roll	-0.435	-1.37
		dutch roll	-0.457 ± 3.18i	-2.05 ± 13.0i
1.5	10,000	spiral	-0.535	0.0006
		roll	0.0015	-1.54
		dutch roll	-0.925 ± 3.04i	-4.12 ± 12.5i
0.5	0	spiral	-1.5	0.026
		roll	0.022	-4.84
		dutch roll	- 0.64 ± 2.01i	-3.1 ± 8.24i

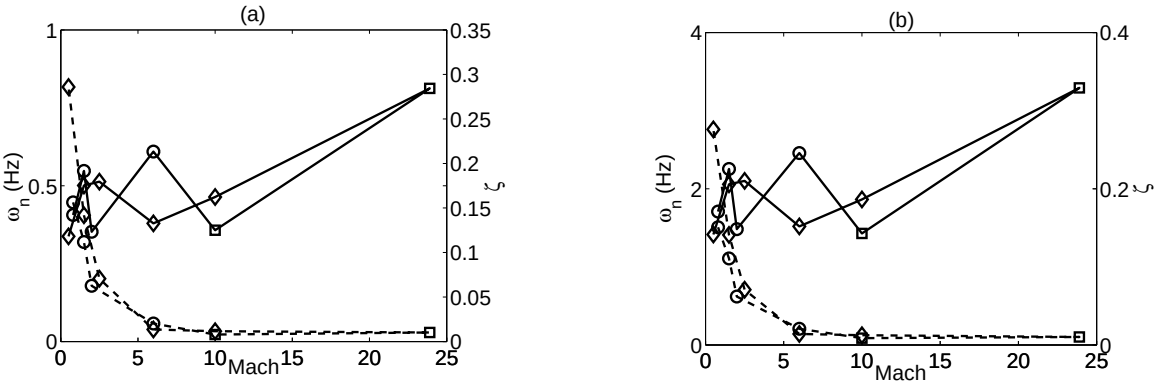

Figure 3.12: Dutch roll natural frequency and damping ratio, for (a) Full-size vehicle, and (b) Missile-size vehicle. Solid Line: natural frequency (Hz); Dash Line: damping ratio. ∘: Ascent; □: Cruise; ♢: Descent

3.5 Closed-Loop Control

Stability is not the only consideration when specifying requirements for an aircraft control system, another key consideration is flying qualities. One standard used by the US military to specify acceptable flying qualities for piloted aircraft is MIL-F-8785C (USDoD, 1980). This standard specifies requirements for several classes of aircraft and is independent of the design of the flight control system. Qualities are assessed and assigned a level, based on the ability of the pilot to successfully complete different phases of a mission. The relevant requirements can be found in literature (USDoD, 1980; Nelson, 1989; Stevens and Lewis, 2003).

To achieve acceptable flying qualities, open-loop dynamics (i.e. natural frequency and damping ratio) are modified. In this work, the modifications were made using a pole placement technique (Kautsky et al., 1985). The result of the modifications is to change the vehicle's behaviour to certain inputs, such that it is able to be flown with a reasonable level of confidence.

For example, in the open-loop system, a control input to the elevator will excite both the phugoid and short-period modes. If the frequency or damping of these modes is too high or too low, poor flying qualities result. Therefore, the frequency and/or damping ratio is modified to improve the flying qualities to within acceptable limits.

As the closed-loop model is linear, if no deflection or rate limits are applied to the actuators, any dynamic properties can be achieved. Here, 30° deflection limits and a rate limit of 10.5 rad/s (600 deg/s) are placed on the elevators, ailerons, and rudder, corresponding to the maximum 10 Hz peak-to-peak bandwidth achievable with aerodynamic control. The implications of variable rate limits achievable with reaction control jets is addressed in Chapter 9. No limits are applied to the throttle rate, but maximum throttle settings of $0 < \delta_T < 2$ are applied, corresponding to the limits of the GHAME propulsion database.

MIL-F-8785C is only applicable for piloted aircraft, so may not be a requirement for a missile. However, this standard would be applicable to missile-size Unmanned Aerial

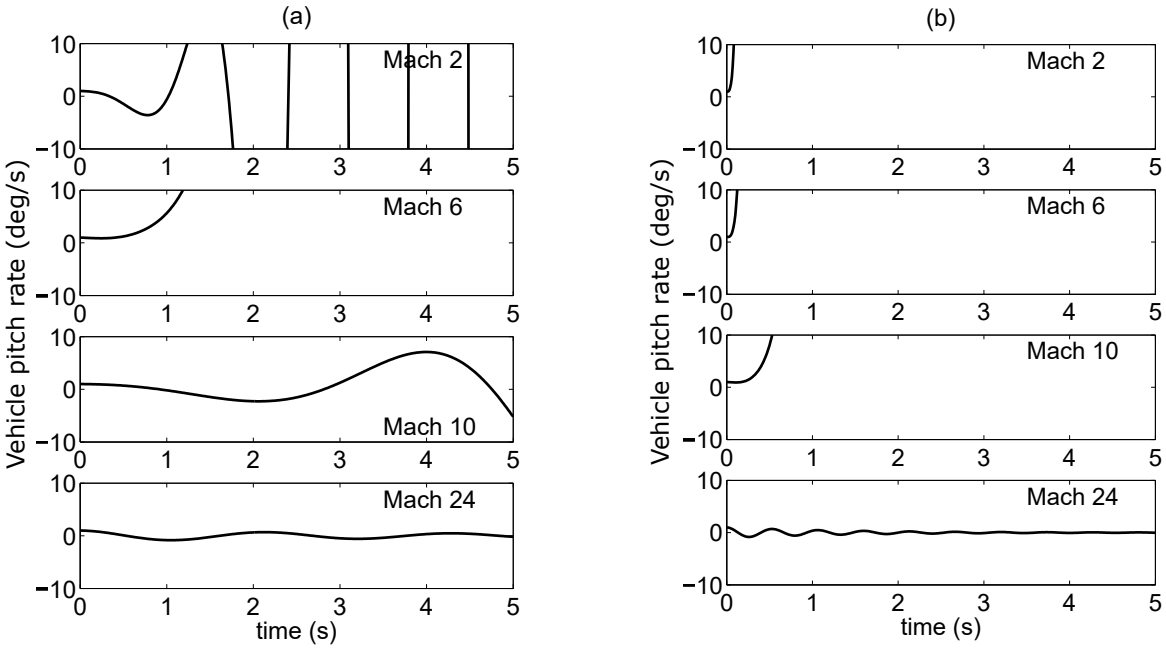

Figure 3.13: Open-loop response to 1 deg/s pitch rate perturbation, for (a) Full-size vehicle, and (b) Missile-size vehicle.

Vehicles (UAVs), and provides a useful, quantifiable set of requirements for a control system. As such, both the full-size and missile-size vehicles are considered. Longitudinal dynamics, including short-period natural frequency and damping ratio, and phugoid damping ratio are set to achieve Level 1 flying qualities, defined as *"clearly adequate for the mission flight phase"* (USDoD, 1980). The longitudinal dynamics requirements are independent of aircraft type. Lateral modes are set to achieve Level 1 flying qualities for a high manoeuvrability aircraft (Class I or IV in MIL-F-8785C).

3.5.1 Longitudinal Motion

In the longitudinal case, phugoid damping and short-period frequency are already acceptable for both vehicles. The only change required is to short-period damping ratio, which must be modified to fall between 0.35 and 1.30 (USDoD, 1980). This is done with a closed-loop control system, which uses the elevator and propulsion system to provide additional forces and moments.

If the short-period is excited by a small pitch rate perturbation of 1 deg/s, the open-loop response at selected flight conditions is shown in Figure 3.13. The full dataset of all flight conditions is provided in Appendix A. At all Mach numbers except Mach 24, both vehicles are unstable. In the case of the missile-size vehicle, the divergence is exponential and is rapid, due to the high frequency unstable pole on the real axis. At Mach 24, stable oscillatory behaviour is observed, with very low damping. Although the vehicle is stable at high Mach number, the short-period damping is insufficient so the open-loop flying qualities are unacceptable. This behaviour is typical of air-breathing hypersonic vehicles with an integrated propulsion system, as described in Chapter 2.

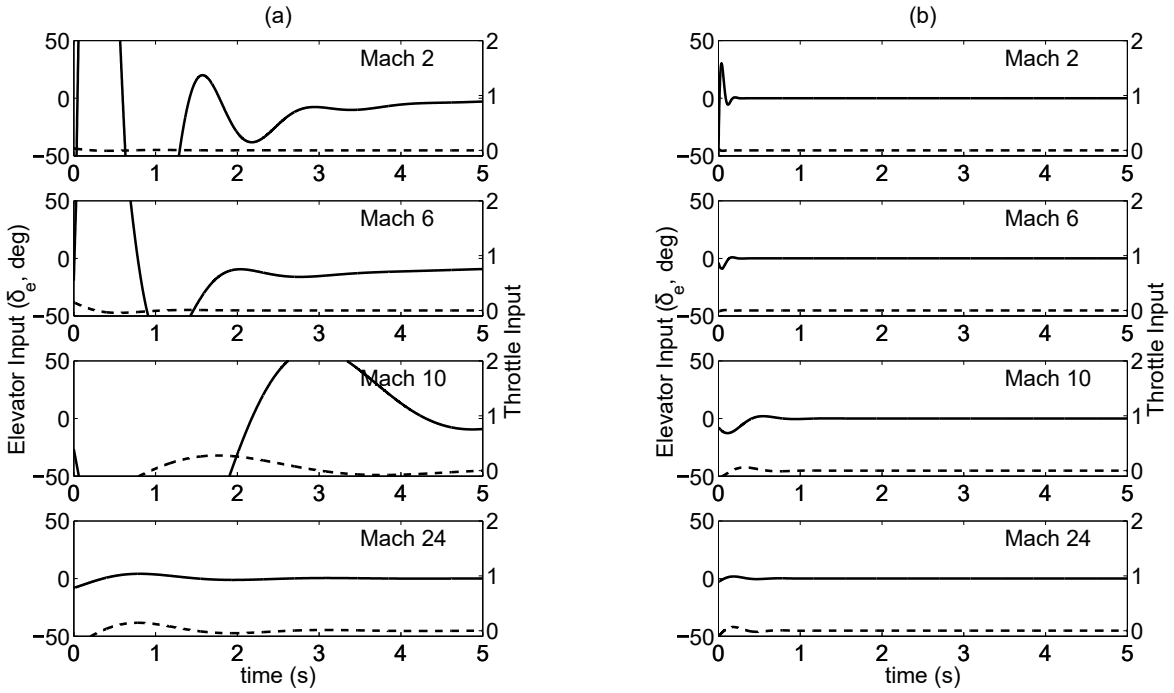

Figure 3.14: Closed-loop elevator response to 1 deg/s pitch rate perturbation, for (a) Full-size vehicle, and (b) Missile-size vehicle. Solid Line: Elevator deflection (deg); Dash Line: Throttle position.

The control effort required to alter the response such that the vehicle exhibits acceptable flying qualities is shown in Fig. 3.14. This is the ideal behaviour, before the control deflection and rate limits are applied.

For the full-size vehicle, the control inputs from the elevator are large, with $|\delta_e| > 30°$, while the throttle inputs are small but non-zero. Control deflection limits are exceeded for 8 out of the 11 flight conditions. The deflections for the missile-size vehicle are smaller, but still exceed the deflection limits at 8 out of 11 flight conditions.

When the control deflection and rate limits are applied, Fig. 3.15 shows that the elevator becomes saturated and control is lost for both vehicles at Mach 2, for the full-size vehicle at Mach 6, and the missile-size vehicle at Mach 24. At Mach 10, the full-size vehicle has high control deflection, but is able to remain stable without exceeding deflection limits. The results are summarised in Table 3.4.

The rate and deflection limitations inherent with aerodynamic control, compared with the unstable dynamics of air-breathing hypersonic vehicles, mean that the vehicle cannot achieve acceptable flying qualities at certain points within the flight envelope. For the full-size vehicle, flying qualities are unacceptable at 8 of the 11 conditions considered. The missile-size vehicle also has unacceptable flying qualities at 8 of the 11 conditions. Therefore, alternative actuators that provide higher bandwidth control, and higher control authority, are required.

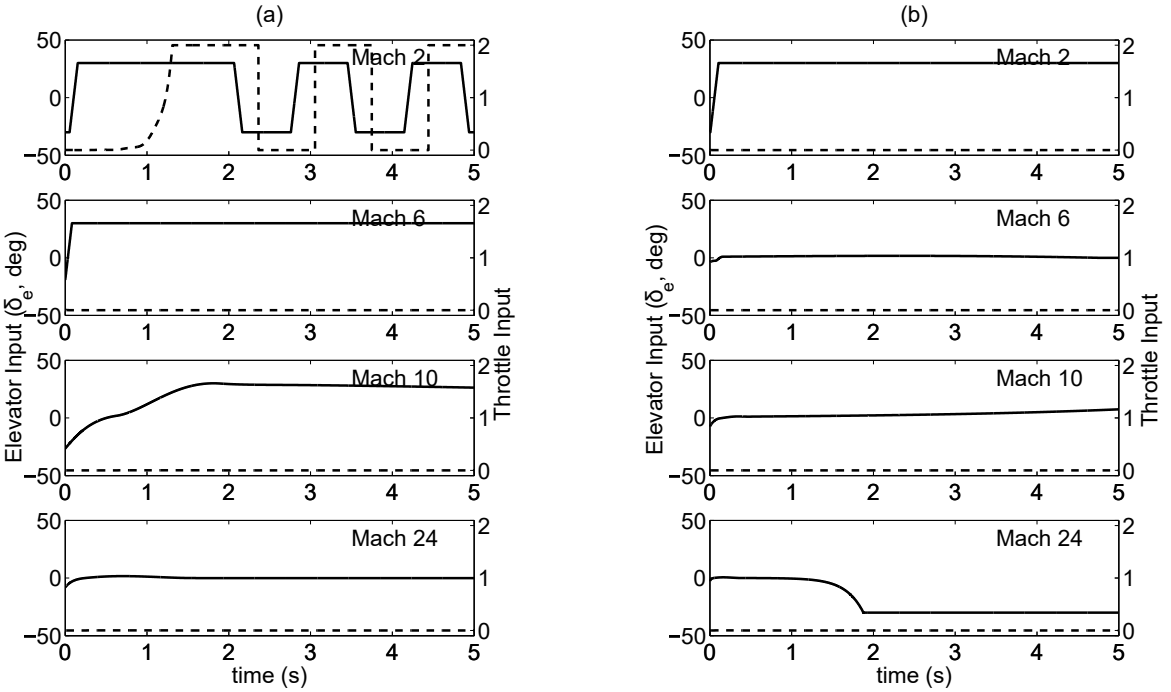

Figure 3.15: Closed-loop elevator response to 1 deg/s pitch rate perturbation with actuator deflection and rate limits, for (a) Full-size vehicle, and (b) Missile-size vehicle. Solid Line = Elevator deflection (deg); Dash Line: Throttle position.

Table 3.4: Ability to achieve acceptable flying qualities, using pole placement technique with actuator rate and deflection limits applied.

Mach number	Altitude (m)	Full-size	Missile-size
0.8	305	Not Suitable	Not Suitable
1.5	6,096	Not Suitable	Not Suitable
2.0	15,240	Not Suitable	Not Suitable
6.0	20,000	Not Suitable	Suitable
10	33,000	Suitable	Suitable
24	33,000	Suitable	Not Suitable
10	30,000	Not Suitable	Suitable
6.0	27,500	Not Suitable	Not Suitable
2.5	15,000	Not Suitable	Not Suitable
1.5	10,000	Suitable	Not Suitable
0.5	0	Not Suitable	Not Suitable

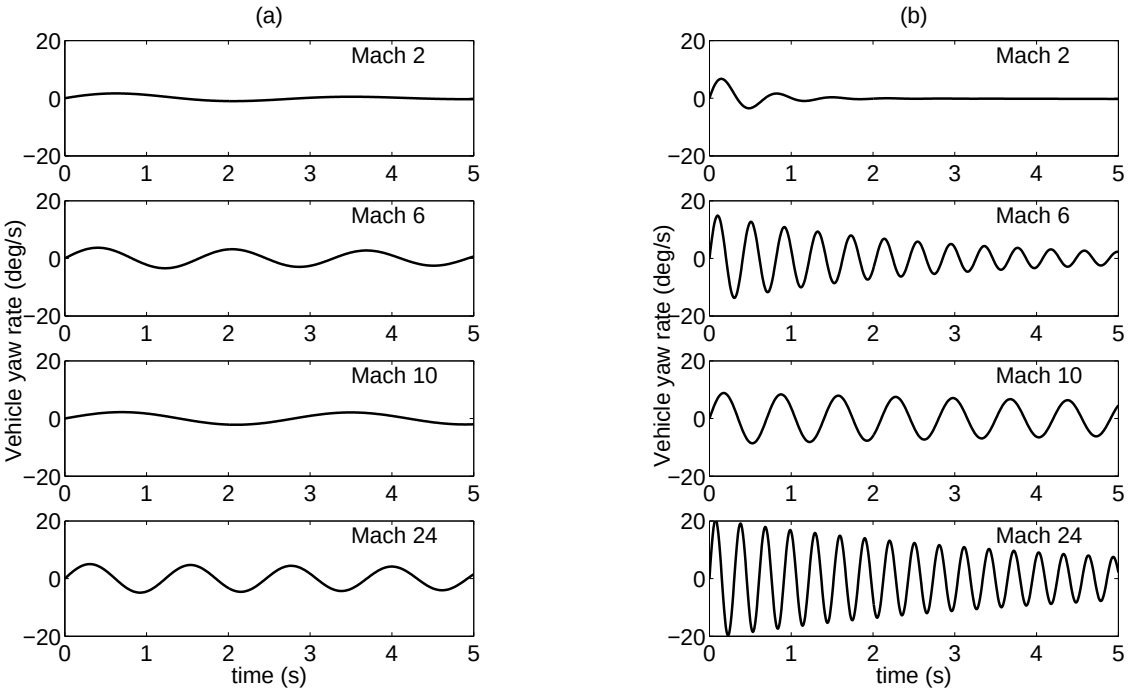

Figure 3.16: Open-loop response to 1 deg side-slip perturbation, for (a) Full-size vehicle, and (b) Missile-size vehicle.

3.5.2 Lateral Motion

MIL-F-8785C also considers flying qualities requirements for the lateral rigid-body motion of an aircraft (USDoD, 1980; Stevens and Lewis, 2003; Nelson, 1989). These requirements include minimum time-to-double amplitude for unstable first-order modes (i.e. spiral and roll modes), as well as frequency and damping limitations for the dutch roll mode. As with the longitudinal modes, these requirements have been implemented via closed-loop control using the pole placement technique described by Kautsky et al. (1985).

The open-loop spiral mode response is excited when the vehicle is perturbed by side-slip. The spiral mode does not exhibit the expected behaviour for a first-order system, as it is highly coupled with the second-order dutch roll mode, which is also excited by side-slip perturbations (Nelson, 1989). The spiral mode yaw rate response to a 1 deg initial side-slip angle is shown in Figure 3.16. The missile's spiral mode is unstable at several flight conditions, but with a long time constant (see Table 3.3). Therefore, the open-loop behaviour over the time period shown is dominated by the dutch roll response. Dutch roll behaviour is stable for both vehicles at all Mach numbers, although the damping is low at high Mach numbers.

The roll mode is excited by a 1 deg/s roll rate perturbation, and the open-loop response is shown in Figure 3.17. The roll mode behaviour closely resembles a first-order system, as the roll mode is not highly coupled to the spiral and dutch roll modes. The open-loop behaviour is stable, with the exception of the missile-size vehicle, which is unstable at Mach 2.

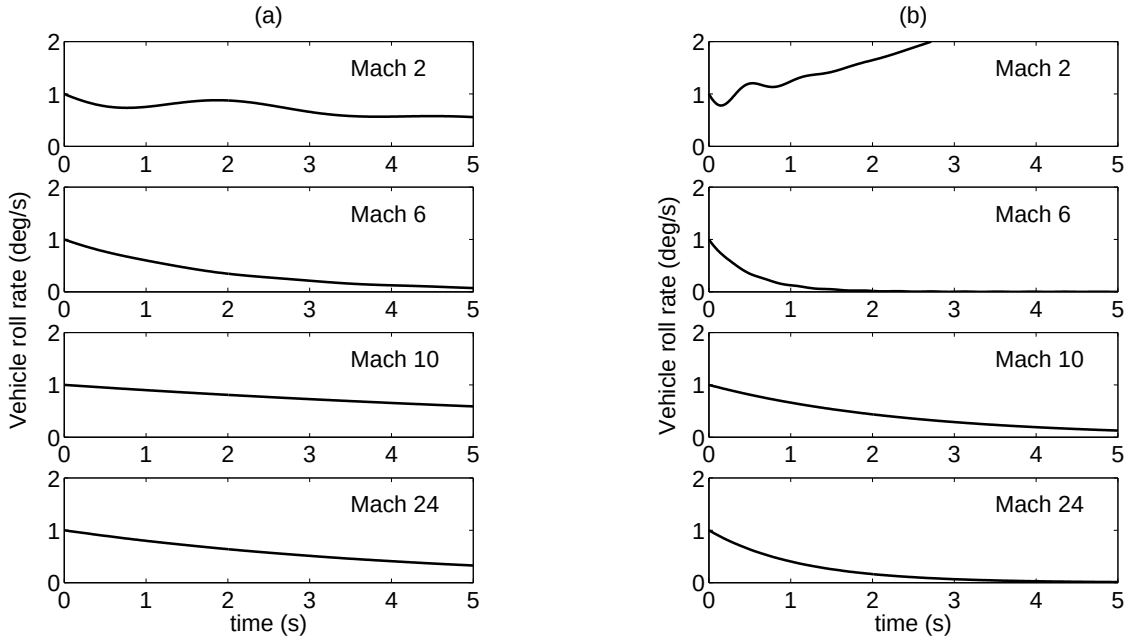

Figure 3.17: Open-loop response to 1 deg/s roll rate perturbation, for (a) Full-size vehicle, and (b) Missile-size vehicle.

Closed-loop control changes the vehicle response to within acceptable limits. The control effort required to alter the response is shown in Figure 3.18 for the spiral and dutch roll modes, and Figure 3.19 for the roll mode.

The control deflection required for the spiral and dutch roll mode exceeds 30° for both vehicles, while the control rates are slow. When the control limits are applied, the vehicle remains controllable at all flight conditions. These results are not shown for brevity, the full data-set is included at Appendix A.

3.6 Atmospheric Turbulence

Another aspect of MIL-F-8785C is the behaviour of the aircraft in the presence of atmospheric turbulence. The Von Karman *severe* turbulence model (USDoD, 1980) has been applied to the closed-loop vehicle and the longitudinal motion has been investigated. The response of the uncoupled lateral modes was not investigated.

An example of the perturbations caused by the Von Karman *severe* turbulence model is provided in Figure 3.20. Free-stream velocity changes are approximately 10 m/s both horizontally and vertically, independent of Mach number. Pitch rate is perturbed by up to 5 deg/s at all flight conditions, while flight path angle, θ, is unaffected. Both the magnitude and frequency of the turbulent wind profile is similar for all Mach numbers.

To maintain acceptable flying qualities in the presence of turbulence, the closed-loop control system must use the elevator and throttle inputs. This is identical to the previous section, except that instead of a step input to pitch rate, the vehicle is subject to time-dependent perturbations to airspeed and pitch rate.

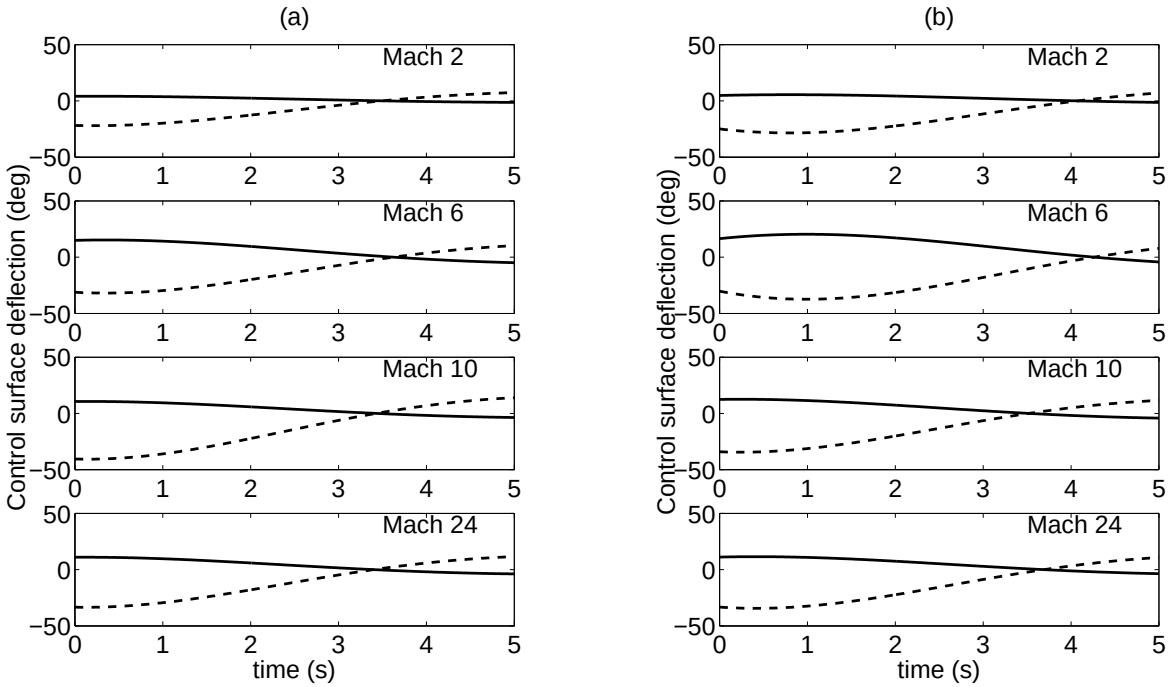

Figure 3.18: Closed-loop control surface response to side-slip perturbation, for (a) Full-size vehicle, and (b) Missile-size vehicle. Solid line: Aileron, Dotted line: Rudder.

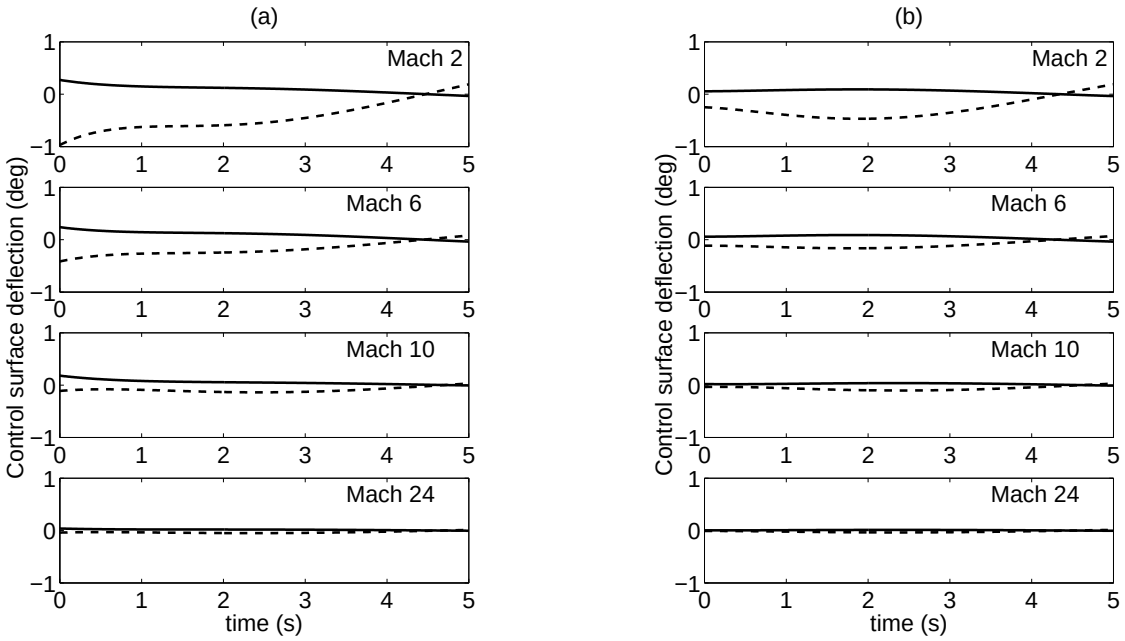

Figure 3.19: Closed-loop control surface response to roll rate perturbation, for (a) Full-size vehicle, and (b) Missile-size vehicle. Solid line: Aileron, Dotted line: Rudder.

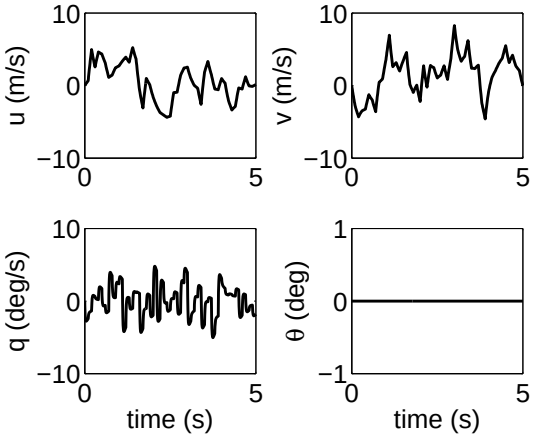

Figure 3.20: Perturbations caused by the Von Karman *severe* turbulence model. (a) Horizontal airspeed, u, (b) Vertical airspeed, v, (c) Pitch rate, q, and (d) Flight path angle, θ.

When the control deflection and rate limitations are included, Fig. 3.21 shows the elevator becomes saturated and control is lost in all cases except the full-size vehicle at Mach 24. At Mach 2 and Mach 6, the elevator saturates almost immediately, and pitch rate diverges due to the longitudinal instability. At Mach 10, the divergence is slower, and is oscillatory for the full-size vehicle. At Mach 24, the full-size vehicle is able to be controlled while the missile-size vehicle eventually saturates and control is lost.

3.7 Comparison to Uncoupled Vehicle

To quantify the effect that dynamic propulsion-pitch coupling has on the longitudinal dynamics, the response of a vehicle without a propulsion-pitch coupling model was also considered. Without coupling, the vehicle is stable at each flight condition. The data is provided in Appendix A. The poles all have low frequency and relatively high damping, which will result in improved open-loop flying qualities.

At Mach 2, the open-loop flying qualities are acceptable, so no control input is required for the closed-loop system. At all other Mach numbers the dynamics are not significantly modified to achieve acceptable flying qualities, so control inputs are small.

The response of the uncoupled vehicle to *severe* Von Karman atmospheric turbulence was also investigated. The longitudinal stability of the vehicle means that the turbulent perturbations are naturally resisted. Therefore, the control inputs required to maintain steady level flight were negligible.

This highlights the impact of the propulsion-pitch coupling on the vehicle dynamics, which is one of the reasons that control systems remain one of the key challenges in air-breathing hypersonic vehicle design (Zhang et al., 2016).

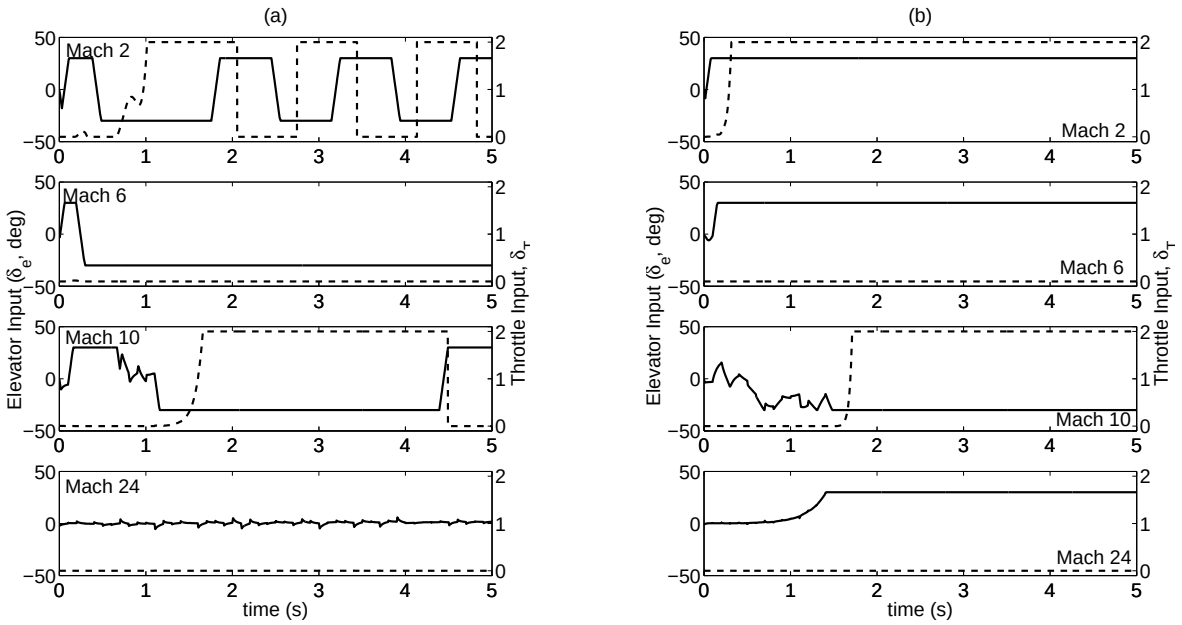

Figure 3.21: Closed-loop elevator response to turbulence, for (a) Full-size vehicle, and (b) Missile-size vehicle. Solid line: Elevator deflection (deg); Dash line: Throttle setting.

3.8 Conclusions

The control authority and bandwidth requirements have been estimated for two generic, propulsion-pitch coupled air-breathing hypersonic vehicles. The analysis shows that the control authority of both vehicles is poor in the transonic region when elevator deflections are limited to a maximum of 30°. Control authority improves in the transonic and supersonic flight regimes, and is very high at the Mach 24 flight condition, due to the high dynamic pressure. However, it is expected that other limitations, such as aerodynamic heating at high dynamic pressure, would limit control deflections and manoeuvrability at this Mach number.

Large control deflections are required to overcome the pitching moment from the propulsion system at trim. When using aerodynamic control, trim drag is very high, resulting in a low L/D. Therefore, alternative higher-lift actuators may be beneficial to improve efficiency.

The longitudinal rigid-body modes are unstable when dynamic propulsion-pitch coupling is included in the model. This instability is severe at transonic Mach numbers where high drag requires high thrust. Previous studies have focused on dynamic behaviour at hypersonic free-stream conditions ($5 < M < 10$), and the lack of control authority and bandwidth in the transonic regime is previously unpublished.

A robust control system requires a bandwidth of 27 Hz for the full-size vehicle and 180 Hz for the missile-size vehicle, which far exceeds the capability of aerodynamic control surfaces. The limitations of aerodynamic control are demonstrated when the dynamics are modified to achieve acceptable flying qualities. The control deflection and

rate limits result in unacceptable flying qualities at 8 of 11 flight conditions for both vehicles. It is clear that the rate and deflection limitations imposed by aerodynamic control prevent successful operation of the vehicle. This is a unique property of air-breathing hypersonic vehicles, caused by dynamic propulsion-pitch coupling. When an uncoupled vehicle model is used, the actuators are able to maintain control at all flight conditions.

Lateral rigid-body modes show some instability at certain flight conditions for both the spiral and roll modes. However, the frequency (or time constant) of the unstable modes is quite low, and can be controlled to achieve acceptable flying qualities with aerodynamic control surfaces. The difference between the two vehicles follows a consistent trend, with the smaller vehicle having faster dynamics.

The response to turbulence is poor for the coupled vehicles, due to their longitudinal instability. The control surfaces quickly saturate and control is lost at all conditions except Mach 24.

The differences in dynamics between the coupled and uncoupled vehicles are stark. The instability caused by the propulsion-pitch coupling, combined with the limitations imposed by aerodynamic control surfaces, means the coupled vehicle cannot be flown at several flight conditions, and cannot withstand severe turbulence at speeds below Mach 24. This is compared to the uncoupled vehicle, which is stable, and provides a relatively benign environment for control.

The GHAME aerodynamics model (White et al., 1992) used in this work has some limitations. The accuracy of the aerodynamics, especially at high Mach number, is questionable (Maughmer et al., 1993), and ignores some important hypersonic flow phenomena, including thermo-chemical non-equilibrium (Hassan et al., 1993), which can impact pitching moments (Pezzella and Viviani, 2016; Anderson, 2006). In addition, the methodology used to generate the data was found to provide inaccurate lateral control moments in the supersonic regime, and cannot account for phenomena such as shock interactions and flow separation. However, the model is suitable as a generic vehicle with a representative integrated configuration (Banerjee et al., 2016). Further, the method developed in the work can be used with any aerodynamic model.

This work provides a new approach to the modeling and simulation of the dynamic coupling caused by propulsion-airframe integration in air-breathing hypersonic vehicles. This approach allows the consideration of the rigid-body dynamics at a wide range of flight conditions.

The model has been used to investigate the control properties of two generic air-breathing hypersonic vehicles, based on the GHAME model. It has been shown that the control authority and bandwidth limitations of aerodynamic control surfaces limits the ability of the aircraft to operate at several points along a representative single-stage-to-orbit flight profile. Therefore, the design of air-breathing hypersonic vehicles may require the consideration of supplementary actuators, such as reaction control jets.

Chapter 4

Numerical Methodology

This chapter describes the numerical techniques applied within this thesis; the governing equations, discretisation methods, numerical algorithms, and turbulence models are detailed. The ability of this method to accurately simulate flows of interest is established through the verification and validation process detailed in Chapter 5

The simulations were conducted using OpenFOAM v2.1.1 (Weller et al., 1998). Temporal and spatial discretisation schemes are outlined, as well as the solution algorithms. In all cases, the flow is treated as a continuous medium that obeys the conservation of mass, momentum and energy.

4.1 Governing Equations

The governing equations for a compressible, unsteady flow of a Newtonian fluid with no external (body) forces, and no internal volumetric heat addition, assuming Fourier's law of thermal conductivity, are (Greenshields et al., 2010):

$$\frac{\partial \rho}{\partial t} + \nabla \bullet (\rho \mathbf{u}) = 0 \tag{4.1}$$

$$\frac{\partial \rho \mathbf{u}}{\partial t} + \nabla \bullet (\rho \mathbf{u}\mathbf{u}) + \nabla p - \nabla \bullet \boldsymbol{\tau} = 0 \tag{4.2}$$

$$\frac{\partial \rho E}{\partial t} + \nabla \bullet (\rho E \mathbf{u}) + \nabla \bullet (p\mathbf{u}) - \nabla \bullet (k \nabla T) - \nabla \bullet (\boldsymbol{\tau} \bullet \mathbf{u}) = 0 \tag{4.3}$$

For a three dimensional flow:

$$\mathbf{u} = u\mathbf{i} + v\mathbf{j} + w\mathbf{k} \tag{4.4}$$

$$\nabla \bullet \mathbf{u} = \frac{\partial u}{\partial x} + \frac{\partial v}{\partial y} + \frac{\partial w}{\partial z} \tag{4.5}$$

$$\nabla \phi = \frac{\partial \phi}{\partial x} + \frac{\partial \phi}{\partial y} + \frac{\partial \phi}{\partial z} \tag{4.6}$$

where, ρ is the density of the fluid, $\mathbf{u}$ is the velocity, p is the pressure, E is the total energy density, calculated as $E = e + \frac{\mathbf{u}^2}{2}$, where e is the specific internal energy. k is

the thermal conductivity, T is the temperature, and $\boldsymbol{\tau}$ is the deviatoric component of the viscous stress tensor, represented by Newton's law, assuming zero bulk viscosity, as follows:

$$\boldsymbol{\tau} = 2\mu \text{dev}(\mathbf{D}) \tag{4.7}$$

where μ is the dynamic viscosity, $\mathbf{D}$ is the deformation gradient tensor:

$$\mathbf{D} = \frac{1}{2}[\nabla \mathbf{u} + (\nabla \mathbf{u})^T] \tag{4.8}$$

whose deviatoric component is:

$$\text{dev}(\mathbf{D}) = \mathbf{D} - \frac{1}{3}\text{tr}(\mathbf{D})\mathbf{I} \tag{4.9}$$

where $\mathbf{I}$ is the unit tensor and $\text{tr}(\mathbf{D})$ is the trace of $\mathbf{D}$.

In this work, only perfect gases are considered, for which:

$$p = \rho R_s T \tag{4.10}$$

$$e = c_v T = \frac{R_s}{(\gamma - 1)} T \tag{4.11}$$

where R_s is the specific gas constant and γ is the ratio of specific heats, which is assumed to be constant in all cases.

Noting the similarities in the structure of the terms in Equations 4.1, 4.2 and 4.3, Versteeg and Malalasekera (1995) introduced a generic transport equation for a general variable, ϕ, as follows:

$$\underbrace{\frac{\partial(\rho\phi)}{\partial t}}_{\text{temporal derivative}} + \underbrace{\nabla \bullet (\rho\phi\mathbf{u})}_{\text{convection term}} - \underbrace{\nabla \bullet (\Gamma \nabla\phi)}_{\text{diffusion term}} = \underbrace{S_\phi}_{\text{source term}} \tag{4.12}$$

Expressing the equation in this form highlights the various transport processes: the rate of change, convection, diffusion, and source terms. By setting ϕ equal to 1, $\mathbf{u}$, and e, and setting appropriate values for diffusion coefficient, Γ, and source terms, Equations 4.1 ($\phi = 1$), 4.2 ($\phi = \mathbf{u}$), and 4.3 ($\phi = e$) can be returned.

4.2 Discretisation of the Governing Equations

OpenFOAM uses the finite volume method to transform partial differential equations into a system of algebraic equations. This is done by discretising the solution domain into a finite number of discrete regions, called control volumes. The temporal domain is also split into a finite number of intervals, or time-steps. Figure 4.1 shows an example of a finite volume of fluid. Quantities such as mass, momentum and energy are conserved in each volume. This requires the integration of the governing equations, represented

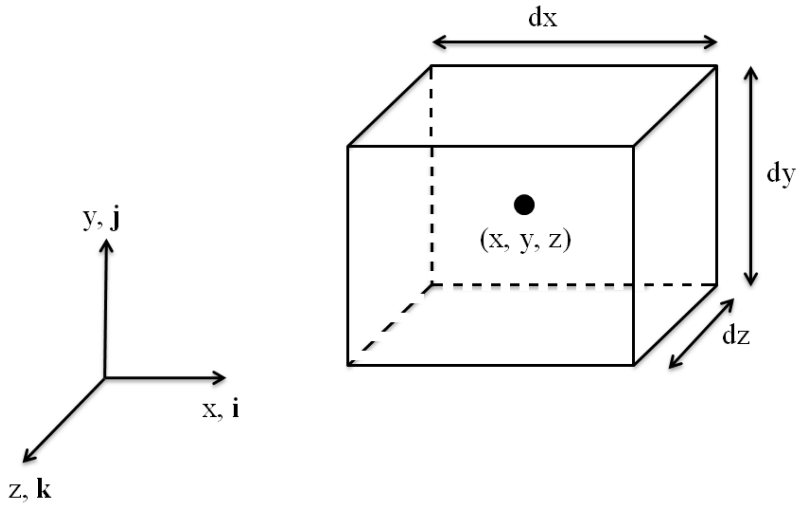

Figure 4.1: Finite volume of fluid.

in the general form by Equation 4.12, over the three-dimensional control volume, V, and over the small time interval, Δt, as follows (Versteeg and Malalasekera, 1995):

$$\int_{\Delta t}\left[\frac{\partial}{\partial t}\int_V \rho\phi dV + \int_V \nabla \bullet (\rho\phi\mathbf{u})\, dV - \int_V \nabla \bullet (\Gamma\nabla\phi)\, dV\right] dt = \int_{\Delta t}\left[\int_V S_\phi dV\right] dt \tag{4.13}$$

A system of algebraic equations is generated that solves Equation 4.13. The discretisation of Equation 4.13 will now be examined term by term.

4.2.1 Discretisation of the Convective Term

The convective term of Equation 4.13 can be expressed to second-order accuracy, assuming a linear variation of ϕ over the control volume, and using Gauss' theorem, as follows (Jasak, 1996):

$$\begin{aligned}\int_V \nabla \bullet (\rho\phi\mathbf{u})dV &= \sum_f \mathbf{S}.(\rho\phi\mathbf{u})_f \\ &= \sum_f \mathbf{S}.(\rho\mathbf{u})_f\phi_f \\ &= \sum_f F\phi_f\end{aligned} \tag{4.14}$$

where F represents the mass flux through the face f and $\mathbf{S}$ is the surface area of the face f. The value of ϕ at the face f must be obtained from the values at the centre of the adjoining cells, as OpenFOAM uses a co-located variable scheme, where all variables use the same control volume and are calculated and stored at the cell centres. There are a number of ways to estimate ϕ at the face f, and these methods are called convection differencing schemes.

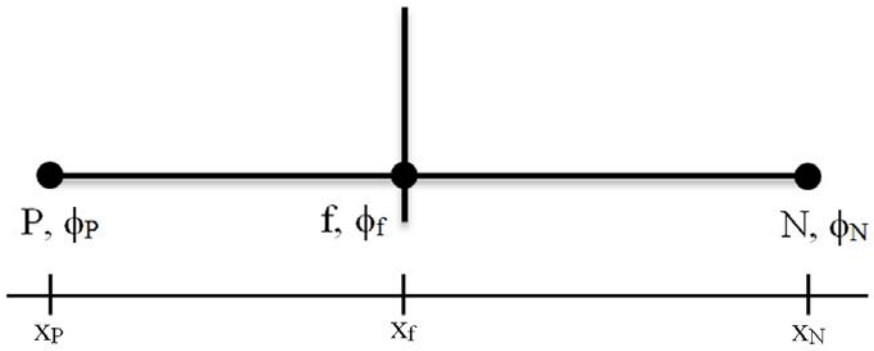

Figure 4.2: One-dimensional schematic of cell P with nearest neighbour cell N and face f.

4.2.1.1 Convection Differencing Scheme

OpenFOAM is designed for arbitrary, unstructured meshes. Therefore, it is impractical to use any values other than the current cell centre (i.e. the "owner" cell) and its nearest neighbours to calculate the value of ϕ (Jasak, 1996). A one-dimensional schematic of the "owner" cell P, its nearest neighbour N and the adjoining face f is shown in Figure 4.2.

Assuming a linear variation of ϕ between cells P and N allows ϕ_f to be calculated by linear interpolation, as follows:

$$\phi_f = f_x \phi_P + (1 - f_x)\phi_N \tag{4.15}$$

Here, the interpolation factor f_x is the ratio of distances:

$$f_x = \frac{x_N - x_f}{x_N - x_P} \tag{4.16}$$

This is referred to as **Central Differencing** (CD) and is second-order accurate (Ferziger and Peric, 2002). However, it has been well documented that CD can be unbounded (Versteeg and Malalasekera, 1995), resulting in oscillatory behaviour which prevents iterative convergence.

An alternative, bounded scheme is **Upwind Differencing** (UD), where the ϕ_f is determined by the direction of the flow, i.e.:

$$\phi_f = \begin{cases} \phi_P & \text{if } F \geq 0 \\ \phi_N & \text{if } F < 0 \end{cases} \tag{4.17}$$

However, UD is only first-order accurate, so boundedness is obtained at the expense of accuracy.

For compressible flows, fluid properties are not only transported by the flow, but also by the propagation of waves, which can travel in either positive or negative directions at varying speeds. The wave speeds are u, $u + a$, and $u - a$, where a is the local speed of sound, u is associated with the convection of the fluid, while $u + a$ and $u - a$ are associated with sound waves (Lomax et al., 2001). To account for this,

the OpenFOAM solver *rhoCentralFoam* uses either: the method proposed by Kurganov and Tadmor (2000), called the "KT Method"; or the method of Kurganov et al. (2001), called the "KNP Method". In these methods, the interpolation procedure is split into two directions, $f+$ and $f-$, corresponding to flow outward and inward to the cell respectively. The discretisation is as follows (Greenshields et al., 2010):

$$\sum_f V_f \phi_f = \sum_f [\alpha V_{f+} \phi_{f+} + (1-\alpha) V_{f-} \phi_{f-} + \omega_f (\phi_{f-} - \phi_{f+})] \tag{4.18}$$

where $V_f = \mathbf{S} \bullet \mathbf{u} = F/\rho$ is the volumetric flux through face f. The first two terms on the right hand side of Equation 4.18 are the flux evaluations in the $f+$ and $f-$ directions respectively, with a weighting term α. The third term is only required in cases where the convection term is part of a substantial derivative (Greenshields et al., 2010). It is an additional diffusion term using a diffusive volumetric flux ω_f based on the maximum speed of propagation of any discontinuity that may exist at a face between values interpolated in the $f+$ and $f-$ directions.

Volumetric fluxes associated with local speed of propagation, ψ, are calculated as follows (Greenshields et al., 2010):

$$\psi_{f+} = \max(a_{f+} |\mathbf{S}| + V_{f+}, a_{f-} |\mathbf{S}| + V_{f-}, 0) \tag{4.19}$$

$$\psi_{f-} = \max(a_{f+} |\mathbf{S}| - V_{f+}, a_{f-} |\mathbf{S}| - V_{f-}, 0) \tag{4.20}$$

where $a_{f+} = \sqrt{\gamma R T_{f+}}$ is the local speed of sound of the gas at face f, in the outward $(f+)$ direction. The diffusive volumetric flux is calculated as follows:

$$\omega_f = \begin{cases} \alpha \max(\psi_{f+}, \psi_{f-}) & \text{for the KT method} \\ \alpha(1-\alpha)(\psi_{f+} + \psi_{f-}) & \text{for the KNP method} \end{cases} \tag{4.21}$$

The weighting coefficient α is calculated using volumetric fluxes as follows:

$$\alpha = \begin{cases} \frac{1}{2} & \text{for the KT method} \\ \frac{\psi_{f+}}{\psi_{f+} + \psi_{f-}} & \text{for the KNP method} \end{cases} \tag{4.22}$$

The KT method weights the $f+$ and $f-$ contribution equally, so is called a central scheme. The KNP method calculates α based on the local speeds of propagation and is upwind biased, so is called a central-upwind scheme.

The interpolation procedure uses a limiter to switch between low and high order schemes based on a flux limiter function, $\beta(r)$, where r is the ratio of successive gradients of the interpolated variable, constrained to $r \geq 0$. For scalar ϕ on a polyhedral mesh, r as calculated as follows for the $f+$ direction (Greenshields et al., 2010):

$$r = 2 \frac{\mathbf{d} \bullet (\nabla \phi)_P}{(\nabla_d \phi)_f} - 1 \tag{4.23}$$

where $(\nabla \phi)_P$ is the gradient calculated at the "owner" cell P, as described in Section 4.2.3, $(\nabla_d \phi)_f = \phi_N - \phi_P$ is the gradient component normal to the face, scaled by $|\mathbf{d}|$,

and $\mathbf{d}$ is the vector connecting cell centres P and N. For vector fields, r is calculated based on the "worst case" direction, i.e. the direction of the steepest gradient of ϕ at the cell face, as follows (Greenshields et al., 2010):

$$r = 2\frac{(\nabla\phi)_f \bullet \mathbf{d} \bullet (\nabla\phi)_P}{(\nabla_d\phi)_f \bullet (\nabla_d\phi)_f} - 1 \tag{4.24}$$

The limiter chosen in this study is the Total Variation Diminishing (TVD) limiter of van Leer (1974) to switch between standard first-order upwind and second-order linear interpolation:

$$\beta(r) = \frac{r + |r|}{1 + r} \tag{4.25}$$

The $f+$ interpolation of ϕ is:

$$\phi_{f+} = (1 - g_{f+})\phi_P + g_{f+}\phi_N \tag{4.26}$$

where $g_{f+} = \beta(1 - f_x)$. It can be seen that $\beta = 0$ corresponds to upwind interpolation, while $\beta = 1$ is linear interpolation. Finally, V_{f+} is calculated directly as $V_{f+} = \mathbf{S} \bullet \mathbf{u}_{f+}$, where $\mathbf{u}_{f+}$ is a particular example of the general variable ϕ_{f+}.

4.2.2 Discretisation of the Diffusion Term

The diffusion term of Equation 4.13 can be expressed to second-order accuracy, assuming a linear variation of ϕ over the control volume of cell P, V_P, using Gauss' theorem, as the diffusion terms are stable when using central differencing. The discretisation is as follows (Jasak, 1996):

$$\begin{aligned}\int_{V_P} \nabla \bullet (\rho\Gamma_\phi \nabla\phi) dV &= \sum_f \mathbf{S}.(\rho\Gamma_\phi \nabla\phi)_f \\ &= \sum_f (\rho\Gamma_\phi)_f \mathbf{S}.(\nabla\phi)_f\end{aligned} \tag{4.27}$$

Jasak (1996) indicates that if the mesh is orthogonal, it is possible to use:

$$\mathbf{S}.(\nabla\phi)_f = |\mathbf{S}| \frac{\phi_N - \phi_P}{x_N - x_P} \tag{4.28}$$

and that the diffusion term exhibits boundedness. Here, Γ_ϕ is linearly interpolated from cell centre values.

For non-orthogonal grids, $\mathbf{S}.(\nabla\phi)_f$ is generally split into two parts, an orthogonal contribution, and a non-orthogonal contribution, as follows:

$$\mathbf{S}.(\nabla\phi)_f = \underbrace{A(\phi_N - \phi_P)}_{\text{orthogonal}} + \underbrace{\mathbf{a} \bullet (\nabla\phi)_f}_{\text{non-orthogonal}} \tag{4.29}$$

where $A = |\mathbf{S}|^2 / (\mathbf{S} \bullet \mathbf{d})$, $\mathbf{a} = \mathbf{S} - A\mathbf{d}$, and $\mathbf{d}$ is the vector connecting cell centres P and N, as shown in Figure 4.3. This non-orthogonal contribution reduces the accuracy of the

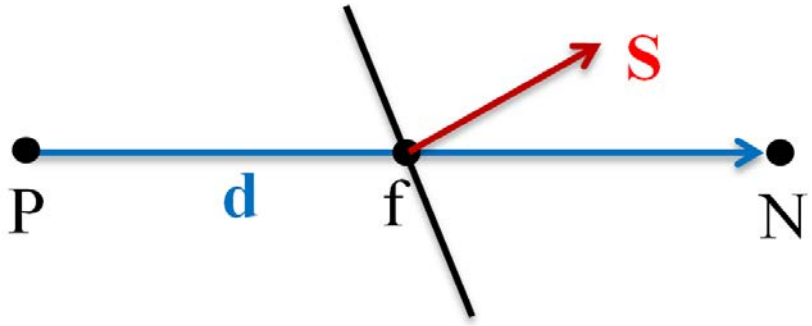

Figure 4.3: Vectors **d** and **S** on a non-orthogonal mesh, adapted from Jasak (1996).

method and potentially creates unboundedness, particularly if mesh non-orthogonality is high (Jasak, 1996).

4.2.3 Discretisation of the Gradient Terms

The gradient terms can be discretised as follows:

$$\int_{V_P} \nabla \phi dV = \sum_f \mathbf{S}.\phi_f \tag{4.30}$$

The KT and KNP schemes again split the interpolation into $f+$ and $f-$ directions as follows:

$$\sum_f \mathbf{S}.\phi_f = \sum_f [\alpha \mathbf{S}.\phi_{f+} + (1-\alpha)\mathbf{S}.\phi_{f-}] \tag{4.31}$$

where the $f+$ and $f-$ interpolations are second-order, and use the van Leer limiter as described in Section 4.2.1.

4.2.4 Discretisation of the Source Terms

Generally, the source term, $S_\phi(\phi)$, can take any form. In OpenFOAM, the source term is linearised prior to discretisation, such that the volume integral is calculated as (Jasak, 1996):

$$\int_{V_P} S_\phi(\phi) dV = SuV_P + SpV_P\phi_P \tag{4.32}$$

As Equations 4.1, 4.2 and 4.3 do not contain source terms, further discussion is not warranted.

4.2.5 Discretisation of the Temporal Derivative

Once all the spatial terms of Equation 4.13 have been discretised, they can be written in "semi-discretised" form, assuming the control volumes do not change with time, as follows:

$$\int_{\Delta t}\left[\left(\frac{\partial \rho\phi}{\partial t}\right)_P V_P + \sum_f F\phi_f - \sum_f (\rho\Gamma_\phi)_f \mathbf{S}.(\nabla\phi)_f\right] dt = \int_{\Delta t}(SuV_P + SpV_P\phi_P)dt \quad (4.33)$$

Two types of temporal discretisation methods can be employed, implicit and explicit. Explicit methods only use the previous time-step, while implicit methods also use the new (or current) time-step. Explicit methods require lower computational effort, but suffer stability problems when the Courant-Friedrichs-Lewy (CFL) number is greater than one. Implicit methods require increased computational effort, but provide more robust solutions.

In this work, the second-order, implicit **Crank-Nicholson** method is employed. Assuming the variation is linear in time as well as space, i.e.:

$$\phi^n = \phi^o + \Delta t\left(\frac{\partial\phi}{\partial t}\right)^o \quad (4.34)$$

where:

$$\phi^n = \phi(t+\Delta t) \quad (4.35)$$

$$\phi^o = \phi(t) \quad (4.36)$$

Time derivatives and integrals are calculated directly:

$$\left(\frac{\partial \rho\phi}{\partial t}\right)_P = \frac{\rho_P^n\phi_P^n - \rho_P^o\phi_P^o}{\Delta t} \quad (4.37)$$

$$\int_{\Delta t}\phi(t)dt = \frac{1}{2}(\phi^o + \phi^n)\Delta t \quad (4.38)$$

Using Equations 4.34, 4.35, 4.36, 4.37, and 4.38, and assuming the diffusivity, Γ_ϕ, does not change with time, Equation 4.33 can be re-written as follows:

$$\begin{aligned}\frac{\rho_P^n\phi_P^n - \rho_P^o\phi_P^o}{\Delta t}V_P &+ \frac{1}{2}\sum_f F\phi_f{}^o - \frac{1}{2}\sum_f(\rho^o\Gamma_\phi)_f\mathbf{S}.(\nabla\phi)_f{}^o \\ &+ \frac{1}{2}\sum_f F\phi_f{}^n - \frac{1}{2}\sum_f(\rho^n\Gamma_\phi)_f\mathbf{S}.(\nabla\phi)_f{}^n \\ &= SuV_P + \frac{1}{2}SpV_P\phi_P{}^o + \frac{1}{2}SpV_P\phi_P{}^n \end{aligned} \quad (4.39)$$

The Crank-Nicholson method is unconditionally stable, but does not guarantee boundedness (Jasak, 1996).

4.2.6 Solution of Discretised Equations

Equation 4.39 creates a system of algebraic equations for every control volume, which is of the form:

$$a_P {\phi_P}^n + \sum_N a_N {\phi_N}^n = R_P \tag{4.40}$$

The task is to determine ${\phi_P}^n$, which depends on the values in the neighbouring cells ${\phi_N}^n$, and on the source term vector R_P, which includes all terms that can be evaluated without knowing ${\phi_N}^n$, i.e. the constant part of the source term, and the parts of the temporal derivative, convection, and diffusion terms corresponding to the previous time-step ${\phi_N}^o$. Note that ϕ_f and $(\nabla\phi)_f$ also depend on ϕ_N.

This system can be solved via either direct methods, or by iteration. Direct methods are useful for systems with few variables, but the number of operations scales with the number of equations squared. Iterative methods are more economical, but are more difficult to implement and pose requirements in terms of the matrix layout. The two specific methods used in this study, for inviscid and viscous flow, are outlined separately.

4.2.6.1 Inviscid Flow

For an unsteady, compressible, three-dimensional, inviscid flow, viscous stress, $\boldsymbol{\tau} = 0$, and diffusive heat flux, $k\nabla T = 0$, allowing Equations 4.1, 4.2, and 4.3 to be simplified to the Euler equations:

$$\frac{\partial \rho}{\partial t} + \nabla \bullet (\rho \mathbf{u}) = 0 \tag{4.41}$$

$$\frac{\partial \rho \mathbf{u}}{\partial t} + \nabla \bullet (\rho \mathbf{u}\mathbf{u}) + \nabla p = 0 \tag{4.42}$$

$$\frac{\partial \rho E}{\partial t} + \nabla \bullet (\rho E \mathbf{u}) + \nabla \bullet (p\mathbf{u}) = 0 \tag{4.43}$$

In *rhoCentralFoam*, these equations are solved explicitly in an iterative sequence for density weighted fields ρ, $\rho\mathbf{u}$, and ρE. Fluxes of other fields are calculated from these three variables.

Note that solving for ρ, $\rho\mathbf{u}$, and ρE, then updating T via an equation of state, causes boundedness problems in T, as $\rho\mathbf{u}$ and ρE contain some values from previous time-steps (Greenshields et al., 2010). To prevent this, $f+$ and $f-$ interpolations of ρE are formed from $f-$ and $f+$ interpolations of ρ, $\rho\mathbf{u}$, and T in the discretisation of $\nabla \bullet (\rho E \mathbf{u})$, i.e.:

$$\rho E_{f+} = \rho_{f+} \left(c_v T_{f+} + \frac{|\mathbf{u}_{f+}|^2}{2} \right) \tag{4.44}$$

Therefore, ρ, $\rho\mathbf{u}$, and T are interpolated in the $f+$ and $f-$ directions, and all other variables are calculated from these. The procedure is (Greenshields et al., 2010):

- Set $t = t + \Delta t$.
- Evaluate $\rho_{f+,-}$, $\rho\mathbf{u}_{f+,-}$, and $T_{f+,-}$ from Equation 4.26.

- Calculate $\mathbf{u}_{f+,-}$, $F_{f+,-}$, and $a_{f+,-}$ then using the equation of state, calculate $p_{f+,-}$.
- Calculate convection and gradient terms from Equations 4.18 and 4.31 respectively.
- Solve Equation 4.41 for ρ (density equation).
- Solve Equation 4.42 for $\rho\mathbf{u}$ (inviscid momentum equation).
- Update $\mathbf{u}$.
- Solve Equation 4.43 for ρE (inviscid energy equation).
- Update p using the equation of state.

4.2.6.2 Viscous Flow

Viscosity and heat diffusion are introduced to the solver by the inclusion of diffusion terms in the governing equations.

The diffusion terms are functions of $\mathbf{u}$ and E and therefore can also be solved explicitly. However, this would result in a completely explicit solver, which can suffer severe time-step limitations (Greenshields et al., 2010). Therefore, *rhoCentralFoam* applies sequential operator splitting to introduce diffusive terms as implicit corrections to the inviscid equations. The velocity diffusion correction equation is (Greenshields et al., 2010):

$$\frac{\partial(\rho\mathbf{u})}{\partial t} - \nabla \bullet (\mu\nabla\mathbf{u}) - \nabla \bullet (\boldsymbol{\tau}_{exp}) = 0 \tag{4.45}$$

where the terms in the stress tensor containing inter-component coupling are treated explicitly, $\boldsymbol{\tau}_{exp} = \mu\left[(\nabla\mathbf{u})^T - \frac{2}{3}\mathrm{tr}(\nabla\mathbf{u})\mathbf{I}\right]$, and the Laplacian term is implemented implicitly. A similar diffusion correction equation is applied for T. The inviscid prediction is:

$$\frac{\partial\rho E}{\partial t} + \nabla \bullet (\rho E\mathbf{u}) + \nabla \bullet (p\mathbf{u}) - \nabla \bullet (\boldsymbol{\tau}_{exp} \bullet \mathbf{u}) = 0 \tag{4.46}$$

The diffusion correction equation for T is:

$$\frac{\partial(\rho c_v T)}{\partial t} - \nabla \bullet (k\nabla T) = 0 \tag{4.47}$$

The implicit momentum and temperature correction equations are solved using Gauss-Seidel iteration. Therefore, the procedure is (Greenshields et al., 2010):

- Set $t = t + \Delta t$.
- Evaluate $\rho_{f+,-}$, $\rho\mathbf{u}_{f+,-}$, and $T_{f+,-}$ from Equation 4.26.
- Calculate $\mathbf{u}_{f+,-}$, $F_{f+,-}$, and $a_{f+,-}$ then using the equation of state, calculate $p_{f+,-}$.

- Calculate convection and gradient terms from Equations 4.18 and 4.31 respectively.
- Update $\boldsymbol{\tau}_{exp}$, μ, and k.
- Solve Equation 4.41 for ρ (density equation).
- Solve Equation 4.42 for $\rho\mathbf{u}$ (momentum prediction).
- Update $\mathbf{u}$.
- Solve Equation 4.45 for $\mathbf{u}$ (momentum correction).
- Solve Equation 4.43 for ρE (energy prediction).
- Update T from ρE, $\mathbf{u}$, and ρ using the equation of state.
- Solve Equation 4.47 for T (temperature correction).
- Update p using the equation of state.

4.3 Large-Eddy Simulation

The numerical schemes described in Section 4.2.6 are developed on the assumption that all the relevant features of the flow are resolved in the finite volume discretisation. In practice, this is rarely the case.

When all scales of the flow are resolved, the simulation is commonly referred to as a Direct Numerical Simulation (DNS). The computational requirement to resolve all scales and achieve DNS increases with Reynolds number cubed (Tennekes and Lumley, 1972). This makes DNS impractical for high Reynolds number flows. The two commonly used alternatives are to either model the smallest scales, via Reynolds Averaged Simulation (RAS), or to use a hybrid approach, called Large-Eddy Simulation (LES).

In RAS, the ensemble-averaged mean flow is solved for, with an appropriate model being used to describe the effect of the fluctuations of the flow around this mean (Fureby, 1996). As one of the primary aims of this work is to identify and characterise the unsteady development of shock and turbulent structures, it is undesirable to model these phenomena, making RAS unsuitable.

LES provides an alternative, with lower computational cost than DNS. The principle of LES relies on Kolmogorov's theory, which states that the energy content of isotropic turbulence is dependent only on the rate of dissipation, ϵ, which at the smallest scales of turbulence convert kinetic energy into heat (Kolmogorov et al., 1991). This implies, provided the length scale at which the turbulence energy is injected into the system is sufficiently far removed from that at which the energy dissipates into heat, that the character of the turbulence will be independent of both the large forcing scales, and

molecular viscosity; a conjecture which has been found to hold true for a wide range of flows, including jet flows (de Villiers, 2006).

Kolmogorov's law is expressed as a spectrum of turbulent kinetic energy:

$$E(\kappa) = C_k \epsilon^{2/3} \kappa^{-5/3} \tag{4.48}$$

where κ is the wave number, defined as $2\pi/\ell$, where ℓ is the integral length scale, ϵ is the dissipation rate of turbulent kinetic energy, $\epsilon \approx u_0^3/\ell$, and C_k is the Kolmogorov constant.

The spectrum can be subdivided into several sections. The energy-containing or integral scales are the scales at which kinetic energy is introduced into the system; these scales are made up of the "large eddies". A second section contains the inertial sub-range; these scales obey Kolmogorov's law, i.e. they are independent of the integral scales, yet are dominated by inertial forces rather than viscosity. Finally, the dissipative range contains scales smaller than the Kolmogorov length scale, η. In the dissipative range, viscous effects start to damp the turbulent motion (de Villiers, 2006). The independence of the integral scales from the inertial sub-range allows the small scales to be approximated, while the large scales are calculated directly. This forms the bases of LES.

LES relies on a spatial and temporal filtering technique that eliminates fluctuations smaller than a predefined cut-off, determined by the grid size. While filtering the smallest scales of the flow greatly reduces computational requirements, it is critical to ensure that only the inertial sub-range is filtered, and not the integral length scales. Filtering the governing equations requires treatment of additional terms to close the system of equations in a similar fashion to the Reynolds Averaged Navier-Stokes (RANS) turbulence models. The additional terms are treated via a sub-grid scale (SGS) model. In this way, large eddies are explicitly computed and the influence of smaller eddies on larger eddies is calculated by the SGS model. Temporal filtering is implicit in the spatial filtering, as the smallest resolved time scale can be associated with the size of the smallest resolved length scale. The level of filtering is a trade-off between accuracy and computational resources. A general rule is that at least 80% to 90% of the total kinetic energy should be resolved on the grid (Pope, 2000; Fureby, 2012).

The filtered velocity is defined as follows (Ferziger and Peric, 2002):

$$\overline{\mathbf{u}} = \int_{-\infty}^{\infty} G(x-\zeta)\mathbf{u}(\zeta)d\zeta \tag{4.49}$$

where G is the filter kernel. OpenFOAM applies the "Top Hat" filter, defined as:

$$\mathrm{G}(x-\zeta) = \begin{cases} \frac{1}{\Delta} & \text{if } |x-\zeta| \leq \frac{\Delta}{2} \\ 0 & \text{otherwise} \end{cases} \tag{4.50}$$

where Δ is the filter width. The filtered equations for conservation of mass, momentum, and energy for a compressible, Newtonian fluid with no external body forces, and

no internal volumetric heating, assuming Fourier's law of thermal conductivity, are (Fureby, 2012):

$$\frac{\partial \bar{\rho}}{\partial t} + \nabla \bullet (\bar{\rho}\bar{\mathbf{u}}) = 0 \tag{4.51}$$

$$\frac{\partial \bar{\rho}\bar{\mathbf{u}}}{\partial t} + \nabla \bullet (\bar{\rho}\bar{\mathbf{u}}\bar{\mathbf{u}}) + \nabla \bar{p} - \nabla \bullet \bar{\boldsymbol{\tau}} - \nabla \bullet \mathbf{B} = 0 \tag{4.52}$$

$$\frac{\partial \bar{\rho}\bar{E}}{\partial t} + \nabla \bullet (\bar{\rho}\bar{E}\bar{\mathbf{u}}) + \nabla \bullet (\bar{p}\bar{\mathbf{u}}) - \nabla \bullet (k\nabla \bar{T}) - \nabla \bullet (\bar{\boldsymbol{\tau}} \bullet \bar{\mathbf{u}}) - \nabla \bullet \mathbf{b_E} = 0 \tag{4.53}$$

where: $\bar{\rho}$, $\bar{\mathbf{u}}$, and $\bar{T}$ are the filtered density, velocity, and temperature respectively. For an ideal gas, $\bar{p} = \bar{\rho} R_s \bar{T}$, $\bar{E}$ is the filtered energy density, calculated as $\bar{E} = \bar{e} + \frac{\bar{\mathbf{u}}^2}{2}$, and $\bar{\boldsymbol{\tau}}$ is the deviatoric component of the filtered viscous stress tensor, as follows:

$$\bar{\boldsymbol{\tau}} = 2\mu \mathrm{dev}(\bar{\mathbf{D}}) \tag{4.54}$$

where $\bar{\mathbf{D}}$ is the filtered deformation gradient tensor:

$$\bar{\mathbf{D}} = \frac{1}{2}[\nabla \bar{\mathbf{u}} + (\nabla \bar{\mathbf{u}})^T] \tag{4.55}$$

The additional terms: $\mathbf{B}$ and $\mathbf{b_E}$ are the sub-grid stress and flux terms respectively, and are defined as (Fureby, 2012):

$$\mathbf{B} = \bar{\rho}(\overline{\mathbf{u}\mathbf{u}} - \bar{\mathbf{u}}\bar{\mathbf{u}}) \tag{4.56}$$

$$\mathbf{b_E} = \bar{\rho}(\overline{\mathbf{u}E} - \bar{\mathbf{u}}\bar{E}) \tag{4.57}$$

4.3.1 Sub-Grid Scale Models

To close the filtered LES equations, a sub-grid model is required to describe the effects of the unresolved flow on the resolved flow, using the resolved variables. SGS models are described as functional or structural, depending on whether they mimic the kinetic energy cascade from large to small scales, or if they mimic the structure of the sub-grid stress tensor. Functional models are most widely used, and are formulated as (Fureby, 2012):

$$\mathbf{B} = 2\mu_k \mathrm{dev}(\bar{\mathbf{D}}) \tag{4.58}$$

$$\mathbf{b_E} = \frac{\mu_k}{Pr_t} \nabla \bar{E} \tag{4.59}$$

where μ_k is the dynamic sub-grid viscosity and Pr_t is the turbulent Prandtl number. One example is the Smagorinsky model, for which (Pope, 2000):

$$\mu_k = \bar{\rho} c_D \Delta^2 ||\bar{\mathbf{D}}|| \tag{4.60}$$

$$k = c_t \Delta^2 ||\bar{\mathbf{D}}||^2 \tag{4.61}$$

where c_D and c_t are empirical model constants, commonly set as 0.02 and 0.07 respectively (Pope, 2000).

4.3.2 Implicit LES

An alternative to SGS models, which attempt to explicitly estimate the sub-grid viscosity, is to use the inherent dissipation of the numerical scheme to provide the required damping. Numerical schemes that utilise flux-limiting schemes implicitly provide a SGS model (Fureby, 1996). This approach is referred to as Monotone Integrated Large-Eddy Simulation (MILES). The implicit SGS model inherent in a finite volume discretisation of the compressible Navier-Stokes equations has been derived by Grinstein and Fureby (2007) using modified equations analysis. The implicit SGS model is of the eddy-viscosity type (Fureby, 1996).

MILES has been used to study a wide range of flow-fields, including channel flows, Kelvin-Helmholtz instability, and vortex ring dynamics (Grinstein et al., 2005); good agreement has been demonstrated between MILES and conventional LES. A thorough review of MILES and its validity for a broad range of applications is provided by Grinstein et al. (2005). Importantly, MILES has shown performance comparable to conventional LES for flows relevant to the current work, including jets in supersonic crossflow (Grinstein et al., 2005; Kawai and Lele, 2009; Rana et al., 2011; Andre et al., 2017), at reduced computational cost. As MILES does not explicitly add dissipation, it can accurately capture a laminar flow, where conventional LES requires complex dynamic procedures to limit the operation of the sub-grid viscosity to regions of turbulence. It has also been shown that less diffusive limiters, such as the Superbee limiter (Roe, 1986), outperform the more diffusive van Leer limiter in some cases. The performance of different limiter schemes will be addressed in Chapter 5.

4.4 Summary

The numerical techniques applied within this thesis have been described. The governing equations are the compressible, unsteady conservation equations of mass, momentum, and energy. The equations are solved in dimensional form using the *rhoCentralFoam* finite volume solver, which implements the central-upwind scheme of Kurganov et al. (2001), with the van Leer limiter. Solution algorithms have been provided for inviscid and viscous flows.

An implicit large-eddy simulation technique has been adopted to model turbulence. Implicit LES uses the inherent dissipation of the numerical scheme to provide the sub-grid viscosity associated with small-scale turbulence, and has been used successfully in a number of applications.

Chapter 5

Verification and Validation

The aim of this chapter is to establish confidence in the time-accurate numerical simulations of a jet in hypersonic crossflow. This chapter is based on the work published in: Miller, W., P. Medwell, M. Kim, and C. Doolan. "Computational Methodology for Investigating the Transient Interaction between a Reaction Control Jet and a Hypersonic Crossflow". In *Aerospace Sciences Meeting*, AIAA, San Diego, CA, (2016).

5.1 Approach

Verification and validation (V&V) are the two primary methods of building and quantifying confidence in CFD simulations. Oberkampf and Trucano (2002) provide the following definitions of verification and validation:

> **Verification** is the process of determining that a model implementation accurately represents the developer's conceptual description of the model, and the solution to the model.
>
> **Validation** is the process of determining the degree to which a model is an accurate representation of the real world, from the perspective of the intended uses of the model.

In verification, the relationship of the simulation to the real world is not considered. Verification provides substantiation that the computerised model represents a conceptual model, within specified limits of accuracy. More simply, verification considers whether the model is implemented correctly. Validation concerns the relationship between computation and the real word, by comparison to experimental data. Specifically, validation ensures the model represents the real world.

In CFD, the conceptual model is the system of partial differential equations (PDEs) for conservation of mass, momentum, and energy described in Chapter 4.

Model verification is the process of identifying and quantifying sources of error in the computational model. To quantify errors, highly accurate solutions must be available for comparison. Such solutions are generally only available for simplified problems.

Oberkampf and Trucano (2002) have identified five major sources of error in a CFD solution. These are: (i) insufficient spatial discretisation convergence, (ii) insufficient temporal discretisation convergence, (iii) insufficient convergence of the numerical procedure, (iv) computer round-off, and (v) computer programming errors.

Spatial and temporal discretisation errors result from the discretisation of the solution domain into a finite number of regions and time intervals, and are inherent in the finite volume methodology. These errors can be quantified through convergence studies, which aim to determine: whether the solution converges to the exact solution when the mesh spacing is reduced, the effective order of the discretisation, and the magnitude of the discretisation error.

Numerical convergence error is related to convergence of the iterative procedure used to solve the governing equations. OpenFOAM allows the numerical convergence error to be controlled by the user. Therefore, this error may be reduced to an arbitrary level (Jasak, 1996).

Computer round-off and programming errors are neglected in the verification process, but may be addressed through validation.

There may be other sources of error, such as errors in the description of the system via the PDEs. In the case of laminar flows, these errors are negligible (Jasak, 1996); however, when using turbulence models, or LES, errors will be introduced. These errors are a reflection on the ability of the conceptual model (the PDEs) to represent the real world. These errors are quantified through validation.

Detailed, relevant experimental data is not available for validation of the transient interaction between a jet and a hypersonic crossflow. Therefore, a structured approach to V&V is critical to establish confidence in the CFD results. In this chapter, a comprehensive V&V study is undertaken, using a hierarchical approach. This approach decomposes the problem into progressively simpler tiers. The ability of the model to provide valid approximations at each tier is used as justification for the validity of the model to simulate the complete system, where high fidelity experimental data is unavailable for comparison. The hierarchical structure also assists verification, as high fidelity solutions suitable for verification are only feasible for simplified problems. The hierarchical V&V structure used in this study is shown in Table 5.1.

The simplest problems, which have been decomposed to a single aspect of the flow physics, are called unit problems. The unit problems considered in this work are: a one-dimensional shock tube, steady supersonic flow over a wedge, steady supersonic flow over a diamond shaped airfoil, and the transient supersonic flow over a forward step. These problems are detailed in Section 5.2. Highly accurate experimental and analytical data is available for each of these unit problems, allowing detailed comparison and estimation of errors. These cases cover many aspects of the fundamental flow physics that are present in the interaction of a jet with a hypersonic crossflow, and allow the numerical scheme to be verified.

More complex cases have partially coupled flow physics and use simplified geometries. These cases bridge the gap between fundamental unit problems and the full case

Table 5.1: Verification and validation cases, following a hierarchical structure.

Complete system	Transient Jet in Crossflow (MILES)			
Subsystems	Steady Jet in Crossflow (MILES)		Jet in Quiescent Atmosphere (Inviscid & MILES)	
Unit problems	Shock Tube (Inviscid)	Wedge (Inviscid)	Diamond Airfoil (Inviscid)	Forward Step (Inviscid)

of a transient jet in a hypersonic crossflow, and are referred to as subsystem cases. This work uses the transient simulation of a jet in a quiescent atmosphere, detailed in Section 5.3, and the steady interaction of a jet with a hypersonic crossflow, detailed in Chapter 6 (Sections $6.2 - 6.4$). Finally, the complete system is the transient simulation of a jet in hypersonic crossflow. Simulations of the complete system are not considered part of the V&V process, these results are contained in Chapters 6 (Sections $6.5 - 6.12$), 7, and 8.

5.2 Unit Problems

The unit problems are outlined in this section. The accuracy of the model is quantified, and the sources of error discussed for each case.

5.2.1 One-dimensional Shock Tube

The one-dimensional, inviscid shock tube was simulated and compared to an analytical solution developed by Anderson (2004). The shock tube comprises two reservoirs of ideal gas that are initially separated by a diaphragm. The gases are initially at rest, with densities $\rho_L = 1.0$ kg/m^3 and $\rho_R = 0.125$ kg/m^3, where subscripts L and R denote the left and right reservoirs, with the diaphragm located at $x = 0$. Initial pressures $p_L = 10^5$ Pa and $p_R = 10^4$ Pa correspond to temperatures $T_L = 348.4$ K and $T_R = 278.7$ K. A uniform mesh of 100 cells was used within a one-dimensional solution domain in the range -5 m $\leq x \leq 5$ m. The KNP numerical scheme with the van Leer limiter was used, as described in Chapter 4.

The diaphragm was removed at time $t = 0$, and the density profile in the fluid at $t = 7$ ms is shown in Figure 5.1 (a) with time-steps corresponding to different CFL numbers, using the van Leer limiter. For CFL $= 0.2$ the solution is poor, oscillatory behaviour can be seen at the shock ($x \approx 4$ m), extending back to the slip surface ($x \approx 2$ m). This is in contrast to the result of Greenshields et al. (2010), where such oscillations were not observed. The oscillations are a result of the lack of numerical dissipation in

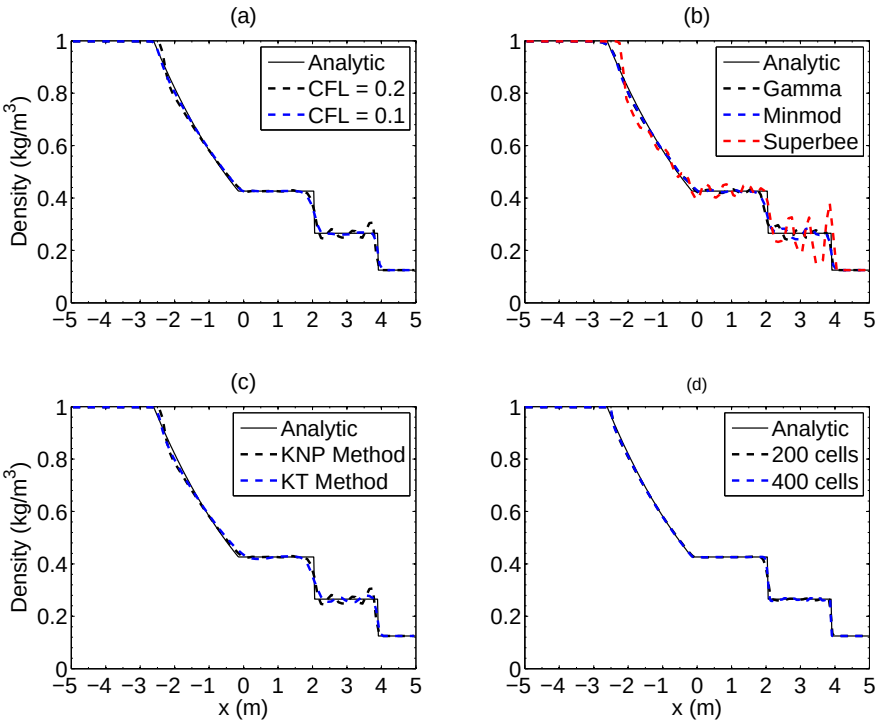

Figure 5.1: Density at $t = 7$ ms in the one-dimensional shock tube for (a) different CFL values; (b) different limiters; (c) different discretisation schemes; and (d) different meshes.

the KNP central-upwind scheme. When a non-dissipative scheme is faced with a flow discontinuity, such as a shock wave, the discretisation is unable to resolve the high wave number content, resulting in a high-frequency pile-up which causes spurious oscillations in the solution (Wendt, 2009). The lack of oscillations observed by Greenshields et al. (2010) at CFL = 0.2 is likely due to the use of a non-uniform mesh. Other than the oscillations, the analytic solution is well predicted. The only region of reduced accuracy is at the slip surface ($x \approx 2$ m), due to resolution of the uniform mesh.

Reducing CFL number from 0.2 to 0.1 removes oscillatory behaviour from the solution, while accuracy in the slip region is maintained.

To further investigate the oscillatory behaviour of the solution, alternative limiter schemes were tested. Figure 5.1 (b) compares the results for the Minmod, Gamma, and Superbee limiters, with the CFL number held at 0.2. Again the results are poor at this CFL number. The Minmod limiter has similar performance to the van Leer limiter results in Figure 5.1 (a), while the Gamma limiter produces oscillations of a similar magnitude, but also decreases accuracy at the slip surface ($x \approx 2$ m). The Superbee limiter performs poorly, with oscillations being amplified and spreading throughout the entire domain.

A comparison of the KNP central-upwind flux scheme and the KT central scheme is provided in Figure 5.1 (c), at CFL = 0.2. The oscillations are still present in the KT scheme, but with slightly reduced amplitude. However, the accuracy of the solution in the expansion and contact regions is reduced. These results are in general agreement with Greenshields et al. (2010), who found that the KNP method had higher accuracy

Table 5.2: Errors in the one-dimensional shock tube on three separate meshes at $t = 7$ ms.

Mesh (Cells)	% Error
100	5.5
200	4.4
400	2.3

than the KT method, and that the van Leer limiter provided the best performance of the limiting schemes considered. However, in contrast to Greenshields et al. (2010), a CFL number of 0.1 was required to produce oscillation-free solutions in this work, as discussed previously.

To investigate the consistency of the numerical method, additional simulations were performed with the van Leer limiter, at CFL = 0.1 on finer meshes, with 200 and 400 cells respectively. The solution for density at $t = 7$ ms on the two additional meshes is shown in Figure 5.1 (d). To quantitatively assess the accuracy, errors were estimated according to:

$$\%\text{Error} = 100 \times \sqrt{\frac{\sum_{n=1}^{N_{\text{Cells}}} \left[\left(\frac{\rho - \rho_{\text{Analytic}}}{\rho_{\text{Analytic}}} \right)_n \right]^2}{N_{\text{Cells}}}} \tag{5.1}$$

The error on each mesh is shown in Table 5.2. As expected, the error magnitude decreases with an increase in mesh density, indicating consistency in the numerical method.

5.2.2 Two-dimensional Wedge

The conservatism of the numerical scheme was assessed by simulating two-dimensional, steady, inviscid, supersonic flow over a wedge. The success is measured by the accuracy of the shock angle, θ_s, and downstream flow conditions (Mach number, M_2, pressure, p_2, and temperature, T_2) when compared to the analytic solution of Anderson (2004).

The geometry of the wedge is shown in Figure 5.2. The inviscid flow-field was solved using *rhoCentralFoam* for free-stream Mach numbers, M_∞, from 2 to 10, on a two-dimensional mesh consisting of 50 000 hexahedral cells. The free-stream static pressure, p_∞, and temperature, T_∞, were specified as 100 kPa and 270 K respectively at the inlet, and a *waveTransmissive* boundary condition was applied at the outlet. The *waveTransmissive* boundary condition is a simplified version of the Poinsot and Lele (1992) Navier-Stokes characteristic boundary condition. An inviscid (slip) wall boundary condition was applied on the surface of the wedge, and far-field (Neumann)

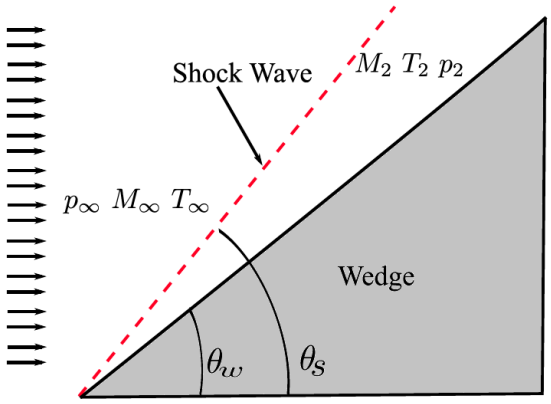

Figure 5.2: Schematic of the two-dimensional wedge case (Marcantoni et al., 2012).

boundary conditions are applied at the top of the domain. The wedge angle, θ_w, was set at 15° and the simulations were run at a CFL number of 0.1 using the KNP central-upwind discretisation scheme with the van Leer limiter.

The simulated downstream flow conditions are provided in Figure 5.3. The *rhoCentralFoam* prediction matches the analytical prediction with very good accuracy at all supersonic Mach numbers. The errors in downstream Mach number are less than 1% for all free-stream Mach numbers. Similarly, shock angles were predicted within 1% for all free-stream Mach numbers. Errors in pressure and temperature were as high as 2% and 3% respectively when $M_\infty = 10$, and tend to increase with increasing free-stream Mach number. However, the accuracy is acceptable within the limits of mesh resolution. Therefore, it is concluded that the current numerical scheme is conservative, and correctly predicts oblique shocks for free-stream Mach numbers from 2 to 10.

5.2.3 Diamond Airfoil

Steady, two-dimensional, inviscid, supersonic flow over a diamond shaped airfoil combines the physics of oblique shocks with Prandtl-Meyer expansion fans. Again, simulations were performed using *rhoCentralFoam* and compared to the analytic solution provided by Anderson (2004). The airfoil geometry is shown in Figure 5.4, and matches simulations conducted by Marcantoni et al. (2012). The case was run with CFL = 0.1 using the van Leer limiter and KNP numerical scheme, with a 10° wedge angle, θ_w, at a 15° angle-of-attack, α, and an 86 300 hexahedral cell mesh. Boundary conditions mimic the two-dimensional wedge, except in this case the top and bottom boundary are also *waveTransmissive* outlets, and the inlet Mach number is set to 2.5.

Mach number, pressure, and temperature were compared to analytic predictions in the regions (II), (III), (IV), and (V) as shown in Figure 5.4, with results provided in Table 5.3. Results are provided in terms of Mach number, temperature ratio, T/T_∞, and pressure coefficient, defined as:

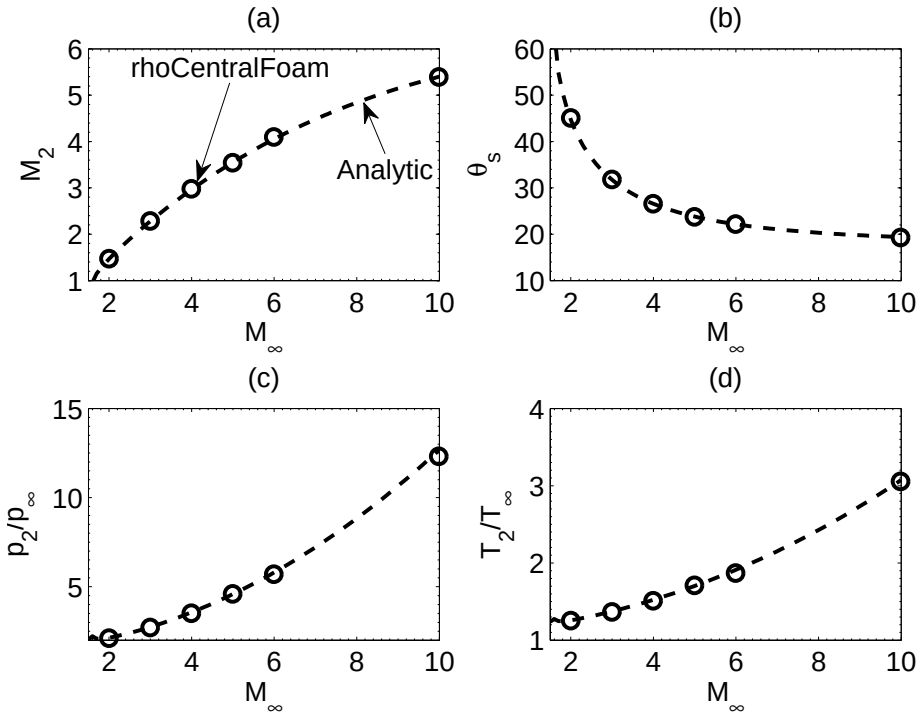

Figure 5.3: Results of the two-dimensional wedge case, showing: (a) Mach number, M_2, (b) shock angle, θ_s, (c) pressure ratio, p_2/p_∞, and (d) temperature ratio, T_2/T_∞. Dash line: analytic prediction; ∘: rhoCentralFoam.

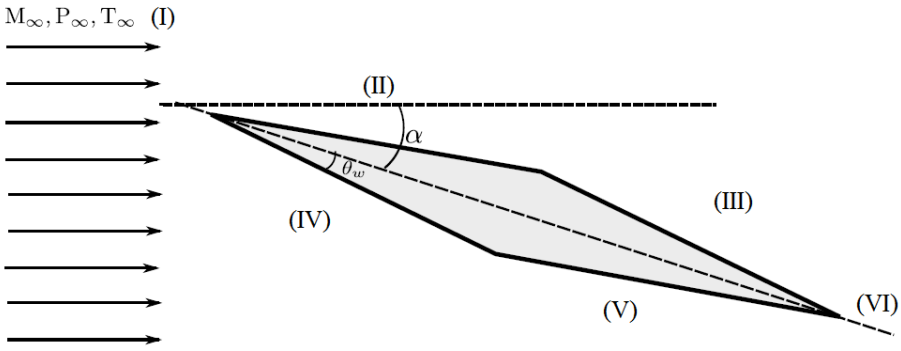

Figure 5.4: Schematic of the two-dimensional diamond airfoil case, adapted from Marcantoni et al. (2012).

Table 5.3: Diamond shaped airfoil results on 86 300 cell mesh.

Region	Analytical			*rhoCentralFoam*			% Error		
	M	C_P	T/T_∞	M	C_P	T/T_∞	M	C_P	T/T_∞
II	2.72	-0.067	0.91	2.72	-0.061	0.91	0.03 %	9.0 %	0.9 %
III	3.85	-0.197	0.57	3.90	-0.181	0.60	1.2 %	8.1 %	4.9 %
IV	1.38	0.717	1.62	1.38	0.652	1.58	0.04 %	9.1 %	2.8 %
V	2.07	0.110	1.21	2.07	0.100	1.21	0.1 %	9.1 %	0.2 %

Table 5.4: Diamond shaped airfoil errors on successively finer meshes.

Region	86 300 cells			172 600 cells			345 200 cells		
	M	C_P	T/T_∞	M	C_P	T/T_∞	M	C_P	T/T_∞
II	0.03%	9.0%	0.9%	0.04%	5.7%	0.54%	0.004%	9.0%	0.7%
III	1.2%	8.1%	4.9%	0.04%	7.2%	2.7%	0.5%	8.0%	5.1%
IV	0.04%	9.1%	2.8%	0.07%	9.0%	2.2%	0.11%	8.9%	3.4%
V	0.1%	9.1%	0.2%	0.1%	8.0%	1.0%	0.02%	8.8%	1.9%

$$C_P = \frac{p - p_\infty}{\frac{1}{2}\rho_\infty U_\infty^2} \tag{5.2}$$

Errors in Mach number and temperature ratio were small throughout ($< 5\%$), but errors in pressure coefficient were large, approximately 9% in all regions. The magnitude of pressure errors reported here is slightly higher than the previous simulations by Marcantoni et al. (2012), who reported errors below 5%. To further investigate, the simulations were run on two successively finer meshes, with 172 600 cells and 345 200 cells respectively. The results provided in Table 5.4 show that the increase in mesh resolution, without significant refinement near the shocks and expansion fans, does not significantly change the error magnitudes. Possible reasons for the pressure discrepancy are insufficient mesh resolution around expansion fans, temporal oscillation of the shock waves, or a computational domain that is too small. Overall, given the simplicity of the mesh used in this work, and the previous success in simulating this flow-field with the *rhoCentralFoam* solver, the results are acceptable.

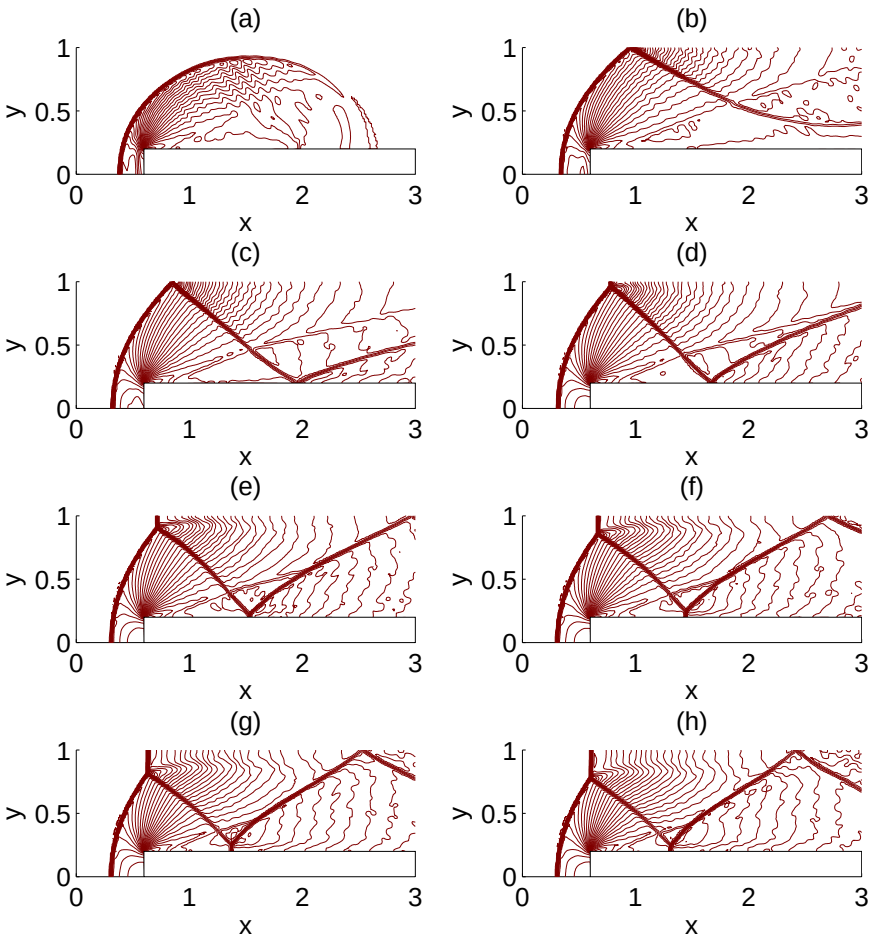

Figure 5.5: Density contours for the forward step, at various times; 40 density contours in the range $0 < \rho < 8$: (a) $t = 0.5$ s; (b) $t = 1.0$ s; (c) $t = 1.5$ s; (d) $t = 2.0$ s; (e) $t = 2.5$ s; (f) $t = 3.0$ s; (g) $t = 3.5$ s; and (h) $t = 4.0$ s.

5.2.4 Forward Step

The forward step problem of Woodward and Colella (1984) was used by Greenshields et al. (2010) as a verification case for the time dependent shock structure evolution with *rhoCentralFoam*, and is replicated in this work. Consistent with previous work, the two-dimensional mesh is 80 cells high × 240 cells long within a domain of 1 unit length high × 3 units long, with a step height of 0.2 units. The inviscid gas was initialised at Mach 3 with non-dimensional gas properties: $p = 1$, $T = 1$, and $\gamma = 1.4$. Inviscid (slip) walls and a *waveTransmissive* outlet complete the domain. The simulation was run with a CFL number of 0.2 to match previous work. This is in contrast to the CFL number of 0.1 required to remove oscillation is the shock tube case. The simulated evolution of the flow-field is shown in Figure 5.5 in terms of density contours, which closely match the previous simulations of Woodward and Colella (1984); Cockburn and Shu (1998); Greenshields et al. (2010) (see Figure 5.6). There are some oscillations present, but these are reduced in comparison to the shock tube case and are acceptably small when CFL = 0.2.

The flow-field at $t = 4$ s is shown on three meshes, a coarse mesh (80 × 240),

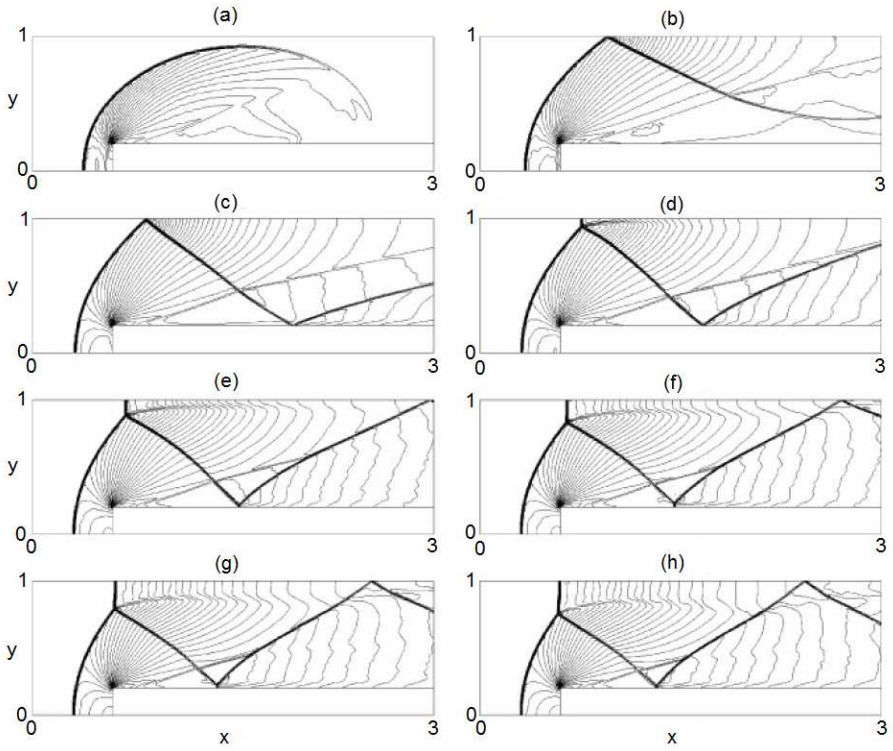

Figure 5.6: Greenshields (2010) density contours for the forward step, at various times; 40 density contours in the range $0 < \rho < 8$: (a) $t = 0.5$ s; (b) $t = 1.0$ s; (c) $t = 1.5$ s; (d) $t = 2.0$ s; (e) $t = 2.5$ s; (f) $t = 3.0$ s; (g) $t = 3.5$ s; and (h) $t = 4.0$ s.

intermediate mesh (160×480), and fine mesh (320×960) in Figure 5.7. All features of the flow were captured by the simulation, and the resolution of the shock increases with increased grid density, again indicating consistency in the numerical method. However, the mesh refinement does increase the oscillations, which further emphasises the advantage of running the simulation with a CFL number below 0.2.

5.3 Transient Jet in Quiescent Atmosphere

The simulation of a jet issuing into a quiescent atmosphere provides a simplified case to investigate the transient development of shock and turbulent structures in a jet flow. Over several years, Naboko and co-workers undertook a series of experimental and computational studies into the transient formation of sonic and supersonic jets exiting from a shock tube into a quiescent atmosphere (Belavin et al., 1973; Eremin et al., 1978; Naboko et al., 1979). A schematic showing each of the flow structures is provided in Figure 5.8, which has been adapted from Radulescu and Law (2007).

High pressure gas (gas A) is initially separated from a low pressure gas (gas B), with both gases at rest. At the beginning of the simulation, gas A is allowed to flow freely into gas B through an orifice of radius $\overline{r}$ at $\overline{x} = 0$. Throughout this section, an overbar indicates a dimensional quantity, and results will be presented in non-dimensional co-ordinates, defined as follows:

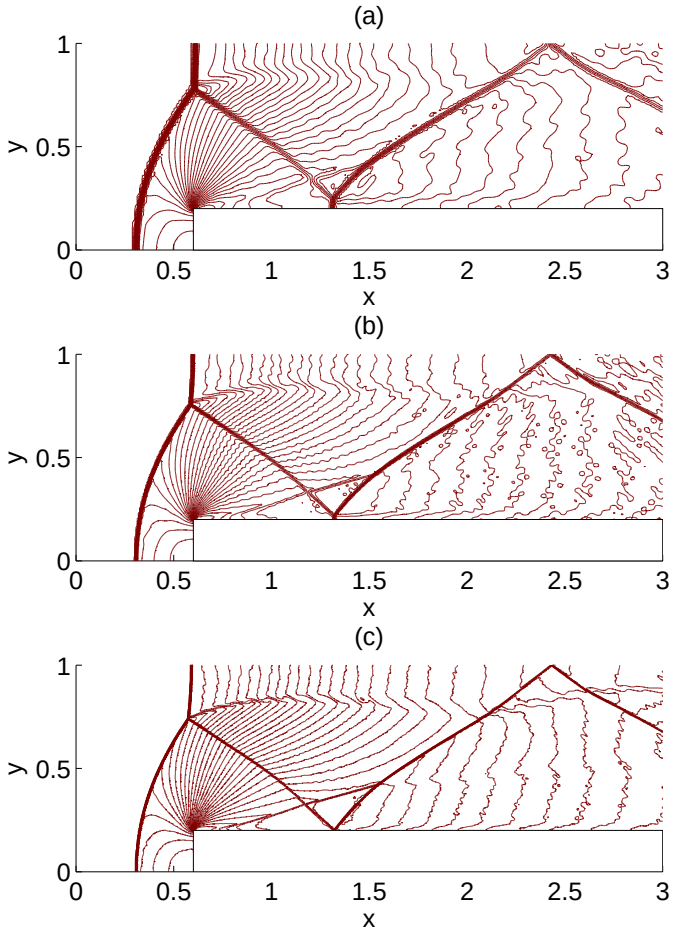

Figure 5.7: Density contours for the forward step at $t = 4.0$ s for various meshes; 30 density contours in the range $0.2568 < \rho < 6.067$: (a) coarse mesh; (b) intermediate mesh; and (c) fine mesh.

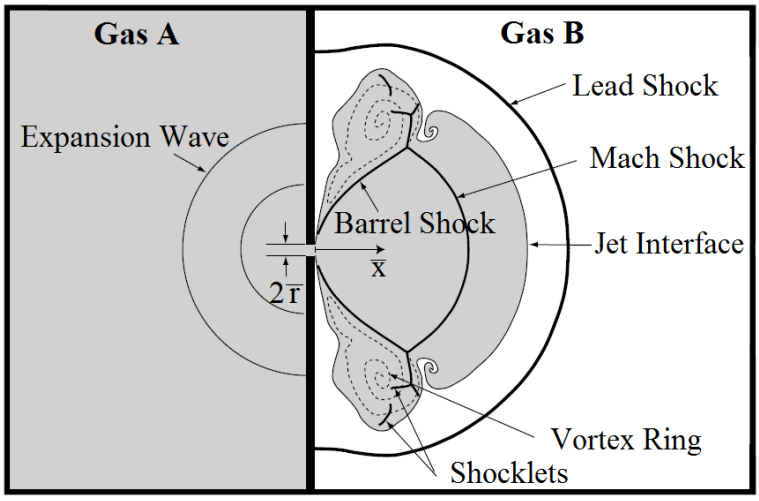

Figure 5.8: Schematic showing structures of a jet in a quiescent atmosphere, adapted from Radulescu and Law (2007).

$$x \equiv \frac{\overline{x}}{\overline{r}}; u_i \equiv \frac{\overline{u_i}}{\overline{a}_{Ac}}; \rho \equiv \frac{\overline{\rho}}{\overline{\rho}_{Ac}}; p \equiv \frac{\overline{p}}{\overline{\rho}_{Ac}\overline{a^2}_{Ac}} = \frac{\overline{p}}{\gamma_A \overline{p}_{Ac}}; t \equiv \frac{\overline{t}\overline{a}_{Ac}}{\overline{r}} \tag{5.3}$$

where $\overline{a}_{Ac}$ and $\overline{\rho}_{Ac}$ are calculated for a steady isentropic expansion from the stagnation state of gas A as follows (Radulescu and Law, 2007):

$$\overline{a}_{Ac} = \overline{a}_{A0}\left(\frac{2}{\gamma_A + 1}\right)^{\frac{1}{2}}; \overline{\rho}_{Ac} = \overline{\rho}_{A0}\left(\frac{2}{\gamma_A + 1}\right)^{\frac{1}{(\gamma_A - 1)}} \tag{5.4}$$

where a is the speed of sound, and subscripts c and 0 refer to the choked and stagnation states respectively.

Due to the inherent symmetry of the problem, the computational domain consists only of the upper half of the flow, with an axis of symmetry applied at the jet centre-line ($\overline{y} = 0$). The domain includes chambers of both gases A and B with walls sufficiently far away that shocks are not reflected and the flow is not affected. This results in a 2 m $\times$ 1 m domain, with an orifice radius, $\overline{r}$, of 1 mm. Gases A and B are separated by a wall of thickness 0.125 mm.

The high pressure jet flow (gas A) initially forces a strong shock into the second chamber (gas B). The strength of this shock diminishes with downstream distance before disappearing completely. Secondary shocks are formed around the orifice due to the rapid lateral expansion of the gas, and the shape of these shocks changes from almost spherical to virtually flat before they eventually weaken and disappear. Vortex rings develop at the edge of the nozzle. As the flow forces these vortex rings downstream, they increase in size, decay, and the jet becomes turbulent.

The development of vortex rings in a jet flow was studied by Gharib et al. (1998), who showed that, for jet injections with a short pulse, almost all the jet fluid is entrained within a starting vortex, which is generated via separation of the boundary layer at the edge of the orifice. However, for jet injections with a longer pulse, the starting vortex reaches a limiting size, which is insensitive to a range of jet parameters, including diameter, velocity, and Reynolds number. Beyond this limiting size, the remaining vorticity remains in the shear-layer, and is not entrained in the starting vortex.

Two-dimensional, inviscid simulations of an air jet into quiescent air with pressure ratios between 88 and 700 were performed. All simulations were conducted using *rhoCentralFoam*, with the KNP central-upwind flux scheme, and the van Leer limiter. A small time-step was used, corresponding to CFL = 0.1, to reduce oscillations. It was assumed that the air behaves as a perfect gas, with $\gamma = 1.4$, and that all walls are adiabatic. Table 5.5 gives the initial conditions for gases A and B in each simulation.

5.3.1 Mesh Convergence Study

A mesh convergence study was undertaken to estimate the effective order of the discretisation scheme, to quantify discretisation errors, and to determine whether the solution converges when mesh spacing is reduced.

Table 5.5: Initial conditions for gases A and B in jet in quiescent atmosphere simulations.

Case	Gas A / Gas B	p_{Ao}/p_{Bo}	ρ_{Ao}/ρ_{Bo}	T_A/T_B
1	Air / Air	88.0	6.1	1.0
2	Air / Air	337	23	1.0
3	Air / Air	700	48	1.0

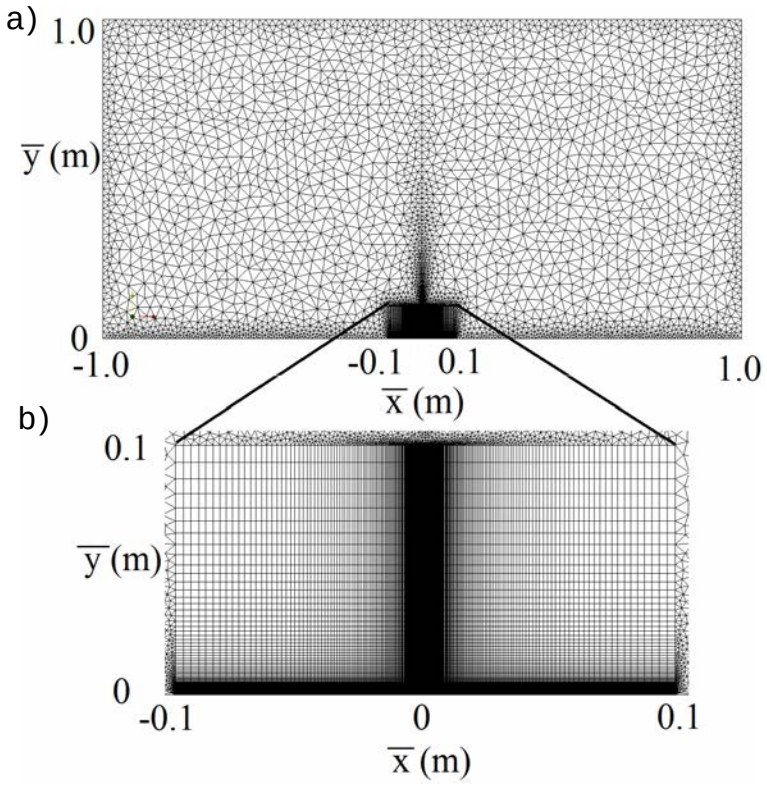

Figure 5.9: Mesh B structure for (a) the complete mesh, and (b) the structured region near the jet orifice.

Simulations corresponding to the Case 1 flow conditions were conducted on four meshes. The first three meshes, called mesh A, B, and C, have 100×210 cells, 200×425 cells, and 400×850 cells respectively in the structured inner region, giving a mesh size ratio $r = r_1 = r_2 = 2$, where r_1 and r_2 are the ratio of cell size between mesh A and B, and mesh B and C, respectively. The fourth mesh, mesh D, is highly refined, and consists of 750×1500 cells in the structured inner region. All mesh configurations consist of structured cells, with an additional buffer of unstructured mesh before the domain walls to ensure no reflected waves affect the flow-field. In all cases, the structured grid spacing is increased linearly with distance from the jet orifice in both x and y directions. Figure 5.9 shows the cell distribution for mesh B (200×425 cells).

The parameters of interest for the convergence study are shock velocity, and peak temperature. Shock velocity is measured by the time taken for the shock to reach a

location at $x = 10$, $y = 0.5$, and peak temperature is measured at the same location.

5.3.2 Richardson Extrapolation

The method used to conduct the mesh convergence study is Richardson extrapolation (Richardson and Gaunt, 1927).

The solution of a flow parameter, f, on any particular grid, g_i, can be related to the exact solution, f_{exact}, i.e. the solution when the mesh spacing approaches zero, as follows (Roache, 1997):

$$f = f_{exact} + a_1 g_1 + a_2 {g_2}^2 + a_3 g_3^2 + ... \tag{5.5}$$

where constants a_i are the coefficients of the Taylor series expansion, and are independent of grid size. For a second-order method, $a_1 = 0$, and the exact solution can be estimated as (Roache, 1997):

$$f_{exact} \approx f_1 + \frac{f_1 - f_2}{r^2 - 1} \tag{5.6}$$

where f_i is the solution of the flow parameter f on grid g_i. In the generalised case for a p^{th} order method:

$$f_{exact} \approx f_1 + \frac{f_1 - f_2}{r^p - 1} \tag{5.7}$$

The extrapolated value, f_{exact}, depends on the observed order of accuracy of the solution, which may differ from the formal order of accuracy of the algorithm. This is especially true when non-linear flux limiters such as the van Leer limiter are used, as the order of the solution is reduced in regions of a discontinuity. When $r_1 = r_2 = r$, the observed order of accuracy can be calculated using the following equation (Roache, 1997), where subscript 1 corresponds to the finest mesh, and 3 the coarsest:

$$p = \ln\left(\frac{f_3 - f_2}{f_2 - f_1}\right) / \ln(r) \tag{5.8}$$

In the case where the parameter of interest is a distribution, rather than a point estimate, the L^2-Norm of the cell-centred values can be used to estimate the spatially averaged order of accuracy, according to (Stern et al., 1999):

$$\langle p \rangle = \ln\left(\frac{||\epsilon_{32}||_2}{||\epsilon_{21}||_2}\right) / \ln(r) \tag{5.9}$$

where:

$$\epsilon_{ij} = f_i - f_j \tag{5.10}$$

and:

$$||\epsilon_{ij}||_2 = \left(\sum_{k=1}^{N} (\epsilon_{ij})_k^2\right)^{1/2} \tag{5.11}$$

Table 5.6: Shock velocity and peak temperature for jet in quiescent atmosphere Case 1, on meshes A, B, and C.

Mesh	Peak temperature (K)	Shock velocity (m/s)
A	198.1	394
B	202.1	355
C	202.6	348
D	201.5	342

The observed order of convergence calculated in this way relies on asymptotic, or monotonic convergence. Therefore, the convergence conditions must first be assessed. Possible convergence conditions are: monotonic convergence ($0 < R < 1$); oscillatory convergence ($R < 0$); and divergence ($R > 1$). Here, R is the convergence ratio, defined as:

$$R = \frac{\epsilon_{21}}{\epsilon_{32}} \tag{5.12}$$

or, in the case of a distribution, the spatially averaged global convergence ratio:

$$\langle R \rangle = \frac{||\epsilon_{21}||_2}{||\epsilon_{32}||_2} \tag{5.13}$$

A standardised method for reporting discretisation errors is the Grid Convergence Index (GCI), which is based on generalised Richardson extrapolation. GCI is defined as (Roache, 1997):

$$GCI_{ij} = F_s \left| \frac{\epsilon_{ij}}{1 - r^p} \right| \tag{5.14}$$

or, for the spatially averaged case:

$$GCI_{ij} = F_s \left| \frac{||\epsilon_{ij}||_2}{1 - r^p} \right| \tag{5.15}$$

where F_s is a safety factor, set to 1.25.

5.3.2.1 Order of the Discretisation Scheme

The Richardson extrapolation procedure was applied to meshes A, B, and C for the jet in quiescent atmosphere. Values for shock velocity and peak temperature for Case 1 are provided in Table 5.6.

The first step is to assess the convergence conditions. For peak temperature, $R = 0.125$, while for shock velocity, $R = 0.180$. Therefore, in both cases, monotonic convergence is observed and the observed order of convergence calculated using Richardson extrapolation is valid.

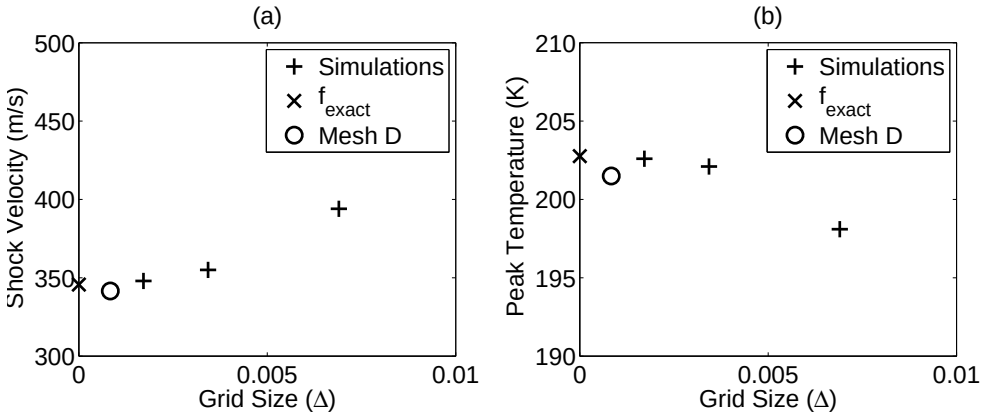

Figure 5.10: (a) Average shock velocity for Case 1 to x = 10, y = 0.5, and (b) Peak temperature for Case 1 at x = 10, y = 0.5.

The results for peak temperature and shock velocity are provided graphically in Figure 5.10, where they are plotted against a representative cell size measure, Δ, defined as:

$$\Delta = \sqrt{1/N_{cells}} \text{ for a two-dimensional mesh}$$
$$\Delta = \sqrt[3]{1/N_{cells}} \text{ for a three-dimensional mesh}$$

The calculated values of f_{exact} are also included in Figure 5.10. The observed order of accuracy, p, is 2.5 for shock velocity, and 3 for peak temperature. This indicates that, although the numerical scheme is at best second-order, and reverts to first-order in shock regions through the van Leer limiter, better than second-order convergence is observed in these variables.

It must be noted that, while the mesh resolution is sufficient to show convergence using these parameters (i.e. shock velocity and peak temperature), a solution of such a flow with large density gradients and regions of high vorticity, using inviscid equations is not truly independent of the chosen mesh resolution (Radulescu and Law, 2007). Therefore, similar convergence performance will not necessarily be observed for all variables, nor will it be maintained for further grid refinement. The small scales of the barrel shock and vortex ring can only converge if the dissipation is correctly modelled. Nevertheless, the simulations were able to capture development and motion of the shocks and vortex regions and show better than second-order convergence for the parameters considered.

Further confidence is gained by plotting the same variables for Mesh D (see Figure 5.10). This shows that further mesh refinement doesn't significantly change the result, although it does impact the observed order of convergence. Monotonic convergence is still observed for shock velocity, but the order of convergence is reduced to $p < 1$. Further, monotonic convergence is no longer observed for peak temperature. This highlights the limitation of an inviscid solution at small scales. The refined mesh (mesh D) does allow additional physical phenomena to be resolved, that are not present with

Table 5.7: Richardson extrapolation results for the jet in quiescent atmosphere.

Variable	ϵ_{32}	ϵ_{21}	R	p	GCI_{32}	GCI_{21}
Shock velocity	39 m/s	7 m/s	0.180	2.5	3.0 %	0.55 %
Peak temperature	$-4°$ C	$-0.5°$ C	0.125	3	0.35 %	0.04 %

a coarser mesh. Specifically, shocklets and shock-vortex interactions are resolved on mesh D that are not present in the other simulations.

It is concluded that the coarse meshes A, B, and C are adequate to capture the major flow features, but if a detailed investigation of smaller structures, such as shocklets and shock-vortex interactions, is required, a finer mesh is appropriate. Further, the inviscid assumption is suitable to accurately capture major shocks and vortices in this flow.

5.3.2.2 Discretisation Errors

The Richardson extrapolation procedure allows the comparison of the estimated values of shock velocity against the predicted value at infinite grid resolution, f_{exact}. A summary of the data obtained via Richardson extrapolation is provided in Table 5.7. This gives an error in shock velocity of 14 %, 2.7 %, and 0.7 % respectively for mesh A, B, and C. The estimated errors for peak temperature are 2.3 %, 0.3 %, and 0.09 % for meshes A, B, and C respectively.

The error between mesh D and f_{exact} is 1.2% for shock velocity, and 0.64% for peak temperature, which re-iterates that the mesh D results are not a significant improvement over the coarser meshes for estimating the primary shock and vortex structures in this flow.

5.3.2.3 Grid Convergence

For completeness, grid convergence index (GCI) results for the jet in quiescent atmosphere simulations are included in Table 5.7. There is a reduction in GCI for successive grid refinements (i.e. $GCI_{21} < GCI_{32}$), and the value of GCI_{21} is small ($< 1\%$). This indicates that the solution on mesh C is very close to grid independence, and discretisation errors are small.

5.3.3 Model Validation

The evolution of the flow-field was captured by Naboko et al. (1972) via Schlieren photography, and is compared qualitatively to the mesh D simulation results in Figure 5.11. The major shock structures, including lead shock, Mach shock, and barrel shock, were captured by the simulation. The relative speed of shock and jet gas propagation

differs, owing to the different jet gases between experiment and simulation (i.e. argon vs. air), as expected. The vortex ring has also been captured.

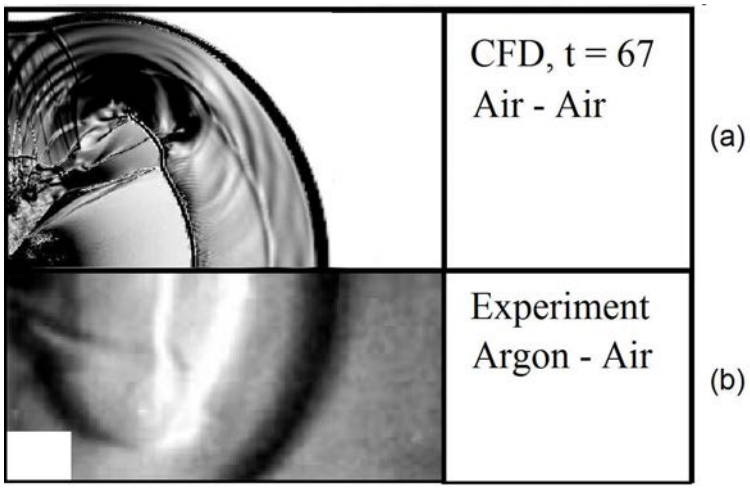

Figure 5.11: Comparison of transient jet development. (a) $|\nabla p|$ for Case 2 (mesh D); (b) experimental Schlieren (Naboko et al. (1972) adapted from Radulescu and Law (2007)).

Figure 5.11 also shows detailed resolution of structures that are not captured by a lower mesh resolution, as previously described. The flow structures corresponding to the shock vortex interaction were also observed by Zhang et al. (2015) and Radulescu and Law (2007). The presence of these structures contributes to the non-monotonic convergence behaviour, as both shock velocity and temperature will be affected by the shocklets and small vortices that develop.

Quantitative validation is performed by comparison of shock and fluid interface locations obtained on the intermediate mesh (mesh B, 200 × 425 cells) for Case 2. The results are compared to published experimental, numerical, and analytical results. Figure 5.12 shows the shock and fluid interface locations, in non-dimensionalised co-ordinates for distance (ϵ) and time (τ), defined as follows (Radulescu and Law, 2007):

$$\epsilon \equiv \rho_{B0}{}^{\frac{1}{j}} \frac{x}{\Lambda}; \tau \equiv \rho_{B0}{}^{\frac{1}{j}} \frac{t}{\Lambda} \tag{5.16}$$

The non-dimensionalised co-ordinates allow one-dimensional comparison between slit and round jets, and between different jet gases. Here, ρ_{B0} is the initial density of gas B, j is the geometric index, and Λ is the non-dimensional radius of the choked source. For a slit jet, $j = 1$ and $\Lambda = 1$.

Excellent agreement is obtained between the current simulations and previous experimental data, indicating that the simulation does indeed predict the correct shock and interface velocity. With errors estimated using Equation 5.1, the simulations match the model of Radulescu and Law (2007) within 8% for the shock location, and within 7% for the flow interface. Therefore, the conclusion can be drawn that the inviscid simulations adequately represent the flow-field and predict the motion and evolution of both the shocks and the jet fluid, with acceptable error.

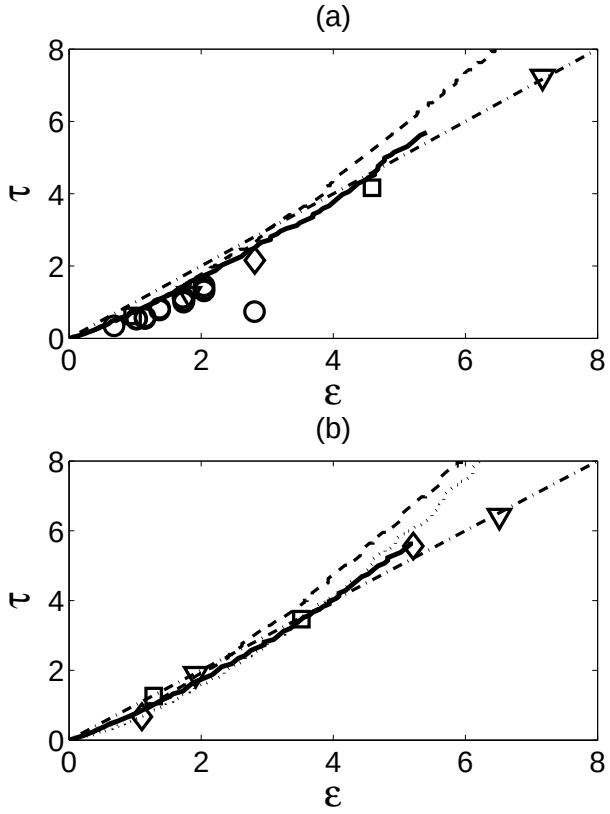

Figure 5.12: Comparison of the predicted (a) shock, and (b) fluid interface location with experimental, numerical and analytical data, using non-dimensional co-ordinates. Solid line: Case 2 prediction (Air − Air); dot-dash line: Radulescu and Law (2007) (H_2− Air); dash line: Radulescu and Law (2007) model; dotted line: Chekmarev and Stankus (1984) model; ∘: Buckmaster (1964) (Air − Air); ▽: Belavin et al. (1973) ($N_2 - N_2$); □: Belavin et al. (1973) ($CO_2 - CO_2$); and ⋄: Belavin et al. (1973) (Ar − Ar).

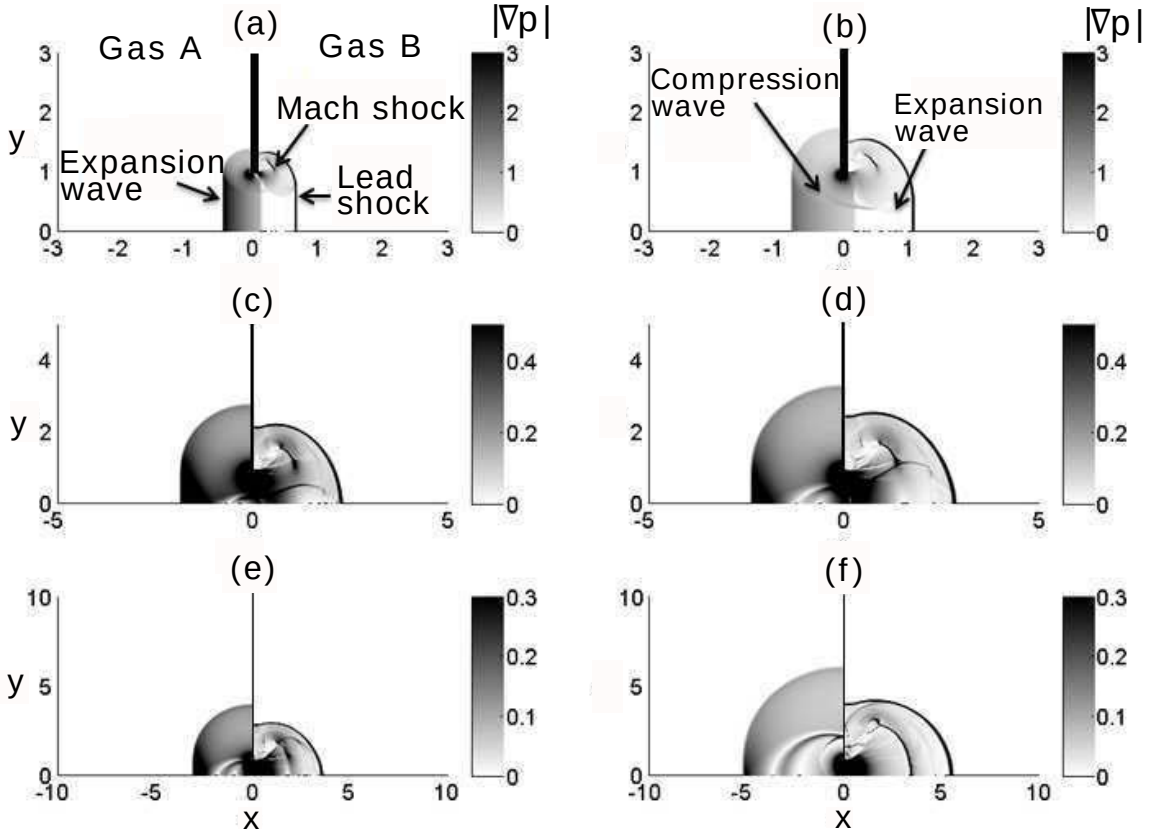

Figure 5.13: Contours of non-dimensional pressure gradient showing development of shock structure for Case 2 at (a) $t = 0.5$, (b) $t = 1$, (c) $t = 2$, (d) $t = 2.5$, (e) $t = 3.2$, and (f) $t = 6.3$.

5.3.4 Flow Visualisation

Gas A, initially at rest, flows through the orifice into gas B, which is also initially at rest. The high pressure jet flow from gas A forms a time-dependent shock structure. The pressure gradients formed during the early stages of flow development, during the period $t = 0 - 6.3$, are shown in Figure 5.13. The shock structure is in agreement with the structure of a hydrogen jet (Radulescu and Law, 2007). The lead shock forms immediately and is normal to the flow through the orifice, before being curved by the lateral jet expansion at the edge of the orifice. Following this initial phase, the lead shock develops and maintains an almost circular shape and reduces in strength as the flow-field evolves. As predicted by experiment (Naboko et al., 1979), the strength of the Mach shock, as measured by the pressure gradient, diminishes with downstream distance. The Mach shock and barrel shock form by lateral expansion of the jet gas around the orifice corner. As such, the Mach shock is not initially present at the jet axis ($y = 0$). A one-dimensional expansion centred at $x = 0$ is also formed. Additional expansion and compression waves are formed due to the lateral expansion of the flow. The expansion wave reflects, and is amplified behind the Mach shock by the negative pressure and density gradients to form an additional shock, which traverses the Mach and barrel shocks.

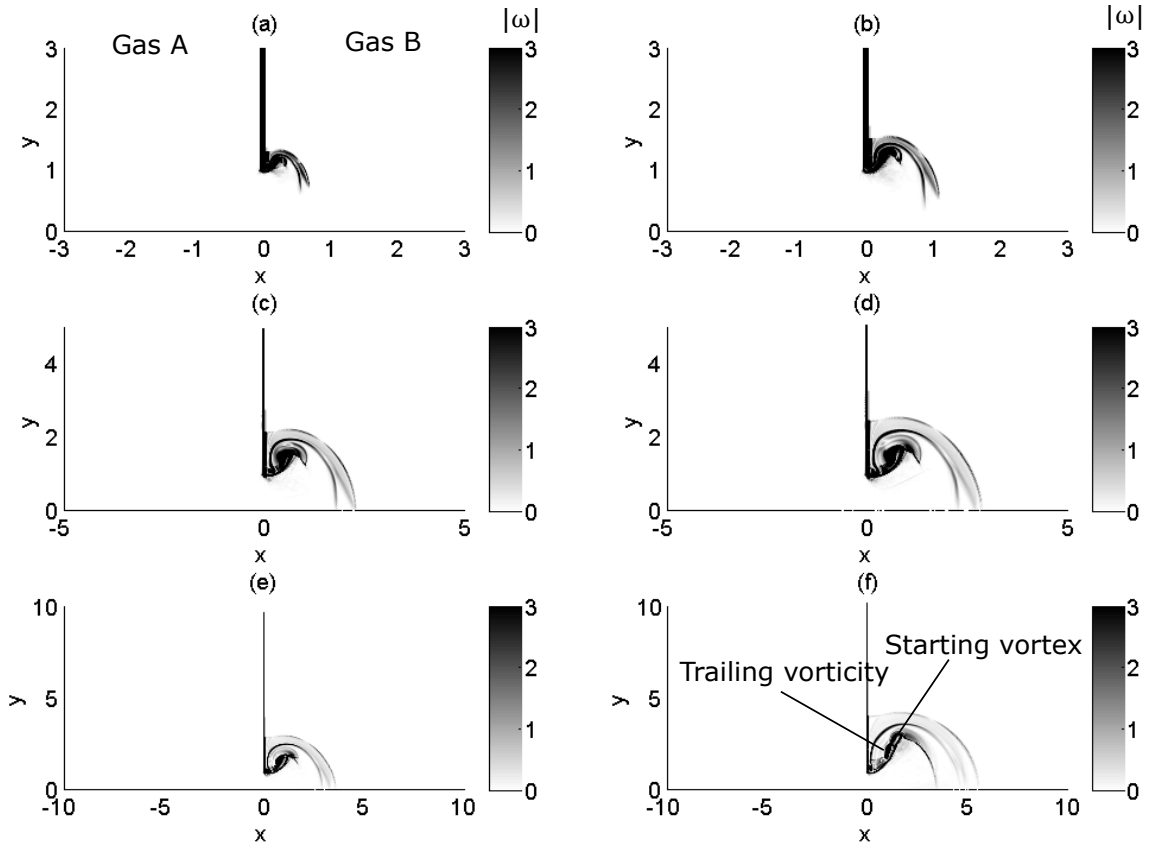

Figure 5.14: Contours of non-dimensional vorticity magnitude showing development of turbulent structure for Case 2 at (a) $t = 0.5$, (b) $t = 1$, (c) $t = 2$, (d) $t = 2.5$, (e) $t = 3.2$, and (f) $t = 6.3$.

The vorticity magnitude, $|\omega|$, fields corresponding to the pressure gradients in Figure 5.13 are shown in Figure 5.14. Initially, vorticity forms at the jet orifice and is entrained into both the lead shock and the Mach shock as well as the starting vortex. As the flow evolves, vorticity continues to be produced at the corner of the orifice, forming a vortex structure that closely replicates the long jet pulse described by Gharib et al. (1998).

Shocklets form in the shear-layer and vortex ring, caused by shock / vortex interactions. Similar features have been reported by Radulescu and Law (2007) for hydrogen jets, and Zhang et al. (2015) for air jets.

At later times, after $t = 15$, the Mach shock evolves to join at the jet centre-line and the barrel shock remains attached to the corner of the orifice, and grows in length as the Mach shock moves downstream with the fluid interface. As shown in Figure 5.15, this forms the well known steady jet shock and turbulence structure, referred to as the dynamically similar regime by Radulescu and Law (2007). This transition to a dynamically similar regime occurs much later than reported by Radulescu and Law (2007), due to the differences between hydrogen and air jets. The corresponding vorticity field seems to evolve over the same time scale to be dynamically similar after $t = 15$.

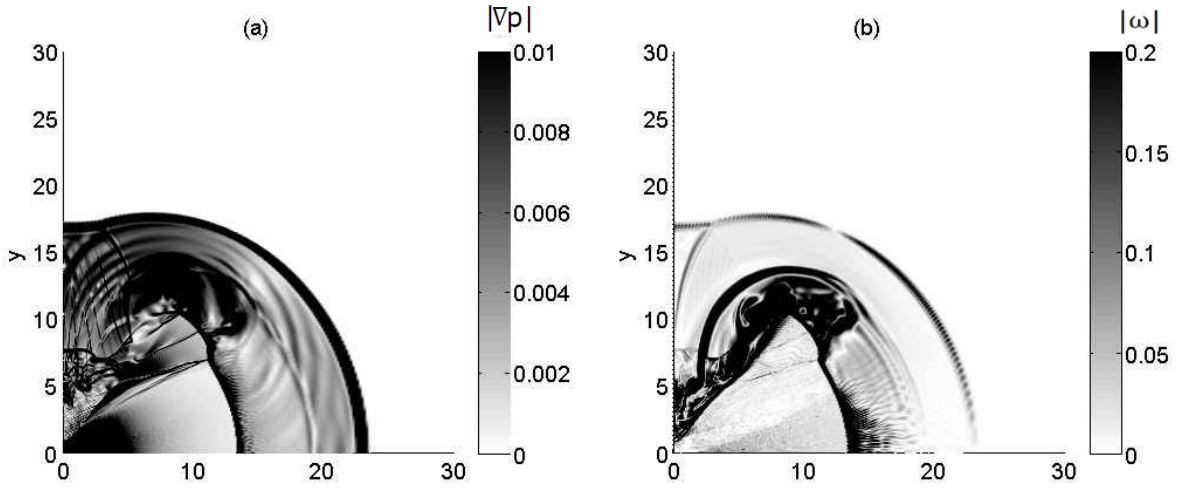

Figure 5.15: Contours of (a) non-dimensional pressure gradient, and (b) non-dimensional vorticity magnitude showing fully developed shock and turbulent structures for Case 2 (mesh D) at $t = 50$.

The effect of viscosity on the flow-field can be predicted by comparing a viscous MILES simulation to the inviscid result. During the initial start-up period, the viscous result is indistinguishable from the inviscid result shown in Figure 5.13. However, viscosity does have an effect on the flow-field at later times. The inviscid result is compared to the viscous result at $t = 50$ in Figure 5.16. The addition of viscosity has the effect of damping the shocklets in the shear region, and may also stabilise the numerical scheme, preventing unphysical oscillations, but does not change the overall structure of the flow-field.

5.3.5 Conclusions

This section has presented a numerical convergence study and flow visualisation study for the case of an inviscid jet flowing into quiescent air, which is considered as one subsystem of the jet in hypersonic crossflow. The mesh convergence study showed that, while convergence was not monotonic in all cases, the solution does indeed converge, and the accuracy of the solution on a coarse mesh is acceptable for predicting the development of large scale structures. For the parameters considered, the grid convergence index was small ($< 1\%$) for mesh B. If an accurate representation of small scales is an objective of the simulation, a refined mesh and viscous simulation was required, however, this was not required to resolve the primary flow features.

Validation was performed, with the results matching previous work, within 8% for shock location and within 7% for flow interface location, across a broad range of jet gas types.

The flow visualisation study investigated the development of the shock and turbulent structures. The results compared very well with previous studies, with all relevant features of the flow correctly captured. This provides confidence that the

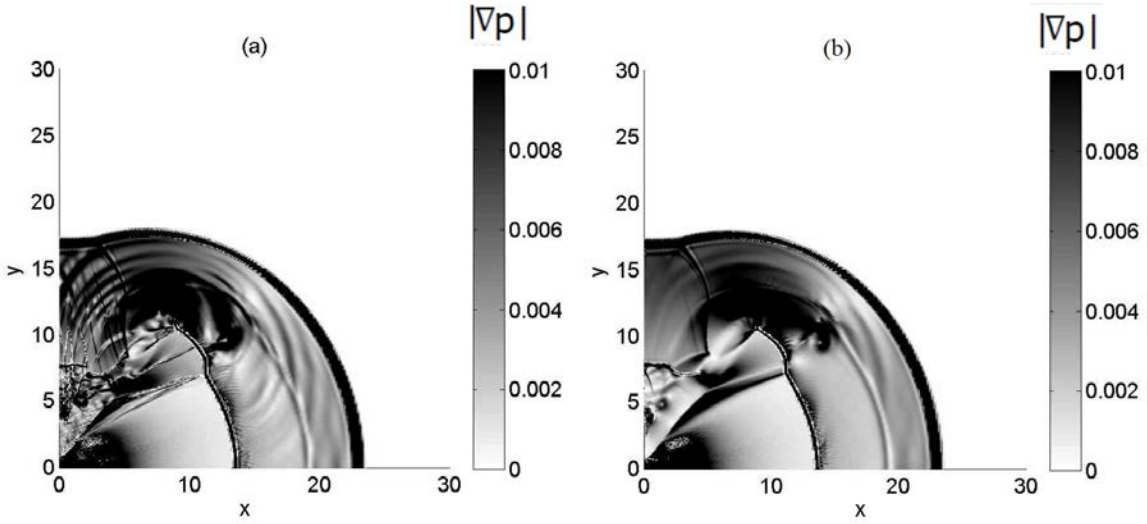

Figure 5.16: Contours of non-dimensional pressure gradient showing fully developed shock and turbulent structures for Case 2 (mesh D) at $t = 50$ for (a) inviscid simulation, and (b) viscous (MILES) simulation.

numerical methodology is suitable for estimating the development and time-accurate motion of shock and vortex structures in a jet flow.

5.4 Summary and Conclusions

Due to the lack of experimental data in relation to unsteady jets in hypersonic crossflow, a hierarchical approach has been taken to V&V. The computational methodology has been compared to analytical solutions of four canonical supersonic flows, and to experimental data for a transient jet issuing into a quiescent atmosphere.

In all cases, the simulation is able to reproduce all physical features of the flow. In the shock tube case, the Minmod and van Leer limiters were shown to have the best performance, and CFL numbers of 0.1 were required to reduce numerical oscillations. Supersonic wedge simulations showed that predictions of shock angle and location were consistently accurate at all Mach numbers tested ($2 < \mathrm{M} < 10$), while small discrepancies were observed when estimating pressure and temperature. These pressure and temperature discrepancies were also present in the diamond airfoil simulations, where errors reached approximately 9%.

The unsteady development of flow features was shown to be accurate when compared to experimental data for both a forward step, and a jet issuing into a quiescent atmosphere. Limitations of the numerical scheme have been identified and quantified. Overall, the numerical scheme is fit for purpose to examine both the steady and time-dependent flow features of a jet in hypersonic crossflow. The ability of the numerical scheme to capture the development of physical features of the flow, with acceptable accuracy, has been confirmed.

Chapter 6

Steady Jet in Hypersonic Crossflow

This chapter considers the viscous simulation of a steady, sonic jet issuing from a flat plate into a hypersonic (Mach 5), perfect air crossflow, and is based on the work published in: Miller, W., P. Medwell, C. Doolan, and M. Kim. "Transient interaction between a reaction control jet and a hypersonic crossflow". *Physics of Fluids* Vol. 30, 046102 (2018).

The case is described in Section 6.1. This flow has been investigated experimentally by Erdem (2011). The time-averaged results are used as a final subsystem case for verification in Section 6.2, and validation in Section 6.3. Conclusions related to the verification and validation are provided in Section 6.4.

Analysis of the unsteady simulation results is also included in this chapter. The overall flow structure is described in Section 6.5, and the surface pressure is described in Section 6.6. Detailed analysis of specific vortex and shock structures are provided in Section 6.7 (horseshoe vortices), Section 6.8 (shear-layer vortices), Section 6.9 (longitudinal counter-rotating vortices), Section 6.10 (wake vortices), and Section 6.11 (shock structure). The resulting jet force is described in Section 6.12. Conclusions relating to the unsteady interaction between a sonic jet and hypersonic crossflow are provided in Section 6.13.

6.1 Flow Conditions

The initial conditions of the steady, sonic jet in hypersonic crossflow simulation are shown in Table 6.1. A three-dimensional computational domain was generated to approximate the experimental geometry, which is represented schematically in Figure 6.1. The upstream edge of the domain consists of a supersonic inlet, placed 10 mm upstream from the leading edge of the sharp-edged flat plate. A supersonic (Neumann) outlet was placed at the downstream edge of the plate. The plate itself was modelled as an adiabatic wall, with a circular sonic inlet with diameter $d_j = 2$ mm representing the jet, placed 105 mm downstream from the leading edge. Geometric symmetry allows the domain to be split in half, with a symmetry condition applied in a plane parallel to the free-stream flow, through the centre-line of the jet outlet. In the unsteady flow-field,

Table 6.1: Initial conditions of the steady jet in hypersonic crossflow simulation.

Free-stream				Jet				
M_∞	p_∞ (Pa)	T_∞ (K)	Re ($\times 10^6$ /m)	M_j	T_j (K)	p_{0j}/p_∞	Re_{dj} ($\times 10^3$)	J
5	1210	62.5	13.1	1	250	251	88.5	5.3

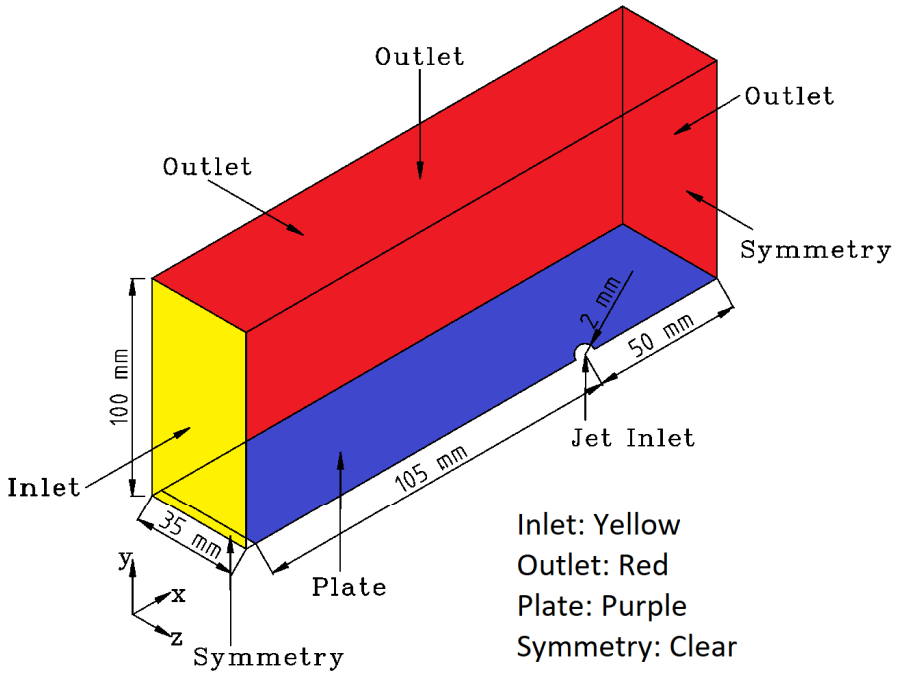

Figure 6.1: Schematic of the geometric configuration for the jet in hypersonic crossflow simulation.

this symmetry condition represents a significant approximation, which must be tested and verified. Far-field (Neumann) boundary conditions were placed at the top and side, at a distance of 100 mm and 35 mm respectively, to complete the domain. These distances are sufficient to capture all relevant flow structures. The jet was assumed to have a step velocity profile, no boundary layer inlet plenum was modelled. This is a common simplification when considering choked nozzle flows, and has been shown to have little or no effect on the shock formation in the crossflow (Viti, 2002; Andre et al., 2017).

Simulations were run using the KNP numerical scheme with the van Leer limiter. No non-equilibrium flow is expected (Garnier et al., 2009; Nishihara et al., 2012), only perfect gases were considered, with a constant Prandtl number of 0.7, and viscosity was modeled using Sutherland's law (Sutherland, 1893). Turbulence was modelled using the MILES methodology described in Chapter 4. In the experiment, the boundary layer is laminar over the entire flat plate when the jet is not present, so the application of an explicit turbulence model is not required to accurately simulate this region. Using LES will not allow sub-grid scale stresses and fluxes to be resolved in the jet region,

Table 6.2: Mesh resolution and flow properties for steady jet in crossflow mesh verification study.

Mesh	N_{cells} ($\times 10^6$)	Cell size ($\times 1/\delta$) (x, y, z)	First cell height (y^+)	Mach disk height ($\times d_j$)	Lead shock angle (deg)
Coarse	1.9	(34, 34, 31)	1.5	3.2	13.8
Intermediate	6.4	(50, 50, 49)	0.75	3.3	12.9
Fine	15.5	(68, 68, 63)	0.75	3.3	13.0

but is still expected to produce accurate results for the grid-scale motion of relevance to this work. Note that running an inviscid solution for this case produces a different flow-field. Therefore, the flat plate boundary layer is an important feature of the flow.

The simulation was initialised without the jet present, to allow a steady laminar boundary layer to be established on the plate. The jet was then started by instantaneously applying the pressure, temperature, and velocity values shown in Table 6.1 at the jet inlet for an initial start-up period of $\tau = 200$, where τ is a non-dimensional time parameter, defined as:

$$\tau = \frac{t \times U_\infty}{d_j} \tag{6.1}$$

This corresponds to 2.4 total domain flow-through periods, or 6 times the time taken for the jet flow to reach the outlet, which is sufficient for the normal force on the plate to reach a quasi-steady state. After this initial start-up period, time-averaged results were obtained over approximately 5 domain flow-through periods ($\tau = 400$, or $t \approx 1$ ms).

6.2 Mesh Verification

A mesh verification study was undertaken to establish confidence that the mesh resolution was sufficient to capture the relevant flow physics using the MILES methodology. Simulations were conducted on three meshes, with the properties shown in Table 6.2.

Each mesh was structured, with hexahedral cells concentrated in the region of the jet orifice, as well as through the boundary layer and on the leading edge of the flat plate. The mesh spacing was increased linearly in all directions from these concentrated regions. Figure 6.2 shows the cell distribution for the coarse mesh, which has 38 cells across the jet diameter, and 34 cells within the experimentally measured boundary layer thickness, δ, upstream of the separation point, where $\delta = 0.85 d_j$ (Erdem and Kontis, 2010).

Table 6.2 shows the time-averaged vertical distance between the flat plate and the centre of the Mach disk, i.e. the Mach disk height, h, is almost identical between

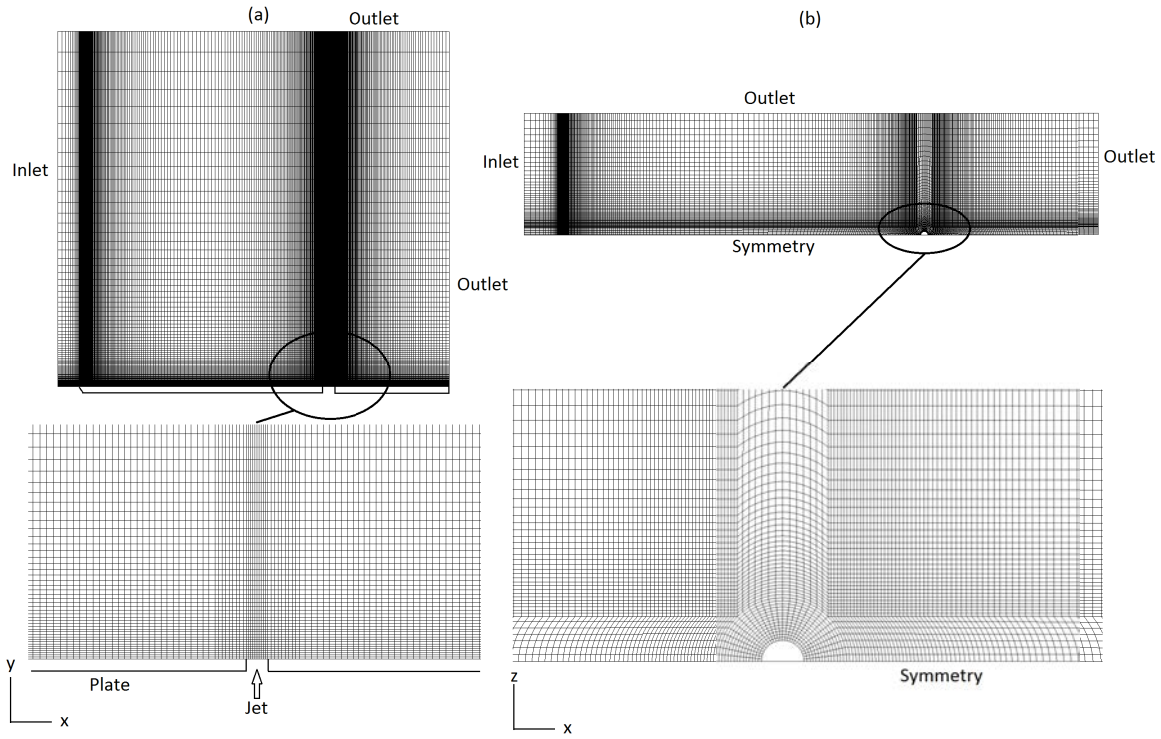

Figure 6.2: Coarse mesh for jet in hypersonic crossflow simulations. (a) Side view; (b) Top view.

the three meshes, with less than 2% variation. Table 6.2 also includes lead shock location on each mesh. In this case, the error between the coarse and fine mesh is 6%, reducing to below 1% between the intermediate and fine meshes. The lead shock angle, θ, is measured in a region of low mesh resolution, far upstream from the jet orifice. Figure 6.3 (a) shows the lead shock angle prediction on the three meshes, with error bars representing the thickness of the shock, where thickness is measured as the distance between free-stream density and peak density. As expected, shock thickness decreases from $1.0 \times d_j$ on the coarse mesh, to $0.6 \times d_j$ on the intermediate mesh, and $0.4 \times d_j$ on the fine mesh. This, combined with the consistent Mach disk locations, confirms that the time-averaged locations of shock structures are near mesh independence on the intermediate mesh.

Figure 6.3 (b) shows the Mach disk heights in a similar format. Here, data points represent time-averaged values and error bars show instantaneous fluctuations from the mean. Fluctuations occur in the barrel shocks and Mach disk as shear-layer vortices are convected downstream, as described in Chapter 2. Therefore, Mach disk height is an unsteady parameter. Figure 6.3 (b) shows that the fluctuations become larger as the mesh resolution is increased. As the mesh is refined, more turbulent structures are resolved, resulting in more Mach disk fluctuations and less numerical dissipation. Therefore, while even the coarse mesh is able to correctly predict the presence, and time-averaged location of the Mach disk (see Table 6.2), further mesh refinement does improve the resolution of unsteady flow structures.

A commonly used method to establish whether mesh resolution is sufficient for

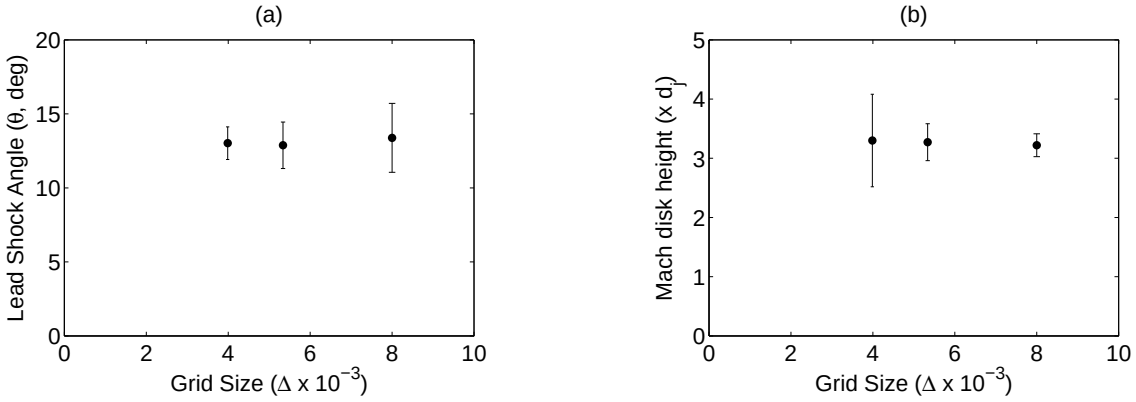

Figure 6.3: (a) Leading edge shock angle prediction, where error bars represent shock thickness, and (b) Mach disk height prediction, where error bars represent visually estimated temporal fluctuations.

LES is to compare the resolved turbulent kinetic energy (TKE) with the total TKE. It is generally recommended that if 80% to 90% of the TKE is resolved, LES can be considered well-resolved (Pope, 2000; Fureby, 2012). When using implicit LES, the unresolved, or sub-grid, TKE is not easily obtained. One possible approach is to directly apply an explicit sub-grid model to an instantaneous snap-shot of the implicit LES solution. One frequently used explicit sub-grid model is the Smagorinksy-Lilly model, where sub-grid TKE per unit mass, k_{SGS}, is expressed as (Pope, 2000):

$$k_{SGS} = \nu_t^2 / (c\Delta)^2 \tag{6.2}$$

where c is an empirical constant, usually set to $c = 0.094$, and Δ denotes the filter width. OpenFOAM uses a "Top Hat" filter, where Δ corresponds to the cell size. ν_t is the turbulent viscosity per unit mass, which can be calculated from the rate of strain tensor as follows:

$$\nu_t = (c\Delta)^2 \sqrt{2 \times S_{ij} \times S_{ij}} \tag{6.3}$$

where the rate of strain tensor is defined as:

$$S_{ij} = \frac{1}{2}\left(\frac{\partial u_i}{\partial x_j} + \frac{\partial u_j}{\partial x_i}\right) \tag{6.4}$$

This method allows a direct estimate of the sub-grid TKE, which can be added to the resolved TKE to compute the total TKE. The resolved TKE per unit mass, k_{GS}, is simply:

$$k_{GS} = \frac{1}{2}\left(u_1^{'2} + u_2^{'2} + u_3^{'2}\right) \tag{6.5}$$

where $u_i^{'} = u_i - \overline{u_i}$, and $\overline{u_i}$ is the time-averaged velocity.

From this analysis, the ratio of resolved to total TKE, integrated over the entire domain, was found to be greater than 99% for the coarse mesh. A comparison of the resolved to total TKE on the coarse mesh is provided in Figure 6.4. Kinetic

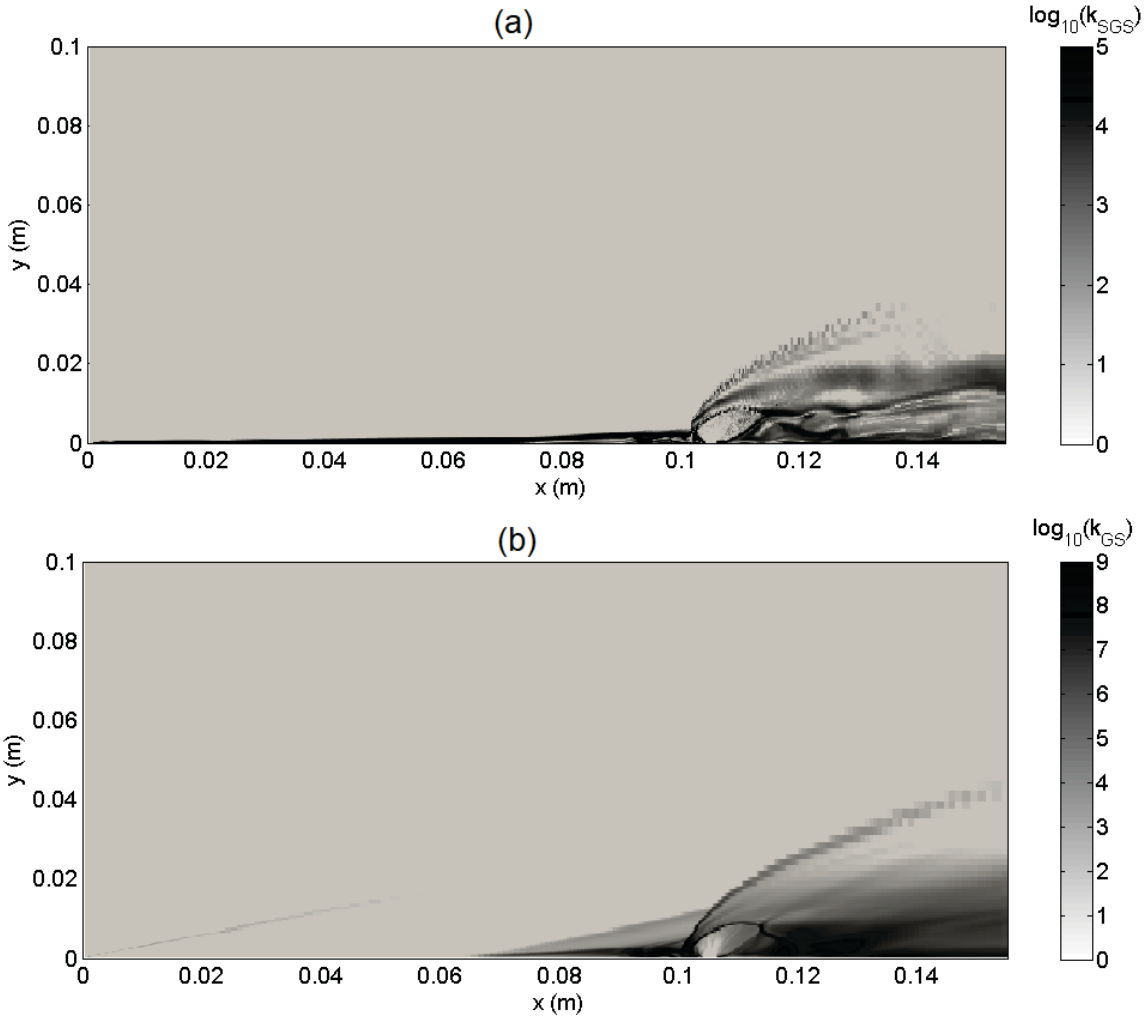

Figure 6.4: (a) Unresolved (sub-grid-scale), and (b) resolved (grid-scale) turbulent kinetic energy for the coarse mesh.

energy resolution is high because the Reynolds number is relatively low, thus allowing resolution of most of the turbulent kinetic energy. In addition, with a laminar inflow, turbulence is limited to a small region of the domain where the jet-in-crossflow interaction occurs. The remainder of the flow-field has zero gradients, and therefore zero eddy viscosity. Therefore, the integrated figure of greater than 99% does not provide conclusive evidence that the LES is well resolved for this flow-field. A more meaningful measure is the ratio of sub-grid to resolved TKE at each individual location within the flow-field. This localised ratio is also very small (i.e. less than 0.1%) at all locations throughout the domain and is maximum at the leading-edge shock, where the gradients correspond to shocks rather than turbulent fluctuations, and far from the jet interaction region where the mesh is concentrated. Performing the same calculation for intermediate and fine meshes shows the unresolved TKE is negligible throughout the domain.

To estimate the order of convergence, a Richardson extrapolation was performed on the leading edge shock thickness. The results are provided in Table 6.3. The observed order of convergence is $p = 1.2$. This matches expected behaviour, as the van Leer

Table 6.3: Richardson extrapolation results for leading edge shock thickness.

Variable	ϵ_{32}	ϵ_{21}	R	p	GCI_{32}	GCI_{21}
Shock thickness	0.76 mm	0.47 mm	0.62	1.2	98%	87%

Table 6.4: Richardson extrapolation results for time-averaged parameters.

Variable	ϵ_{32}	ϵ_{21}	R	p	GCI_{32}	GCI_{21}
θ	-1.3 deg	-0.2 deg	0.15	5.56	2.7%	0.4%
δ	-0.24 mm	-0.002 mm	0.008	14.3	0.3%	0.02%
h	-0.3 mm	-0.1 mm	0.35	3	3.1%	1.1%
x_{sep}	-11.6 mm	-5.2 mm	0.45	2.4	28%	11%

limiter is designed to give first-order behaviour in the region of shocks, while the KNP numerical scheme is second-order accurate.

Time-averaged values of several parameters, including leading edge shock angle, do not exhibit monotonic convergence on the three meshes described in Table 6.2, because the steady flow features are already well-resolved on the coarse mesh, with over 99% TKE resolution. In addition, unsteady parameters have temporal variability larger than the differences in time-averaged values between meshes, making comparison of their time-averaged values less meaningful, and in some cases preventing monotonic convergence.

To attempt to gain monotonic convergence for a broader range of parameters, a fourth (coarser) mesh, consisting of just 492 000 cells, was considered. Using this coarser mesh, along with the coarse and intermediate meshes from Table 6.2, monotonic convergence is observed in the time-averaged values for leading edge shock angle, boundary layer thickness, Mach disk height, and separation length, x_{sep}.

The Richardson extrapolation technique was applied to these four time-averaged parameters, and the results are provided in Table 6.4. Better than second-order convergence is observed in each variable. This indicates that the use of a fourth, coarser mesh, which was required to achieve monotonic convergence, may have resulted in the simulation result on this coarser mesh being outside the asymptotic convergence regime. There is a reduction in GCI for successive grid refinements (i.e. $GCI_{21} < GCI_{32}$). With the exception of the boundary layer separation, the GCI for the finer grid (GCI_{21}) is low ($\approx 1\%$ or less), providing further evidence that a mesh independent solution has nearly been achieved for these time-averaged parameters on the intermediate mesh.

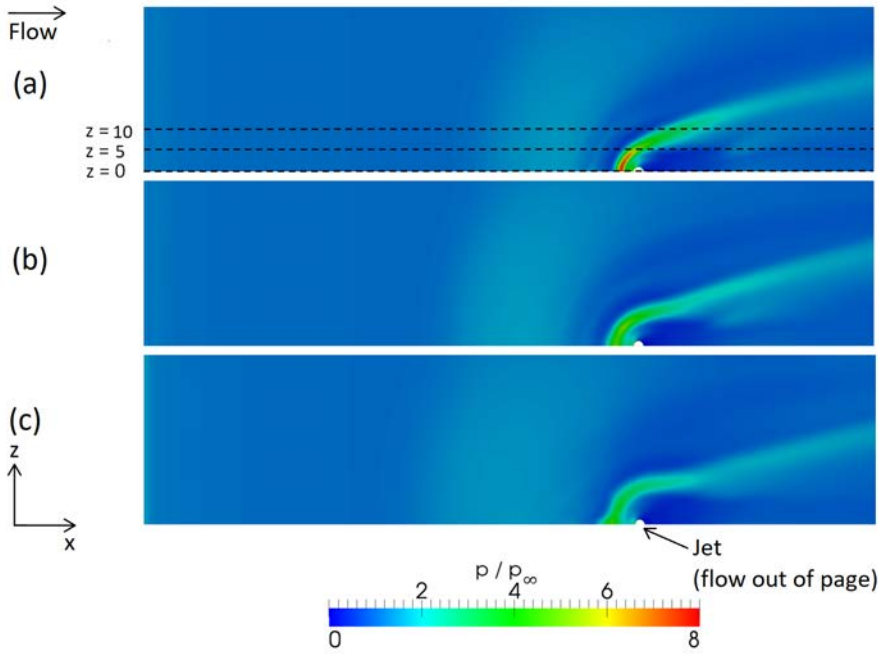

Figure 6.5: Comparison of time-averaged surface pressure distribution for: (a) coarse mesh, (b) intermediate mesh, and (c) fine mesh.

Figure 6.5 shows the time-averaged pressure distribution on the flat plate for the original three meshes from Table 6.2. The coarse mesh solution predicts a higher peak pressure in the re-circulation region upstream of the orifice compared with the intermediate and fine meshes. The fine mesh result shows some distortion in the bow shock, due to the improved resolution of vortical structures. Instantaneous pressure at a series of time intervals corresponding to $\tau = 1$ is shown in Figure 6.6. The coarse mesh shows a consistent upstream high-pressure region, with small periodic fluctuations. The intermediate mesh shows the periodic fluctuations in the the bow shock corresponding to shear-layer vortex shedding, as well as localised high-pressure regions emanating radially from the jet outlet. In addition to the fluctuations induced by shear-layer vortex shedding, the fine mesh resolves highly localised high pressure regions near the bow shock. Qualitatively, the fine mesh result closely matches the intermediate mesh, but has increased resolution of smaller structures.

Figure 6.7 provides a quantitative comparison of the time-averaged surface pressure at three span-wise locations marked on Figure 6.5 (a), and confirms that the solution is similar on the fine and intermediate mesh. The pressure peak on the jet centre-line is within 5% for the intermediate and fine mesh, but is 50% higher on the coarse mesh. The accuracy of the intermediate mesh is improved in comparison to the diamond airfoil result described in Chapter 5, where some difficulty was identified in accurate prediction of surface pressure. The primary difference between the time-averaged intermediate and fine mesh solution is the boundary layer separation point, which moves upstream from the jet outlet as mesh resolution is increased. It has been shown previously that prediction of boundary layer separation is a difficult task in supersonic and hypersonic flows (Li et al., 2017), and this remains true with the current MILES methodology. With

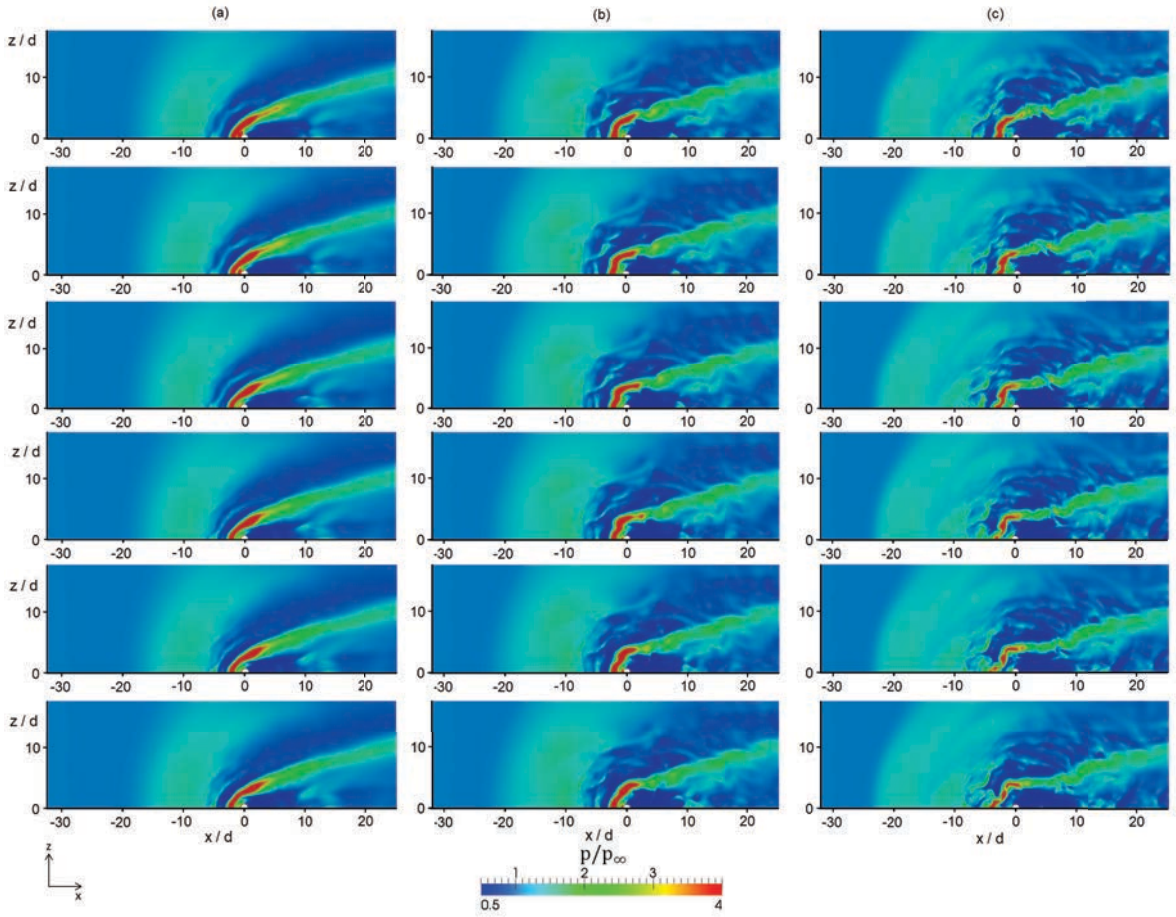

Figure 6.6: Comparison of surface pressure distribution at time intervals corresponding to $\tau = 1$, for: (a) coarse mesh, (b) intermediate mesh, and (c) fine mesh.

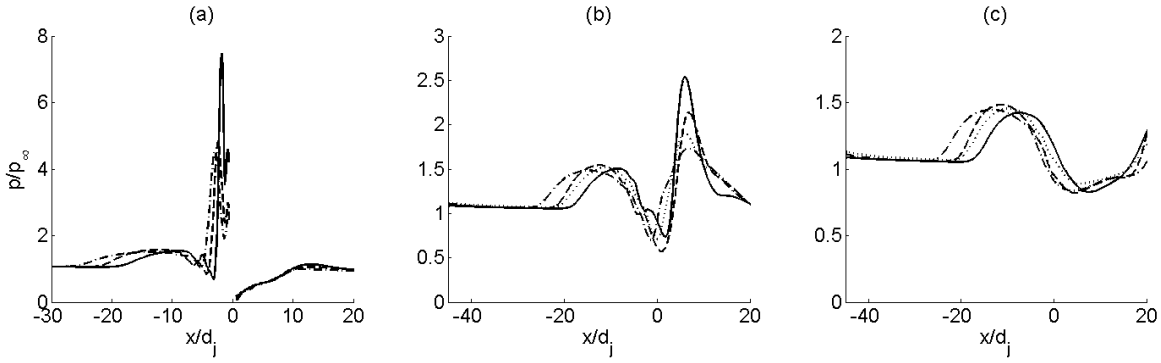

Figure 6.7: Comparison of time-averaged pressure on the plate between meshes for: (a) $z/d_j = 0$, (b) $z/d_j = 5$, and (c) $z/d_j = 10$. Solid line = coarse mesh, dash line = intermediate mesh, dot-dash line = fine mesh, dotted line = Smagorinsky sub-grid model (intermediate mesh).

reference to the intermediate mesh, the separation point is 9% further downstream on the coarse mesh, and 10% further upstream on the fine mesh.

The temporal variation in separation location shows similar behaviour to the Mach disk height. Temporal variations increase from ±3% on the coarse mesh, to ±5% on the intermediate mesh, and ±10% on the fine mesh. Therefore, the time-averaged estimate on the intermediate mesh is within the simulated temporal variations on the fine mesh. In addition, time-averaged Mach disk height predictions are consistent between meshes. Therefore, it is concluded that the intermediate and fine meshes predict consistent time-averaged and unsteady pressure distributions and shock locations.

The time-accurate, unsteady pressure distributions were further investigated by considering the instantaneous variation from the mean pressure, squared (i.e. $p'p'$) in Figure 6.8. On the coarse mesh, a single region of high pressure fluctuations is observed. The intermediate and fine meshes reveal a cellular structure, where individual cells correspond to individual flow structures. While the fine mesh shows better resolution of more individual structures within the flow, the overall behaviour is similar to the intermediate mesh, indicating that these fine structures do not significantly influence the flow-field.

The time-averaged pressure variation (i.e. the mean-squared variation, $\overline{p'p'}$) in Figure 6.9 shows a larger region of pressure variation on the fine mesh, corresponding to additional resolution of fine structures upstream and lateral to the jet outlet. However, the solution is again similar to the intermediate mesh.

Temporal variations in pressure were also measured at a number of discrete locations in the flow, allowing quantitative comparison of the unsteady behaviour on each mesh. The mean and RMS pressure coefficients, C_P, at three locations are provided in Figure 6.10. On the plane of symmetry, 5 jet diameters downstream of the jet outlet, the mean pressure coefficient on each mesh is consistent within 5% (see Figure 6.10 (a)). Consistent with the Mach disk height in Figure 6.3 (b), temporal variations in surface pressure increase as mesh resolution increases, and more turbulent structures are

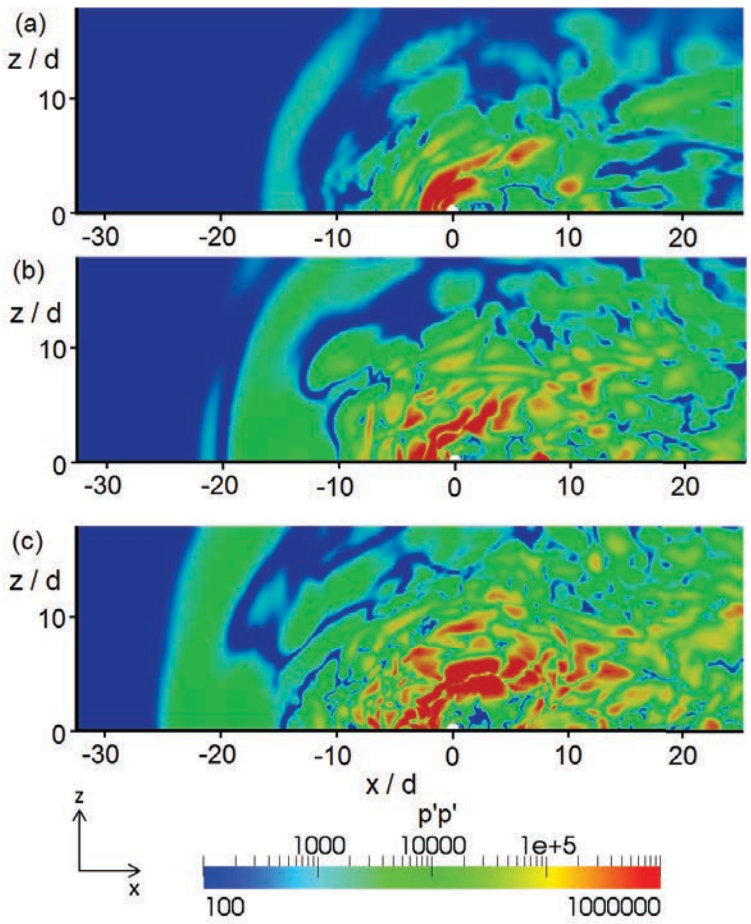

Figure 6.8: Instantaneous variation in pressure on the plate, $p'p'$, plotted on a logarithmic scale for: (a) coarse mesh, (b) intermediate mesh, and (c) fine mesh.

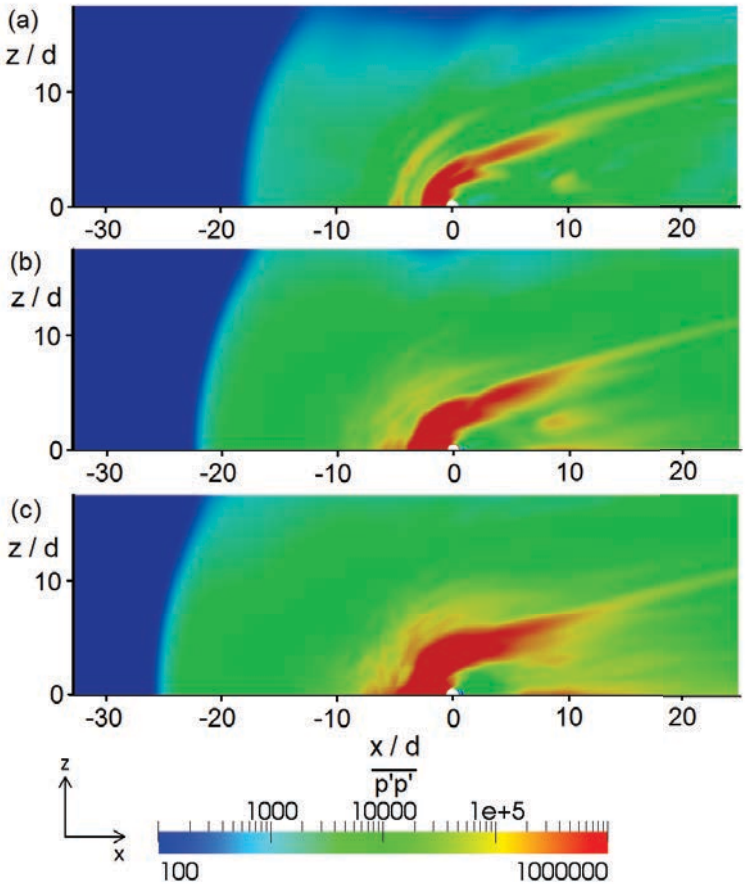

Figure 6.9: Mean-squared variation in pressure on the plate, $\overline{p'p'}$, plotted on a logarithmic scale for: (a) coarse mesh, (b) intermediate mesh, and (c) fine mesh.

Table 6.5: Richardson extrapolation results for RMS pressure coefficient variations on the flat plate, at $(x, y, z) = (20, 0, 0) \times d_j$.

(x, y, z)	ϵ_{32}	ϵ_{21}	R	p	GCI_{32}	GCI_{21}
$(20, 0, 0)$	-0.008	-0.002	0.26	4	21%	4.8%

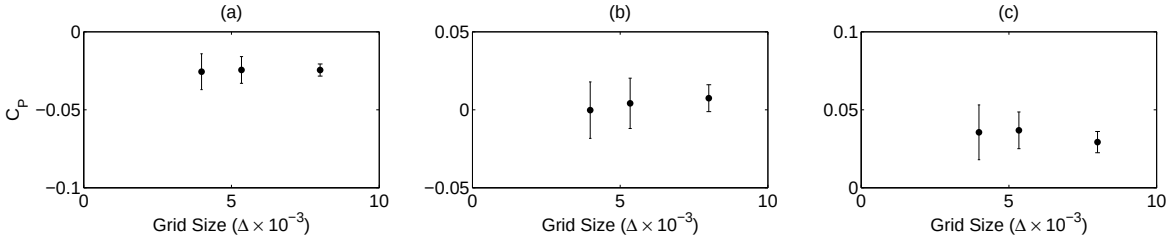

Figure 6.10: Mean and RMS pressure coefficient on the plate for each mesh, (a) $(x, y, z) = (5, 0, 0) \times d_j$, (b) $(x, y, z) = (20, 0, 0) \times d_j$, and (c) $(x, y, z) = (15, 0, 5) \times d_j$.

resolved near the wall. A Richardson extrapolation was performed on the RMS pressure coefficient variations on the coarse, intermediate, and fine mesh at a location 20 jet diameters downstream on the plane of symmetry (see Figure 6.10 (b)). Table 6.5 shows order of convergence of 4, again indicating that the results may not lie within the asymptotic convergence regime. Convergence errors of 10%, 20%, and 57% were observed for the fine, intermediate, and coarse meshes respectively, with a GCI between the intermediate and fine meshes of approximately 5%. This confirms that the temporal variations are being progressively more resolved as mesh resolution increases, and that mesh independence has nearly been achieved. These results are common for other locations (see Figure 6.10).

Further insight can be gained by investigating the spectra of the pressure signals at the same locations, provided in Figure 6.11. Consistent with the results shown above, the spectra are similar for the intermediate and fine mesh at low frequency, with the finer mesh resolving more energy at higher frequency. The coarse mesh has less energy resolution at all but the lowest frequencies.

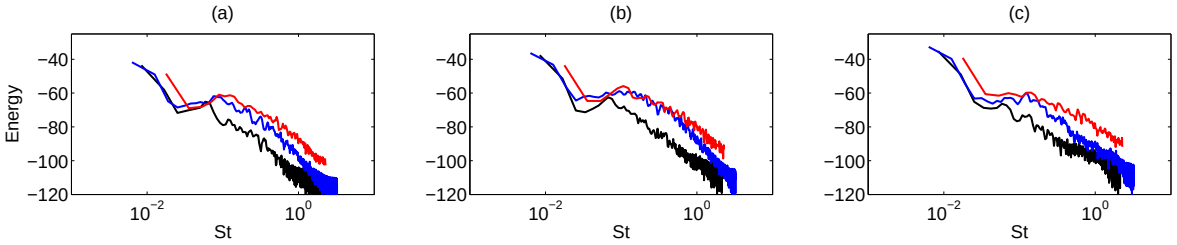

Figure 6.11: Spectra for pressure on the plate, (a) $(x, y, z) = (5, 0, 0) \times d_j$, (b) $(x, y, z) = (20, 0, 0) \times d_j$, and (c) $(x, y, z) = (15, 0, 5) \times d_j$. Red: Fine mesh, Blue: Intermediate mesh, Black: Coarse mesh.

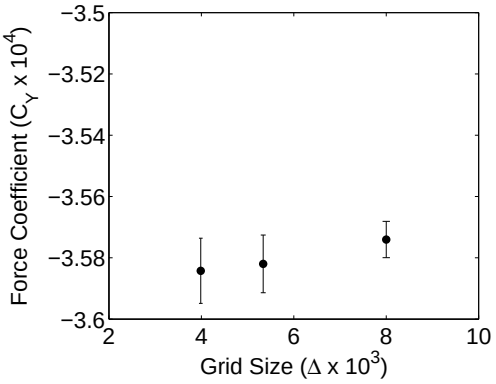

Figure 6.12: Mean and RMS force coefficient on the plate.

Table 6.6: Richardson extrapolation results for mean and RMS force coefficient.

	ϵ_{32}	ϵ_{21}	R	p	GCI_{32}	GCI_{21}
Mean	0.002	0.008	0.28	3.8	0.1%	0.03%
RMS	0.001	0.003	0.35	3.1	24%	7%

By integrating the pressure coefficient over the flat plate, an estimate of the total jet interaction force can be made. The results are presented in Figure 6.12 in terms of force coefficient. Figure 6.12 shows that RMS fluctuations in force coefficient are quite small, at around 3%, compared with 30% for the discrete pressure probes. This is consistent with the hypothesis that the fine mesh is resolving more structures, but these smaller structures are not significantly influencing the primary flow features of interest in this study. The integration procedure has the effect of averaging the oscillations, and produces a result that is almost mesh independent. In this case, the force coefficient varies less than 0.3% between meshes. Richardson extrapolation results for the force coefficient are provided in Table 6.6. Again, while the observed order of convergence remains above the formal order of the numerical scheme, indicating uncertainty in the Richardson extrapolation results, mesh independence is observed for the mean, and nearly observed for the RMS variations, with a GCI comparable to a single pressure probe.

The increased resolution of flow structures can also be visualised via isometric contours of the Q-criterion (Hunt et al., 1988), shown in Figure 6.13. The coarse mesh captures the barrel shocks, horseshoe vortices, and a single longitudinal vortex, but fails to resolve shear-layer vortices. The intermediate mesh resolves shear-layer vortices and the corresponding barrel shock deformation, as well as longitudinal vortices, horseshoe vortices, and wake vortices. The fine mesh resolves the primary flow structures as well as some additional fine structure. However, as stated previously, this fine structure does not affect the primary flow features.

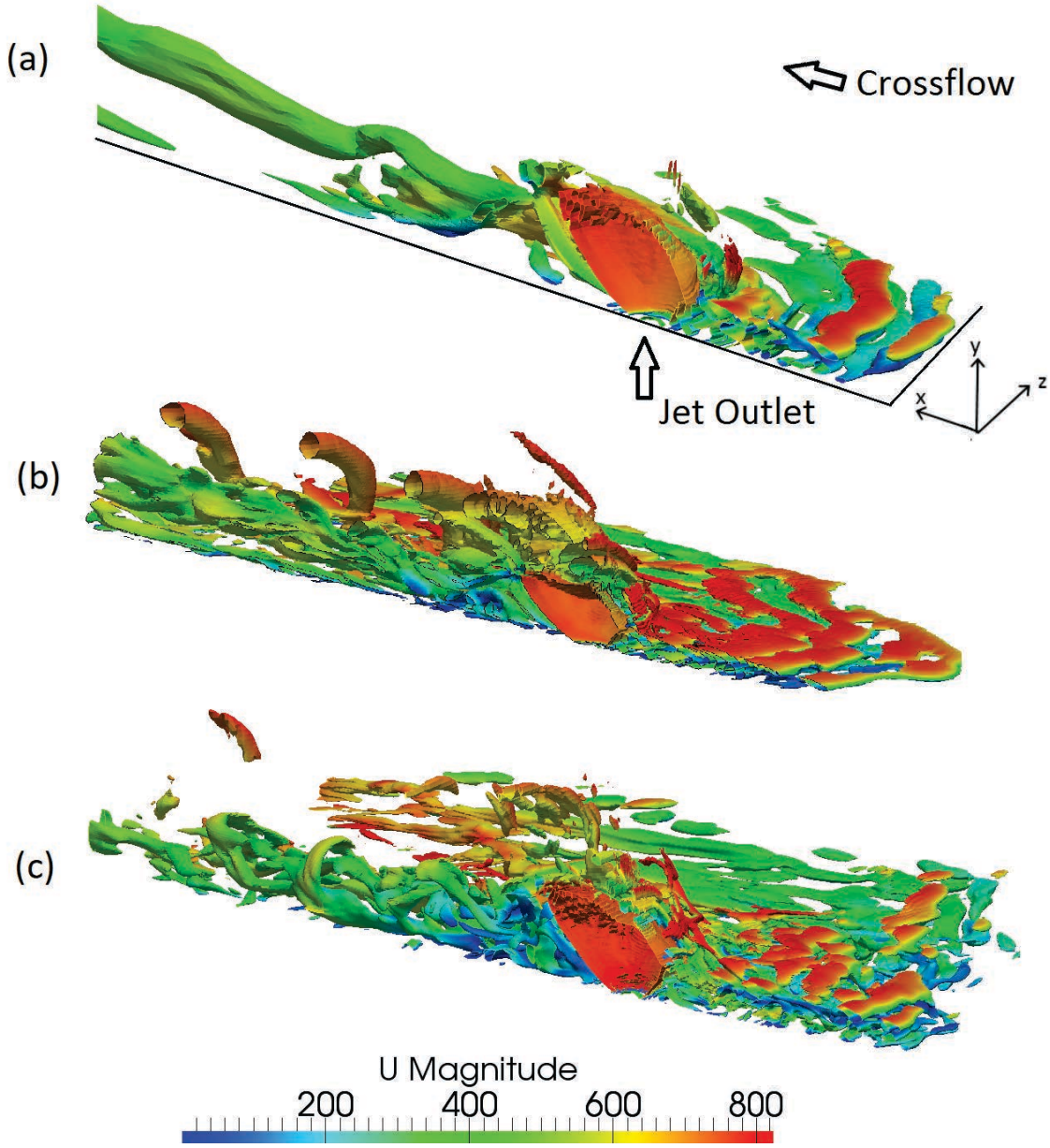

Figure 6.13: Isometric contours of Q-criterion, for $Q = 10^{10}$, coloured by velocity magnitude, showing instantaneous flow structure. (a) Coarse mesh (b) Intermediate mesh, and (c) Fine mesh.

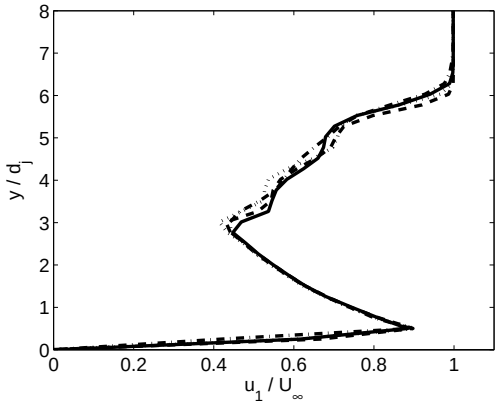

Figure 6.14: Velocity profiles, measured on the jet centre-line, one jet diameter downstream of the orifice ($x = d_j$). Solid line = coarse mesh MILES, dash line = intermediate mesh MILES, dot-dash line = fine mesh MILES, dotted line = Smagorinsky sub-grid model (intermediate mesh).

To evaluate the performance of MILES in comparison to conventional LES, the time-averaged surface pressure results in Figure 6.7 includes a Smagorinksy LES sub-grid model (Pope, 2000) on the intermediate mesh. The conventional LES results are very similar to the MILES. The peak pressure on the jet centre-line is between the coarse and intermediate mesh MILES result, 20% higher than the intermediate mesh MILES. The boundary layer separation point is within 5% of the MILES result on the same mesh. This shows that the MILES methodology has comparable performance to conventional LES when predicting surface pressure; however, the explicit LES model adds additional dissipation. Note that the explicit sub-grid models used in conventional LES are usually coupled with a non-dissipative scheme, and therefore the total dissipation in a conventional LES would be reduced. Further comparison can be made between conventional and implicit LES by considering the velocity profiles downstream of the jet outlet, shown in Figure 6.14. The result is similar on all three meshes, and is also similar to a conventional LES solution. The coarse mesh result slightly under-predicts the maximum velocity deficit, while all three meshes predict the a similar vertical extent of the jet and boundary layer thickness.

Results were also compared between the current computational domain and a full three-dimensional domain on the intermediate mesh, with the plane of symmetry removed from the jet centre-line. The flow structures were similar for both simulations. For example, the instantaneous and time-averaged pressure distributions are shown in Figure 6.15, and contours of Q-criterion in the symmetry plane, outlet plane, and on the flat plate are shown in Figure 6.16. This confirms that the use of a symmetry plane does not significantly influence the results for this flow. The sensitivity of the solution to the limiter scheme was also investigated, by comparing the van Leer results with a Minmod simulation on the intermediate mesh. No discernible differences were observed.

These results provide confidence that the MILES resolves nearly all the TKE,

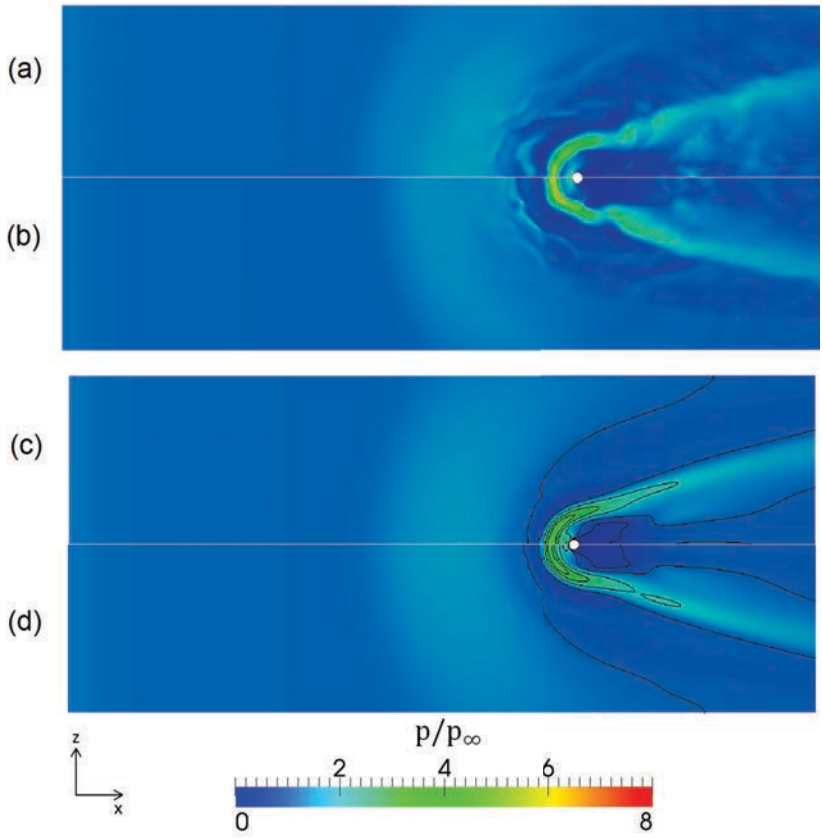

Figure 6.15: Comparison of instantaneous and time-averaged surface pressure distribution. (a) instantaneous, current domain; (b) instantaneous, full three-dimensional domain; (c) time-averaged, current domain, overlaid with contours at $p/p_\infty = 0.5$, 1, 2, 3, 4, and 5; (d) time-averaged, full three-dimensional domain, overlaid with contours at $p/p_\infty = 0.5$, 1, 2, 3, 4, and 5.

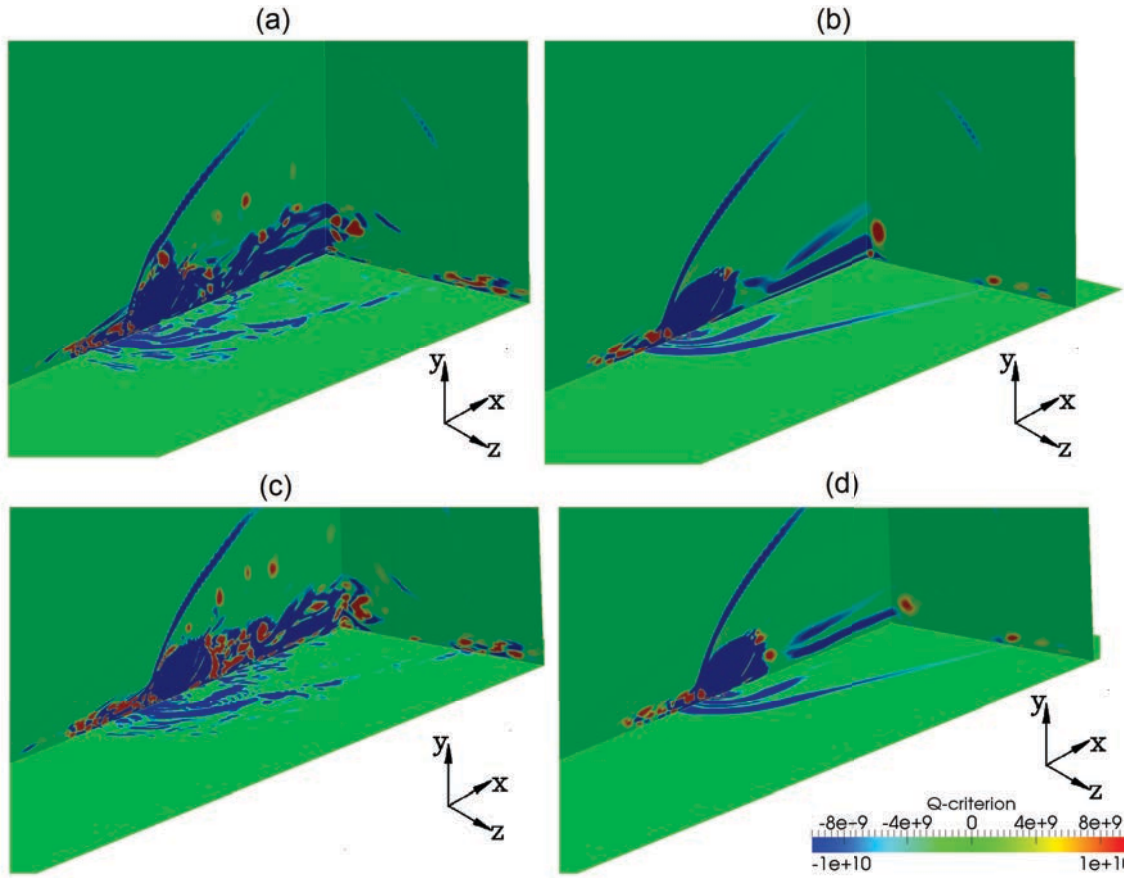

Figure 6.16: Comparison of instantaneous and time-averaged contours of Q-criterion. (a) instantaneous, current domain; (b) time-averaged, current domain; (c) instantaneous, full three-dimensional domain; (d) time-averaged, full three-dimensional domain.

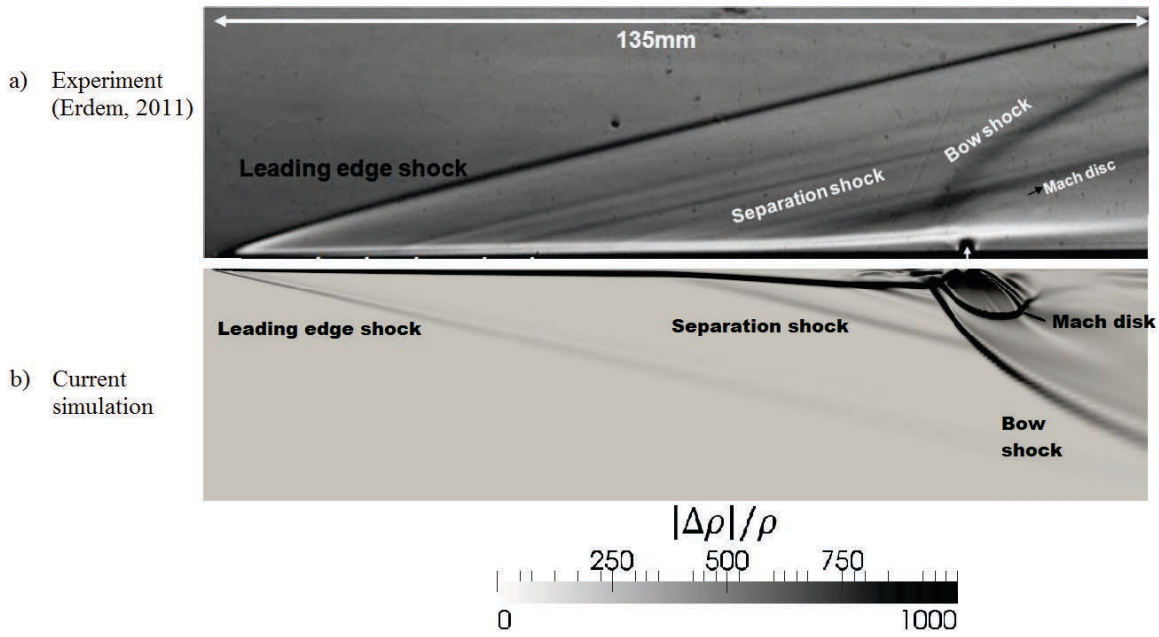

Figure 6.17: Comparison of (a) experimental Schlieren visualisation (Erdem, 2011), and (b) time-averaged density gradient contours in the plane of symmetry.

and progressively resolves more turbulent structures with increased mesh resolution. Richardson extrapolation indicates that the intermediate mesh is able to accurately resolve the time-averaged flow, while temporal RMS variations still show GCI around 5%, indicating that further mesh refinement may resolve additional small-scale structures. This phenomenon is common for LES, where additional refinement will move toward a DNS solution. The consistency between time-averaged parameters, and high TKE resolution, indicates that these small-scale structures do not significantly affect the flow-field. This is demonstrated by similarity in shock structure and pressure distribution between the intermediate and fine mesh. Therefore, the results indicate that the intermediate mesh is sufficient for this study.

6.3 Model Validation

Parameters considered for validation were time-averaged shock structure and surface pressure, and the dimensions associated with primary flow features, specifically mean boundary layer thickness, δ, Mach disk height, h, and separation location, x_{sep}. These parameters were compared to experimental results of Erdem (2011).

Shock structures were compared using time-averaged density gradient contours from the simulation, compared with the experimental Schlieren images in Figure 6.17. All major shock structures in the flow were captured by the simulation, including the leading edge shock, separation shock, bow shock, and Mach disk. A re-compression shock was not directly observed in the plane of symmetry by either the experimental or numerical Schlieren images. Overall, the simulated flow structure is in good agreement with the experiment, and the time-averaged flow features are reasonably well captured.

Table 6.7: Quantitative jet in crossflow validation results.

	δ ($\times d_j$)	h ($\times d_j$)	x_{sep} ($\times d_j$)
Simulation	0.46	3.4	25
Experiment	0.85	4.1	22
Theory	0.6	-	-

Quantitative comparisons are made between simulation and experiment in Table 6.7. Differences are observed in the height of the Mach disk, which is 20% higher in the experiment, and the boundary layer thickness, which is 85% thicker in the experiment. These differences are inter-related, the difference in Mach disk height is caused by the difference in boundary layer thickness, while the difference in boundary layer thickness is caused by the different temperatures and physical properties of the flat plate.

In the experiment, boundary layer thickness was measured on the jet centre-line, $x/d_j = 22$ upstream of the jet. These results, and the corresponding simulation results, are provided in Table 6.7, along with the analytical estimate (Popinski and Ehrlich, 1966) based on a reference temperature method. The discrepancy between simulation and the analytical estimate is due to the temperature of the plate. In the simulation, the flow over the plate was initialised at the free-stream temperature (62.5 K) and no additional heat was added from the plate, due to the adiabatic boundary condition, while the analytical adiabatic wall temperature is 321 K (Popinski and Ehrlich, 1966). As sufficient time has not elapsed in the simulation for the plate temperature to reach a steady-state, the plate temperature remained below the adiabatic wall temperature. An additional simulation was conducted on the coarse mesh, with the plate temperature fixed at 321 K, thus adding heat to the flow. The error between simulated and analytical values was reduced from 23% to 11%. The remaining 11% error is attributed to mesh resolution, the simulated boundary layer thickness on the coarse mesh is within 2 cells of the analytical value. The experimental wall temperature was not published, but is expected to be initially at room temperature ($\approx$ 300 K), close to the adiabatic wall temperature. The experimental boundary layer thickness exceeds the analytical estimate by 42%, and this discrepancy is attributed to physical properties of the plate (for example leading edge bluntness and surface roughness).

The thicker boundary layer in the experiment allows the jet to penetrate further before it is deflected by the crossflow. Therefore, the Mach disk is expected to form further from a plate with a thicker boundary layer. This corresponds to the observed behaviour (see Table 6.7). The influence of boundary layer thickness on Mach disk height was confirmed by running an additional simulation on the coarse mesh with an extended plate length, such that the boundary layer thickness was matched to the experiment at the measurement location. This reduced the discrepancy between

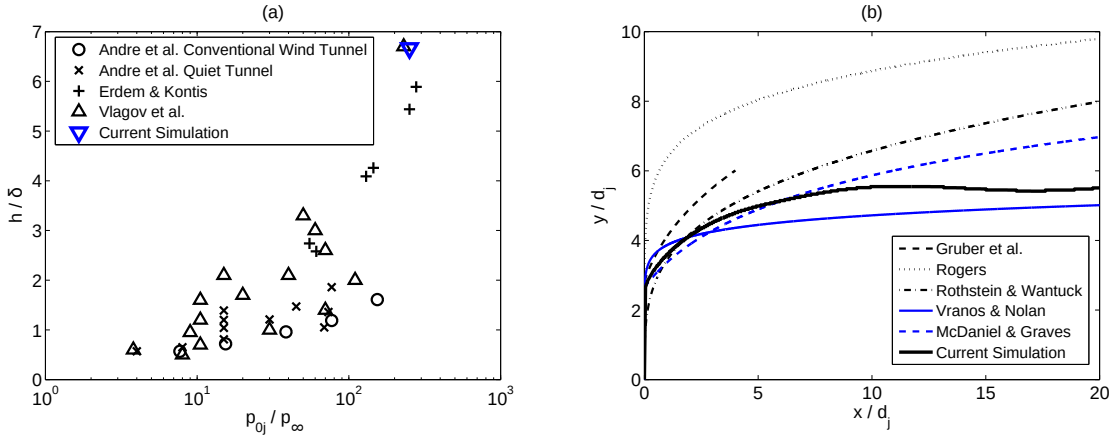

Figure 6.18: (a) Mach disk height as a function of pressure ratio, comparing the current simulation to data compiled by Andre et al. (Andre et al., 2017; Erdem and Kontis, 2009; Vlagov et al., 1980), and (b) Jet trajectory comparing the current simulation to data compiled by Mahesh (Mahesh, 2013; Gruber et al., 1997; Rogers, 1971; Rothstein and Wantuck, 1992; Vranos and Nolan, 1965; McDaniel and Graves, 1988).

experimental and simulated time-averaged Mach disk from 20% to 6.8%. The remaining discrepancy is attributed to mesh resolution, unsteadiness in the Mach disk, and to the idealised "top hat" jet inlet velocity profile used in the simulation. Further confirmation is provided in Figure 6.18 (a), where Mach disk height is normalised by boundary layer thickness and compared to previously published data. The current simulation fits well within published experimental data. The error between the simulation and the experimental result of Erdem (2011) is 11%, as mentioned previously, while the simulation results are within 0.5% of the experimental results of Vlagov et al. (1980).

Figure 6.18 (b) compares the jet trajectory, normalised by jet diameter, d_j, and jet-to-crossflow momentum ratio, J, and shows that the current simulation again fits well with published data. The exception is Rogers (1971), who observed increased penetration due to a thicker in-flow boundary layer.

Wall pressure distribution is compared between simulation and experiment in Figure 6.19. In the experiment, wall pressure was measured by pressure taps on the plate along the jet centre-line, $z/d_j = 0$, and at lateral distances of $z/d_j = 4.8$ and $z/d_j = 9.1$ (approximate measurement locations are shown in Figure 6.5 (a)). The simulation predicts pressure very well along the jet centre-line. The separation location shows a small discrepancy (12%, see Table 6.7), while the high pressure region upstream of the jet outlet and the low pressure region downstream of the jet are well predicted. In the upstream re-circulation region ($-20 \lesssim x/d \lesssim -5$), the simulation over-predicts pressure by 13%, while in the downstream re-circulation region ($0 \lesssim x/d \lesssim 20$) this error increases to 20%. However, the absolute values of pressure are very low in the downstream re-circulation region, resulting in a small absolute error of approximately 100 Pa.

At $z/d_j = 4.8$, the overall behaviour is predicted correctly. The pressure increases

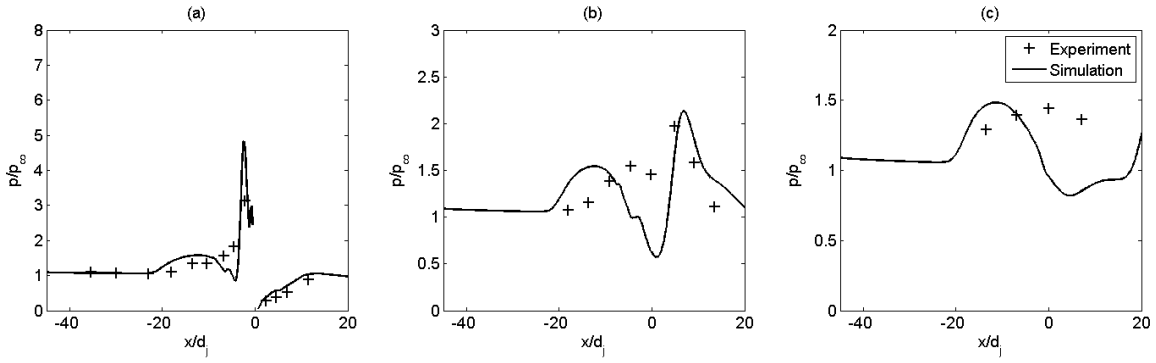

Figure 6.19: Comparison of pressure on the plate between simulation and experiment for: (a) $z/d_j = 0$, (b) $z/d_j = 4.8$, and (c) $z/d_j = 9.1$. + = Experiment; Solid line = Simulation.

at the point of boundary layer separation, which is slightly further upstream in the simulation, then decreases before a large increase at the bow shock location. Behind the bow shock, the pressure recovers to the free-stream value. The simulated pressure drop just upstream of the bow shock (at around $x = 0$) is not captured in the experiment, and is slightly further upstream in the simulation both at the centre-line, and off-centre, due to the separation point being further upstream. Quantitatively, the peak pressure in the upstream re-circulation region is within 1% of the experimental value, but is in a different location due to the 12% difference in separation location, while the downstream re-circulation region was not captured in the experiment. The experimental results did not capture the sharp peak at the bow shock, resulting in the simulation over-predicting peak pressure by 16% in this region ($x/d_j \approx 5$).

At $z/d_j = 9.1$, the comparison appears poor, as the experiment only has pressure probe data from within the upstream re-circulation region, which is located further upstream in the simulation. The pressure drop and the bow shock are not captured in the experiment. However, the simulation does accurately predict the peak pressure in the upstream re-circulation region, within 5% of the experimental result, allowing for the different separation location.

Overall, the agreement with experimental data is good, once the different boundary layer separation point is taken into account.

The final parameter considered is the length of the separation region, x_{sep}, which was reasonably well predicted, within 15% of the experimental value. The discrepancy between simulation and experiment is most likely due to differences in boundary layer thickness, plate temperature, surface roughness, and leading edge bluntness. As noted previously, numerical and experimental measurements for supersonic boundary layer separation position rarely agree, and there are significant temporal variations in the simulated separation point, so this result is reasonable.

Overall, the simulation correctly predicts all major features of the flow observed in the experiment. Differences between simulation and experiment are attributable to differences in plate temperature and physical properties. Simulation results also closely

match analytical estimates and previously published data.

6.4 Steady Jet Verification and Validation Conclusions

Mesh resolution was investigated in detail. This investigation showed that, even on the coarsest mesh considered, the simulation accurately predicts the time-averaged flow features, while accurate resolution of unsteady flow features requires slightly higher mesh resolution. The intermediate mesh is able to provide acceptable resolution of the unsteady fluctuations, and Richardson extrapolation indicates that the simulation is approaching mesh independence on the intermediate mesh. On this mesh, grid convergence indices (GCI) of $< 1\%$ are observed in mean behaviour, while $GCI \approx 5\%$ are observed in RMS quantities.

The MILES methodology has been compared to a conventional Smagorinksy-Lilly LES method. MILES shows similar prediction of time-averaged flow features and better resolution of unsteady features, due to reduced numerical dissipation.

The assumption of symmetry along the jet centre-line was also tested, and was shown to not significantly affect the simulation result.

The simulation results have been compared to experimental results, primarily those of Erdem (2011). The results have shown that all main features of the flow are able to be captured accurately. Differences between simulation and experiment can be explained by the differences in temperature and physical properties of the flat plate. Once these are taken into account, time-averaged Mach disk height is correctly predicted, within 7%, time-averaged boundary layer thickness is predicted within 11%, and time-averaged boundary layer separation is predicted within 15%. In addition, both Mach disk height and jet penetration, once appropriately non-dimensionalised, fall within the range observed in previous experimental studies. Comparison of surface pressures show errors between 5% and 20%, allowing for the different separation location, with the higher errors occurring in locations where there is a lack of resolution in the experimental measurements.

6.5 Unsteady Flow Structure

The instantaneous structure of the flow is shown in Figure 6.20. These images show contours of the Q-criterion, coloured by velocity magnitude.

Horseshoe vortices, hair-pin type shear-layer vortices, wake vortices, and a streamwise counter-rotating vortex are identified. Horseshoe vortices form in the re-circulation region, upstream of the jet outlet, and bend around the jet forming the characteristic horseshoe shape. Here, there are several vortices rather than a single, well-defined horseshoe vortex. Hair-pin type shear-layer vortices travel downstream after being periodically shed from the shear-layer near the upstream barrel shock. The counter-

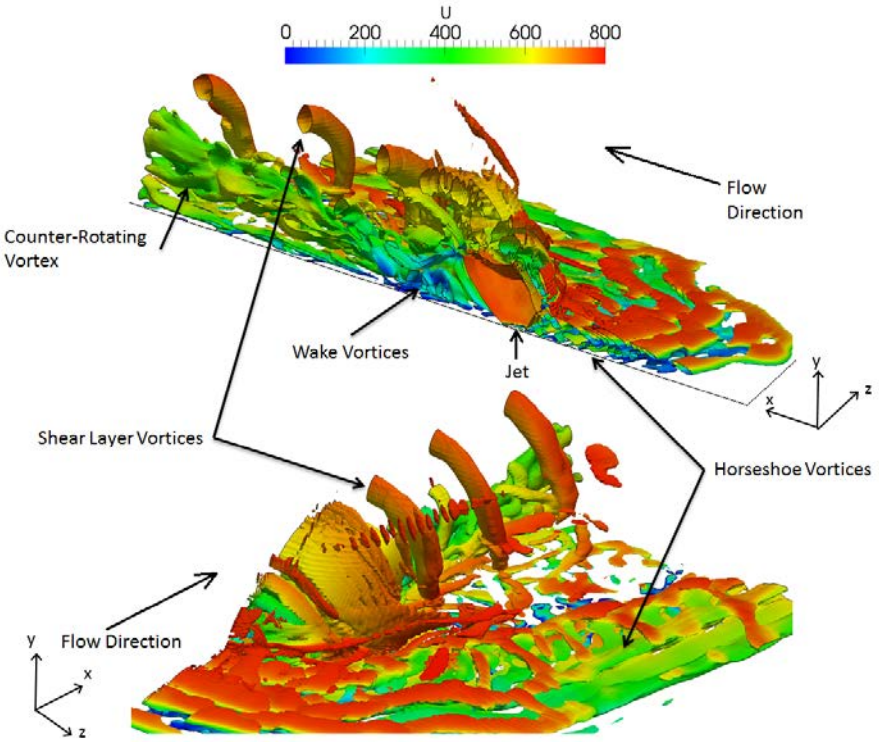

Figure 6.20: Isometric contours of instantaneous Q-criterion, for $Q = 10^{10}$, coloured by velocity magnitude, showing instantaneous flow structure.

rotating vortex also becomes clear in the far-field, while wake vortices are irregularly shed from the vicinity of the leeward barrel shock.

Figure 6.21 shows contours of the Q-criterion in the plane of symmetry, on the plate, and in a span-wise plane perpendicular to the crossflow, $20d_j$ downstream of the jet orifice. Figure 6.21 compares the vortex structures present in the instantaneous and time-averaged flow-fields. In the instantaneous flow-field, a complex system of horseshoe vortices, and distinct shear-layer vortices can be seen in plane of symmetry. The span-wise plane shows the individual vortices that comprise the single stream-wise counter-rotating vortex observed in the time-averaged flow. The span-wise plane also shows the trajectory of the horseshoe vortices. Vortices that form close to the jet merge back into the plane of symmetry, while vortices formed further upstream persist far downstream along the plate.

The shock structure can also be visualised in Figure 6.21, and is similar to the well documented jet-in-supersonic-crossflow shock structure described in Chapter 2 (see Figure 2.2), and to the experimentally measured shock structure in Figure 6.17.

6.6 Surface Pressure

Figure 6.22 (a) shows the time-averaged pressure on the plate. Along the jet centre-line ($z = 0$), there is a clear increase in pressure upstream of the jet outlet, from the point of boundary layer separation, at approximately $-25 \lesssim x/d_j \lesssim -8$. Nearer the jet, the pressure drops, before a large peak in front of the jet outlet, corresponding to

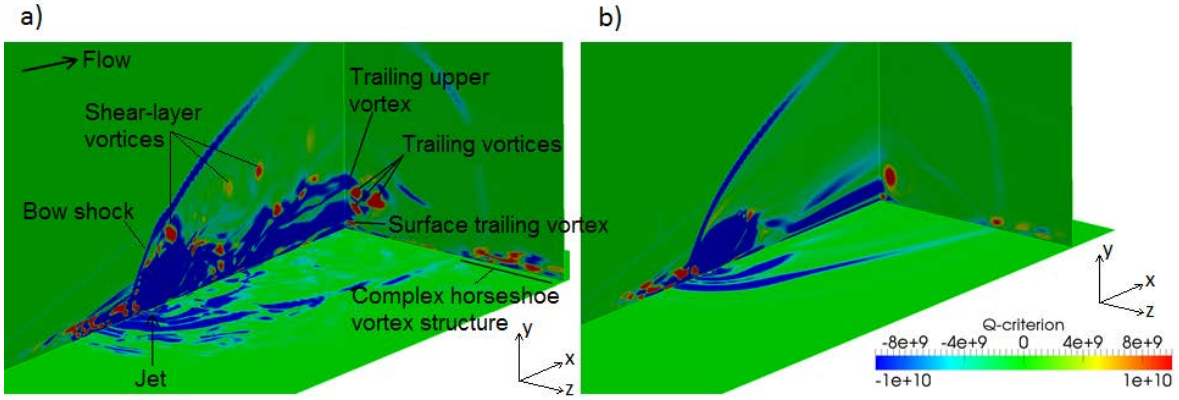

Figure 6.21: Contours of Q-criterion, with cutting planes in the plane of symmetry, on the plate, and perpendicular to the freestream, 20 jet diameters down-stream of the jet outlet, showing (a) Instantaneous, and (b) Time-averaged flow structure.

the bow shock. A re-circulation region forms in this area immediately upstream of the jet outlet. The pressure downstream of the jet is reduced below the free-stream value, as the free-stream flow is obstructed by the jet. Further downstream, at $x/d_j > 10$, the pressure recovers. The pressure in this region exceeds the free-stream value, as the free-stream flow that moved laterally around the bow shock flows back into the wake region. Away from the jet centre-line, the overall behaviour remains the same. The boundary layer separation point, and the jet bow shock curve around the jet outlet, while peak pressure is decreased due to weakening of the bow shock. As indicated on Figure 6.22 (a), there are isolated, localised regions of higher pressure behind the bow shock, both away from the jet centre-line and on the centre-line.

Figure 6.22 (b) shows a snap-shot of the instantaneous pressure on the plate. This allows a more detailed investigation of the individual structures within the flow that influence the pressure distribution. The overall features of the time-averaged pressure field are maintained, but individual flow structures are resolved. Figure 6.22 (b) shows deformation of the high pressure region lateral to the jet that is not present in the time-averaged data, corresponding to the location of a shear-layer vortex. This deformed high pressure region will convect downstream. The instantaneous image also shows small, high pressure regions which give rise to the localised high pressure regions in the time-averaged data.

The development of individual structures that produce the surface pressure distribution is shown in Figure 6.23 (an animation is provided in the supplementary material). The shedding of a shear-layer vortex is shown, as is the motion of the localised high-pressure regions identified in Figure 6.22 (b).

Temporal pressure variations are shown in Figure 6.24. Figure 6.24 (a) shows the square of the time-averaged pressure variation (i.e. the mean-squared variation, $\overline{p'p'}$), while Figure 6.24 (b) shows the instantaneous variation in pressure, squared (i.e. $p'p'$). The instantaneous data reveals a cellular structure, in which individual cells correspond to the location of individual flow structures. The localised regions of high pressure

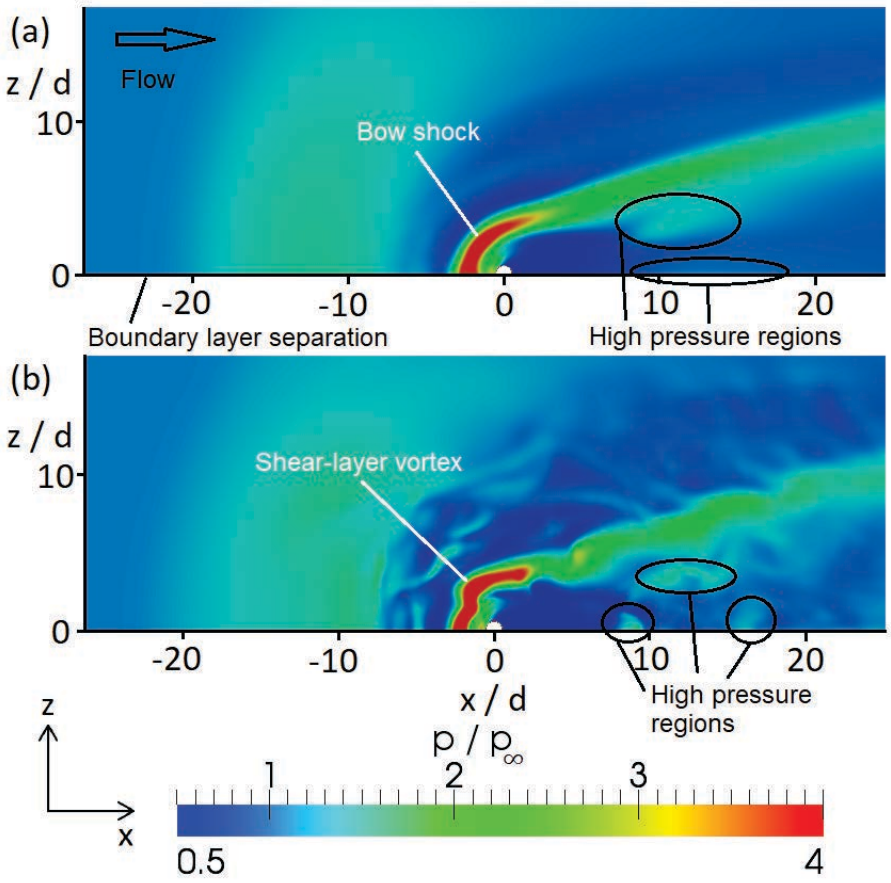

Figure 6.22: (a) Time-averaged, and (b) Instantaneous pressure contours on the plate.

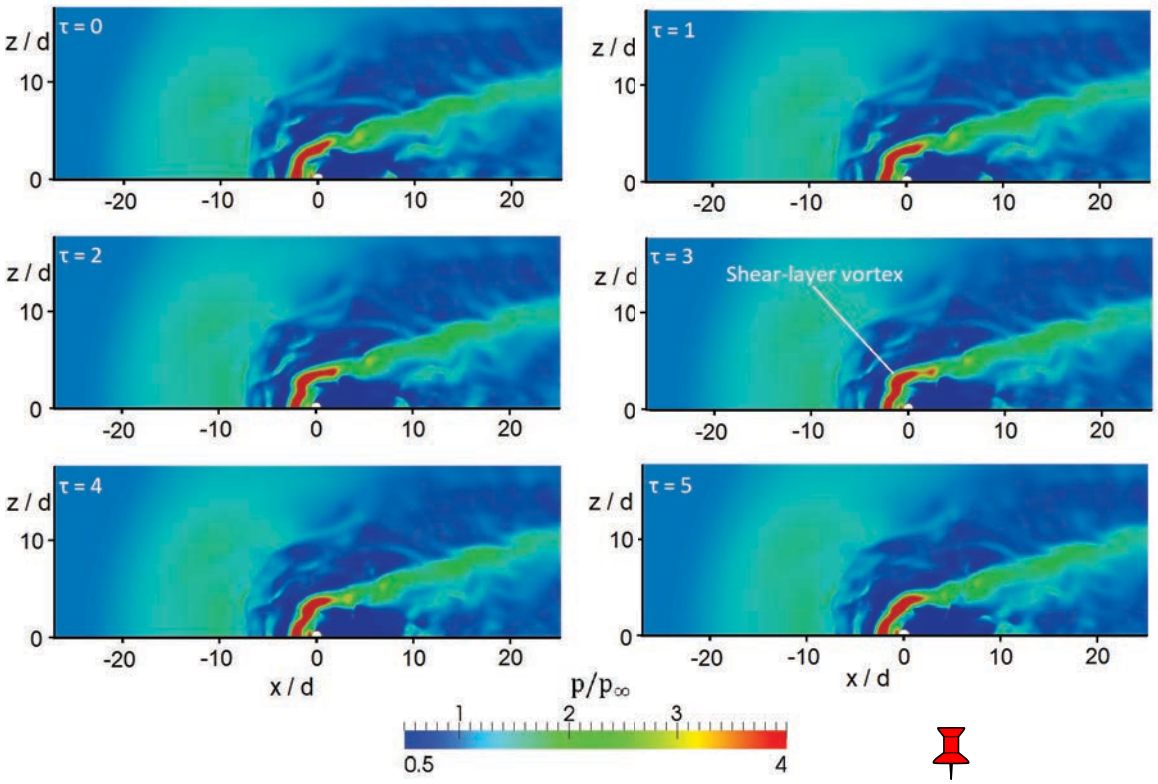

Figure 6.23: Instantaneous pressure contours on the plate at time intervals corresponding to $\tau = 1$.

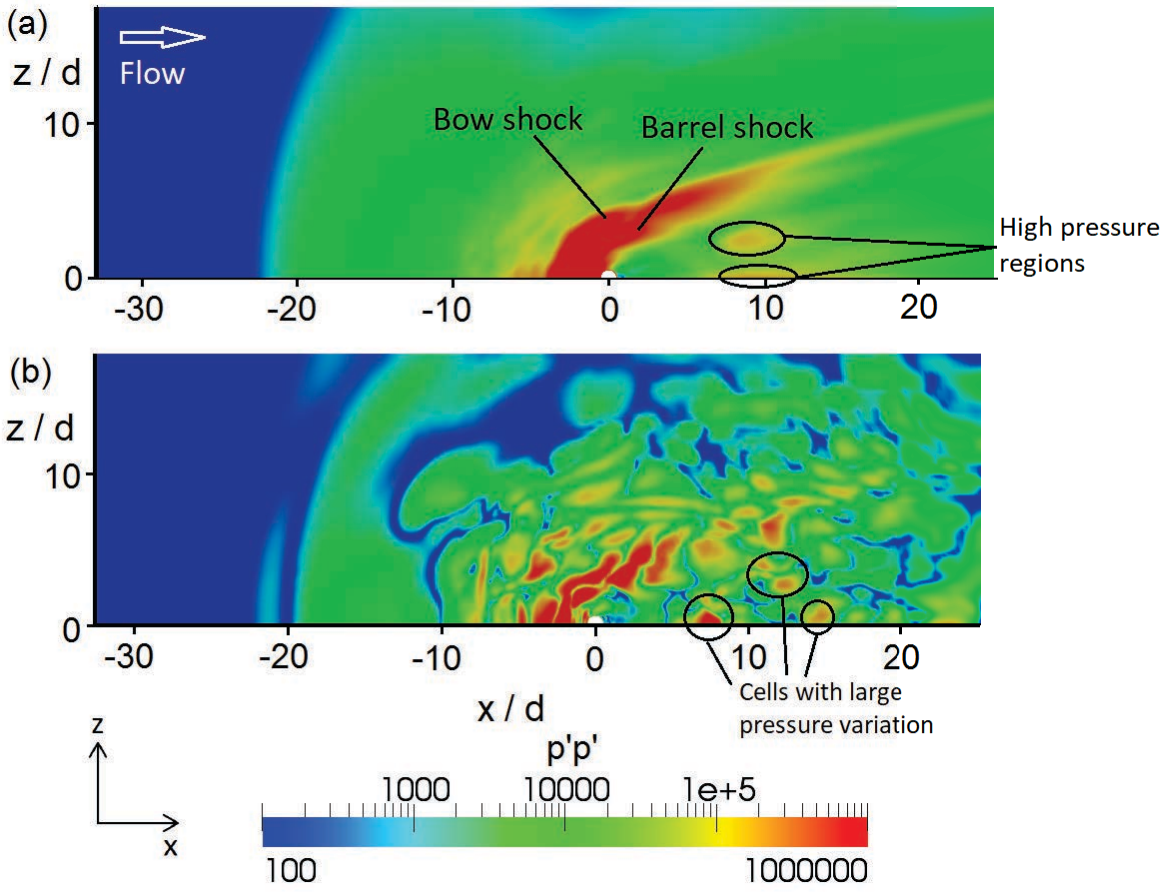

Figure 6.24: Variation in pressure on the plate, plotted on a logarithmic scale. (a) Mean-squared variation, $\overline{p'p'}$, and (b) Instantaneous variation, $p'p'$.

highlighted in Figure 6.22 (a) are identified as regions which also have high temporal variations in pressure. For example, large variations can be observed in the bow shock region, where the pressure is high. The other region with large pressure variations is in the re-circulation region upstream of the bow shock. This is caused by the changing structure of the horseshoe vortices. Lateral to the jet, the region of large fluctuations at the bow shock location splits, two separate regions can be seen in both the time-averaged and the instantaneous data. This is caused by the bow shock and barrel shock deformation that corresponds to shear-layer vortex shedding.

6.7 Horseshoe Vortices

The cellular structure observed within the upstream re-circulation region in Figure 6.24 (b) is driven by the horseshoe vortex structure. The boundary layer separates upstream of the jet, resulting in an adverse pressure gradient and a large region of re-circulating flow. A complex system of horseshoe vortices develops within the re-circulation region. This region of separated flow extends in the stream-wise and span-wise directions.

Figure 6.25 shows instantaneous span-wise vorticity in the symmetry plane,

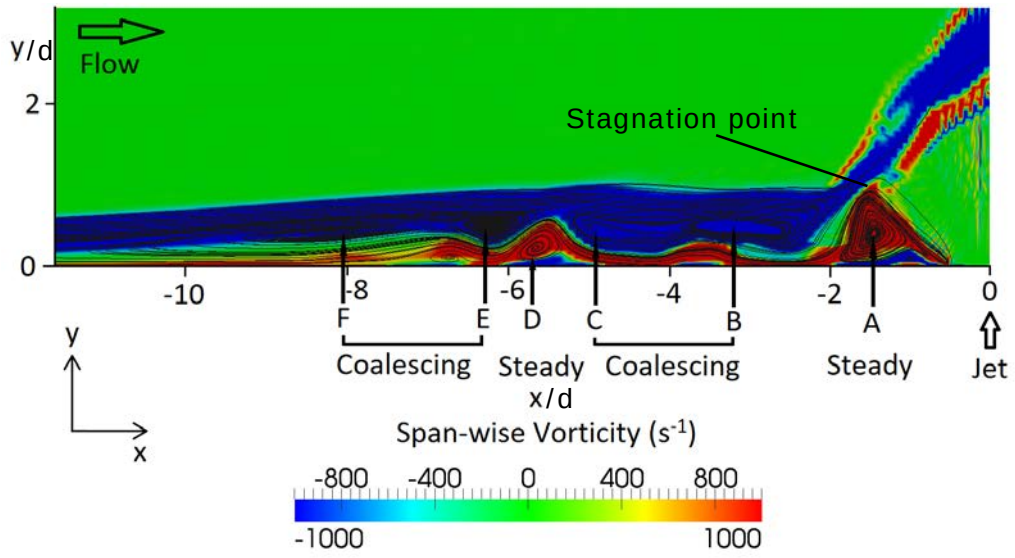

Figure 6.25: Instantaneous span-wise vorticity in the symmetry plane, upstream of the jet outlet, overlaid with streamlines.

upstream of the jet exit, overlaid with streamlines. Six vortices are observed, and the structure is more complex than both subsonic crossflow and supersonic crossflow with turbulent boundary layer cases. Vortex A is the quasi-steady re-circulation vortex immediately upstream of the jet, caused by the free-stream flow deflected downward from the stagnation point. Instead of a single counter-rotating horseshoe vortex, five additional discrete structures can be seen upstream of the re-circulation vortex. These are each labelled Vortex B, C, D, E, and F in Figure 6.25.

Figure 6.26 shows the temporal evolution of the horseshoe vortex system over a period of 10τ (an animation is provided in the supplementary material). Vortex A and D are quasi-steady, and are always present, while Vortex B and C, as well as Vortex E and F, are co-rotating pairs which periodically coalesce. The time period shown in Figure 6.26 approximately represents a single period of coalescence of the vortices, that is, Vortices B and C, and Vortices E and F periodically coalesce with a frequency corresponding to a Strouhal number, $St_\infty \approx 0.1$, where $St_\infty = f \times d_j/U_\infty$. In isolation, Vortex A and B form a counter-rotating pair, consistent with the steady regime identified for subsonic flow (Kelso et al., 1996). As the separated region is much larger for a laminar boundary layer, additional vortices develop.

The three-dimensional nature of the horseshoe vortices is examined in Figure 6.27, which shows streamlines of time-averaged fluid flow through the horseshoe vortex region, overlaid on contours of time-averaged vorticity magnitude. Figure 6.27 shows that the flow from the vortex closest to the jet outlet (Vortex A) wraps tightly around the jet orifice, and is then lifted from the plate and entrained into the longitudinal counter-rotating vortex pair far downstream of the jet outlet. This behaviour is in agreement with Viti et al. (2009). The flow from the upstream vortices (Vortices B, C, E, and F) is distinctly different to Vortex A; the fluid travels around the jet along the flat plate, corresponding to the usual horseshoe vortex behaviour. Flow from Vortex D

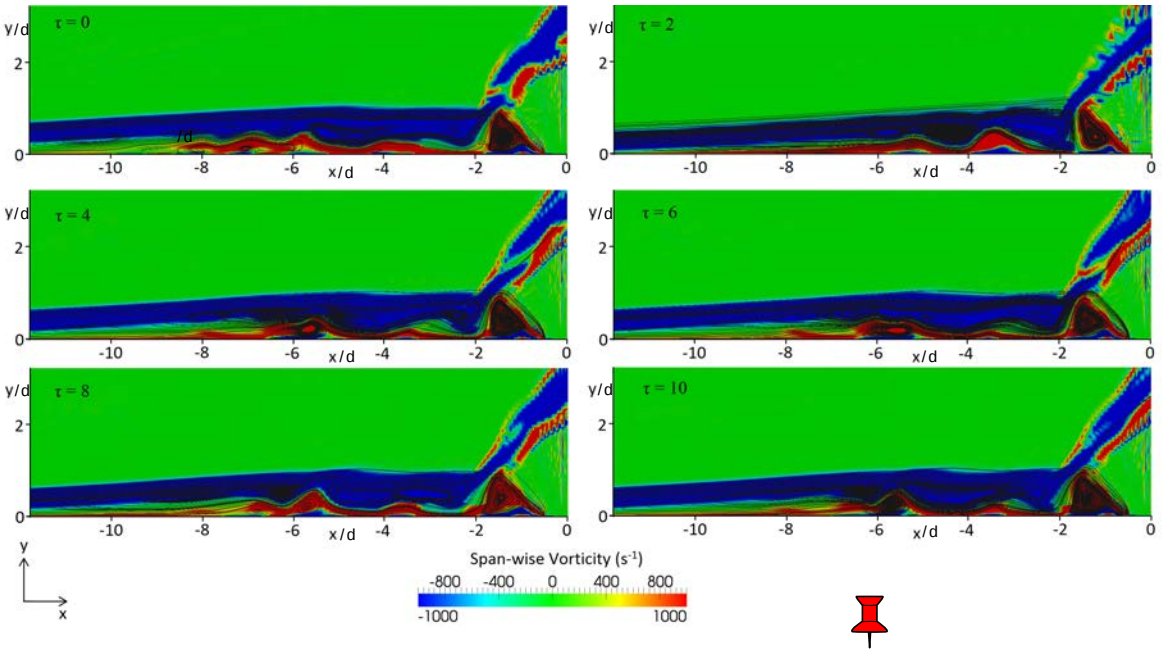

Figure 6.26: Instantaneous span-wise vorticity in the symmetry plane, overlaid with streamlines at successive times, showing temporal evolution of the horseshoe vortex system.

travels upstream and extends far into the span-wise direction. In the instantaneous flow, some of the fluid from the horseshoe vortex system is carried upstream within the boundary layer, back to the point of boundary layer separation. The flow from the upstream vortices remains between the bow shock and separation shock, so does not influence the downstream development of the jet, while flow from Vortex A is entrained within the counter-rotating vortex, as mentioned.

The downward flow from the stagnation point into the re-circulation region (Vortex A) causes the high pressure region immediately upstream of the jet outlet. The orientation of Vortex A is in the opposite direction to the boundary layer vorticity. As a result, the flow is lifted from the plate as it travels downstream around the jet outlet, so the pressure on the plate in the region between the bow shock and the jet outlet reduces in the span-wise direction. As the flow from Vortex A moves around the jet outlet, it moves upward and laterally, until it emerges from the boundary layer and is forced back downward by the free-stream flow accelerating around the jet outlet, and by the suction from the low pressure region behind the jet outlet. This converging flow causes the high pressure region in the plane of symmetry, downstream of the jet outlet, which is clear in the instantaneous flow. This behaviour is observed in Figure 6.28 (a), which shows instantaneous streamlines of flow from Vortex A, overlaid on contours of instantaneous pressure variation, $p'p'$. This high pressure region is elongated in the time-averaged flow (Figure 6.24 (a)), as the convergence point changes with time. The pressure in this area is high, and has high temporal variability. Similar behaviour was also identified by Santiago and Dutton (1997) for a jet in supersonic crossflow with a turbulent boundary layer.

The high pressure region away from the jet centre-line, observed in Figure 6.22, is

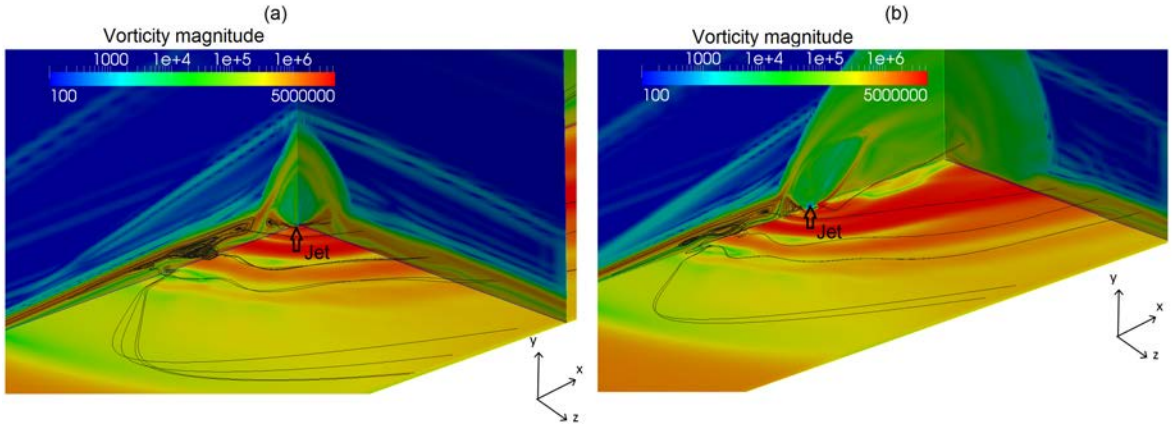

Figure 6.27: Streamlines from horseshoe vortices overlaid on contours of time-averaged vorticity magnitude, with span-wise cutting planes at: (a) jet outlet, and (b) $10d_j$ downstream.

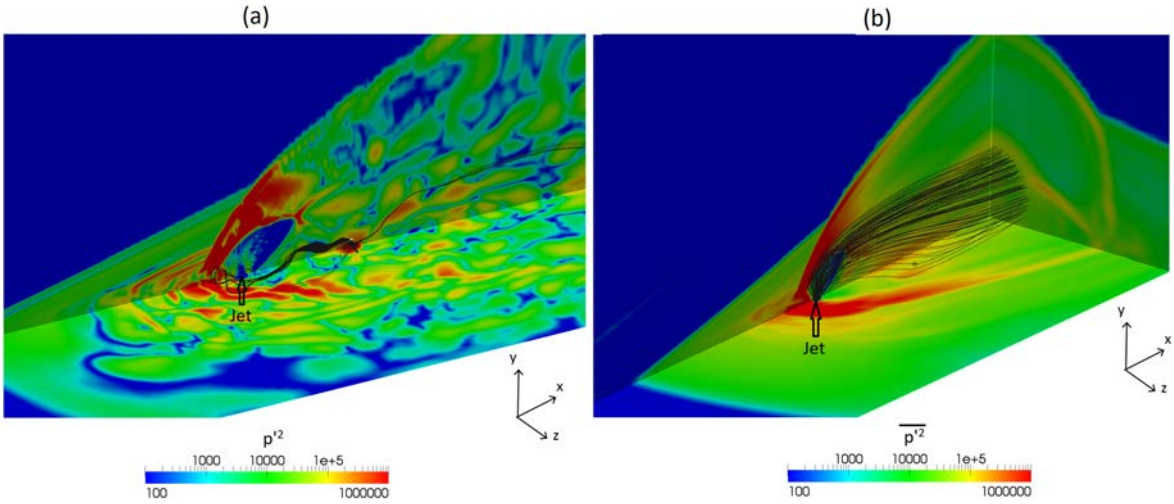

Figure 6.28: Streamlines overlaid on (a) instantaneous pressure variation, $p'p'$, and (b) mean-squared pressure variation, $\overline{p'p'}$, showing flow into regions with high instantaneous pressure.

caused by jet flow. The lateral expansion of the jet and the three-dimensional nature of the barrel shock results in jet flow being deflected downward. Figure 6.28 (b) shows this behaviour in the time-averaged flow. The downward flow in this region causes a slightly elevated mean pressure (see Figure 6.22 (a)), while the unsteady nature of the barrel shocks also makes this a region with large temporal pressure variations (see Figure 6.24 (a)).

6.8 Shear-layer Vortices

The shear-layer vortices are important to the jet force, as the periodic shedding of these vortices induces high pressure regions on the plate, and affects the shape and location of the Mach disk and barrel shock structures. Shear-layer vortices form in the shear-layer between the upstream barrel shock and the bow shock. These vortices do not form immediately at the jet exit, but rather form above the stagnation point, approximately three jet diameters from the outlet. Once formed, the shear-layer vortices initially travel parallel to the leading edge of the jet barrel shock, which is deformed by the presence of the shedding vortices. This behaviour corresponds to the observations of Santiago and Dutton (1997), who observed periodic flattening on the windward side of the barrel shocks. The physics here differs from previous studies, where turbulent in-flow boundary layers were considered (Santiago and Dutton, 1997; Ben-Yakar et al., 2006; Kawai and Lele, 2009; Rana et al., 2011). The laminar boundary layer in this study is thicker, which causes the shear-layer vortices to form much further from the jet outlet, while the hypersonic crossflow causes the vortices, once formed, to be quickly turned and convected downstream with a high velocity. The jet-to-crossflow momentum ratio here ($J = 5.3$) is also higher than previous studies, where $J < 2$.

At small downstream distances ($x/d_j < 3$), the vortices form and appear to travel almost vertically along the leading edge of the jet barrel shock, which is deformed by the presence of the shedding vortices. As shown in Figure 6.29 (a), the convection velocity of the shear-layer vortices is constant in the region $3 < x/d_j < 20$, and has a magnitude of approximately 0.8 U_∞. At large downstream distances ($x/d_j > 20$), this convection velocity increases slightly, to approximately 0.85 U_∞, in agreement with previous work (Gruber et al., 1997; Ben-Yakar et al., 2006).

As the shear-layer vortices convect downstream, they are stretched, compressed, and rotated (Ben-Yakar et al., 2006). The height and width of the vortices were measured in the plane of symmetry, using a threshold value of the Q-criterion of 10^9, with the results shown in Figure 6.29 (b). In this case, the shear-layer vortices all have a similar shape, with an average width approximately equal to the jet diameter, and an average height of approximately $1.5 \times d_j$. One of the five vortices shown reduces in size as it convects downstream, as shown in Figure 6.29 (b), while the other vortices maintain their shape. The contours of the Q-criterion showing these vortices at successive times are shown in Figure 6.30 (an animation is provided in the supplementary material).

The trajectory of the vortices as they convect downstream is shown in Figure

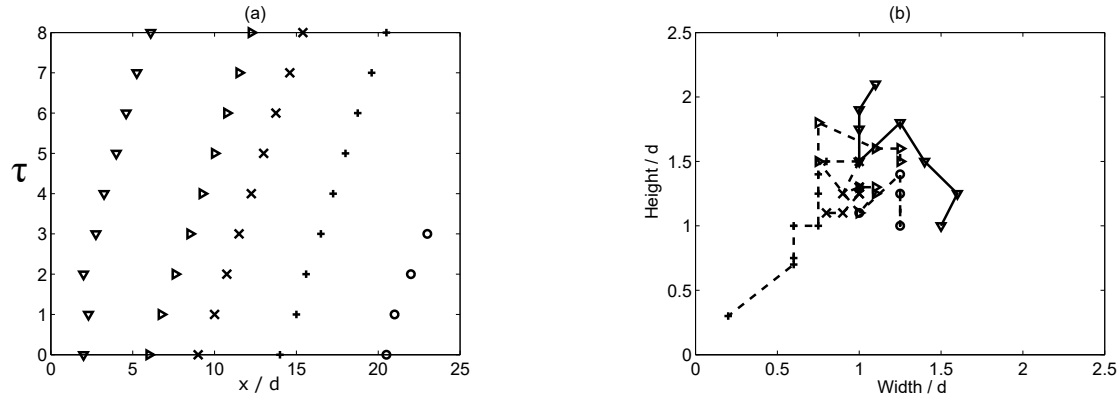

Figure 6.29: (a) Downstream position vs. time, and (b) Shape of identified shear-layer vortices. ○: Vortex 1; +: Vortex 2; ×: Vortex 3; ▷: Vortex 4; ▽: Vortex 5.

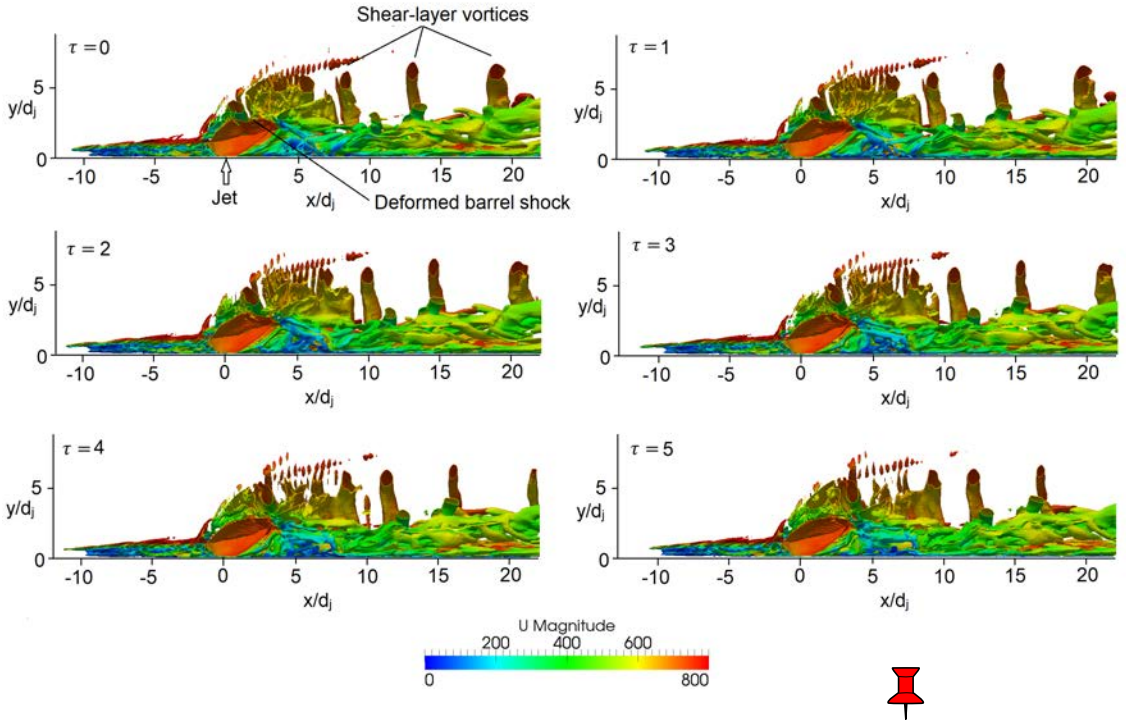

Figure 6.30: Contours of $Q = 10^9$ coloured by velocity magnitude in the plane of symmetry at successive times, showing shear-layer vortex shedding, and deformation of the barrel shock.

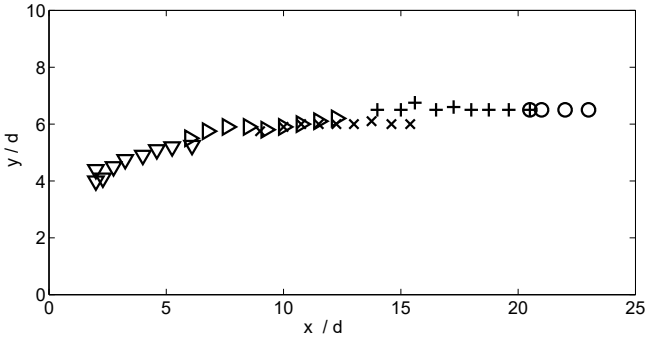

Figure 6.31: Trajectory of identified shear layer vortices. ○: Vortex 1; +: Vortex 2; ×: Vortex 3; ▷: Vortex 4; ▽: Vortex 5.

6.31. Close to the jet, the trajectory has a vertical component, although individual vortices cannot be resolved within 4 jet diameters from the orifice. Far downstream, the trajectory becomes parallel with the freestream flow, in the x direction. The transition from near-vertical motion to near-horizontal motion is rapid, due to the high velocity crossflow.

Under the current conditions, the jet shear-layer vortex shedding frequency is measured as $St_j = f \times d_j/U_j \approx 0.4$, based on the jet outlet diameter and jet velocity. If the Strouhal number is based on the jet diameter and the free-stream velocity, then $St_\infty = f \times d_j/U_\infty \approx 0.17$, which closely corresponds to previous laminar boundary layer simulations at lower supersonic Mach number (Kawai and Lele, 2010). Ben-Yakar et al. (2006) reported $St_j \approx 1$ for a variety of jet injection velocities. However, Ben-Yakar et al. (2006) were able to resolve shear-layer vortices much closer to the jet outlet, within one jet diameter, due to the turbulent in-flow boundary layer and smaller re-circulation region. This highlights the influence of a laminar boundary layer on the physical mechanism for vortex shedding. The shear-layer vortices form further from the jet outlet, and shed at a lower frequency, but remain intact far downstream when the in-flow boundary layer is laminar.

Kawai and Lele (2009) observed shear-layer vortex shedding at $St_\infty \approx 0.4 - 0.6$ with a turbulent in-flow boundary layer in a Mach 1.6 crossflow, with $J = 1.7$. This frequency reduced to $St_\infty = 0.2$ with a laminar boundary layer of equal thickness (Kawai and Lele, 2010). Chai et al. (2015) reported shedding at $St_\infty \approx 0.3$ at the same condition, with a turbulent boundary layer.

In a subsonic crossflow with a turbulent in-flow boundary layer, the oscillation frequency of the horseshoe vortices is much lower than the shedding frequency of the shear-layer vortices (Kelso et al., 1996). The current simulation supports this finding, with shear-layer shedding at $St_\infty = 0.17$ and horseshoe vortex coalescence at $St_\infty = 0.1$. In this case, the frequencies are much closer than those observed in subsonic flow, where horseshoe vortices oscillated with a frequency 40 times lower than the shear-layer vortex shedding frequency (Kelso et al., 1996). The frequency of shear-layer vortex shedding in supersonic crossflow is higher than subsonic crossflow, where values of

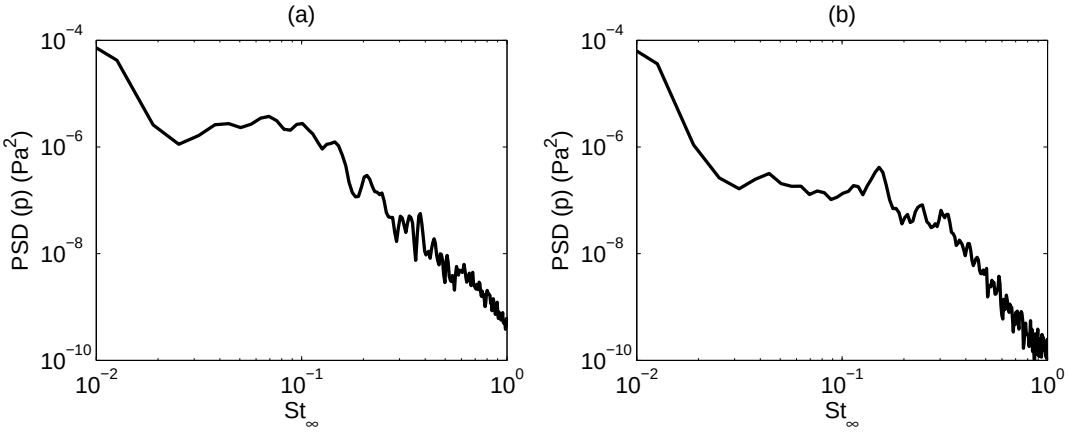

Figure 6.32: Power spectral density (PSD) of pressure signal measured on the flat plate ($y = 0$), on the jet centre-line ($z = 0$) (a) 5 jet diameters upstream, and (b) 20 jet diameters downstream.

$St_j = 0.2$ have been reported (Ruiz et al., 2015).

Further insight into the dominant frequencies can be gained by investigating spectra of the pressure signals. Both span-wise velocity and pressure spectra show peaks at the same frequency, due to strong coupling between the pressure fluctuations inside the re-circulation region, and the dynamics of the shocks accompanying vortex formation (Kawai and Lele, 2010). Figure 6.32 shows the pressure spectra at two locations on the flat plate ($y = 0$), and on the jet centre-line ($z = 0$): inside the upstream re-circulation region ($x/d_j = -5$), and far downstream ($x/d_j = 20$).

In the upstream re-circulation region, there is a series of small peaks in the pressure spectrum. One peak corresponds to horseshoe vortex coalescence at $St_\infty = 0.1$, while other peaks are present at lower frequency. This behaviour differs from previous work (Kawai and Lele, 2010), where a distinct peak was observed in the upstream re-circulation region with a laminar in-flow boundary layer. However, the broad spectrum closely matches data from turbulent in-flow boundary layers (Kawai and Lele, 2010; Chai et al., 2015). Downstream, there is a distinct peak corresponding to the shear-layer vortex shedding, at $St_\infty = 0.17$. This agrees with Chai et al. (2015), and confirms that shear-layer vortex shedding is a significant unsteady component of the flow in the downstream region.

6.9 Counter-rotating Vortex

Previous studies have identified the longitudinal counter-rotating vortex to be a significant contributor to the overall time-averaged pressure distribution, as this vortex structure dominates the interaction in the far-field (Cassel, 2003). The location and strength of this vortex plays a major role in determining the control force, as it is able to influence the pressure on the body over a large area.

The instantaneous and time-averaged counter-rotating vortex structure, 20 jet diameters downstream of the outlet, is shown in Figure 6.33. In the time-averaged

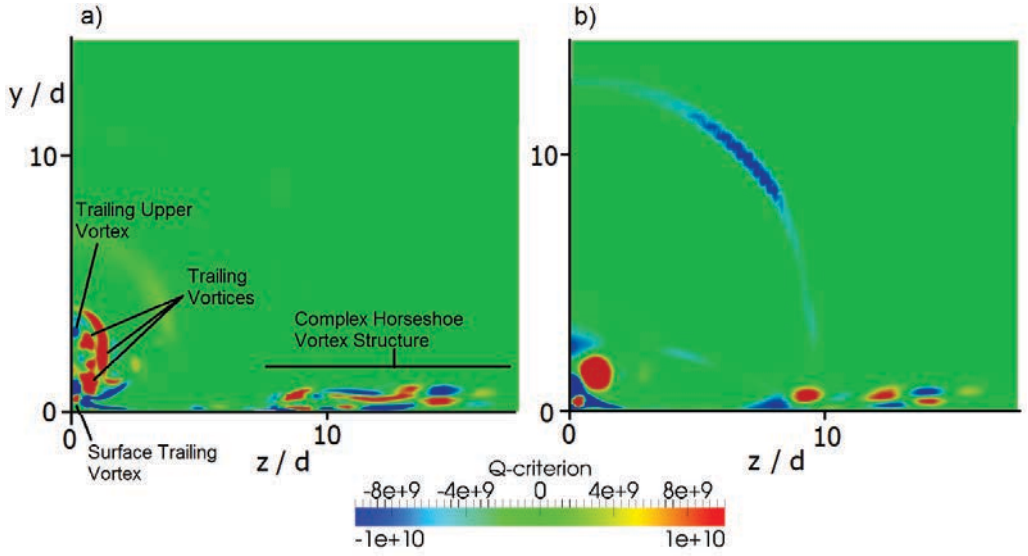

Figure 6.33: Contours of Q-criterion in the $y - z$ plane, perpendicular to the free-stream, 20 jet diameters down-stream of the jet outlet, showing (a) instantaneous, and (b) time-averaged flow structure.

flow, a single stream-wise vortex is the dominant feature. The instantaneous structure consists of a series of trailing vortices, which rotate about a common axis, consistent with previous studies (Viti et al., 2009). The extent of the time-averaged vortex $20d_j$ downstream is approximately $3d_j \times 3d_j$ and is centred at $(y, z) = (2d_j, 2d_j)$. The single, coherent longitudinal vortex is not formed until $x/d_j > 15$, which supports previous findings (Viti et al., 2009). Closer to the jet outlet, the flow is irregular and unsteady, influenced by the bow shock and a series of upright wake vortices, which shed from the leeward barrel shock.

The overall influence of this vortex is to entrain fluid from near the plate, causing an extended region of low pressure far downstream of the jet outlet. This behaviour is consistent with previous studies, and is not strongly influenced by the laminar in-flow boundary layer. The vortex is in closer proximity to the plate when compared with jets in supersonic crossflow with the same momentum ratio, J, due to the higher crossflow velocity.

6.10 Wake Vortices

The final vortex system present in the jet-in-crossflow interaction is the wake vortices. These are upright vortical structures present in the wake region of the instantaneous flow identified in Figure 6.20. Figure 6.34 shows streamlines of flow first being entrained within the horseshoe vortex (Vortex A), then passing laterally around the jet outlet, before being entrained within wake vortices and lifted into the forming stream-wise counter-rotating vortex system. These streamlines are overlaid on contours of instantaneous vorticity magnitude, which shows that the stream-wise vortex is located below a mixing layer, which is located below the shear-layer vortices. This mixing layer

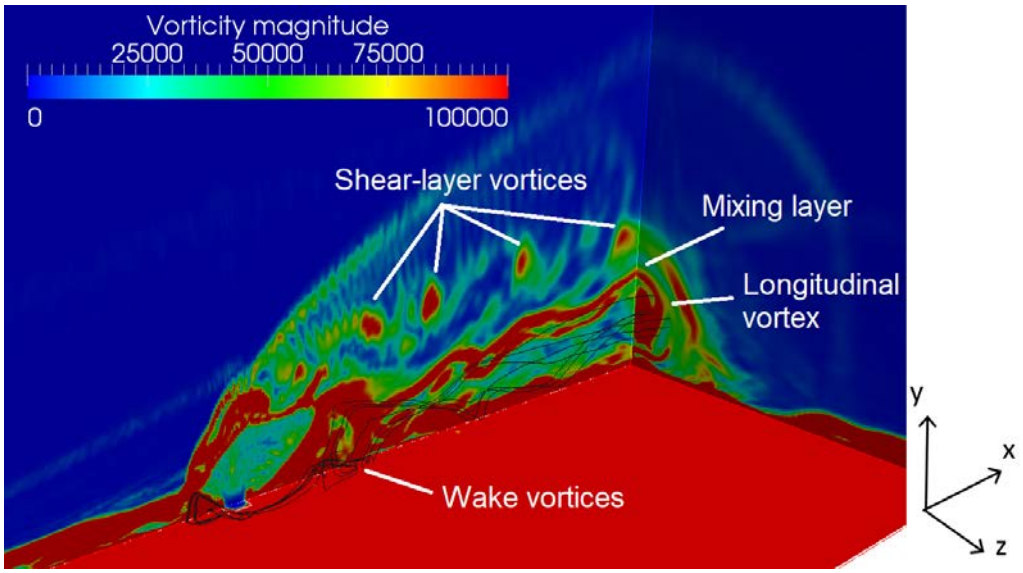

Figure 6.34: Streamlines overlaid on instantaneous vorticity magnitude, showing wake vortices.

formation was observed in previous studies of supersonic jets in crossflow (Chai and Mahesh, 2011; Mahesh, 2013). In the stream-wise direction, wake vortices form between the leeward barrel shock and the re-compression shock, and are most prominent when the jet fluid has completed most of its turning. Additionally, no upright vortices are observed near the jet outlet. These observations agree with previous descriptions for jets in supersonic crossflow with turbulent in-flow boundary layers (van Lerberghe et al., 2000).

In the current simulation, wake vortices of alternating sign develop at $St_\infty \approx 1-1.5$, and are convected downstream with a velocity of approximately 0.5 U_∞. Wake vortices of the same sign develop at $St_\infty \approx 0.5 - 0.7$. Comparing this time-series to the wake vortex shedding regimes outlined in Chapter 2 shows that neither of the conventional regimes apply. In this case, the shedding is more complex and involves breakdown and coalescing of the vortical structures.

As shown in Figures 6.20 and 6.34, upright wake vortices are not observed for $x/d_j > 15$, where the stream-wise counter-rotating vortices dominate the flow-field. In addition, wake vortices are an unsteady phenomenon, and are not present in the time-averaged flowfield (see for example Figure 6.21 (b)).

An alternate view of the wake vortices is provided in Figure 6.35, which shows a time-series of the vertical (y) component of vorticity, in a plane parallel to the flat plate, at a distance of $y/d_j = 1.5$ (an animation is provided in the supplementary material). This highlights the complex, incoherent nature of wake vortex formation, which does not follow a conventional shedding regime, as observed in subsonic crossflow.

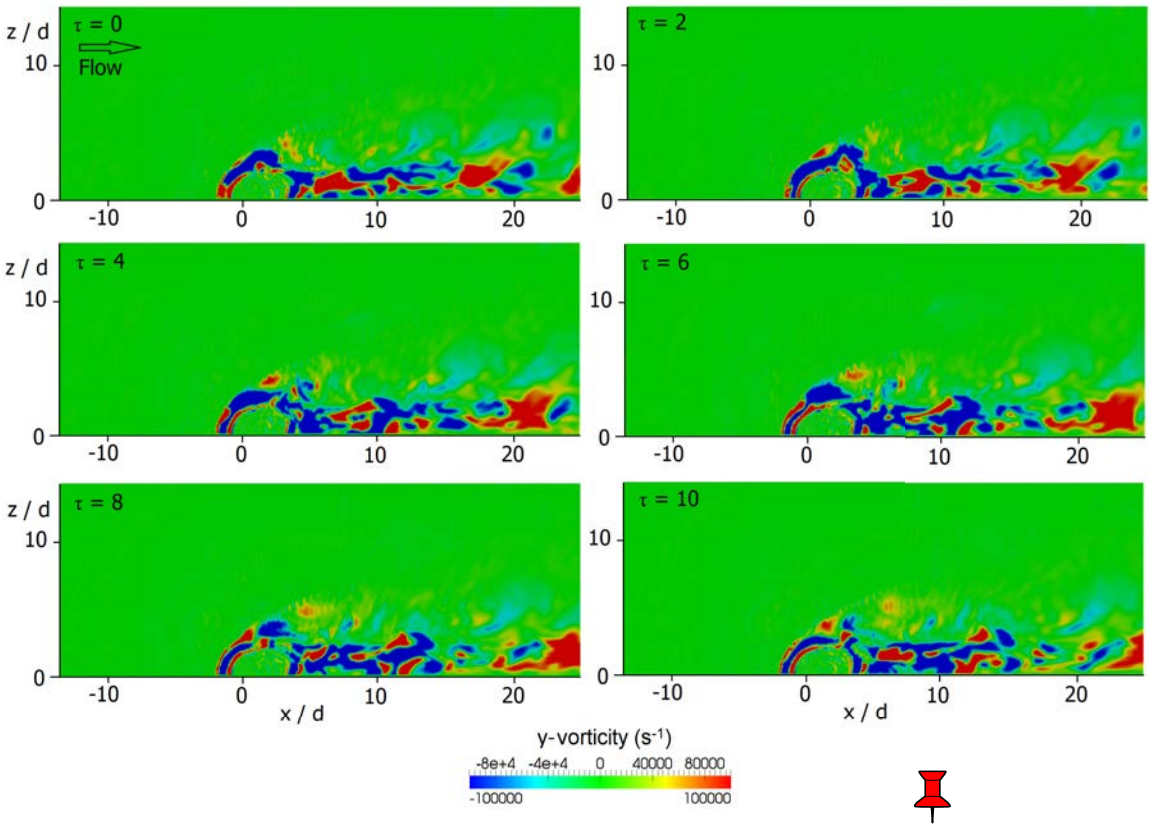

Figure 6.35: Time-series of the vertical (y) component of vorticity at intervals corresponding to $\tau = 2$, showing downstream convection of wake vortices.

6.11 Shock Structure

Figure 6.17 shows the time-averaged shock structure, consisting of a bow shock, barrel shocks, a separation shock, and a Mach disk. A successive series of instantaneous shock structure images are provided in Figure 6.36, at time intervals corresponding to $\tau = 1$ (an animation is provided in the supplementary material). The re-compression shock downstream is unsteady and is not present in the time-averaged flow-field. The downstream reflected shock can be seen to extend from the triple point, where the barrel shock intersects the Mach disk, and impinges on the plate. The slip-line that forms downstream of the triple point generates a mixing layer, as shown previously in Figure 6.34.

In contrast to results at lower Mach numbers (Viti et al., 2009), a short portion of the upstream reflected shock is also visible. The bow shock is the strongest shock in the flow, and is located at the shear-layer between the jet and the free-stream, just upstream of the windward barrel shock. As shown in Figure 6.36, the bow shock is periodically perturbed by shear-layer vortex shedding, as the shear-layer vortices form at the edge of the boundary layer between the bow shock and the barrel shock. With a hypersonic crossflow, the bow shock is in close proximity to the windward barrel shock. As shear-layer vortices form in the small space between the two shocks, both shocks deform concurrently. The formation of the shear-layer vortices can be seen in Figure 6.30, which shows an identical time-series to Figure 6.36 for $0 \leq \tau \leq 3$. Bow

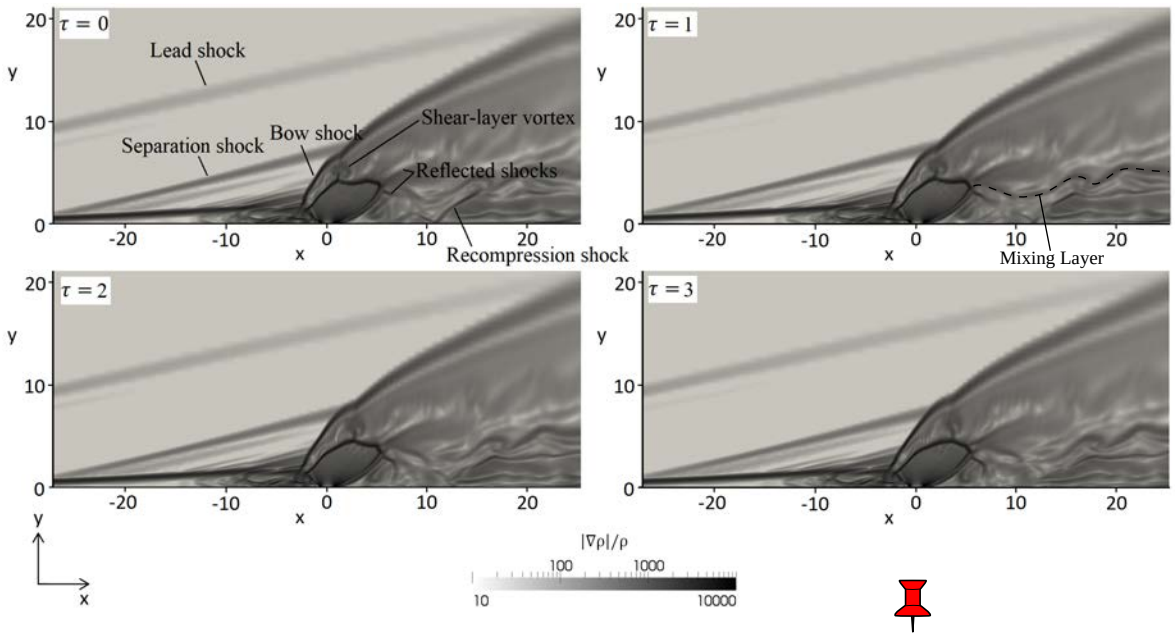

Figure 6.36: Density gradient contours in the plane of symmetry, showing temporal variations in the shock structure.

shock perturbations have been reported previously Kawai and Lele (2009), but the outward motion of this bow shock perturbation is previously unreported.

The deformation of the bow shock is matched by a flattening of the windward barrel shock, which was observed by Santiago and Dutton (1997), and is observed in Figure 6.36 at time $\tau = 0$. The perturbation travels downstream along both the bow shock and the windward barrel shock as the shear-layer vortex convects downstream. A small local shock is also formed, and extends vertically from the sharp intersection of the two straight sections of the deformed windward barrel shock. This local shock also moves downstream with the shear-layer vortex.

During this process, the size and location of the Mach disk varies. The deformation of the windward barrel shock forces the two triple points closer together, and shortens the Mach disk. The Mach disk height, measured from the plate, also changes, and there are corresponding changes in the leeward barrel shock, although this is much steadier and weaker than the windward barrel shock. These fluctuations in Mach disk height result in fluctuations in the height of the mixing layer. As shown in Figure 6.37, two distinct regions of pressure variation correspond to the deformation of the bow shock and windward barrel shock as shear-layer vortices are shed. As the location of the barrel shock and bow shock diverge at larger distances from the jet outlet, the two distinct regions of high variation become apparent. This distinction is also replicated in the pressure variation on the plate (see Figure 6.24 (a)), where the large variations in pressure upstream of the jet outlet splits into two separate components. The variations are caused by the changes in location of the bow shock and windward barrel shocks, as the shear-layer vortices shed.

Another feature of the flow is the motion of the reflected shocks. The size, strength and location of both the windward and leeward reflected shocks change due to the

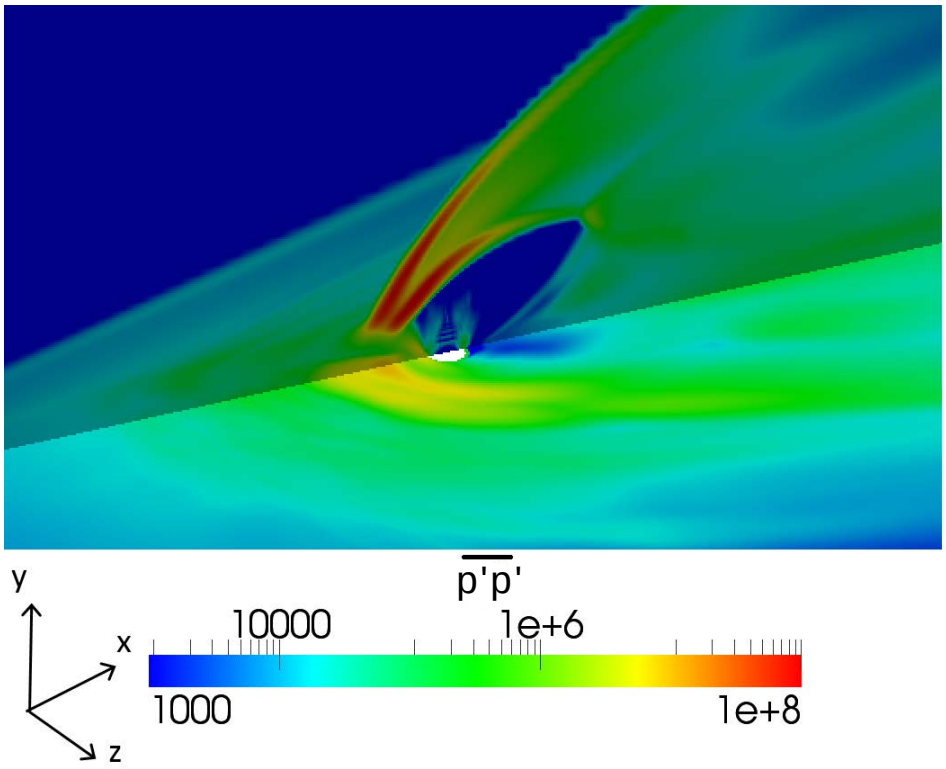

Figure 6.37: Mean-square pressure variations, $\overline{p'p'}$, in the plane of symmetry, due to perturbations in the bow shock and barrel shock, caused by periodic shear-layer vortex shedding.

deformation of the windward barrel shock, and changes to the Mach disk. This behaviour also appears cyclic, as shear-layer vortices are periodically shed.

Close to the jet outlet, the shape of the barrel shocks is steady due to the steady jet in-flow condition. The crossflow has a negligible impact on the jet flow in the immediate vicinity of the jet outlet, due to the in-flow boundary layer. Downstream of the jet, the re-compression shock is present in Figure 6.36 at $\tau = 0$, but is disturbed by the wake flow, and not present at other times, or in the time-averaged flow.

6.12 Jet Force

The total jet interaction force, F, was obtained by integrating the surface pressure, as shown Equation 6.6. The results are provided graphically in Figure 6.38 (a). The force is non-dimensionalised by the jet density, ρ_j, exit area, A_j, and peak velocity, U_j to represent a force coefficient, C_F, as shown in Equation 6.7.

$$F = \int_{Plate} p dA \tag{6.6}$$

$$C_F = \left(1/\rho_j A_j U_j^2\right) \times F \tag{6.7}$$

The time-averaged force due to the laminar flat plate boundary layer, with

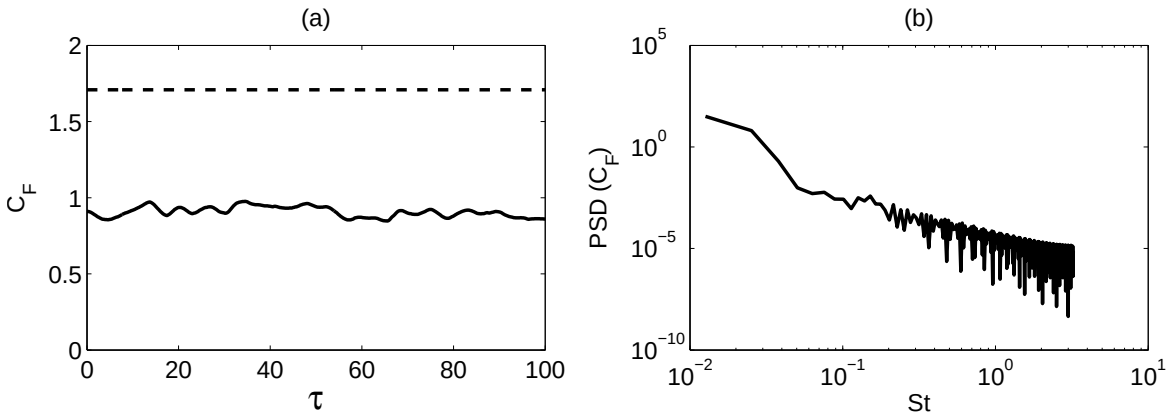

Figure 6.38: (a) Jet interaction force (C_F, Solid line) and jet thrust (C_T, Dash line); and (b) Spectrum of jet interaction force.

the jet off, has been subtracted from the interaction force. The jet thrust, T, is also shown in Figure 6.38 (a), calculated according to the general thrust equation (Equation 6.8, Anderson (2001)), and converted to a coefficient, C_T, in the same manner as Equation 6.7 (see Equation 6.9).

$$T = [\dot{m}_j U_j + A_j (p_j - p_a)] \tag{6.8}$$

$$C_T = \left(1/\rho_j A_j U_j^2\right) \times T \tag{6.9}$$

Note that the interaction force and jet thrust act in opposite directions, the induced interaction force counters the thrust from the jet. Figure 6.38 (a) shows that the interaction force is less than the jet thrust, but is a significant contributor to the overall force. The time-averaged interaction force coefficient, $\overline{C_F} = 0.9$ is 53% of the jet thrust coefficient, $\overline{C_T} = 1.7$.

A spectrum of the unsteady components of the interaction force is shown in Figure 6.38 (b). A small peak is observed at $St_\infty \approx 0.17$, corresponding to the shear-layer vortex shedding. No peak is observed at the horseshoe vortex coalescing frequency of $St_\infty \approx 0.1$, or at the wake vortex shedding frequency of $St_\infty \approx 1 - 1.5$, indicating that the unsteady motion of these vortices is a smaller contributor to the temporal fluctuations in the overall interaction force. The lack of additional peaks in the spectrum indicates that the primary flow features determining the interaction force are the steady features, such as the bow shock, barrel shocks, and the longitudinal vortices within the low pressure region downstream of the jet outlet. Shear-layer vortex shedding has a small influence, due to the deformation of the bow shock and barrel shocks, while the other unsteady flow features, including horseshoe vortices and wake vortices, do not significantly influence the interaction force.

6.13 Conclusions

In this chapter, the interaction between a sonic jet and a hypersonic crossflow over a flat plate with a laminar boundary layer at high jet-to-crossflow momentum ratio has been investigated. The unsteady and time-averaged behaviour of shock and vortex structures in this regime is important, as the dimensions and motion of these structures influence the pressure distribution and control force produced by a reaction control jet.

The results reveal significantly different behaviour of both the horseshoe vortices and shear-layer vortices in comparison to previous studies, where turbulent in-flow boundary layers and lower free-stream Mach numbers were used. The high free-stream Mach number also causes periodic deformation of the bow shock not previously observed. Other shock structures and wake vortices show similar behaviour to previous studies. The locations of the structures and their influence on the control force has been detailed.

The laminar in-flow boundary layer causes a complex horseshoe vortex structure to form in the large region of separated flow upstream of the jet. The horseshoe vortex structure consists of a quasi-steady re-circulation vortex directly upstream of the jet exit, two pairs of co-rotating vortices which periodically coalesce, and an additional quasi-steady vortex. This structure results in a low pressure region immediately upstream of the bow shock.

There is a high pressure region immediately upstream of the jet outlet which wraps around the jet outlet. The pressure is highly unsteady in this region, and variations are driven by the motion of the horseshoe vortex structure, and the movement of the bow shock and barrel shock, corresponding to shear-layer vortex shedding. The development of shear-layer vortices is delayed by the thicker laminar boundary layer in comparison with previous studies, where a thinner turbulent boundary layer was present. Once formed, these vortices shed at lower frequency than in lower Mach number flows, and convect far downstream causing fast moving, localised high pressure regions on the plate.

A complex and unstructured series of wake vortices is observed in the region between the leeward barrel shock and the re-compression shock. Wake vortices form in a region of low pressure and have a high shedding frequency, with little influence on the control force.

The close proximity of the bow shock to the windward barrel shock means that the bow shock is deformed by the development and convection of shear-layer vortices. Periodic deformation of the windward barrel shock and formation of a local shock matches previous observations; however, the subsequent deformation of the bow shock has not previously been reported.

Chapter 7

Unsteady Jet in Hypersonic Crossflow

The aim of this chapter is to gain an in-depth understanding of the time dependent flow physics of unsteady, pulsed reaction control jets in hypersonic crossflow. This chapter is based on the work published in: Miller, W., P. Medwell, C. Doolan, and M. Kim. "Numerical investigation of a pulsed reaction control jet in hypersonic crossflow". *Physics of Fluids* Vol. 30, 106108 (2018).

Reaction control jets operated at high frequency are analogous to pulsed jets in crossflow. As highlighted in Chapter 2, pulsed jets exhibit several unique phenomena, including increased penetration, at certain flow conditions. The flow conditions for each case are described in Section 7.1, while the shock and vortex structures are investigated in Section 7.2. Jet penetration is considered in Section 7.3, where pulsed jet results are compared with steady injection. The induced surface pressure, and jet interaction force for pulsed jets are outlined in Section 7.4. Conclusions regarding the unsteady behaviour of pulsed jets in hypersonic crossflow are provided in Section 7.5.

7.1 Flow Conditions

The simulations in this chapter utilise the numerical scheme described in Chapter 4. The free-stream flow conditions and simulation geometry are based on those measured experimentally by Erdem (2011), and are identical to those investigated in detail in Chapter 6. Free-stream flow conditions were shown in Table 6.1 and a schematic of the geometry was presented in Figure 6.1. Based on the outcomes of the mesh verification study presented in Chapter 6, the intermediate mesh was used in all cases described in this chapter.

The jet was pulsed by modulating jet out-flow static temperature, pressure, and velocity at high frequency, using an ideal square waveform. A square waveform was identified as the best waveform for increased penetration for low velocity ratio jets in a subsonic crossflow (Karagozian, 2014). Sau and Mahesh (2010) indicated that the flow-field does not differ appreciably between ideal square waveforms and imperfect

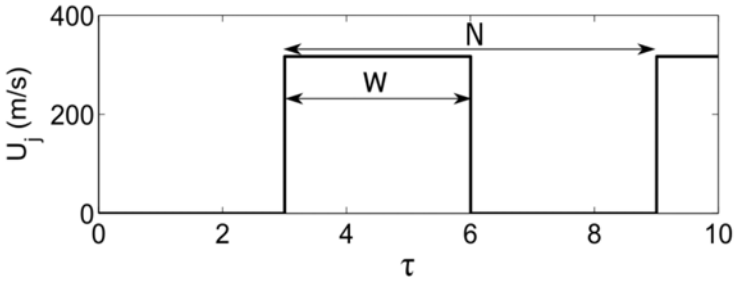

Figure 7.1: Waveform for pulsed jet Case I ($\alpha = 0.5$, $St_\infty = 1/6$).

square waves produced experimentally, so an ideal square waveform was used in this work. The waveform for Case I is provided in Figure 7.1.

Only fully modulated jets were considered. Jet velocity, U_j, was set to zero when the pulse is off, and 317 m/s (corresponding to Mach 1 with $T_j = 250$ K) in a top-hat profile when the pulse is on. When the jet is on, static temperature, pressure, and velocity are specified explicitly at the jet inlet, corresponding to a pressure ratio, p_{0j}/p_∞, of 251, and a momentum ratio, J, of 5.3. Pulse frequency, f, may be non-dimensionalised using the free-stream velocity, U_∞, and the nozzle exit diameter, d_j. This yields the Strouhal number, $St_\infty = f \times d_j/U_\infty$. Similarly, time is non-dimensionalised using $\tau = t \times U_\infty/d_j$. Duty-cycle, α, is defined as the ratio of pulse width, w, to the pulsing time period, N ($\alpha = w/N$), as shown in Figure 7.1. The jet Reynolds number, based on peak jet velocity (i.e. jet velocity when the jet is switched on), U_j, and jet diameter, d_j, Re_j, is 88.5×10^3 for all simulations in this chapter. As described in Chapter 4, only perfect gases are considered, and viscosity is calculated using Sutherland's law.

Jet pulsing profiles can be characterised by three parameters: frequency, St_∞, duty-cycle, α, and stroke ratio, L/D, defined as a column of fluid with length L ejected through a nozzle with exit diameter D. Previous studies have shown that the pulsed jet interaction has a strong dependence on duty-cycle (Johari et al., 1999) and therefore stroke ratio. At a given pulsing frequency, an increase in duty-cycle corresponds to an increase in L/D. Similarly, an increase in pulsing frequency at constant duty-cycle corresponds to a decrease in L/D. Therefore, only two of the three variables are required to completely characterise the jet pulse. However, changes in frequency, duty-cycle, and stroke ratio affect the flow in different ways, so it is important to consider all three variables.

Strouhal numbers for pulsing were selected based on analysis of the natural shear-layer vortex shedding frequency for steady injection in Chapter 6, which was $St_\infty = 1/6$. For the current configuration, with $U_\infty = 790$ m/s and $d_j = 2$ mm, this results in a dimensional frequency of 66 kHz. When scaled to a large hypersonic vehicle, such as the full-size GHAME (White et al., 1992), or the Space Shuttle (Chazen and Sanscrainte, 1974), the dimensional frequency is approximately $100 - 1000$ Hz.

Table 7.1 lists the pulsed jet simulations performed in this chapter. Case I has 50% duty-cycle at $St_\infty = 1/6$, corresponding to $L/D = 1.2$. Case II has a reduced duty-cycle, 33%, at $St_\infty = 1/6$, while Case III has an increased frequency, $St_\infty = 1/3$, while

Table 7.1: Simulations performed for pulsed jet cases.

Case	Duty-cycle, α (%)	Frequency, St_∞	Stroke ratio, L/D
Steady	100	0	∞
I	50	1/6	1.2
II	33	1/6	0.8
III	50	1/3	0.6
IV	75	1/4	1.2

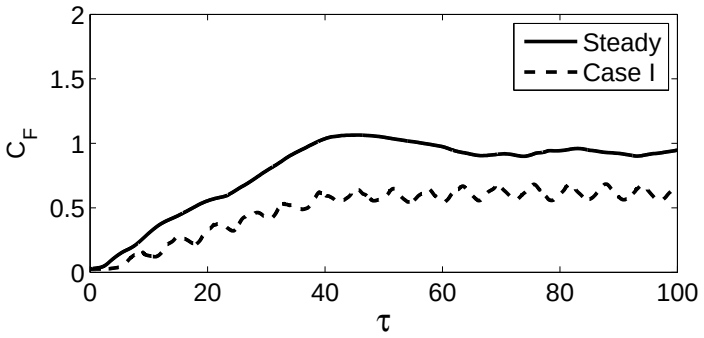

Figure 7.2: Temporal convergence of the jet interaction force coefficient, C_F, to a quasi-steady state. Solid line: Steady jet, Dash line: Pulsed Case I.

retaining the 50% duty-cycle of Case I. Finally, Case IV has the same stroke ratio as Case I, which is achieved at a higher duty-cycle of 75%, corresponding to a frequency of $St_\infty = 1/4$.

The simulation was initialised without the jet present and run at a CFL number of 0.2, corresponding to time-steps of $\tau \approx 0.003$, or $t \approx 7.8 \times 10^{-9}$ s, for $\tau = 200$, or 2.4 total domain flow-through times, to allow a steady laminar in-flow boundary layer to be established on the plate before initiation of the jet. Results in this chapter correspond to pulsed jet simulations in the quasi-steady phase, once the jet is fully established. This required an additional $\tau \approx 60$ (≈ 0.7 domain flow-through times, or 2.2 flow-through times from the jet inlet to the domain outlet) to allow a quasi-steady state to establish. Quasi-steady state was defined by convergence of the jet interaction force coefficient, C_F, defined as the integrated pressure over the flat plate with the jet on, minus the time-averaged force due to the laminar flat plate boundary layer, as shown in Figure 7.2. The jet interaction force coefficient converges over a longer time period than individual pressure probes. Start-up results for the pulsed jet during the period $0 < \tau < 60$ are provided in Chapter 8.

The validity of the mesh resolution study was re-affirmed by comparing pulsed jet results on the intermediate mesh with those generated on the fine mesh and full 3D mesh, described in Chapter 6. The high frequency pulsing case (Case III) was run with the full 3D mesh to investigate removing the symmetry boundary condition in the jet centre-line. A high degree if symmetry was maintained in both the instantaneous and time-averaged pulsed jet flow-fields, as shown in Figures 7.3 and 7.4, which show

velocity statistics at the outlet, and pressure statistics on the flat plate respectively. The high degree of symmetry in the full 3D case means that the use of a symmetry plane is valid. Further confirmation is provided by a direct comparison of the flow-fields, between the full 3D mesh and the intermediate mesh, as shown in Figures 7.5 and 7.6.

Figure 7.5 shows that the instantaneous and time-averaged velocity fields are unchanged when a symmetry boundary condition is applied, while Figure 7.6 (a) shows that the time-averaged pressure fields are also very similar between the full mesh and half mesh cases. Pressure fluctuations are shown in Figure 7.6 (b), and are also very similar in the jet region, and downstream of the jet. The pressure fluctuations differ far upstream of the jet, within the re-circulation region, with higher fluctuations observed to penetrate further upstream in the full 3D mesh case. However, this discrepancy is limited to the upstream re-circulation region where pressure fluctuations are small, and does not affect the near-field and downstream regions of the jet interaction flow-field.

The mesh resolution was confirmed by running the pulsed jet Case I on the fine mesh (15.5M cells, as described in Chapter 6). Qualitatively, the overall flow-field is very similar, as shown in Figures 7.7 and 7.8. The time-averaged pressure distribution on the flat plate shows some differences in upstream separation location, which was also observed in the steady jet case, while the pressure variation and shock structures are very similar between the current mesh and the fine mesh. Quantitatively, the time-averaged Mach disk height is 3.0 mm for both cases, indicating that the near-field shock structure is correctly captured. In the downstream wake region, the same shock structures are captured, and resolution is increased on the fine mesh. Therefore, the use of the intermediate mesh from Chapter 6 is justified.

7.2 Flow Structure

Figure 7.9 shows instantaneous contours of span-wise (z) vorticity in the plane of symmetry ($z = 0$), and compares the steady jet with pulsed jet operation. In the steady case (Figure 7.9 (a)), the naturally occurring hair-pin type shear-layer vortices are shed at a frequency corresponding to $St_\infty = 1/6$, as described in Chapter 6. For the pulsed Case I ($\alpha = 0.5$, $St_\infty = 1/6$, see Figure 7.9 (b)), the jet is forced at the same frequency. As a result, the shear-layer vortex shedding occurs once for each jet pulse, and the strength and separation of the shear-layer vortices are similar to the steady case. However, there are differences in the shape of the shear-layer vortices. In the steady case, the vortices are approximately circular in the plane of symmetry, with a radius approximately equal to the jet diameter. Compared to the steady case, the vortices in the pulsed Case I are elongated in the stream-wise (x) direction. The shear-layer vortex elongation is caused by the motion and interaction of shocks. Similar to the steady jet, in the pulsed case the shear-layer vortices are not observed near the jet outlet; vortex formation is delayed by the presence of the thick, laminar in-flow boundary layer and large upstream re-circulation region. The slip line that forms

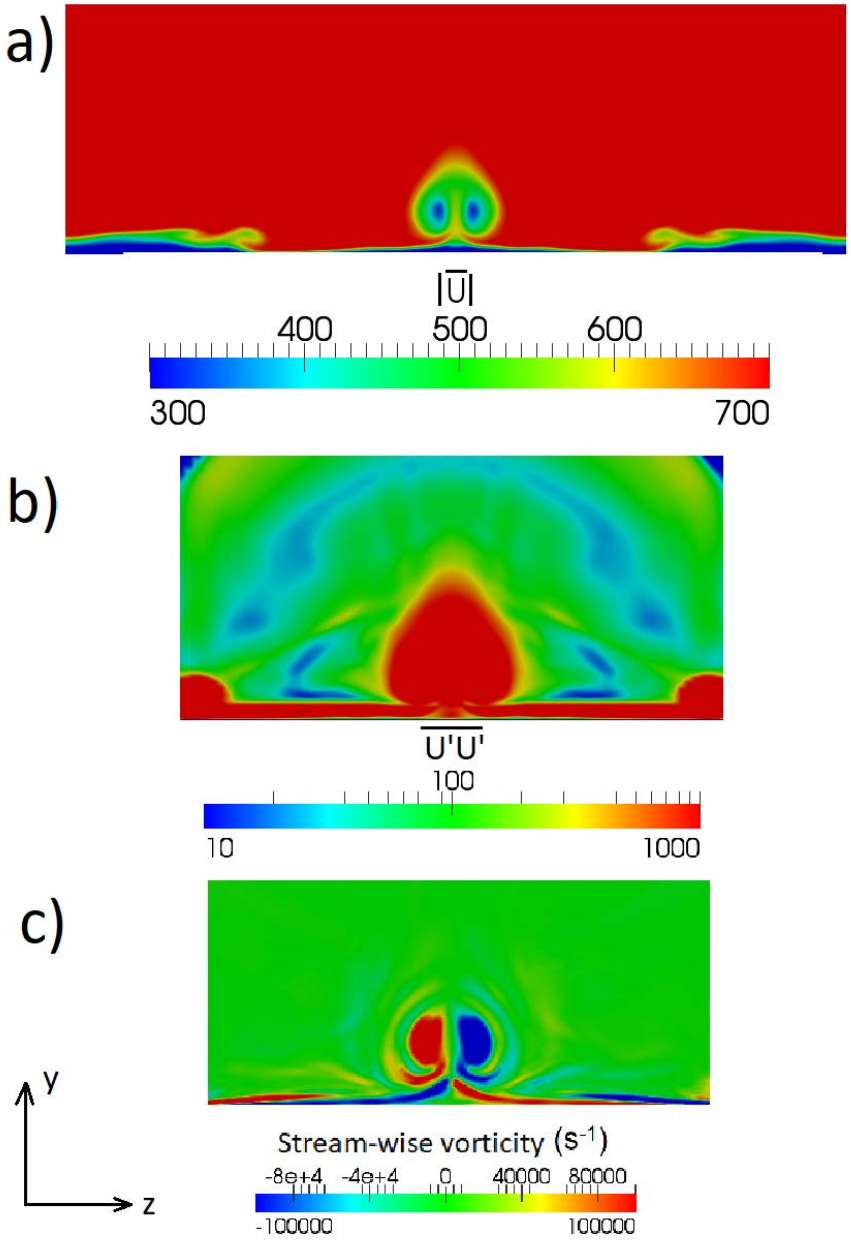

Figure 7.3: Velocity statistics at the outlet of the full 3D mesh. (a) Time-averaged velocity, $\overline{U}$, (b) mean-square velocity variation, $\overline{U'U'}$, and (c) span-wise vorticity.

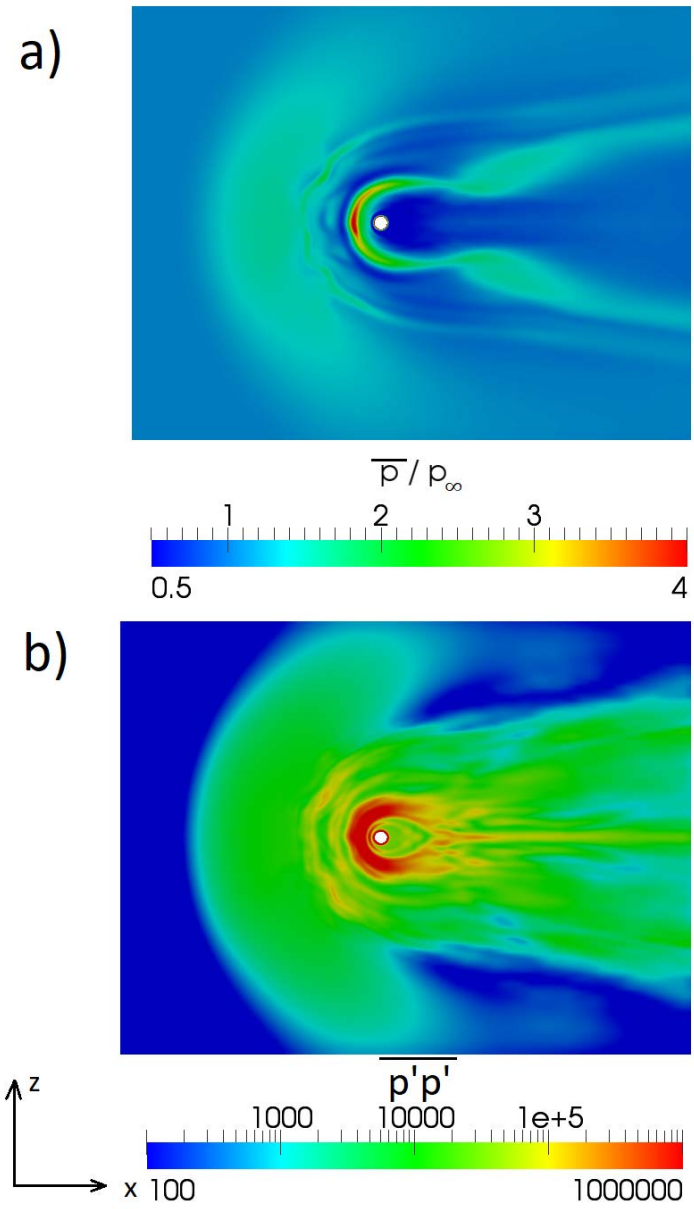

Figure 7.4: Pressure statistics on the flat plate of the full 3D mesh. (a) Time-averaged pressure, $\overline{p}$, and (b) mean-square pressure variation, $\overline{p'p'}$.

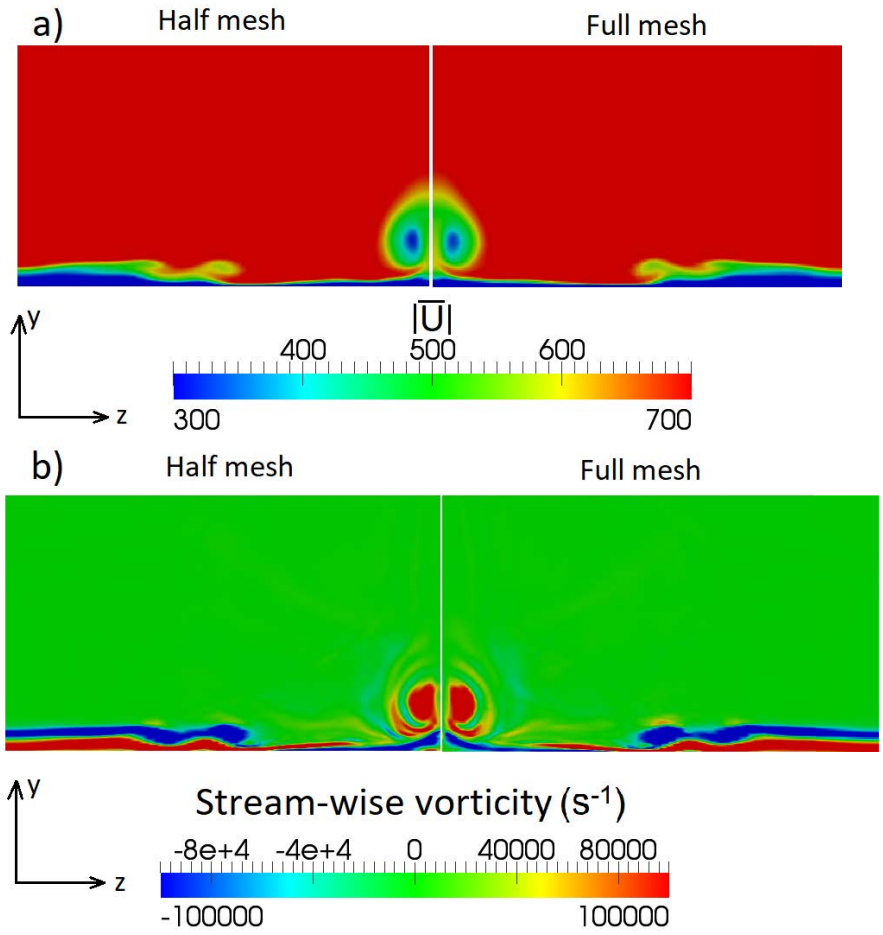

Figure 7.5: Velocity statistics at the outlet, comparing the full 3D mesh with the intermediate mesh. (a) Time-averaged velocity, $\overline{U}$, and (b) span-wise vorticity.

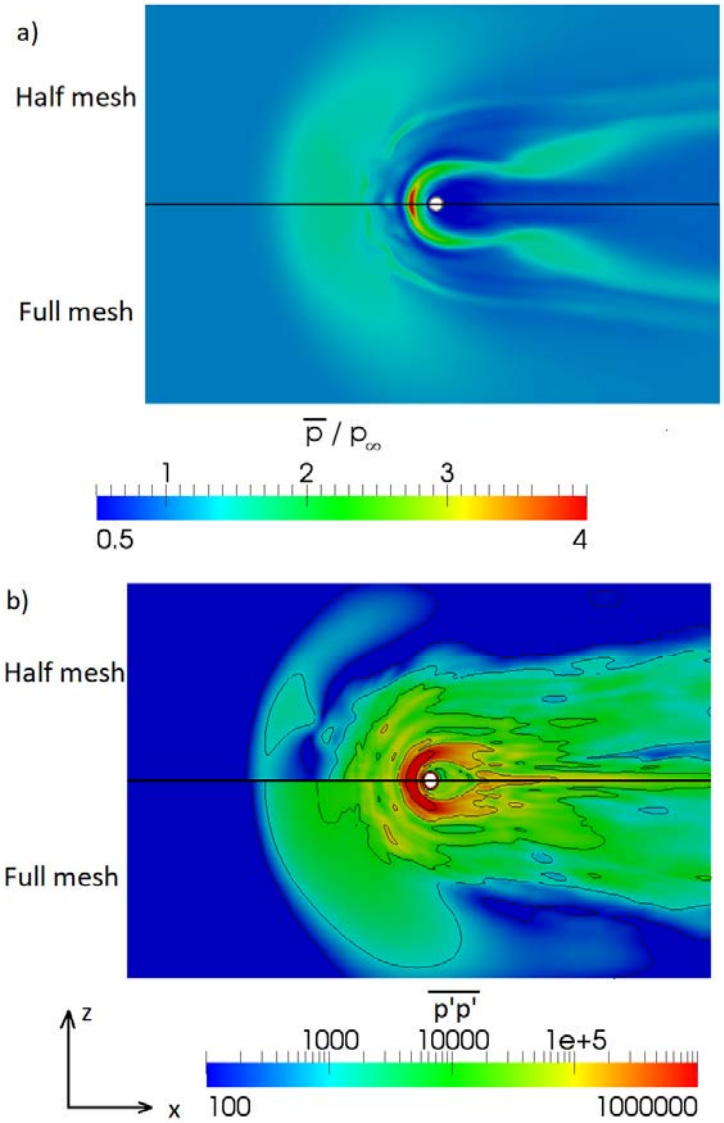

Figure 7.6: Pressure statistics on the flat plate, comparing the full 3D mesh with the intermediate mesh. (a) Time-averaged pressure, $\overline{p}$, and (b) mean-square pressure variation, $\overline{p'p'}$, overlaid with contours at $\overline{p'p'} = 10^2$, 10^3, 10^4, 10^5, and 10^6.

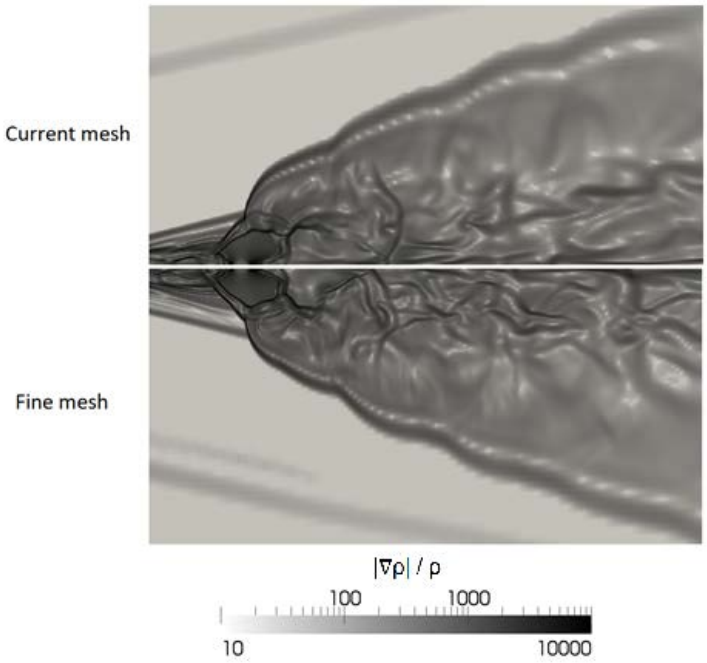

Figure 7.7: Density gradient contours in the plane of symmetry for the intermediate and fine mesh.

downstream of the Mach disk forms a shear-layer in the steady case, beneath the shear-layer vortices, but above the longitudinal counter-rotating vortices. This slip line is clearly shown in Figure 7.9 (a), and is periodically deformed by the shear-layer vortex shedding, as described in Chapter 6. The periodic deformation of this shear-layer becomes more pronounced in the pulsed case, where the periodic collapse of the shock structure when the jet is off allows entrainment of the free-stream flow, which disrupts and breaks down this shear-layer. In the pulsed cases, every jet pulse forces a lead shock into the flow, analogous to a jet in quiescent atmosphere (Radulescu and Law, 2007). Therefore, with pulsing frequencies at or above the natural shear-layer vortex shedding frequency, such as the cases considered in this chapter, there is a lead shock that separates each successive shear-layer vortex. A secondary shear-layer is formed due to triple points that form at the intersection of these successive lead shocks and the flat plate boundary layer, due to Mach reflection. However, this secondary shear-layer is not clearly observed in the pulsed Case I, as it is also disrupted by the entrainment of free-stream flow during the jet-off time period in this case. The Mach reflection of the lead shocks from the flat plate boundary layer cause the boundary layer to separate down-stream of the jet outlet. This separation can be observed for $x/d_j > 10$ in Case I in Figure 7.9 (b).

The instantaneous span-wise vorticity contours for Case II ($\alpha = 0.33$, $St_\infty = 1/6$) are shown in Figure 7.9 (c). In this case the pulsing frequency is the same as Case I and the duty-cycle is reduced from 50% to 33%, resulting in a shorter stroke ratio and longer jet-off time period. This shorter pulse results in larger, weaker shear-layer vortices than either the steady case, or the case with a 50% duty-cycle (i.e. Case I). The

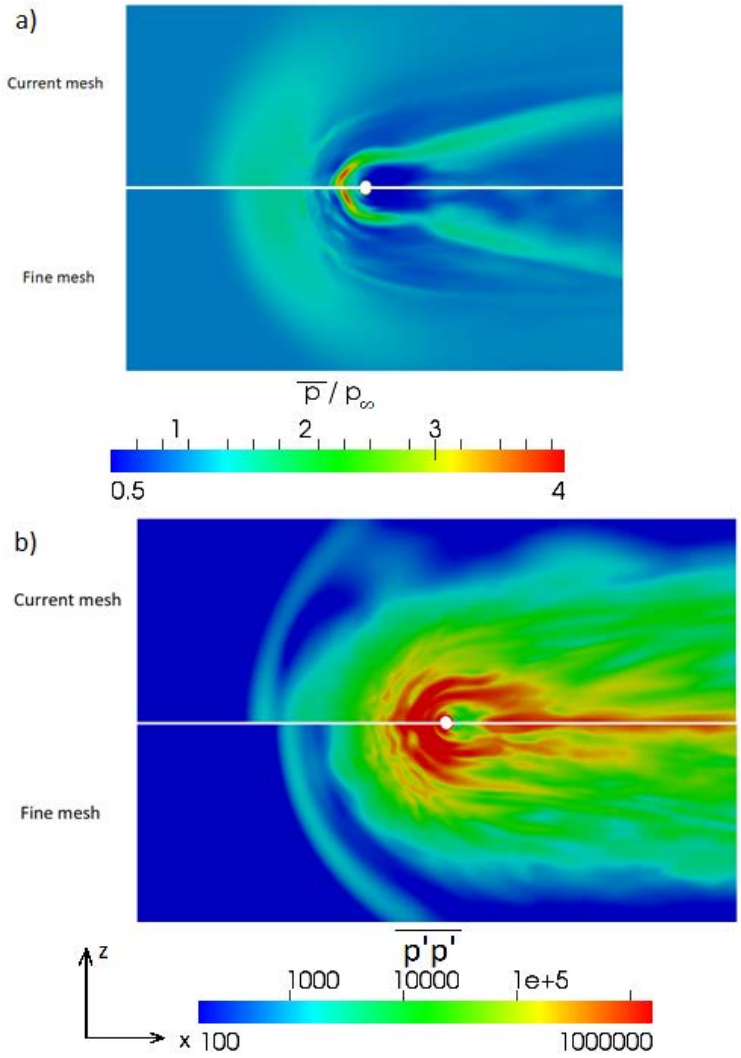

Figure 7.8: Pressure contours on the flat plate for the intermediate and fine mesh. (a) Time-averaged pressure, $\overline{p}$, and (b) mean-square pressure variation, $\overline{p'p'}$.

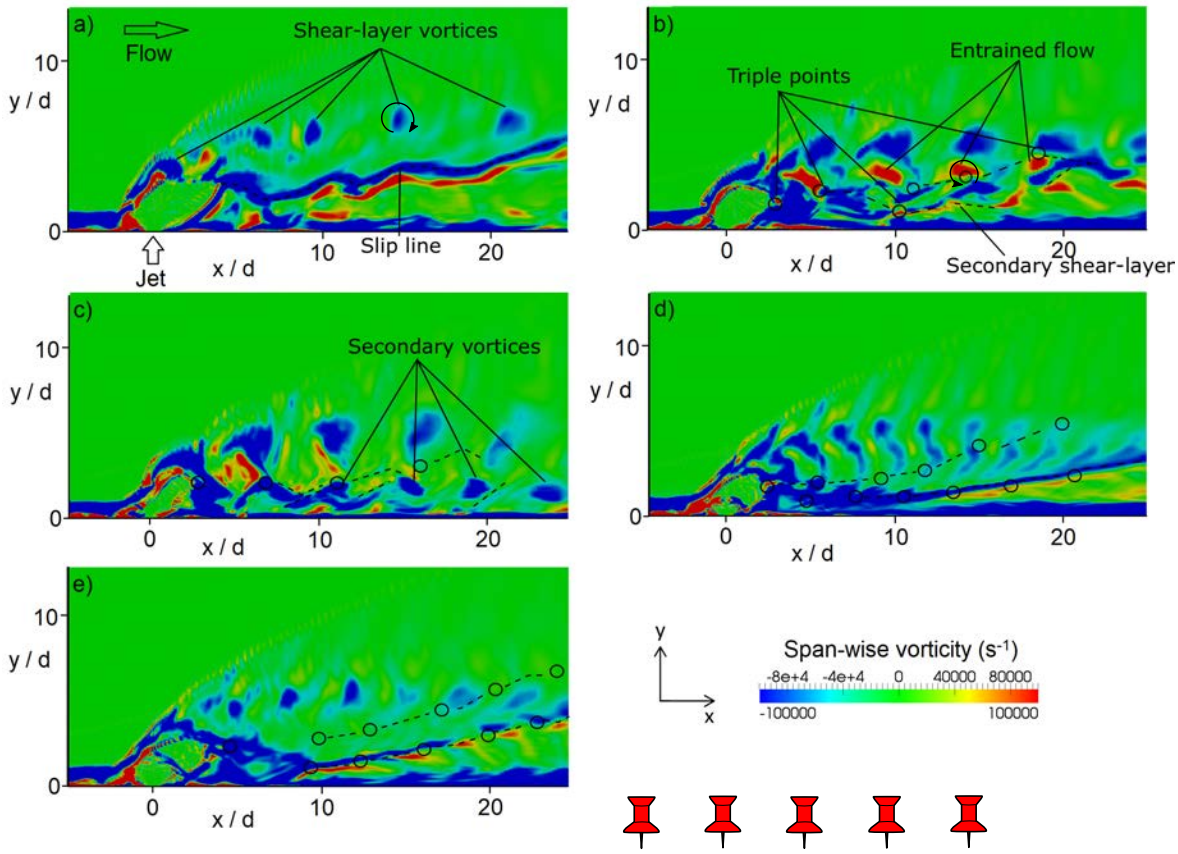

Figure 7.9: Contours of instantaneous span-wise vorticity at jet startup ($\tau = 0$) in the plane of symmetry, for (a) Steady jet, (b) Pulsed jet (Case I, $\alpha = 0.5$, $St_\infty = 1/6$), (c) Case II ($\alpha = 0.33$, $St_\infty = 1/6$), (d) Case III ($\alpha = 0.5$, $St_\infty = 1/3$), and (e) Case IV ($\alpha = 0.75$, $St_\infty = 1/4$).

shear-layer vortices are shed at the same frequency as the previous cases, at $St_\infty \approx 1/6$, but are not circular, they are elongated in the vertical (y) direction. The longer jet-off time period results in increased entrainment of the free-stream flow. The free-stream flow penetrates through the jet wake and breaks-up both the shear-layer downstream of the Mach disk, and the secondary shear-layer where the lead shocks interact with plate. The break-up of the secondary shear-layer prevents separation of the flat plate boundary layer, and results in a roll-up of vorticity which coincides with the location of the lead shocks. As a result, at large downstream distances ($x/d_j > 10$) the secondary shear-layer resembles a set of span-wise vortices in the jet centre-line that co-rotate with the jet shear-layer vortices. These are labelled as secondary vortices in Figure 7.9 (c).

The weakening and vertical elongation of shear-layer vortices observed in Case II is accentuated when the pulsing frequency is increased and stroke ratio is decreased in Case III ($\alpha = 0.5$, $St_\infty = 1/3$), as shown in Figure 7.9 (d). Weaker shear-layer vortices are formed due to the shorter pulse length. With the increased pulsing frequency, the vortices are shed at higher frequency, at $St_\infty \approx 1/3$, and are highly elongated in the vertical direction. In this case, the high frequency pulsing prevents formation of a distinct shear-layer behind the Mach disk. However, the secondary shear-layer is clearly observed at $x/d_j > 10$. In this case, the secondary shear-layer is enhanced by interaction between lead shocks and the reflection of the lead shock from the previous pulse from the flat plate. This forms a series of triple points and slip lines which merge into a consistent, quasi-steady thin shear-layer. This interaction is most pronounced when the lead shocks are close together, which is a result of high pulsing frequency. The short jet-off time also reduces the entrainment of the free-stream, allowing the formation of the quasi-steady secondary shear-layer, and separation of the flat plate boundary layer.

Case IV ($\alpha = 0.75$, $St_\infty = 1/4$) has a stroke ratio equal to Case I, which is achieved using a higher frequency and a higher duty-cycle, and therefore a short jet-off time. The higher pulsing frequency results in higher frequency shear-layer vortex shedding, at $St_\infty \approx 1/4$, and lead shocks that are closer together than Cases I and II. The vortices are a similar size to the steady case, as the stroke ratio was set to match the natural shear-layer vortex shedding (see Figure 7.9 (e)). As with previous pulsed cases, no distinct shear-layer is observed downstream of the Mach disk. The close proximity of consecutive lead shocks, resulting from increased pulsing frequency and reduced jet-off time, again results in a prominent, quasi-steady secondary shear-layer forming around $x/d_j > 10$, with a separated boundary layer, similar to Case III. The spurious oscillations observed in Figure 7.9 are confined to regions of high velocity gradient, and are independent of the choice of limiter and mesh resolution. These are numerical artifacts, and do not impact the large-scale structures which are the focus of the current work.

Previous studies have indicated that, for high velocity ratio subsonic jets in a subsonic crossflow, interaction between shear-layer vortex rings occurs at high duty-cycle ($\alpha > 0.5$, Sau and Mahesh (2010)). This interaction reduces the mixing and

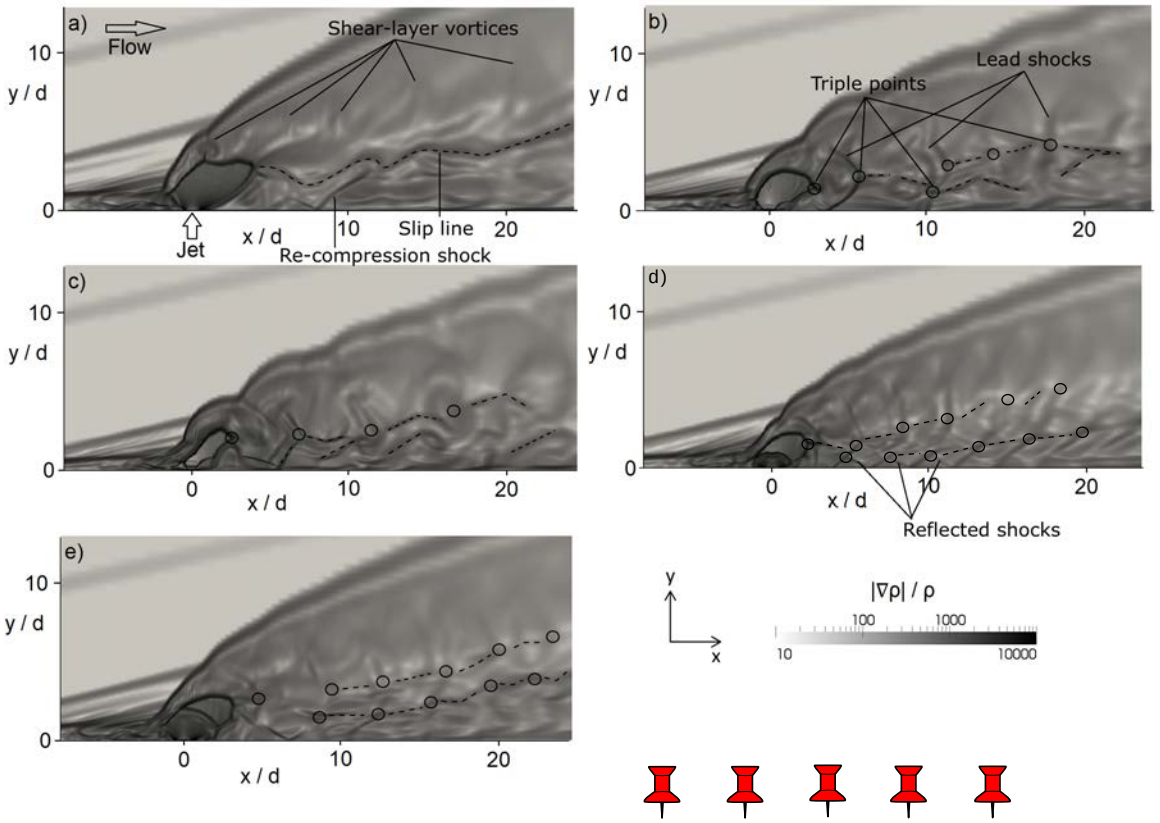

Figure 7.10: Contours of instantaneous density gradient magnitude at jet startup ($\tau = 0$) in the plane of symmetry, for (a) Steady jet, (b) Pulsed jet (Case I, $\alpha = 0.5$, $St_\infty = 1/6$), (c) Case II ($\alpha = 0.33$, $St_\infty = 1/6$), (d) Case III ($\alpha = 0.50$, $St_\infty = 1/3$), and (e) Case IV ($\alpha = 0.75$, $St_\infty = 1/4$).

penetration effectiveness of the pulsed jet at high duty-cycles. In the case of a low velocity ratio sonic jet in a supersonic crossflow, the beginning of each pulse forces a strong lead shock into the flow, in front of the vortex ring, as described previously, and therefore a lead shock separates each successive shear-layer vortex. This shock prevents any interaction between shear-layer vortices. Further, in the low velocity ratio regime, hair-pin type vortices form rather than vortex rings. As a result, the shear-layer vortex formation is not strongly dependent on duty-cycle for high frequency pulsing in supersonic crossflow.

Figure 7.10 compares the shock structure, via contours of $|\nabla\rho|/\rho$, of a steady jet with a pulsed jet. The series of lead shocks can be observed in the pulsed cases, between the shear-layer vortices. This is an important difference between subsonic and supersonic crossflow. The shocks prevent interaction between shear-layer vortices, which may explain the discrepancy in observations between supersonic crossflow (Shi et al., 2016; Williams and Moeller, 2016) and subsonic crossflow (Karagozian, 2014; Gevorkyan et al., 2016). The shock interactions also drive the formation of the secondary shear-layer, through the formation of shock triple points, as described previously.

In the steady case, periodic deformation of the bow shock can be observed,

corresponding to shear-layer vortex shedding, as described in Chapter 6. In the pulsed Case I, this deformation is accentuated as the bow shock and barrel shocks collapse when the jet is off. This effect is further amplified when duty-cycle is decreased, as shown in Figure 7.10 (c) (Case II), but is reduced for longer duty-cycles and high pulsing frequencies, where the shock structure has less time to collapse due to the shorter jet-off time (see Cases III and IV in Figure 7.10 (d) and (e)). The triple points and shear-layers described previously can also be seen in Figure 7.10.

The flow structures can be further explained by inspection of the Q-criterion – contours of Q are projected onto the $x-z$ and $x-y$ planes, and are shown in an isometric perspective in Figure 7.11. The steady case (Figure 7.11 (a)) shows the shear-layer vortices and stream-wise trailing vortices, which form part of the longitudinal counter-rotating vortex pair (CRVP) in the time-averaged flow-field. The CRVP is located below the slip line, as described in Chapter 6. Pulsed Cases I and II (Figure 7.11 (b) and (c)) show a different structure. Shear-layer vortices are still present, but the free-stream entrainment prevents formation of longitudinal counter-rotating vortices in either the instantaneous or the mean flow-field. This lack of longitudinal CRVP was observed in subsonic crossflow, in cases with high momentum ratio ($J \gtrsim 5$) and high velocity ratio ($R \gtrsim 2$), corresponding to a convectively unstable shear-layer (Karagozian, 2014; Getsinger et al., 2014). Here, the presence of a CRVP depends on jet-off time. Cases I and II have a long jet-off time ($\tau = 3$ and 4 respectively), compared with Cases III and IV ($\tau = 1.5$ and 1 respectively). The secondary vortices can also be observed in Case II in the plane of symmetry.

Case III (Figure 7.11 (d)) shows the weak shear-layer vortices, a series of lead shocks, and the quasi-steady secondary shear-layer. The longitudinal CRVP consists of a single vortex in the instantaneous flow-field, in contrast to the steady case where multiple trailing vortices are observed to rotate about a common axis in the instantaneous flow-field, resulting in a single vortex in the mean flow (refer to Chapter 6). Case IV shows similar behavour to Case III, with a quasi-steady secondary shear-layer and a single longitudinal CRVP, indicating that this phenomenon is also related to jet-off time rather than duty-cycle, frequency, or stroke ratio.

Figure 7.12 shows the three-dimensional structure of shocks and vortices, via isometric contours of (a) instantaneous density gradient magnitude, and (b) instantaneous span-wise vorticity. These contours show that the barrel shocks, bow shock, lead shock, and shear-layer vortices wrap around the jet outlet, while the secondary shear-layer, partially visible in Figure 7.12 (b), forms a conical shape. The shear-layer vortices terminate in the boundary layer on the flat plate, and form the classical hair-pin shape, as observed in the steady case in the previous chapter.

A detailed view of the development of shocks and shear-layers within a single pulse cycle is provided in Figures 7.13 (density gradient) and 7.14 (span-wise vorticity) for Case I ($\alpha = 0.5$, $St_\infty = 1/6$); animations are provided for all cases in the supplementary material. At jet start-up ($\tau = 0$), the bow shock and barrel shocks from the previous pulse cycle are partially collapsed, and there is a partially formed shear-layer vortex

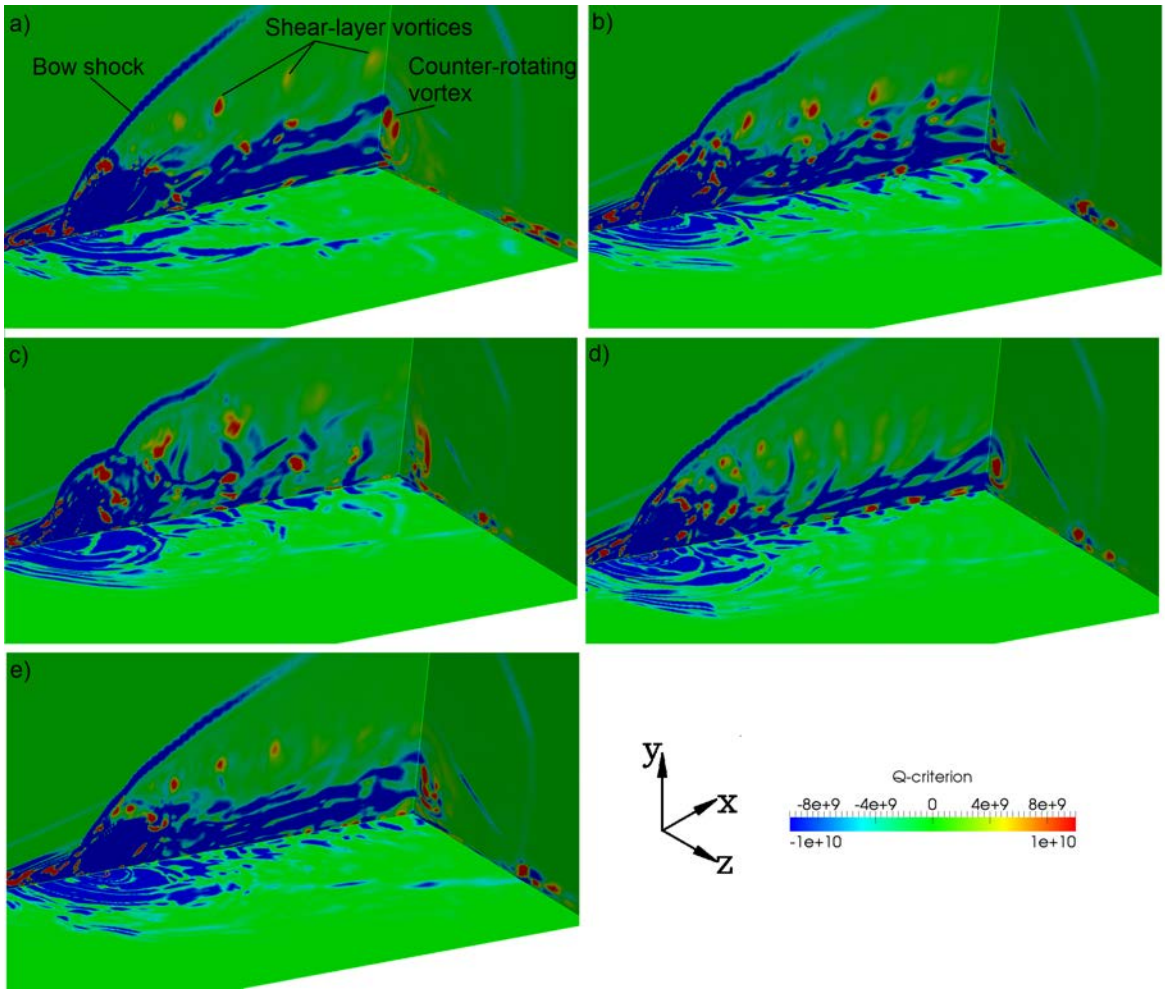

Figure 7.11: Isometric contours of instantaneous Q-criterion at jet startup ($\tau = 0$), for (a) Steady jet, (b) Pulsed jet (Case I, $\alpha = 0.5$, $St_\infty = 1/6$), (c) Case II ($\alpha = 0.33$, $St_\infty = 1/6$), (d) Case III ($\alpha = 0.50$, $St_\infty = 1/3$), and (e) Case IV ($\alpha = 0.75$, $St_\infty = 1/4$).

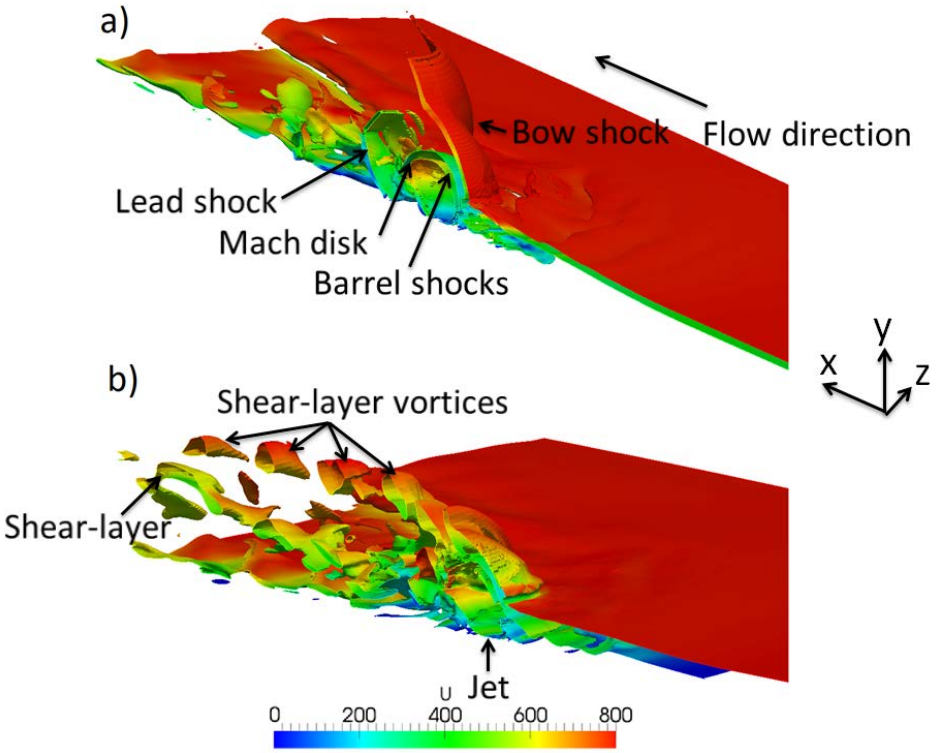

Figure 7.12: Isometric contours of (a) instantaneous density gradient magnitude corresponding to $|\nabla\rho|/\rho = 1000$, and (b) instantaneous span-wise vorticity of 100 000, at jet start-up ($\tau = 0$) for Case I ($\alpha = 0.5$, $St_\infty = 1/6$), coloured by velocity magnitude.

between them, which was also formed during the previous pulse. As the jet starts ($\tau = N/6$), the jet flow and lead shock take a finite time to reach the barrel shock, which is therefore still collapsing. Initially, the jet flow is similar to a jet in quiescent atmosphere (Radulescu and Law, 2007). A lead shock is formed, followed by the jet interface and Mach shock. The shear between the high speed crossflow and the collapsing bow shock means the shear-layer vortex from the previous pulse continues to form (see Figure 7.14).

At $\tau = 2N/6$ the lead shock, jet interface, and forming Mach disk have reached the collapsing barrel shock. The forming Mach disk is influenced by the crossflow and barrel and bow shocks begin to re-form. The jet flow reaching the barrel shocks from the previous pulse stop the collapse of these structures, as the jet interface provides a back pressure. The new forming barrel shocks merge with the collapsing barrel shocks from the previous pulse, the collapsing barrel shock reaches its minimum height, and the shear is reduced due to the reduced height relative to the separated in-flow boundary layer. By this time, the core of the shear-layer vortex which began forming during the previous pulsing cycle has convected downstream, while vorticity is still being generated in the weakened shear-layer, resulting in a stream-wise (x) elongation of the shear-layer vortex as described previously for Case I. This convection combined with the reduction in shear and the entrainment of the free-stream, causes the vortex to break-off, as shown in Figure 7.14. The entrained free-stream flow rotates in the opposite direction to the jet shear-layer vortices.

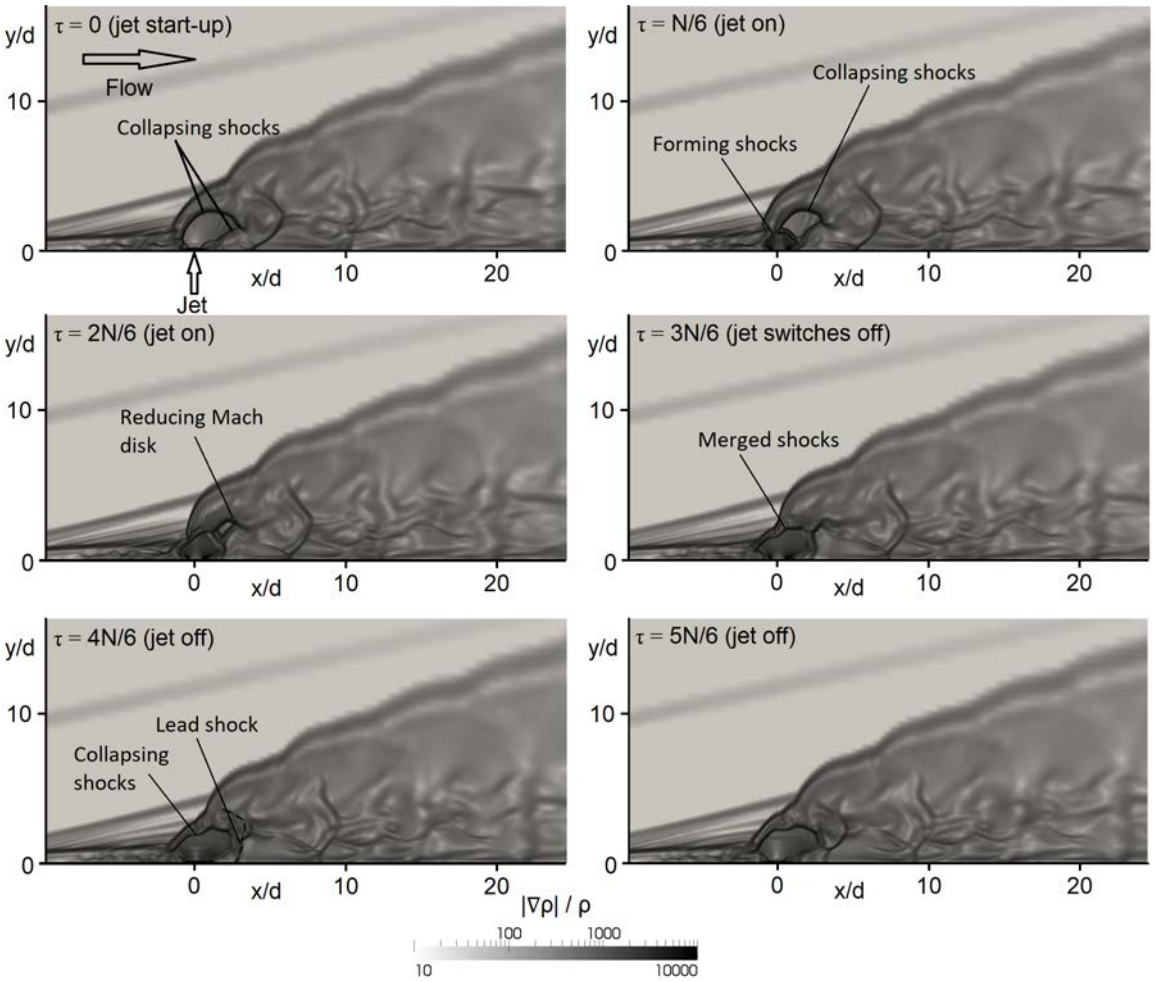

Figure 7.13: Contours of instantaneous density gradient magnitude in the plane of symmetry, showing shock structure during a full pulse cycle for Case I ($\alpha = 0.5$, $St_\infty = 1/6$).

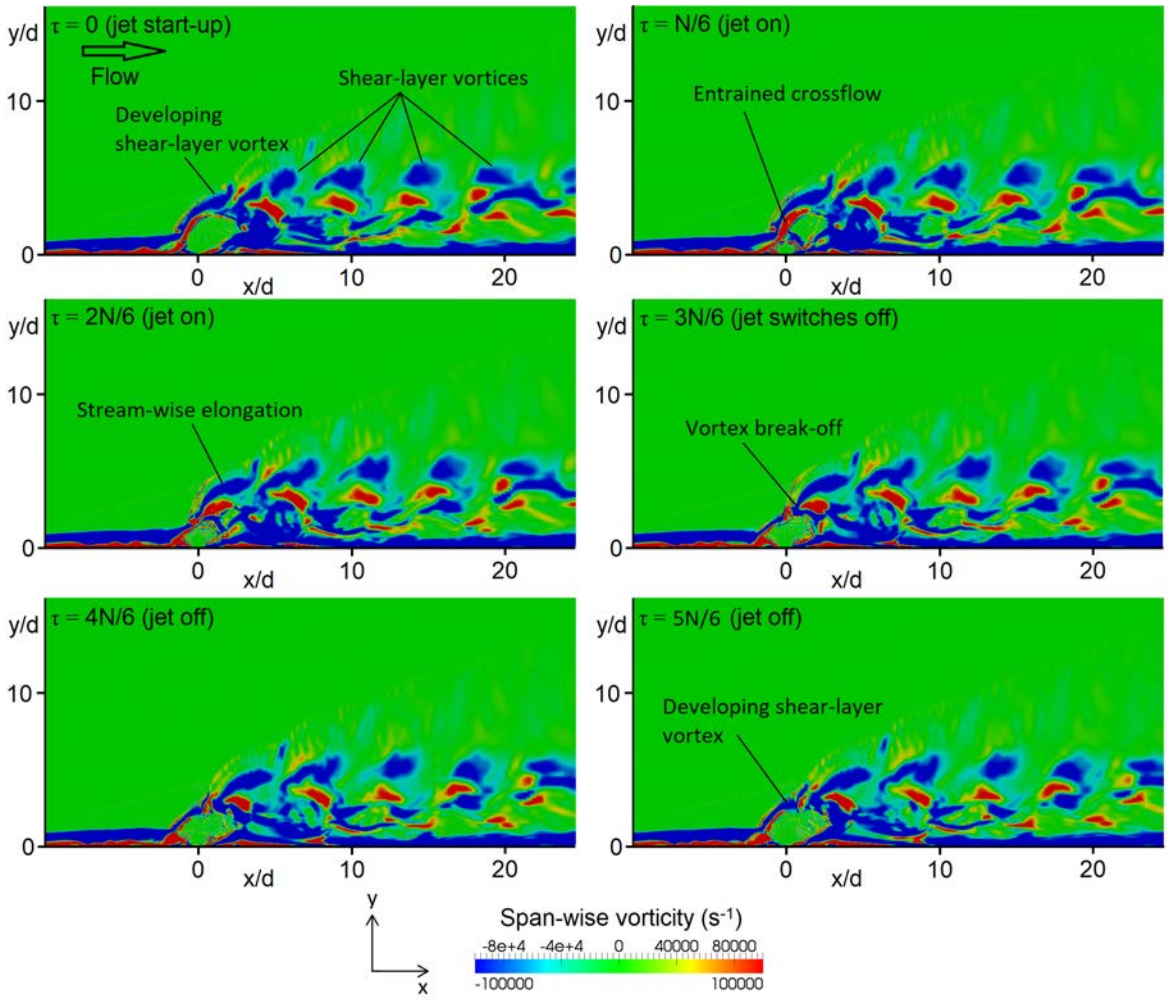

Figure 7.14: Contours of instantaneous span-wise vorticity in the plane of symmetry, showing shear-layer vortex formation during a full pulse cycle for Case I ($\alpha = 0.5$, $St_\infty = 1/6$).

As the bow shock and barrel shocks continue to re-develop, at $\tau = 3N/6$, they move away from the jet orifice and back into the crossflow, preventing further entrainment. The lead shock also continues to move outward into the crossflow. In Case I, $\tau = 3N/6$ is also the time when the jet switches off.

At later times ($\tau > 4N/6$), the barrel shocks begin to collapse again due to the lack of jet pressure, while the lead shock continues to travel downstream. The collapse of the barrel shocks is initially slow, and the windward and leeward barrel shocks move closer together as the length of the Mach disk is reduced. This can be observed in Figure 7.13 at $\tau = N/6$ to $\tau = 3N/6$, resulting in the break-up of the shear-layer. The secondary shear-layer begins to form behind the triple point caused by reflection of the lead shock from the plate is it moves downstream. During this process, the lead shock is rotated by the crossflow, and is near-vertical by $x/d \approx 5$. The Mach reflection of this lead shock, observed at $x/d_j \approx 8$ at $\tau = 4N/6$, causes the boundary layer to separate from the flat plate. The resultant shock structure downstream is a series of near-vertical shocks, corresponding to the jet lead shocks, each with a corresponding reflected shock and triple point. This process is responsible for the stream-wise elongated shear-layer vortices, separated by near-vertical shocks.

The process is analogous to the other pulsed cases considered. In Case II ($\alpha = 0.33$, $St_\infty = 1/6$), with a reduced duty-cycle and longer jet-off time, the barrel and bow shocks collapse further during each cycle. This results in more pronounced distortion of the bow shock, and more entrained flow, resulting in periodic roll-up of the secondary shear-layer. The secondary shear-layer also forms closer to the plate, as the barrel shocks collapse closer to the jet outlet. This also causes the vertical elongation of the shear-layer vortices, which are formed at the shear-layer between the bow shock and the windward barrel shock, and therefore have a vertical trailing column when the windward barrel shock collapses.

In Case III ($\alpha = 0.5$, $St_\infty = 1/3$), the lead shocks are closer together, and the barrel shocks have less time to collapse, resulting in a less distorted bow shock, and reduced free-stream entrainment. The rapid collapse of the windward barrel shock means that the shear-layer vortices become highly elongated in the vertical direction. Additionally, a well-defined shear-layer does not form behind the intermittent Mach disk. The close proximity between successive lead shocks allows interaction between lead shocks and reflected shocks, resulting in the quasi-steady secondary shear-layer and boundary layer separation described previously. The near-vertical lead shocks prevent interaction between shear-layer vortices, and distort their shape, resulting in vertical elongation. Similar behaviour is observed in Case IV ($\alpha = 0.75$, $St_\infty = 1/4$).

This complex interaction between shocks and vortices is the mechanism through which increased jet penetration is achieved in supersonic crossflow. The presence of shocks prevents mixing of distinct shear-layer vortices, which allows deeper penetration compared with a steady jet, over a wide range of pulsing conditions, including at high duty-cycle. Therefore, increased jet penetration per jet mass flow rate is anticipated. In high frequency cases, the frequent collapse of the Mach disk results in a weaker

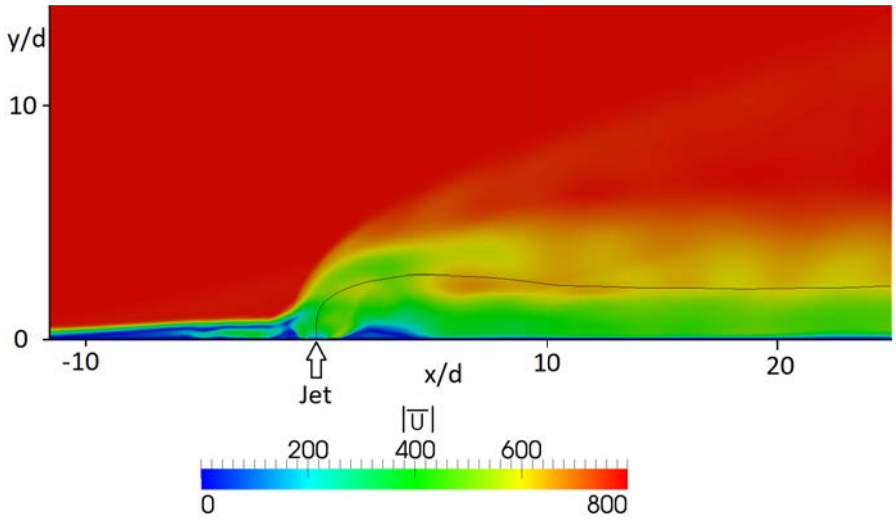

Figure 7.15: Time-averaged stream-line, originating from the centre of the jet outlet, overlaid on contours of time-averaged velocity magnitude in the plane of symmetry for Case II ($\alpha = 0.33$, $St_\infty = 1/6$), showing jet penetration.

shear-layer. The lead shocks form close together, which causes vertically elongated shear-layer vortices. In cases with a short jet-off time, a quasi-steady secondary shear-layer is observed due to interaction between lead shocks and reflected shocks, and the lack of entrainment of free-stream flow.

7.3 Penetration

Table 7.2 shows the jet penetration for the current cases, measured as the maximum height in the y direction of the time-averaged streamline that originates from the centre of the jet outlet, as used by Mahesh (2013), averaged over two complete pulsing cycles (corresponding to a time period of $\tau = 12$ for Case I). With the idealised inlet conditions used in this study, each pulse is identical, so time-averaging over a single pulsing period is sufficient to determine time-averaged results. However, some hysteresis is observed in the simulations, resulting in slightly different behaviour between consecutive pulsing cycles. Therefore, results are time-averaged over two complete cycles, to reduce these effects. Further time-averaging, beyond two complete pulsing cycles, had no affect on the penetration results. A typical example of the time-averaged jet penetration is provided in Figure 7.15.

In the time-averaged flow-field, the penetration of the pulsed jets is reduced in comparison to a steady jet. This is due to the time-averaged results including the periods where the jet is off. During these periods, the shocks are collapsing, and jet penetration is reducing, as there is no pressure from the jet forcing the fluid into the crossflow. To account for the jet off periods during pulsing, the time-averaged jet penetration can be normalised. This is achieved by dividing by duty-cycle, α (i.e. $y/d_j \times 1/\alpha$). With the ideal square wave boundary conditions used in this chapter, this gives penetration per unit jet mass flow rate. When penetration is normalised, Case I

Table 7.2: Jet penetration for the pulsed jet cases in the fully established flow regime.

Case	Time-averaged y/d_j	Duty-cycle α	Normalised $y/d_j \times 1/\alpha$
Steady	5.6	1	5.6
I	4.7	0.5	9.4
II	2.8	0.33	8.4
III	4.3	0.5	8.6
IV	5.5	0.75	7.3

($\alpha = 0.5$, $St_\infty = 1/6$) exceeds the steady case by 68%. When the duty-cycle is changed from 50% to 33% (Case II), the normalised penetration reduces by 11% compared with Case I, while increasing the pulsing frequency and maintaining the duty-cycle at 50% (Case III) reduces the normalised penetration by 8.5% compared with Case I. Finally, the 75% duty-cycle case (Case IV) has normalised penetration depth 22% lower than Case I, but is still 30% deeper than the steady jet. Therefore, the optimal duty-cycle for penetration in this case is 50%. This differs from observations for subsonic jets, where optimal penetration occurs at lower duty-cycles (Sau and Mahesh, 2010). In supersonic crossflow, increased penetration occurs at higher duty-cycles, as interaction between shear-layer vortices is prevented by the lead shocks. Normalised penetration is reduced at duty-cycles above 50%, due to the higher mass flow rate, but deeper penetration per jet unit mass flow rate is still observed compared with a steady jet, consistent with the predicted behaviour. Actual penetration approaches the steady jet result as duty-cycle is increased.

Reducing the pulsing frequency increases penetration at a 50% duty-cycle (see Cases I and III), as longer pulses (or higher stroke ratio) produce stronger shear-layer vortices, in agreement with observations from subsonic jets (Sau and Mahesh, 2010). At constant stroke ratio, the time-averaged penetration decreases with reduced frequency due to a lower duty-cycle, while normalised penetration increases (see Cases I and IV). A longer stroke ratio at constant frequency also increases both actual and normalised penetration (see Cases I and II). The 68% increase in normalised penetration of pulsed jets (Case I) over steady jets is also similar to increases observed in subsonic crossflow (Eroglu and Breidenthal, 2001; Johari et al., 1999).

A comparison between the jet penetration values observed in this study with those from previous studies is provided in Figure 7.16 (a). The penetration closely matches the sonic jet in supersonic crossflow case of Randolph et al. (1994), while Shi et al. (2016) observed reduced penetration using a sinusoidal pulsing profile. Again, this agrees with the behaviour observed in subsonic crossflows, where square wave pulsing shows deeper penetration at low velocity ratio. The jet in subsonic crossflow case of Sau and Mahesh (2010) is included for comparison, to show that much deeper penetration can be achieved for these cases, due to the higher velocity ratio, $R = 8.0$ compared with $R < 1$ for supersonic cases. Figure 7.16 (a) also shows the increased penetration

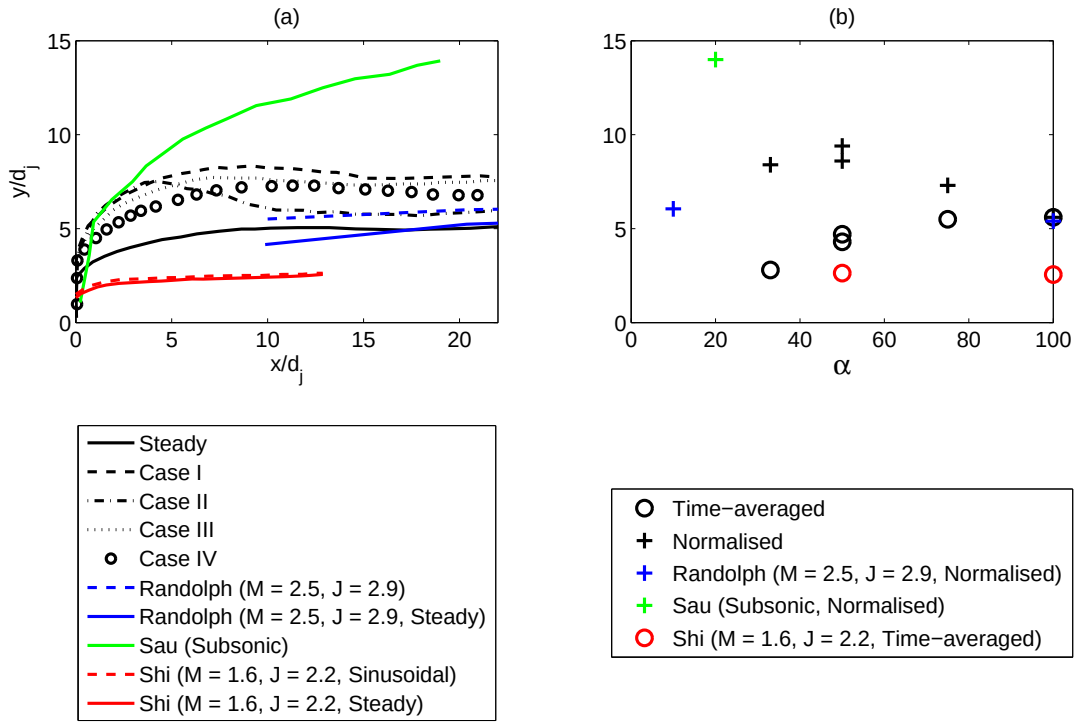

Figure 7.16: Comparison of jet penetration data. (a) Jet trajectories. Black line: Normalised penetration, steady case, Black dash line: Normalised penetration, Case I, Black dot-dash line: Normalised penetration, Case II , Black dotted line: Normalised penetration, Case III , ○: Normalised penetration, Case IV, Blue dash line: Randolph et al. (1994) ($M_\infty = 2.5$, $J = 2.9$), Blue line: Randolph et al. (1994) ($M_\infty = 2.5$, $J = 2.9$) with steady injection, Green line: Sau and Mahesh (2010) ($M_\infty < 1$, $R = 8.0$), Red dash line: Shi et al. (2016) ($M_\infty = 1.6$, $J = 2.2$) sinusoidal pulse, Red line: Shi et al (2016) ($M_\infty = 1.6$, $J = 2.2$) with steady injection. (b) Penetration vs. duty-cycle. Black = current simulation, Blue, Randolph et al. (1994), Red: Shi et al. (2016), Green: Sau and Mahesh (2010). +: Normalised, ○: Time-averaged.

depth observed for pulsed jets over steady jets.

The variation of penetration with duty-cycle is shown in Figure 7.16 (b). Different trends are observed in the time-averaged and normalised data. As described previously, in the time-averaged data, penetration increases with duty-cycle, at a decreasing rate, while normalised data peaks at $\alpha = 50\%$.

The mechanisms proposed by Randolph et al. (1994) for the increased penetration are the finite time taken for the Mach disk to form, and the inertial force caused by the acceleration of the jet flow. Figure 7.13 shows that Mach disk formation is delayed within each pulsing cycle. In Case I, the Mach disk does not form until $\tau \approx 4N/6$, and has collapsed by $\tau \approx 7N/6$ (or $\tau \approx N/6$ in the next cycle). Therefore, for Case I ($\alpha = 0.5$, $St_\infty = 1/6$), the Mach disk is present for less than half the cycle. This provides, for the first time, specific evidence to support the delayed Mach disk mechanism proposed

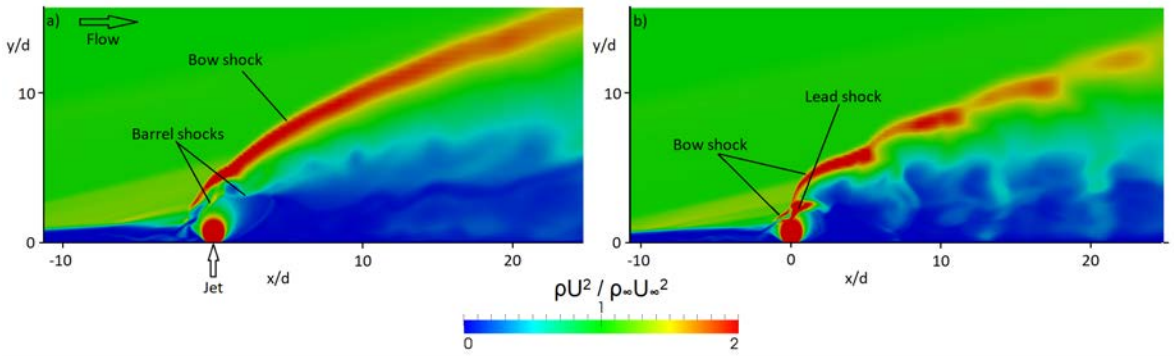

Figure 7.17: Instantaneous contours of momentum, ρU^2, in the plane of symmetry. (a) Steady jet, (b) Case I ($\alpha = 0.5, St_\infty = 1/6$) at $\tau = 3N/6$.

by Randolph et al. (1994).

Two additional mechanisms are also identified, based on the results of the current study. At jet start-up, a lead shock precedes the jet interface and barrel shock into the crossflow. This shock increases the effective jet-to-crossflow momentum ratio, J, in the region of the jet orifice, as shown in Figure 7.17, which allows the jet to penetrate deeper before it is turned by the crossflow. As they travel downstream, the series of lead shocks also prevent interaction between distinct shear-layer vortices, thus allowing deeper penetration at higher duty-cycles ($\alpha > 50\%$) than can be achieved in subsonic crossflow.

Another important parameter in the jet-in-crossflow interaction is total pressure loss. Total pressure loss was calculated using a total pressure loss coefficient, C_{TPL}, defined as follows:

$$C_{TPL} = \left(\int_{outlet} p_0 dA - \int_{inlet} p_0 dA \right) / (q_\infty A_j) \tag{7.1}$$

where p_0 is total pressure, q_∞ is the free-stream dynamic pressure, and A_j is the jet outlet area. The time-averaged results show that the steady jet case has $C_{TPL} = -10.6$. The reduction in total pressure between the inlet and outlet is due to the low velocity flow in the boundary layer and within the downstream re-circulation region behind the jet. The pulsed cases show similar behaviour to the steady case, with low velocity flow present in the boundary layer and downstream re-circulation region. However, pulsed cases exhibit greater total pressure loss. Case I has the greatest total pressure loss, with $C_{TPL} = -22.1$, as well as the deepest penetration. The two-fold increase in total pressure loss over the steady case is due to the presence of multiple lead shocks, as shown in Figure 7.17. Therefore, the increase in penetration directly corresponds to an increase in total pressure loss for the pulsed jet cases over the steady case. Pulsed jet Cases II, III, and IV have pressure loss coefficients of -21.8, -21.5, and -19.7 respectively, indicating that total pressure loss is similar for all pulsed jet cases.

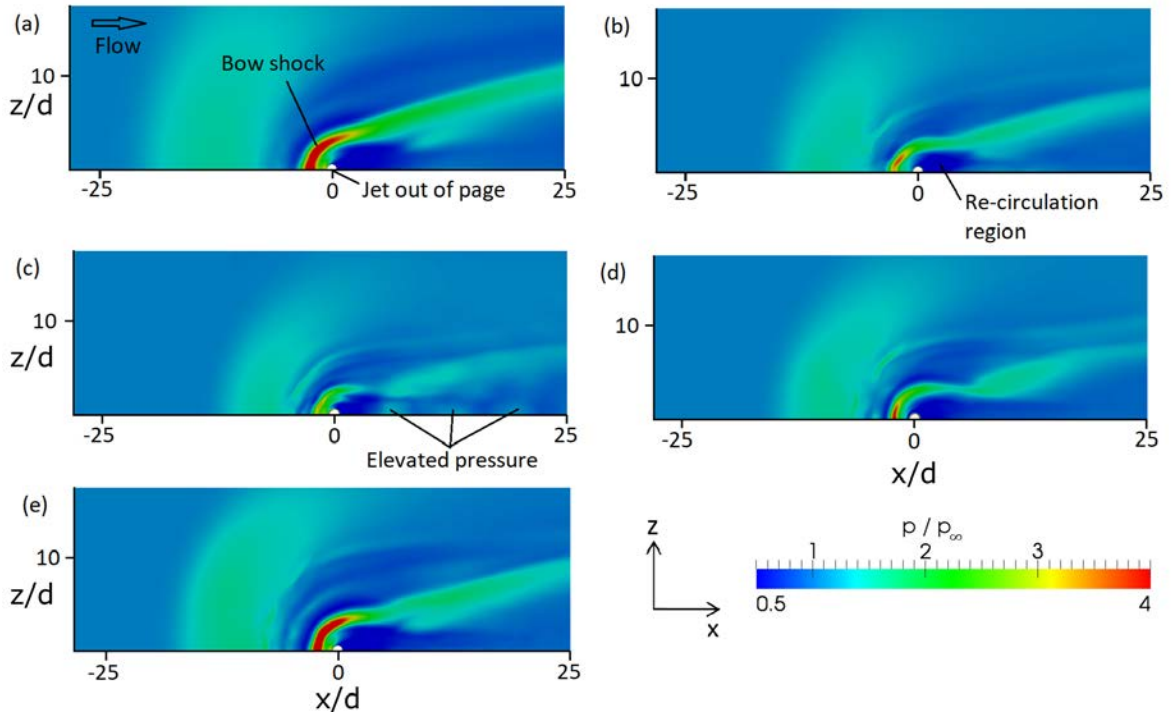

Figure 7.18: Contours of time-averaged pressure distribution on the flat plate. (a) Steady jet, (b) Case I ($\alpha = 0.5, St_\infty = 1/6$), (c) Case II ($\alpha = 0.33, St_\infty = 1/6$), (d) Case III ($\alpha = 0.5, St_\infty = 1/3$), and (e) Case IV ($\alpha = 0.75, St_\infty = 1/4$).

Table 7.3: Time-averaged peak pressure, and its stream-wise location, for pulsed jet cases, in the fully established flow regime.

Case	Peak pressure, p/p_∞	Location, x/d_j
Steady	4.8	-2.4
I	3.7	-2.1
II	3.3	-1.5
III	4.1	-2.1
IV	6.0	-2.1

7.4 Surface Pressure and Jet Force

The time-averaged pressure distribution over the flat plate for each case is provided in Figure 7.18, averaged over two complete pulsing cycles ($\tau = 12$ for Case I). As shown in Table 7.3, the pressure peak in the bow shock region is higher in the high duty-cycle cases (steady and Case IV). The high pressure regions also form further from the jet outlet in the steady case, as the bow shock does not periodically collapse, and maintains its stand-off from the jet orifice. The lower duty-cycle case (Case II) has lower peak pressure, and the high pressure regions are localised closer to the jet outlet.

The 50% duty-cycle pulsed case (Case I) is similar to the steady jet, with a reduction in peak pressure and a smaller low pressure re-circulation region downstream. The lower duty-cycle case (Case II) has the lowest peak pressure. The region of peak pressure is located closer to the jet outlet, due to the periodic collapse of the bow shock. Case II

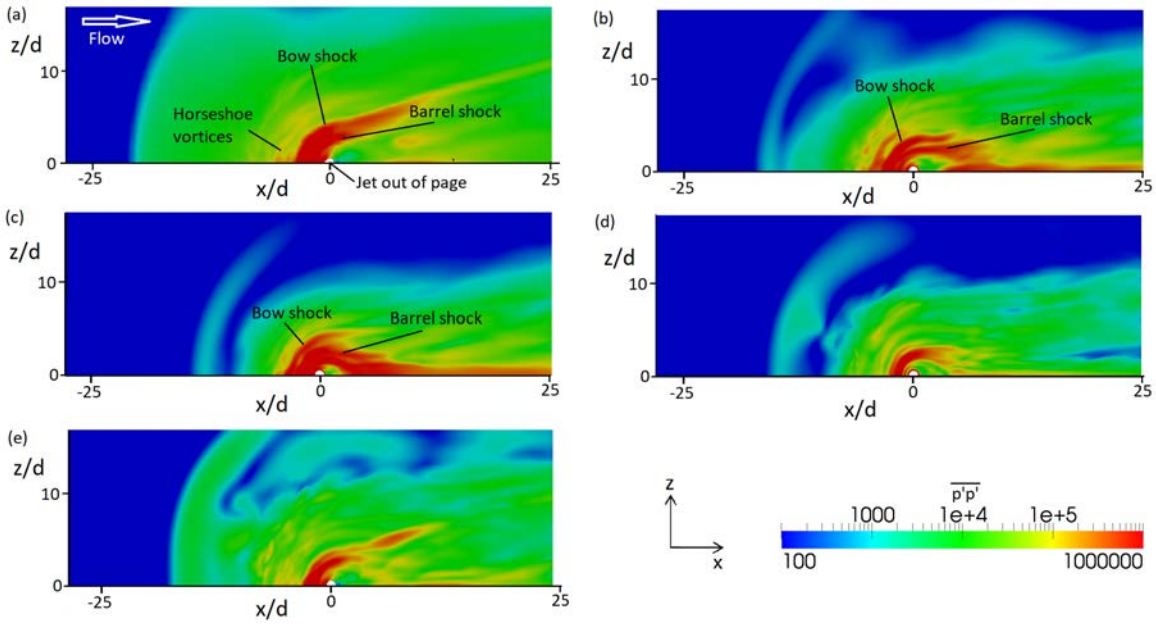

Figure 7.19: Contours of mean-squared variation in pressure, $\overline{p'p'}$, on the plate, plotted on a logarithmic scale. (a) Steady jet, (b) Case I ($\alpha = 0.5, St_\infty = 1/6$), (c) Case II ($\alpha = 0.33, St_\infty = 1/6$), (d) Case III ($\alpha = 0.5, St_\infty = 1/3$), and (e) Case IV ($\alpha = 0.75, St_\infty = 1/4$).

also has distinct regions of elevated pressure in the downstream wake region, near the jet centre-line ($z = 0$). This corresponds to the entrainment of free-stream flow, as discussed previously. Cases III and IV resemble Case I, but have lower pressure downstream ($x/d_j > 15$) due to the reduced entrainment and the presence of the quasi-steady, thin shear-layer. Case IV has a higher peak pressure than the steady jet case. This is due to the intermittent presence of the lead shock, which increases the local pressure as it moves radially out from the jet orifice, increasing the time-averaged peak pressure. This effect is present in all pulsed cases, resulting in all pulsed cases having normalised peak pressure values ($p/p_\infty \times 1/\alpha$) greater than the steady case. Therefore, pulsed cases are more efficient at generating peak pressure, on a per unit jet mass flow basis.

Pressure variations are shown in Figure 7.19, plotted as mean-squared variation, $\overline{p'p'}$. Pressure variations are important to the design of reaction control jet systems, due to the changing aerodynamic load on the surrounding structure. Figure 7.19 shows distinct differences between the pulsed cases. In the steady jet case, the majority of the pressure variation is contained in the bow shock and barrel shock region. This corresponds to shear-layer vortex shedding, which deforms these shocks. There is also a small region of high variation further upstream due to the horseshoe vortices.

For the pulsed Case I, there is a similar region of large variations near the bow shock, but this region is larger, and extends further upstream in comparison with the steady case. The high variability regions corresponding to the bow shock and barrel shocks are spatially separated lateral to the jet outlet. The high variability caused by the barrel shock wraps around the jet orifice. The large pressure variations at the

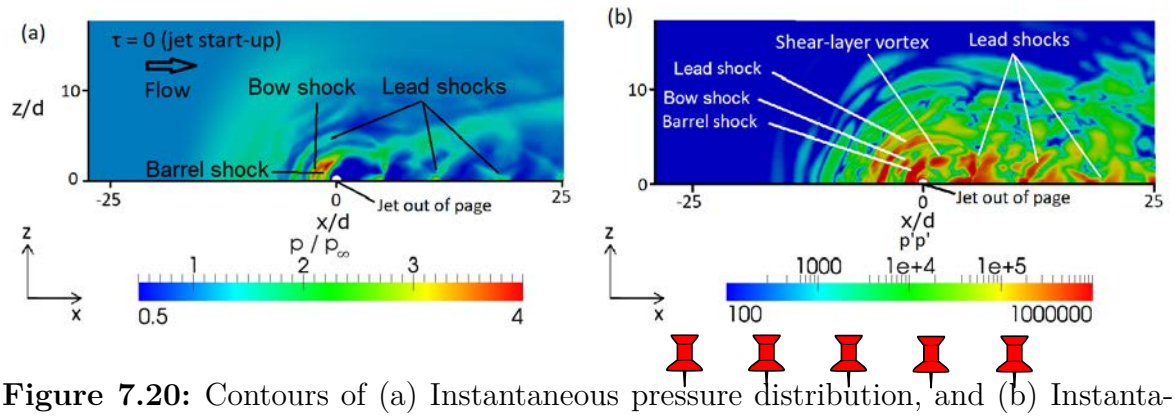

Figure 7.20: Contours of (a) Instantaneous pressure distribution, and (b) Instantaneous variation in pressure, squared , $p'p'$, on the flat plate at $\tau = 0$ for pulsed Case I ($\alpha = 0.5, St_\infty = 1/6$).

bow and barrel shocks are caused by the periodic collapse of these structures. There is also a region of high variability downstream on the centre-line ($z = 0$), as a result of the free-stream entrainment causing break-up of the secondary shear-layer, and the downstream convection of the lead shock.

Case II is similar to Case I, but the pressure variations around the barrel shocks are increased, and occur over a larger area. Once again, this is caused by the periodic collapse of the barrel shocks, which is more significant in Case II, owing to the lower duty-cycle and longer jet-off time. The variability is also increased along the downstream centre-line ($z = 0$) due to more significant entrainment and break-up of the secondary shear-layer.

Case III and Case IV present a significantly different profile to the previously mentioned cases. The small jet-off time reduces the extent to which the barrel shocks and bow shock collapse, thus resulting in a smaller region of variability upstream of the jet outlet. This region is reduced even in comparison to the steady case, indicating that the deformation of the barrel and bow shocks corresponding to shear-layer vortex shedding in the steady case is more significant than the partial collapse during pulsing for these cases. The downstream region for Cases III and IV resembles the steady case, due to the lack of entrainment and the presence of the quasi-steady secondary shear-layer.

The instantaneous pressure distribution at jet start-up ($\tau = 0$) is provided in Figure 7.20 (a) for Case I ($\alpha = 0.5, St_\infty = 1/6$). The main features are similar to the steady case described in Chapter 6. Animations are provided for all cases in the supplementary material. There is a high pressure region upstream of the jet outlet, and following the bow shock downstream. The instantaneous pressure at the bow shock, upstream of the jet outlet, is highest at $\tau = 0$, and $\tau = 5N/6$, corresponding to the end of the cycle, before the jet is switched on. This corresponds to the time when the barrel shock and bow shocks are fully formed, are at a large distance from the jet orifice, and have not yet collapsed. High pressure regions on the downstream centre-line and radially outward from the jet orifice, corresponding to lead shocks, can also be seen.

Figure 7.20 (b) shows the corresponding instantaneous variation in pressure, squared (i.e. $p'p'$), at jet start-up ($\tau = 0$) for Case I ($\alpha = 0.5, St_\infty = 1/6$). Again, these results are similar to the steady case described in Chapter 6. This data reveals a cellular structure, where cells correspond to local flow structures. The hair-pin type shear-layer vortex can be seen shedding from the bow shock region. Lead shocks from previous pulsing cycles correspond to localised high pressure regions moving downstream along the jet centre-line, and radially outward from the orifice.

The resulting interaction force, F, is obtained by integrating the surface pressure as discussed in Chapter 6 (Equation 6.6). The results are provided graphically in Figure 7.21, while the time-averaged data are provided in Table 7.4. The force is non-dimensionalised by the jet density, ρ_j, exit area, A_j, and peak velocity, U_j to represent a force coefficient, C_F, as shown in Chapter 6 (Equation 6.7).

The time-averaged force due to the laminar flat plate boundary layer, with the jet off, has been subtracted from the interaction force. The jet thrust, T, is also shown in Figure 7.21, calculated according to the general thrust equation (see Equation 6.8), and converted to a coefficient, C_T, in the same manner as Chapter 6 (see Equation 6.9).

Note that in all cases the interaction force and jet thrust act in opposite directions, the induced interaction force counters the thrust from the jet. Figure 7.21 shows that the interaction force is less than the jet thrust in all pulsed cases, but is a significant contributor to the overall force. In the steady case, the time-averaged interaction force coefficient is 53% of the jet thrust coefficient. In the pulsed cases, this is reduced depending on duty-cycle. Figure 7.21 also shows that the interaction force is out of phase with the jet thrust. The maximum interaction force occurs when the jet is off. This is consistent with all pulsed cases, and is due to the time taken for the shock and vortex structures to develop. For example, as highlighted previously, the maximum pressure at the bow shock location occurs just before the jet is switched on. The same trend is shown in Figure 7.21, the maximum interaction force occurs near $\tau = 0$. The phase angle is important for reaction jet control applications, when the interaction force is out of phase with the jet thrust there is a residual control force which increases once the jet is switched off. In each case, including the steady case, the interaction force peaks after shear-layer vortices are shed from the windward barrel shock. This also corresponds to the times where the barrel shock structure is fully formed. The peaks observed in the pulsed jet cases are stronger, and more regular than the steady jet case, as shear-layer vortex shedding is forced by the pulsing, and is accompanied by the collapse of the barrel and bow shock structures.

The interaction force for each case is compared in Figure 7.22 (a). The steady case provides the largest interaction force, followed by Case IV ($\alpha = 0.75, St_\infty = 1/4$). Case I ($\alpha = 0.5, St_\infty = 1/6$) and Case III ($\alpha = 0.5, St_\infty = 1/3$) have a similar interaction force, while Case II ($\alpha = 0.33, St_\infty = 1/6$) has the lowest interaction force.

The normalised interaction force ($C_{F\alpha}$), to account for duty-cycle (or jet mass flow rate, i.e. $C_{F\alpha} = C_F \times (1/\alpha)$), is shown in Figure 7.22 (b) and the data are included in Table 7.4. Once the reduced jet mass flow rate is taken into account, Case II ($\alpha =$

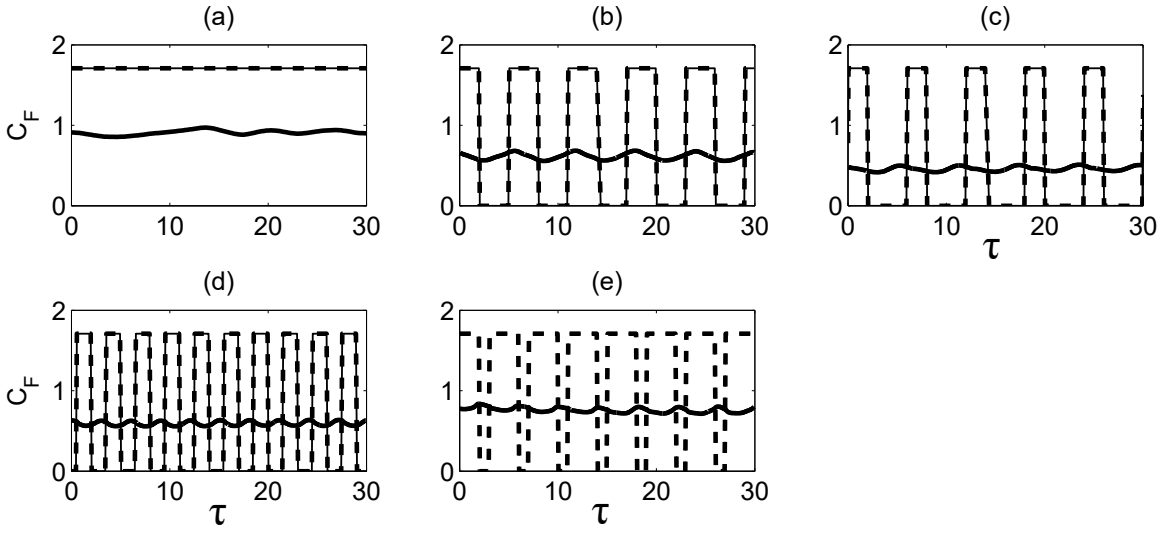

Figure 7.21: Jet interaction force (C_F, Solid line), and jet thrust (C_T, Dash line). (a) Steady jet, (b) Case I ($\alpha = 0.5, St_\infty = 1/6$), (c) Case II ($\alpha = 0.33, St_\infty = 1/6$), (d) Case III ($\alpha = 0.5, St_\infty = 1/3$), and (e) Case IV ($\alpha = 0.75, St_\infty = 1/4$).

Table 7.4: Time-averaged jet interaction force for the pulsed jet cases, in the fully established flow regime.

Case	$\overline{C_F}$	$\overline{C_{F\alpha}}$
Jet Thrust	1.7	1.7
Steady	0.9	0.9
I	0.62	1.23
II	0.45	1.38
III	0.59	1.19
IV	0.78	1.04

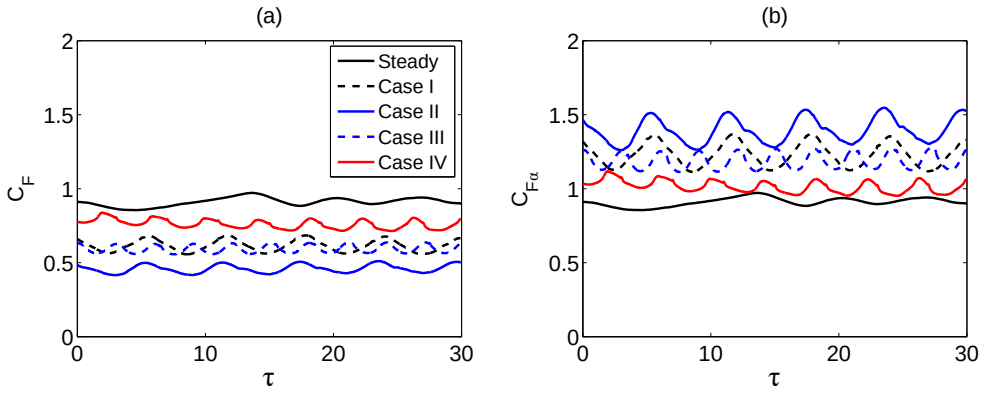

Figure 7.22: Comparison of (a) Jet interaction force coefficient (C_F), and (b) Normalised jet interaction force coefficient ($C_{F\alpha}$). Black line: Steady, Black dash line: Case I ($\alpha = 0.5, St_\infty = 1/6$), Blue line: Case II ($\alpha = 0.33, St_\infty = 1/6$), Blue dash line: Case III ($\alpha = 0.5, St_\infty = 1/3$), Red line: Case IV ($\alpha = 0.75, St_\infty = 1/4$).

$0.33, St_\infty = 1/6$) provides the highest normalised interaction force, followed by the $\alpha = 0.5$ cases (Case I and Case III). Case IV ($\alpha = 0.75, St_\infty = 1/4$) is lower, followed by the steady case ($\alpha = 100\%$), which provides the lowest normalised interaction force. This is another important result for reaction jet control, there is a fuel efficiency benefit in pulsing the jet, and the benefit increases with a reduced duty-cycle but does not depend on frequency within the limited range considered in this study. Therefore, a lower duty-cycle jet (Case II) will give a higher interaction force per unit jet mass flow rate, which may be beneficial for reaction control jet applications when efficiency is of greater importance than overall thrust. This efficiency is caused by the delay between the jet switching off and the collapse of the shock structures. Even in the low duty-cycle cases considered in this study, the shock structure does not completely collapse between cycles, so the interaction force remains present, although slightly reduced, during periods with no jet flow.

Recall that Case I and Case III provide the highest jet penetration, even when normalised by jet mass flow rate, suggesting that increased jet penetration does not lead to increased interaction force.

The interaction force peak-to-peak variations are larger at lower frequencies, due to the more complete collapse of the barrel shocks each cycle. However, the mean interaction force does not strongly depend on pulsing frequency. While the steady jet has a low interaction force with lower peak-to-peak variability than the pulsed cases, the periodic jet shear-layer vortex shedding does cause periodic fluctuations, which can be seen in Figure 7.22. However, these fluctuations are reduced in comparison to the pulsed cases, and are less regular, as described previously.

Spectra of the interaction force variations ($C'_F = C_F - \overline{C_F}$) for each case are provided in Figure 7.23. As outlined in Chapter 6, the steady case has a small peak at the shear-layer vortex shedding frequency, $St_\infty \approx 1/6$. The spectra of the pulsed cases are dominated by peaks at the pulsing frequency, as expected. However, the behaviour differs between cases.

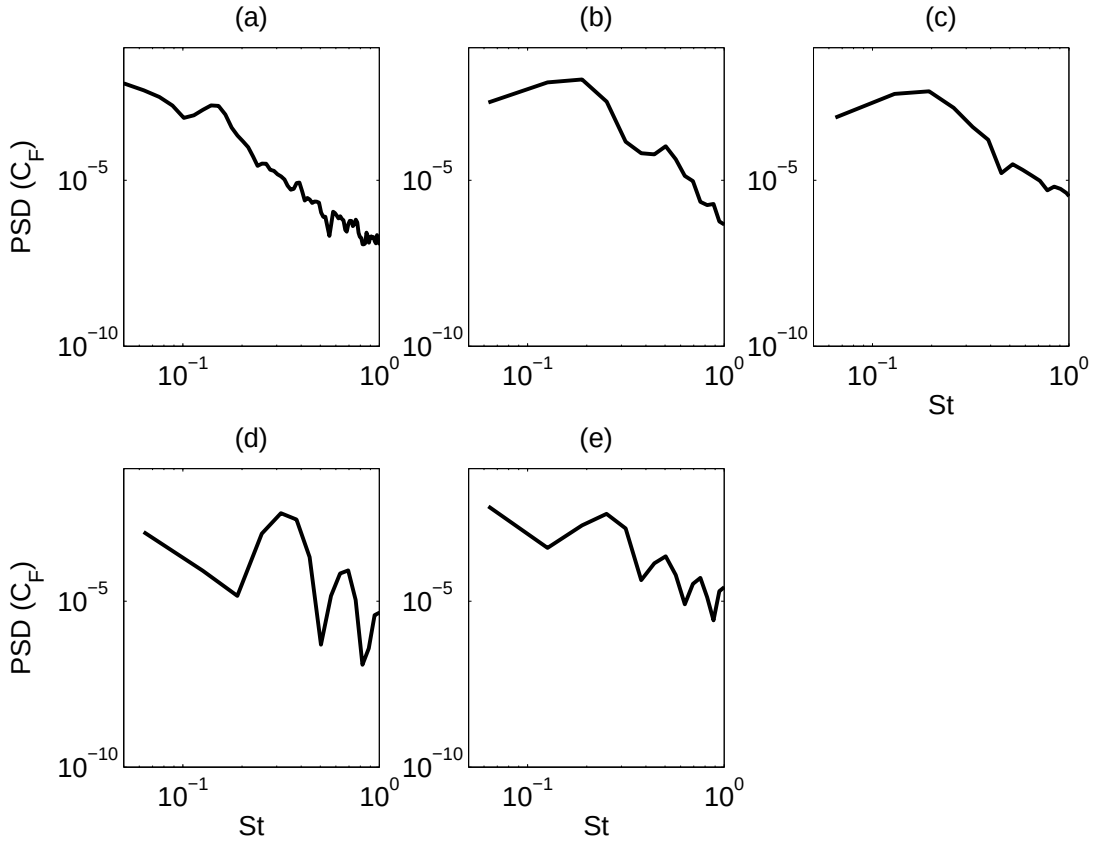

Figure 7.23: Power spectral density of jet interaction force variations. (a) Steady, (b) Case I ($\alpha = 0.5, St_\infty = 1/6$), (c) Case II ($\alpha = 0.33, St_\infty = 1/6$), (d) Case III ($\alpha = 0.5, St_\infty = 1/3$), and (e) Case IV ($\alpha = 0.75, St_\infty = 1/4$).

Cases I and II have single dominant peaks at the pulsing frequency, $St_\infty = 1/6$, with no secondary peak. The higher frequency pulsing case (Case III) has a dominant peak at the pulsing frequency, $St_\infty = 1/3$, and secondary peaks at the higher frequency harmonics, $St_\infty = 2/3$ and $St_\infty = 1$. Finally, Case IV has a dominant peak at the pulsing frequency, $St_\infty = 1/4$, a secondary peaks at the harmonics, $St_\infty = 2/4$, $St_\infty = 3/4$, and $St_\infty = 1$. Therefore, in cases where the jet is pulsed at the natural shear-layer vortex shedding frequency, a single peak is observed in the spectrum, while in other cases, multiple harmonics are present.

In all cases, including the steady jet, the force is primarily driven by the steady flow features: the bow shock, barrel shock, and large low pressure region downstream. The periodic collapse of these structures in the pulsed cases result in large peaks in the spectra at the pulsing frequency. These peaks are more significant and dominate the spectra in Cases I and II, when the jet is pulsed at the natural shear-layer vortex shedding frequency. In cases where the pulsing occurs at a different frequency to the natural shear-layer vortex shedding frequency (i.e. Cases III and IV), the harmonics of the pulsing frequency are observed in the spectra.

7.5 Conclusions

This chapter has investigated the interaction between a pulsed sonic jet and a hypersonic crossflow over a flat plate with a laminar boundary layer at high jet-to-crossflow momentum ratio. The results show that pulsed jets can significantly increase the penetration depth over steady jets. Previously proposed mechanisms for increased penetration have been investigated, and, for the first time, evidence has been provided to support these mechanisms. Two new mechanisms have also been identified, with supporting evidence provided. These results are important for the design of reaction jet control systems, and scramjet fuel injectors, where increased penetration is critical to overall performance. A maximum 68% increase in penetration was observed, corresponding to a low pulsing frequency ($St_\infty = 1/6$), with 50% duty-cycle.

Flow structures, particularly shear-layer vortices, are strongly influenced by the presence of shocks in the flow. When the jet is off, the lack of back pressure allows the barrel shocks to collapse. The extent to which these shocks collapse depends on the jet-off time. Lead shocks are formed during jet start-up, and periodically forced into the flow. The forming barrel shocks combine with the collapsing barrel shocks from the previous cycle, while the lead shocks continue to propagate outward and are turned downstream by the crossflow. In addition, shear-layers are formed behind the Mach disk, and by the reflection of lead shocks from the flat plate. These shear-layers are influenced by entrainment of free-stream flow, caused by the collapse of the barrel and Mach shocks when the jet is off. The presence of lead shocks affects the shape and location of the shear-layer vortices, and prevent their interaction. This allows increased penetration depth to be achieved at higher duty-cycles than in a subsonic crossflow.

Furthermore, the lead shocks reduce the effective jet-to-crossflow momentum ratio in the region of the jet orifice, allowing deeper jet penetration for pulsed jets over steady jets. However, the increased jet penetration comes at a cost, with an increase in total pressure loss.

The presence and structure of the CRVP is influenced by jet-off time. This is a phenomenon not previously observed in pulsed jets in supersonic crossflow. For long jet-off time ($\tau = 3-4$), no clear CRVP is observed for the pulsed cases. This behaviour is analogous to the high J, high R regime in subsonic crossflow. For short jet-off time ($\tau = 1-1.5$), a clear CRVP is observed, consisting of a single vortex in the instantaneous flow. This CRVP structure differs from the steady case, where the single CRVP observed in the mean flow consists of multiple individual structures rotating about a common axis in the instantaneous flow.

Consideration of the surface pressure distribution has identified areas of high pressure, and high variability, which is important to the design of reaction control systems. These regions differ significantly between pulsed jet cases, with large regions of high variability observed far downstream in cases with longer jet-off time.

This study has also revealed two additional results that affect the use of pulsed jets in a reaction control application. First, the interaction force peaks at the end of the pulsing cycle, when the jet is switched off, corresponding to shedding of shear-layer vortices; and second, the interaction force per unit jet mass flow rate increases for lower duty-cycles, due to the continued presence of shock structures during jet-off time periods.

Chapter 8

Jet Start-up in Hypersonic Crossflow

The aim of this chapter is to investigate the start-up process of steady and pulsed jets in hypersonic crossflow. The start-up process is important when the jet is operated at high frequency, as start-up may be a significant portion of the total jet-on period. The start-up of a steady jet is considered in Section 8.1, while pulsed jets are considered in Section 8.2.

8.1 Steady Jet Start-up

8.1.1 Flow Conditions

This section considers the starting process of a sonic jet in hypersonic crossflow, at flow conditions corresponding to the steady case presented in Chapter 6. A square-wave, impulsive start-up is considered, where the jet is instantaneously started into a fully developed hypersonic crossflow, with laminar in-flow boundary layer. As discussed in Chapter 7, Sau and Mahesh (2010) showed that the flow-field does not differ between ideal square waveforms and imperfect square waves produced experimentally. Therefore, consistent with Chapter 7, an ideal square wave start-up is considered. Jet velocity, $U_j = 317$ m/s when the jet is on (corresponding to Mach 1 with $T_j = 250$ K), while jet pressure and density are set to maintain $J = 5.3$, $p_{0j}/p_\infty = 251$, and $Re_j = 88.5 \times 10^3$ as per the previous steady and pulsed cases. The hypersonic crossflow conditions and computational conditions (domain, mesh, boundary conditions) are also identical to those considered in Chapter 6.

8.1.2 Flow Structure

The shock and vortex structures in the jet centre-line ($z = 0$) during the initial jet start-up ($0 < \tau < 10$) are provided in Figures 8.1 (density gradient) and 8.2 (span-wise vorticity) respectively; animations are provided in the supplementary material. The initial shock structures generated are analogous to the jet in quiescent atmosphere,

described in Chapter 5, and consist of a lead shock which travels out into the crossflow, followed by the jet interface, a normal shock (or Mach shock), and a starting vortex, which forms at the edge of the orifice and travels with the jet fluid into the crossflow (see Figure 5.8). By $\tau = 1$, the lead shock has reached beyond the laminar in-flow boundary layer, and has emerged into the hypersonic crossflow. The developing Mach shock remains within the boundary layer, so is unaffected by the crossflow during the early stages of flow development.

By $\tau = 2$, the lead shock and Mach shock both extend into the crossflow, and are deformed. The Mach shock is turned downstream to form a Mach disk, while the two oblique barrel shocks have also formed and been deflected by the crossflow, resulting in different structures between the windward and leeward barrel shocks. The starting vortex continues to develop at either end of the Mach disk, and the plane of this vortex is also rotated by the crossflow, to remain parallel with the Mach disk. A recompression shock can be observed between the leeward barrel shock and the flat plate at $\tau = 3$. At subsequent times, this recompression shock breaks away from the leeward barrel shock and moves downstream, as the obstruction caused by the jet increases, resulting in recompression of free-stream flow that has travelled around the barrel shocks occurring further downstream.

At $\tau = 3$, the adverse pressure gradient caused by the jet flow causes the in-flow boundary layer to separate, and a re-circulation region forms upstream of the jet outlet. A pair of counter-rotating horseshoe vortices form in this developing re-circulation region. These horseshoe vortices correspond to Vortex A and B from the fully developed flow-field described in Chapter 6. The region of separated flow upstream of the jet grows more slowly than the downstream region, and this smaller re-circulation region results in a simplified horseshoe vortex structure compared with the fully developed case.

At $\tau = 4$, the jet flow has extended further downstream. A reflected shock and a slip line form directly downstream of the Mach disk, and extend between the Mach disk and the flow interface. By $\tau = 7$ the barrel shocks and Mach disk appear fully developed. The Mach disk height has reached $2.8d_j$, or 85% of the time-averaged value for the fully developed jet, while the upstream region of separated flow remains small, with flow separation occurring approximately $4.1d_j$ upstream of the jet outlet, only 19% of the time-averaged value for the fully developed jet. Upstream of the jet outlet and outside the boundary layer, the outward motion of the jet flow is prevented by the crossflow. The bow shock forms at the interface between these two flows. Both downstream of the jet orifice, and within the upstream re-circulation region, the lead shock continues to travel radially outward, while the recompression shock has separated from the leeward barrel shock, but remains beneath the Mach disk. The slip line developed downstream of the Mach disk continues to extend downstream with the flow interface. The upstream starting vortex has rotated and now travels approximately parallel with the crossflow, while trailing vorticity continues to form at the upstream barrel shock, in the shear-layer between the upstream starting vortex and the jet outlet.

From $\tau = 7$, the starting vortex begins to separate from the Mach disk, as it convects

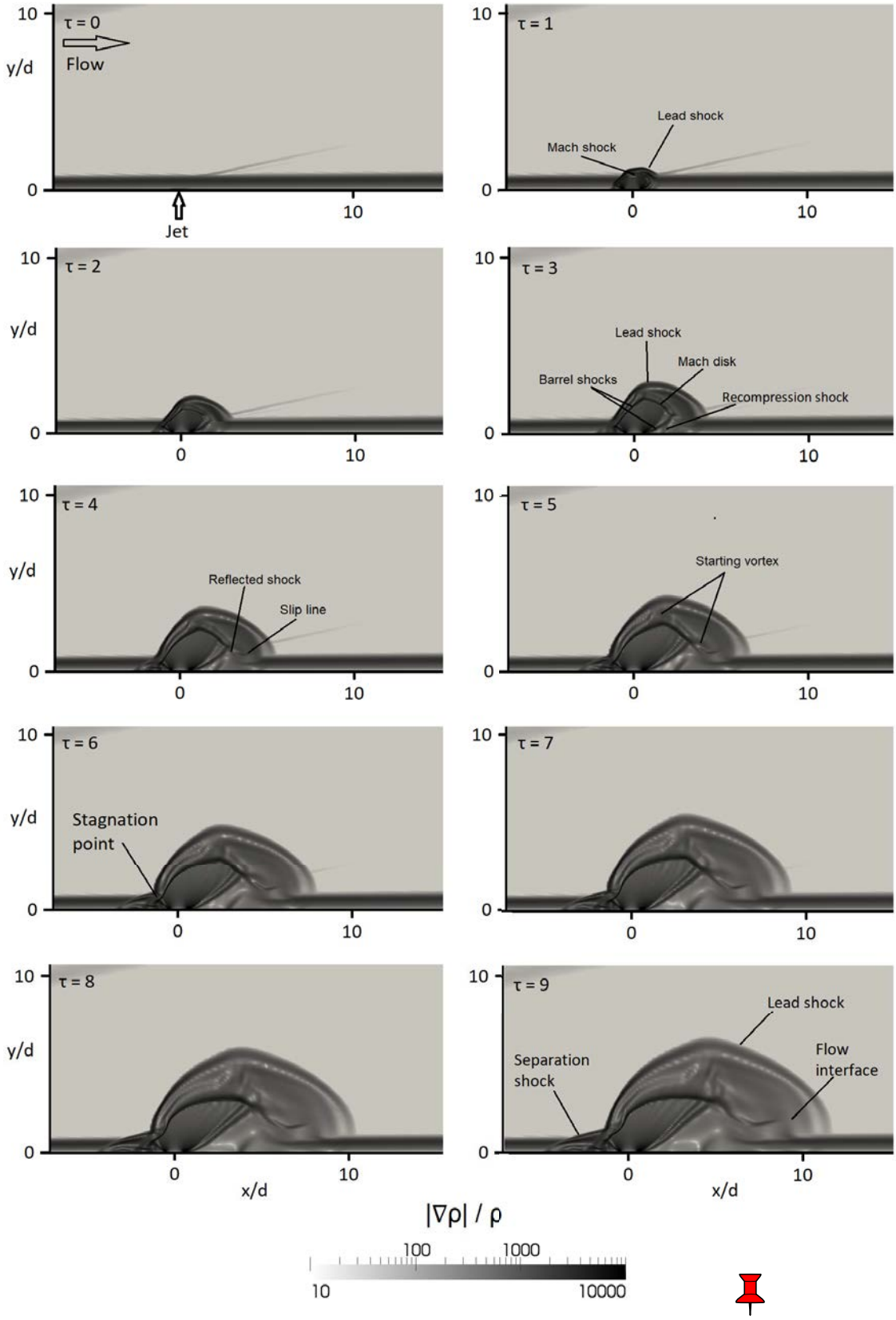

Figure 8.1: Contours of instantaneous density gradient magnitude in the plane of symmetry, showing shock structure during jet start-up, at time intervals corresponding to $\tau = 1$.

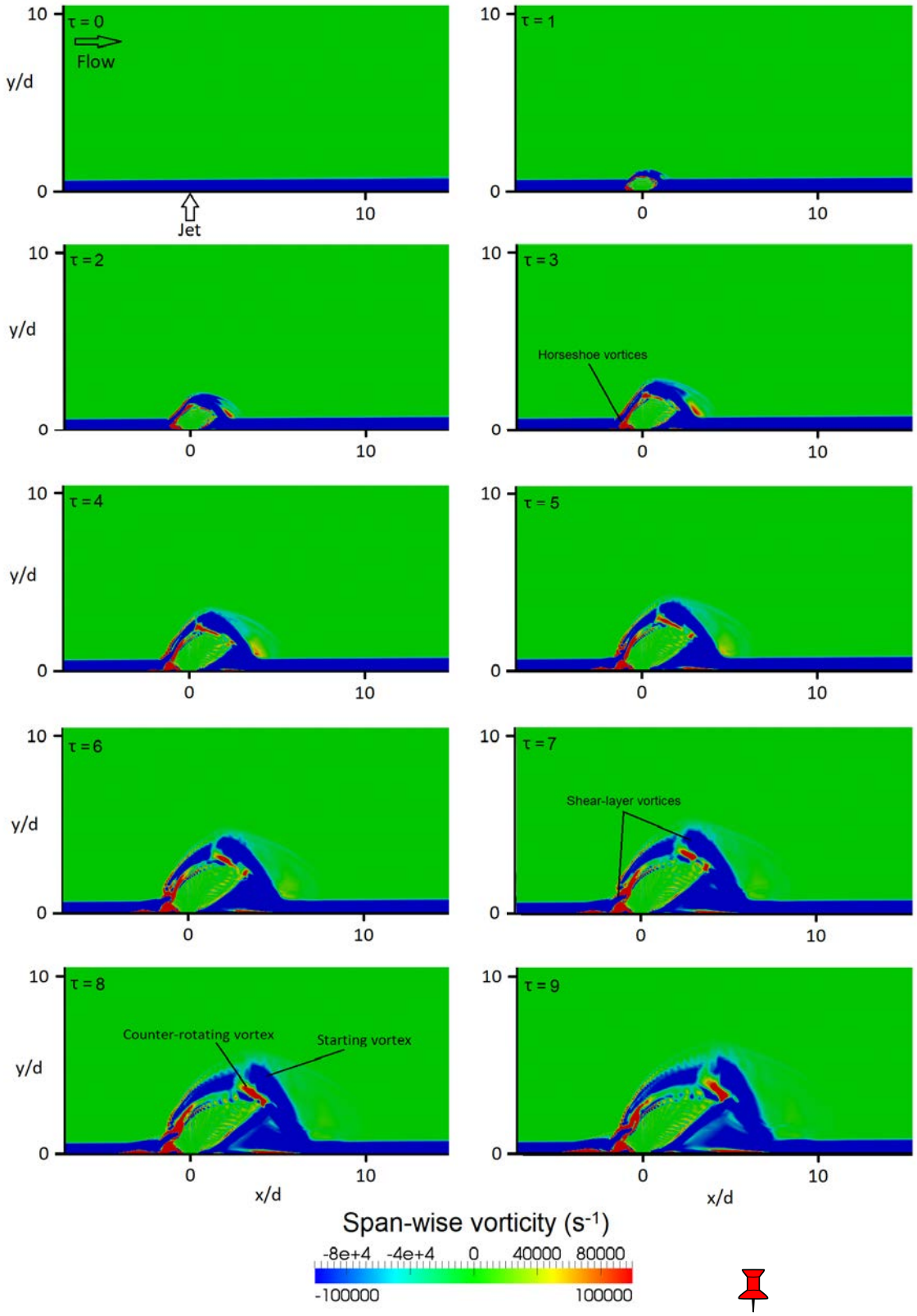

Figure 8.2: Contours of instantaneous span-wise vorticity in the plane of symmetry, showing vortex structure during jet start-up, at time intervals corresponding to $\tau = 1$.

downstream. At the same time, the trailing vorticity rolls-up, leading to the formation of a second vortex, which can be identified as a jet shear-layer vortex. This begins to form above the stagnation point, which remains close to the jet outlet, due to the small separated flow region upstream. This forming shear-layer vortex deforms the bow shock and windward barrel shock. The outward motion of the lead shock downstream of the jet elongates the upstream starting vortex in the vertical (y) direction. Meanwhile the downstream starting vortex also travels downstream, and entrains fluid from the co-rotating vortices in the boundary layer.

At $\tau = 8$, the lead shock extends greater than 10 jet diameters downstream, while the separation shock only extends approximately 5 jet diameters upstream, and the flow interface is approximately 8 jet diameters downstream. As described previously, the starting vortex continues to detach from the windward barrel shock and Mach disk, and convects downstream. This starting vortex is accompanied by a counter-rotating vortex, which originates in the re-circulation region on the flat plate, at the upstream edge of the jet orifice (i.e. horseshoe Vortex A described in Chapter 6).

During the early stages of flow development, the upstream separated flow region is not fully developed. As a result, the jet shear-layer vortices form much closer to the jet outlet. The proximity of the shear-layer to the re-circulation vortex causes the development of distinct counter-rotating vortices which shed with the conventional shear-layer vortices as a counter-rotating pair, as shown in Figure 8.2 at $\tau = 7$ to $\tau = 9$. This counter-rotating shear-layer vortex behaviour was observed by Won et al. (2010) for a sonic jet in supersonic (Mach 3.4) crossflow with a turbulent in-flow boundary layer, but has not been observed in other studies, and was not observed in the fully developed jet case described in Chapter 6. The phenomenon appears to be related to the upstream separated flow region, which affects the proximity of the shear-layer vortex formation to the jet outlet. If the upstream separated region is sufficiently small, the jet shear-layer vortices will form close to the jet outlet, in close proximity to the re-circulation vortex, which has rotation opposite the jet shear-layer vortices. The result is the formation of counter-rotating pairs of shear-layer vortices, rather than a single distinct shear-layer vortex as conventionally described. This fits well with the observation of Won et al. (2010), that the negative span-wise vorticity scales with free-stream velocity, while positive span-wise voriticity scales with jet exit velocity.

The development of the flow at later times, $10 < \tau < 100$, is shown in Figures 8.3 (density gradient) and 8.4 (span-wise vorticity); animations are provided in the supplementary material. At $\tau = 20$, the lead shock has reached the domain outlet, at $x/d_j = 25$, while the slip line has extended further downstream from the Mach disk, to the flow interface, at $x/d_j \approx 18$. At this time, the recompression shock, reflected shock, and slip line all converge to a single point, as observed in Figure 8.3. The barrel shocks and Mach disk are fully developed, and the Mach disk height has reached the time-averaged value for the fully established jet. The upstream separation region continues to grow, and the bow shock continues to form as the lead shock expands radially from the jet orifice.

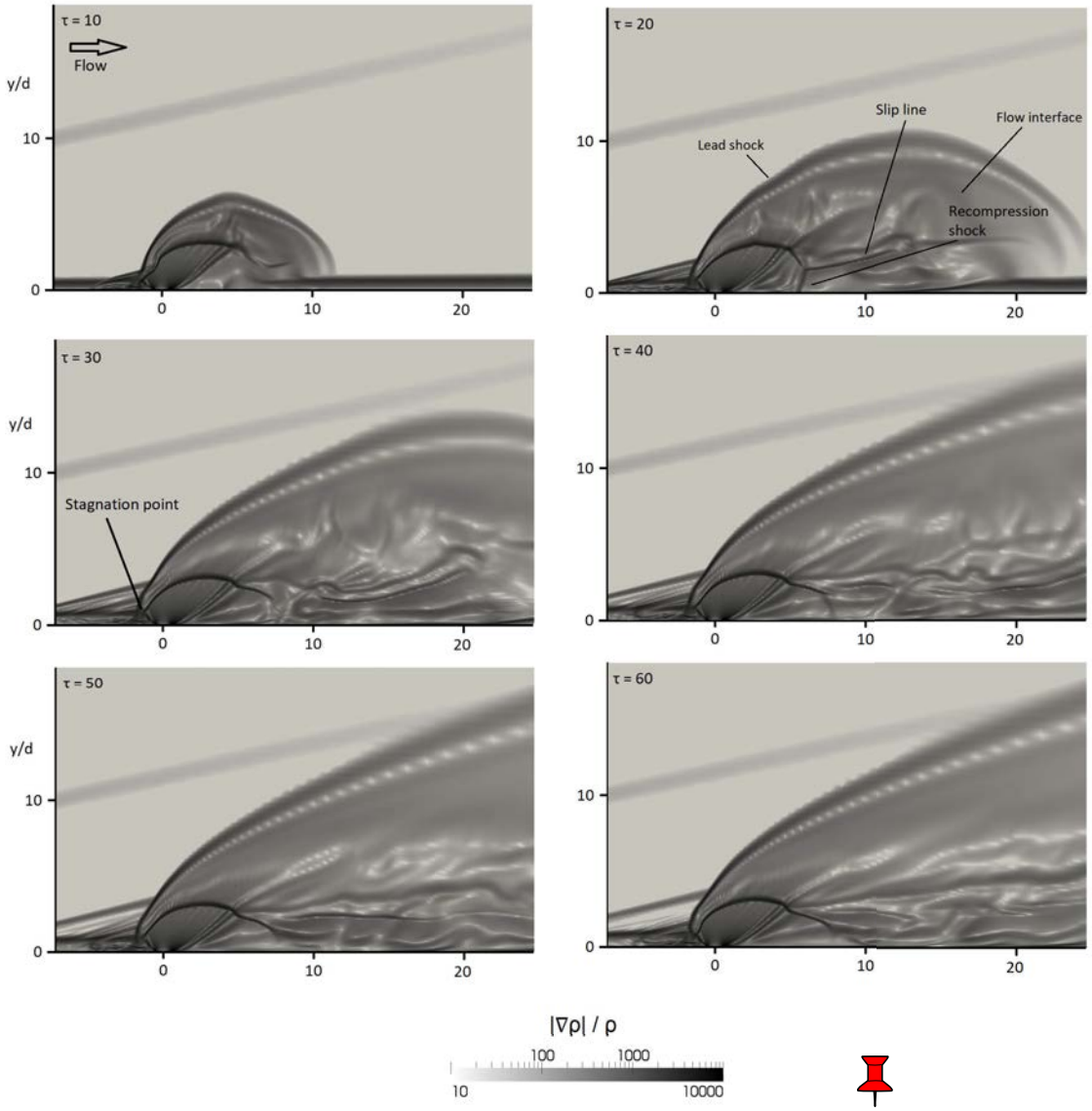

Figure 8.3: Contours of instantaneous density gradient magnitude in the plane of symmetry, showing shock structure during jet start-up, at time intervals corresponding to $\tau = 10$.

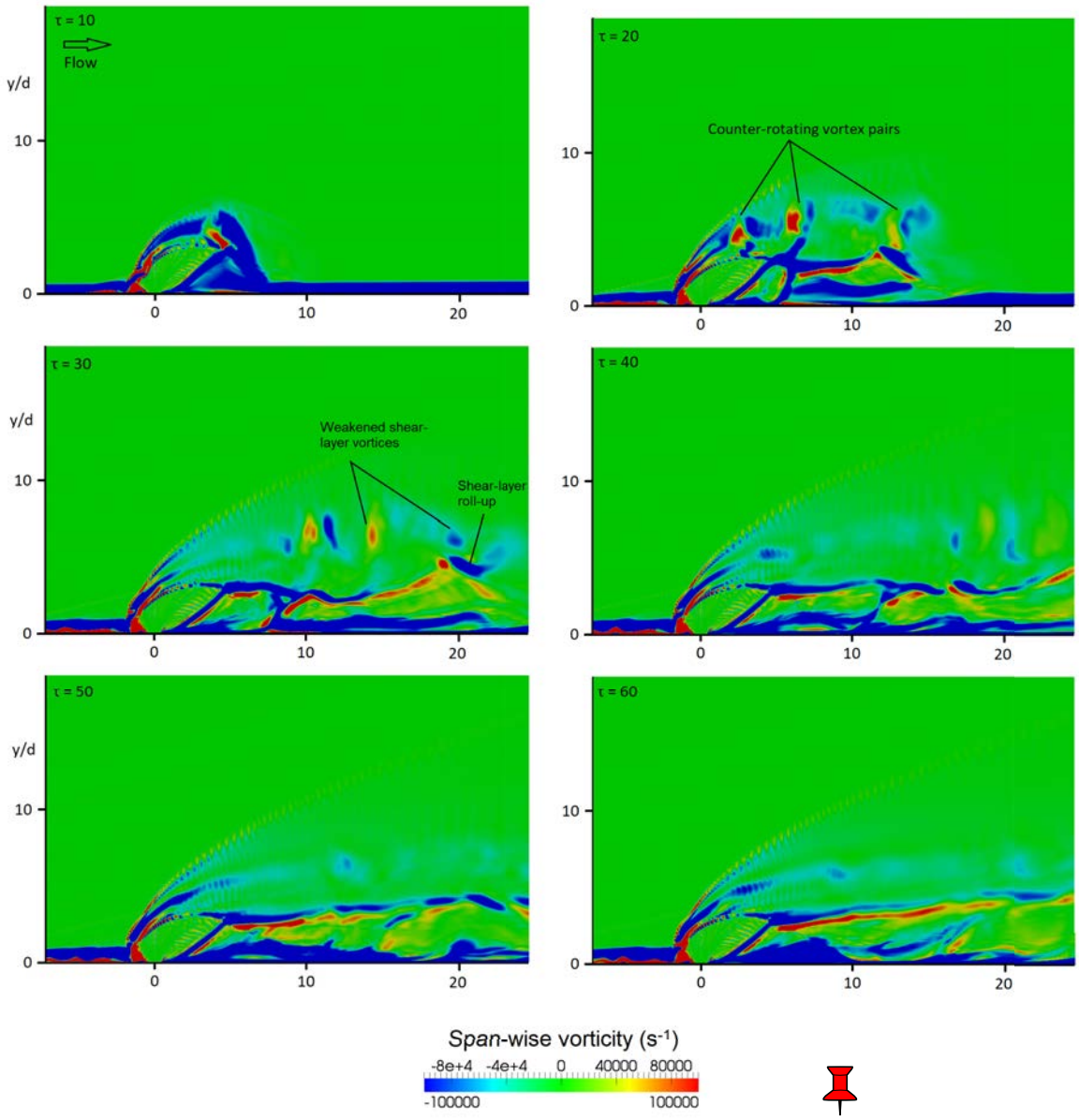

Figure 8.4: Contours of instantaneous span-wise vorticity in the plane of symmetry, showing vortex structure during jet start-up, at time intervals corresponding to $\tau = 10$.

By $\tau = 30$, the slip line has been deformed by shear-layer vortex shedding, and the unsteady recompression shock can no longer be clearly identified in the plane of symmetry. The upstream starting vortex weakens as it travels downstream, while the slip line rolls-up at the flow interface, which has reached $x/d_j \approx 22$. The downstream flow-field continues to develop, with the flow interface reaching the domain outlet at $\tau \approx 40$. At this time, the upstream separated flow region has extended further but continues to develop, the bow shock has fully developed, and the thicker separated boundary layer causes the stagnation point to be located further from the jet outlet, and further from the flat plate, as shown in Figure 8.3.

The development of the upstream separated region continues until $\tau \approx 60$. As a result, for times $\tau < 60$ the stagnation point remains close to the jet orifice, and counter-rotating shear-layer vortices are observed. For $\tau > 60$, the upstream re-circulation region is fully formed, and a series of separation shocks have formed upstream of the stagnation point. As a result, the shear is reduced at the stagnation point and jet shear-layer vortices are not observed close to the jet orifice. This prevents the formation of counter-rotating shear-layer vortices, as the vorticity formed in the re-circulating vortex (horseshoe Vortex A) remains confined to this region. This marks the transition to a quasi-steady state, as described in Chapter 6.

As described, jet shear-layer vortices shed periodically in counter-rotating pairs during jet start-up. During the initial start-up period, $0 < \tau < 20$, the shear-layer vortex shedding frequency is $St_\infty \approx 1/6$, equal to that observed in the fully-developed flow. However, there is a time period $20 < \tau < 60$ where there appears to be no regular shear-layer vortex shedding, only a single vortex pair is shed during this period. This results in reduced barrel shock deformation, and an unperturbed mixing layer during this time period, which supports the conclusions drawn in Chapter 6, that the mixing layer is deformed by the shear-layer vortex shedding. No clear physical mechanism has been identified for the lack of vortex shedding during this period; the barrel shocks and bow shock are established in the jet region, so the Kelvin-Helmholtz instability in the shear-layer is unchanged in comparison to the fully established flow. However, variations in shear-layer vortex shedding frequency are not without precedent, significant aperiodicity has been observed in other studies (Mahesh, 2013). For example, Gutmark and Ho (1983) observed variations in shedding frequency between $St_j = 0.24$ and $St_j = 0.64$ in a laminar free jet, while Ben-Yakar (2000) observed $0.8 < St_j < 1.2$ in a sonic jet in supersonic crossflow. For the current case, the vortex shedding frequency during the period $20 < \tau < 60$ drops to $St_\infty \approx 1/40$, while for $\tau > 60$, jet shear-layer vortex shedding returns to the natural frequency of $St_\infty \approx 1/6$. As discussed previously, counter-rotating vortices are shed during start-up, while $\tau < 60$, single vortices are shed once the flow is fully developed, while $\tau > 60$.

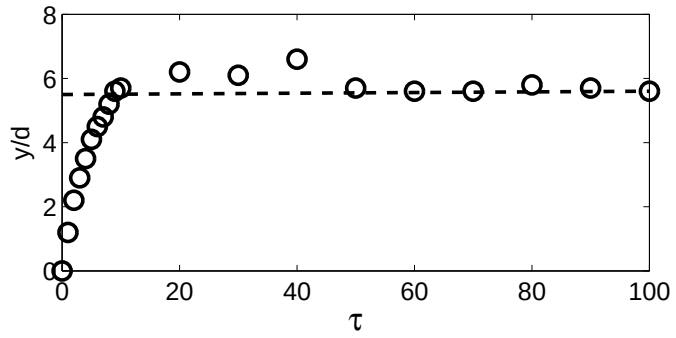

Figure 8.5: Jet penetration vs. time during jet start-up. ∘: Instantaneous penetration, Dash line: time-averaged penetration.

8.1.3 Penetration

Penetration was measured as the maximum height in the y direction of the instantaneous stream-line that originates from the centre of the jet outlet. A plot of penetration vs. time is provided in Figure 8.5. Time-averaged penetration data for the fully established jet from Section 7.3 is also included for comparison.

During the initial start-up, while $\tau < 10$, the penetration increases with time, at a slightly decreasing rate. This corresponds to the period where the barrel shocks and Mach disk are extending out from the jet orifice and being turned by the crossflow. At $\tau = 10$, the jet barrel shocks and Mach disk are formed, and jet penetration reaches the time-averaged value of $y/d_j = 5.6$. When this occurs, the rate of change of penetration depth decreases rapidly. A small overshoot in jet penetration is observed during the period $10 < \tau < 50$, while maximum jet penetration is not achieved until $\tau = 40$, with a value of $y/d_j = 6.6$, corresponding to an 18% overshoot of the time-averaged value. Maximum penetration is not observed immediately, penetration reaches a steady value of $y/d_j = 6.2$ (10% overshoot) during the period $20 < \tau < 30$, before increasing again to the maximum value at $\tau = 40$.

The overshoot in jet penetration corresponds to the period where the intial jet flow is yet to reach the domain outlet. During this time, the jet flow continues to expand in the upward and downstream directions, away from the jet orifice, behind the lead shock. Penetration peaks at $\tau = 40$, when the initial jet flow reaches the domain outlet, and returns to the quasi-steady value by $\tau = 50$. Therefore, the period of overshoot from $10 < \tau < 50$ corresponds to the time period where the initial jet fluid is expanding behind the lead shock, and moving toward the domain outlet. During this time, the upstream separated flow region and the bow shock are still forming, and reduced shear-layer vortex shedding is observed. This behaviour differs from pulsed jets in subsonic crossflow, where increased penetration is linked to formation of strong shear-layer vortex rings which penetrate deeply into the crossflow (Gevorkyan et al., 2016). Here, maximum penetration is observed during the start-up period, as the lead shock extends into the crossflow.

At times $\tau > 40$, the jet penetration returns to the time-averaged value, with

small oscillations about the mean corresponding to the instantaneous flow structure. Instantaneous penetration slightly increases at shear-layer vortex shedding events, for example, at $\tau = 80$.

8.1.4 Surface Pressure and Jet Force

A time-series of instantaneous pressure distribution during jet start-up is provided in Figure 8.6. Pressure variations are only present within the area contained by the lead shock, so only a small region of the plate is affected during the initial start-up. For $\tau < 2$, the lead shock and barrel shocks are indistinguishable from each other, while the individual shock structures can be resolved for $\tau > 3$. The lead shock corresponds to a region of increased pressure that travels radially outward from the jet orifice. The high pressure region generated by the lead shock is able to travel upstream through the in-flow boundary layer, and therefore continues to move upstream along the plate for $\tau > 5$. The presence of the lead shock increases peak pressure, as described in Section 7.4.

In the barrel shock region, the peak pressure increases over the period $0 < \tau < 10$. An additional high pressure region corresponding to the bow shock forms, and wraps around the jet orifice. A low pressure region immediately downstream of the jet orifice forms immediately, due to the obstruction of the free-stream flow caused by the jet. This low pressure region expands between the jet orifice and lead shock in the stream-wise direction, and between the plane of symmetry and the bow shock in the span-wise direction. In the span-wise direction between the bow shock and the lead shock, the pressure remains higher than the free-stream, as the boundary layer is separated in this region.

Within the region upstream of the jet, between the barrel shock and the jet orifice, a small high pressure region develops, corresponding to the upstream re-circulation vortex (horseshoe Vortex A). This high pressure region partially wraps around the jet orifice.

At later times, $10 < \tau < 60$, shown in Figure 8.7 (animations are provided in the supplementary material), the high pressure region caused by the lead shock continues to spread radially from the jet orifice. In the upstream region, this high pressure spreads out as the region of separated flow grows. Downstream, the localised high pressure regions on the jet centre-line at $x/d_j \approx 10$ observed in Chapter 6 are present, corresponding to convergence of the free-stream flow, which was deflected around the jet, back toward the jet centre-line. The region of separated flow behind the lead shock, upstream of the jet orifice, maintains a pressure above the free-stream value, while a low-pressure region forms immediately upstream of the bow shock. The low pressure region immediately downstream of the jet outlet is maintained.

During the period $20 < \tau < 60$, no deformation of the barrel shocks is observed, as shear-layer vortices are not regularly shed. An example of the barrel shock deformation caused by jet shear-layer vortex shedding can be observed at $\tau = 20$ in Figure 8.7. Once

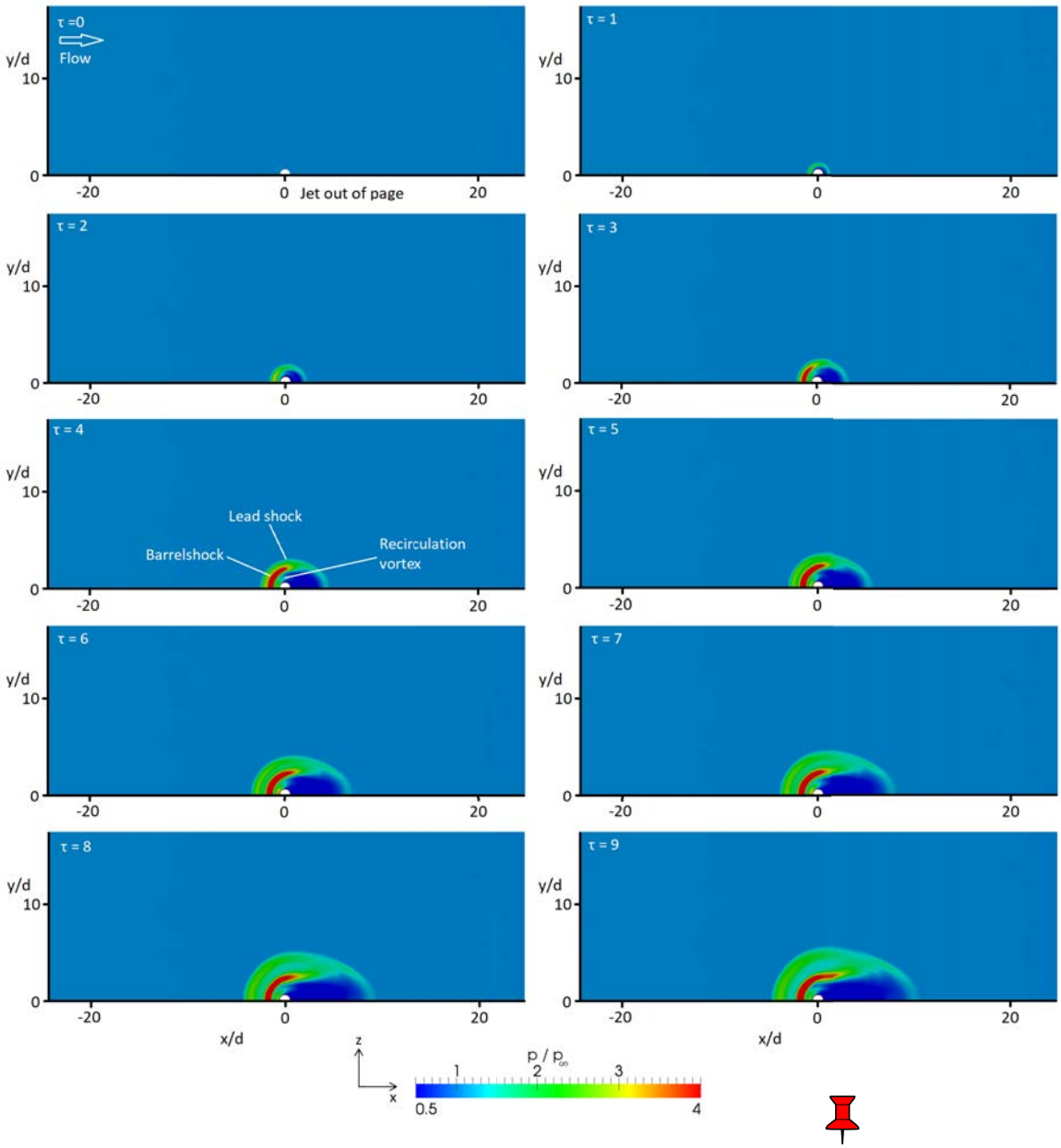

Figure 8.6: Instantaneous surface pressure distribution during jet start-up, at time intervals corresponding to $\tau = 1$.

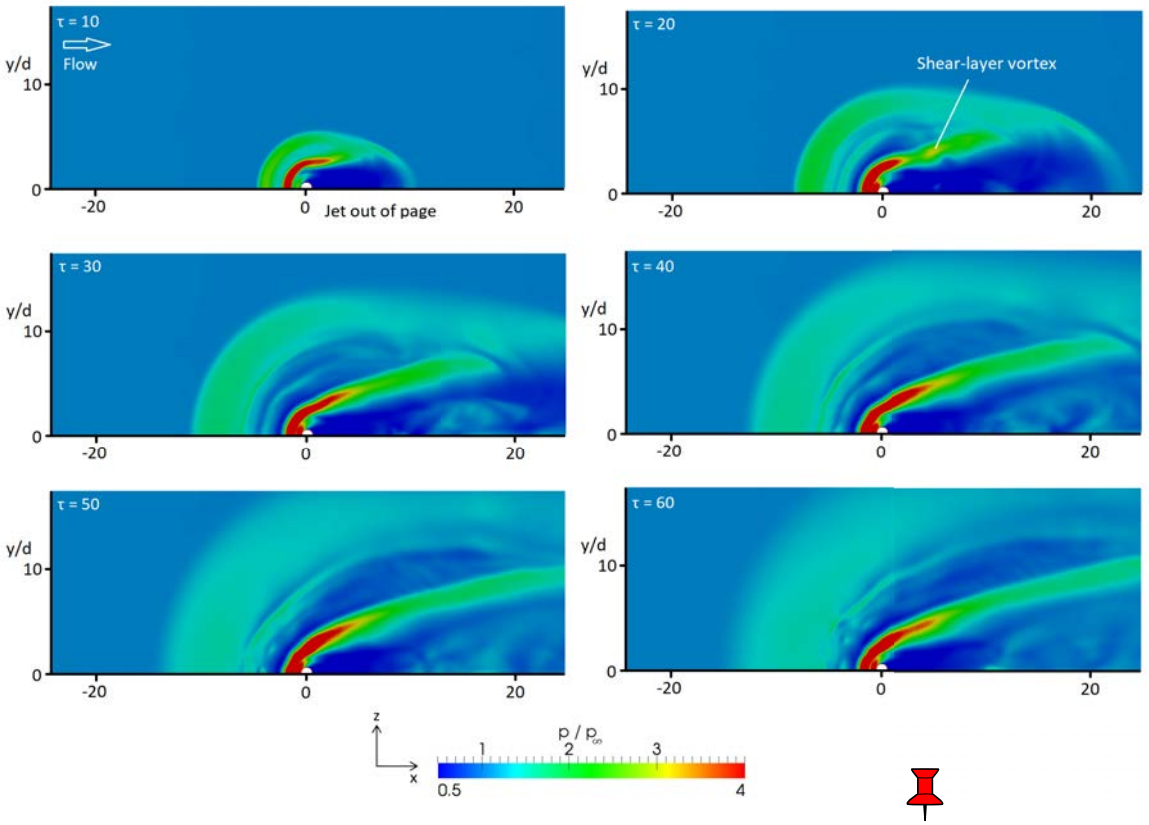

Figure 8.7: Instantaneous surface pressure distribution during jet start-up, at time intervals corresponding to $\tau = 10$.

the lead shock and bow shocks have reached the downstream domain outlet, at $\tau \approx 60$, the surface pressure distribution downstream of the jet outlet resembles that of the fully developed flow described in Chapter 6.

The resulting interaction force, F, can again be obtained by integrating the surface pressure. This result is provided in Figure 8.8, in non-dimensional form, with the jet thrust coefficient and time-averaged jet interaction force, calculated in Chapter 6, also provided for comparison.

Initially, the jet interaction force increases linearly over the period $0 < \tau < 40$. At $\tau = 40$, the interaction force overshoots the time-averaged value of $\overline{C_F} = 0.9$ reported in Chapter 6, by 18%, with a peak value of $C_F = 1.064$. The magnitude and timing of this overshoot directly corresponds to the peak penetration observed during the jet start-up, indicating that penetration and control force are strongly linked. However, the nature of the time dependent force differs from the jet penetration. The time-averaged force is not reached until $\tau = 35$, while time-averaged penetration is achieved within $\tau < 10$. The penetration is driven by the establishment of the barrel and Mach shocks, while the interaction force is driven by the formation of the bow shock, and the expansion of the downstream low pressure region behind the lead shock. As shown in Figure 8.7, the bow shock and downstream low pressure region are established over $\tau \approx 50$; after this time, the downstream region resembles the fully developed flow. As a result, the interaction force evolves over the same time period. During the period $50 < \tau < 60$,

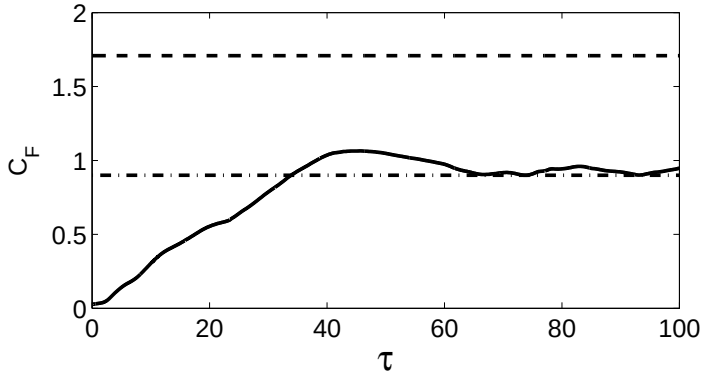

Figure 8.8: Jet thrust coefficient (C_T, Dash line), interaction force coefficient (C_F, Solid line), and time-averaged interaction force coefficient ($\overline{C_F}$, Dot-dash line).

the interaction force continues to decrease, corresponding to the continued formation of the upstream re-circulation region, which is a region of high pressure. Small variations are also observed in the interaction force at later times, corresponding to the formation and motion of individual vortex structures.

While the linear increase in control force is observed over a longer period than the increase in penetration, the development of the jet interaction force occurs over a shorter time period than observed in previous work. DeSpirito (2012) reported that the interaction force development for a sonic jet takes $\tau \approx 160$ in supersonic crossflow, while Ebrahimi (2000) reported a start-up time of $\tau \approx 100$ for a supersonic (Mach 3) jet in a Mach 5 crossflow. Here, the faster development time is due to the simplified geometry of a flat plate, compared with a finned missile configuration used by Ebrahimi (2000) and DeSpirito (2012). With a finned missile, the shocks wrap around the cylindrical body, and a significant force overshoot is observed while the lead shock passes over the fins. Force development is also dependent on the size of the missile or flat plate, a larger downstream area relative to the jet diameter will result slower development of the interaction force. However, this study allows the link to be drawn between the interaction force, and the development of specific flow structures (bow shock, lead shock etc.), which has not been previously documented.

8.2 Pulsed Jet Start-up

8.2.1 Flow Conditions

This section considers the start-up of the pulsed jet cases described in Chapter 7. As described in the previous section, the jets are impulsively started into a fully developed hypersonic crossflow, with a laminar in-flow boundary layer, with jet velocity, momentum ratio, and pressure ratio maintained from Chapter 7.

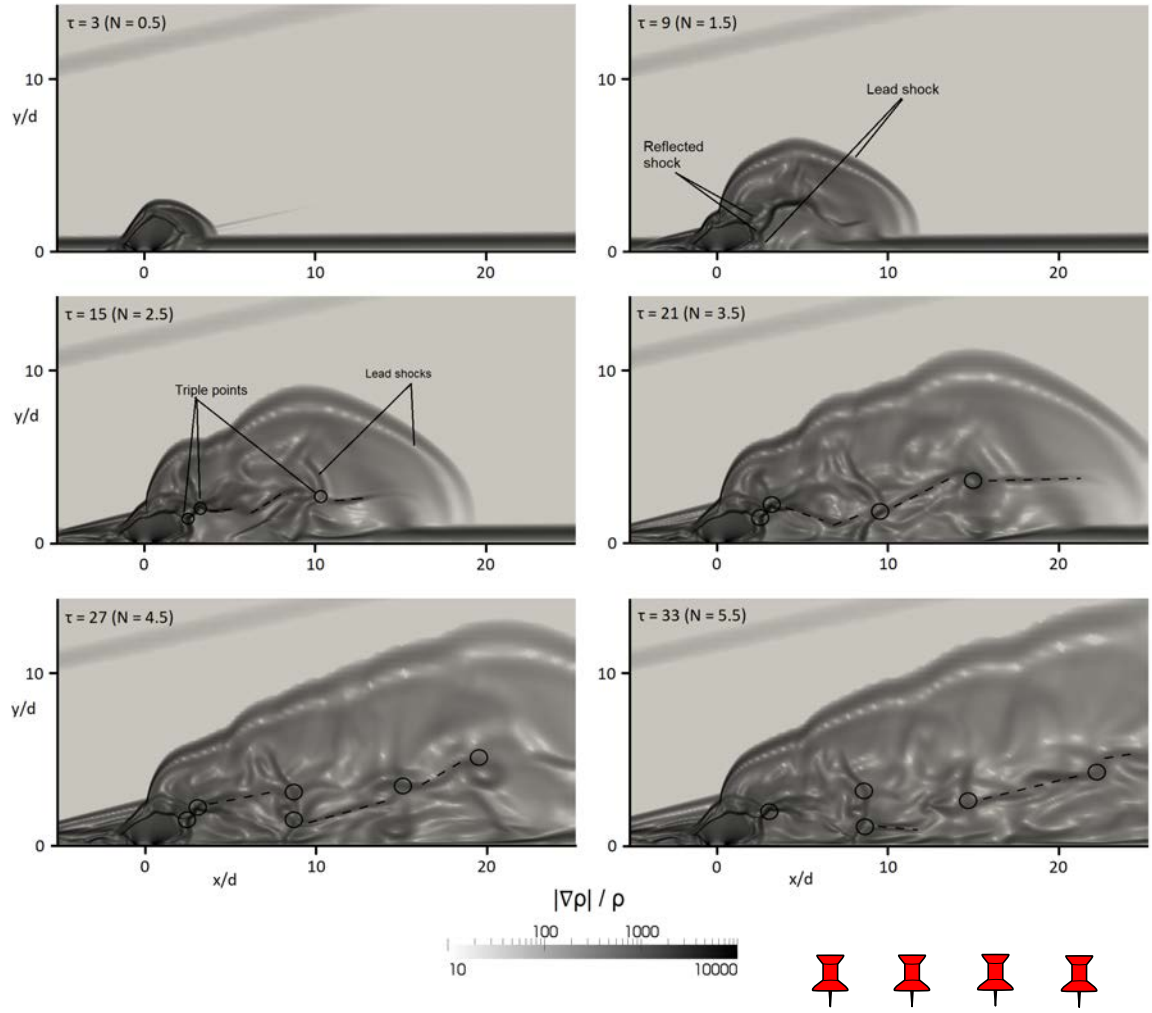

Figure 8.9: Contours of instantaneous density gradient magnitude in the plane of symmetry, showing shock structure during jet start-up for pulsed jet Case I ($\alpha = 0.5$, $St_\infty = 1/6$), at time intervals corresponding to $\tau = 6$ ($\tau = N$).

8.2.2 Flow Structure

The shock and vortex structure of the pulsed jet (Case I) in the jet centre-line ($z = 0$) during jet start-up are provided in Figures 8.9 (density gradient) and 8.10 (span-wise vorticity), respectively. Animations of all pulsed cases are provided in the supplementary material. The initial start-up behaviour of the pulsed jet, during the period $0 < \tau < w$ (i.e. during the initial pulse) is identical to the steady jet start-up. However, during the period $w < \tau < N$ the jet is switched off, resulting in the collapse of the shock structures, as described in Section 7.2. The times shown in Figures 8.9 and 8.10 correspond to the jet switching off at the end of the first six consecutive pulsing cycles.

In the pulsed cases, the Mach and barrel shock structures only develop while the pulse is on. As the pulse width w is identical to the cases considered in Chapter 7, the second and subsequent pulses give a qualitatively similar barrel shock and Mach disk structure to the fully-developed pulsed jet (see Figure 7.13). However, there are

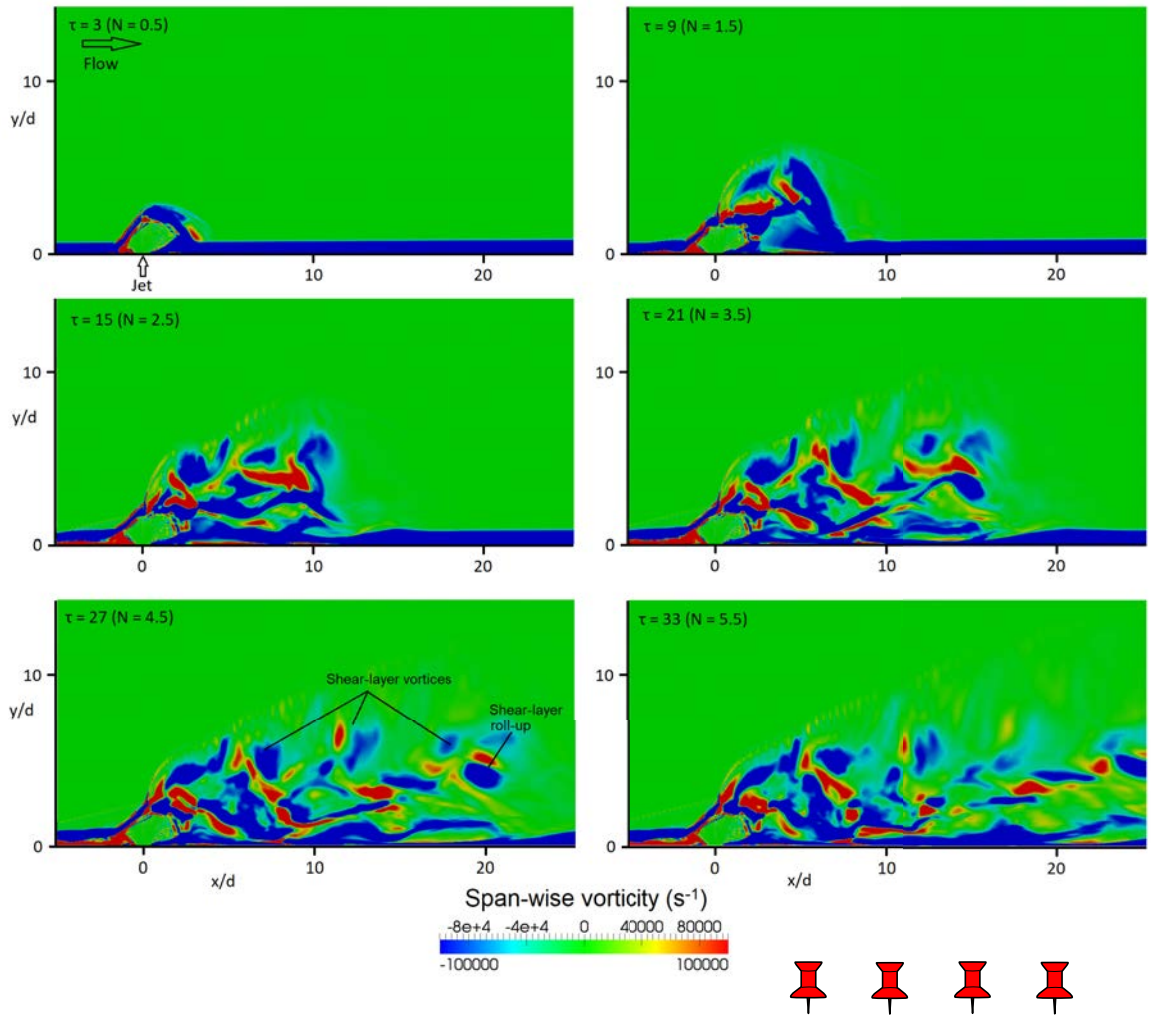

Figure 8.10: Contours of instantaneous span-wise vorticity in the plane of symmetry, showing vortex structure during jet start-up for pulsed jet Case I ($\alpha = 0.5$, $St_\infty = 1/6$), at time intervals corresponding to $\tau = 6$ ($\tau = N$).

slight differences in barrel shock and Mach disk structure, as a result of the upstream re-circulation region, which continues to develop over multiple pulsing cycles. As the upstream re-circulation region increases in size, the stagnation point and windward barrel shock move further from the jet orifice, analogous to the start-up process for the steady jet. This results in an increasing Mach disk height over consecutive pulsing cycles. In the steady jet start-up case, the Mach disk height reached 85% of the time-averaged value by $\tau = 7$, while the time-averaged value was reached by $\tau = 10$. In the pulsed Case I, the Mach disk height reaches 42% of the steady jet time-averaged value when the jet is switched off at the end of the first pulse ($\tau = 3$), 46% at the end of the second pulse ($\tau = 9$), 52% in the third pulse ($\tau = 15$), and for the fourth and subsequent pulses ($\tau > 21$) the Mach disk height is approximately 55% of the steady jet time-averaged value at the end of each pulsing cycle, when the jet is switched off. Therefore, the barrel and Mach shocks show a small dependence on the upstream separated flow region for Case I. Similar behaviour is observed in the other pulsed cases. The high L/D cases (Case I and Case IV) have a higher Mach disk, and therefore the shock structure shows a higher dependence on the development of the upstream re-circulation region. Case II and Case III have a low L/D, resulting in a lower Mach disk, which is nearly independent of the development of the re-circulation region upstream of the jet outlet.

Similar to the steady jet start-up case, counter-rotating shear-layer vortices are observed during the initial period, before the upstream re-circulation region is fully established. The time period over which these counter-rotating vortices are observed depends on the barrel shock and Mach shock structure. In the steady case, transition from counter-rotating shear-layer vortices occurred at $\tau \approx 60$. For the pulsed Case I, the influence of the upstream re-circulation region on the Mach disk and barrel shocks is small in comparison to the steady jet, so the shock structures are fully developed for $\tau > 21$, as described previously. As a result, counter-rotating shear-layer vortices are only observed for $\tau < 21$. In the pulsed cases, the Mach disk height is lower than the steady jet, and the re-circulation vortex is smaller, due to the reduced stroke ratio, as mentioned. Therefore, the transition from counter-rotating jet shear-layer vortices to single shear-layer vortices is expected to occur earlier for lower stroke ratio cases, which have a lower Mach disk. This is consistent with the observed behaviour. In the steady jet case ($L/D = \infty$), transition occurs at $\tau = 60$, for Case I and Case IV ($L/D = 1.2$), the first three shear-layer vortices are counter-rotating, corresponding to transition at $\tau \approx 20$, while in Case II and Case III ($L/D = 0.6$ and 0.8 respectively), only the starting vortex is shed as a counter-rotating pair, corresponding to transition at $\tau < 5$.

In the downstream region, a series of triple points and slip lines are formed during each pulsing cycle, in the region between the barrel shocks and the flow interface. These are analogous to the fully established pulsed jet case, where the bow shock is deformed between cycles and a shear-layer forms downstream of the Mach disk. This shear-layer is periodically deformed by the shedding of shear-layer vortices once per pulse cycle, the collapse of the shock structure when the jet is off, and by the entrainment of free-stream flow which is prevalent in cases with a long jet-off time (i.e. Cases I and II).

The start-up process for the initial lead shock and the separated flow region is similar to the steady jet start-up case. The lead shock has reached the downstream domain outlet by $\tau = 20$, the flow interface reaches the jet outlet at $\tau \approx 40$, while the upstream re-circulation region continues to develop for $\tau < 60$.

The period without shear-layer vortex shedding observed during steady jet start-up is not replicated in the pulsed cases. The pulsing forces a shear-layer vortex to be shed once per pulse cycle. The initial counter-rotating shear-layer vortex pair is observed in all pulsed cases. This vortex pair weakens as it travels downstream, as observed for the steady jet start-up. The shear-layer formed downstream of the Mach disk also rolls-up at the flow interface for all pulsed cases, which was also observed in the steady jet start-up case.

Once the lead shock and flow interface have extended downstream, the secondary shear-layer begins to form, due to the interaction of successive lead shocks with the flat plate, as described in Chapter 7. For Case I, this secondary shear-layer can be observed when $\tau > 20$ in Figures 8.9 and 8.10. This secondary shear-layer is partially developed at $\tau = 27$, and is fully developed by $\tau = 33$, once the flow interface reaches the jet outlet. The development time of the secondary shear-layer is driven by the motion of lead shocks downstream, rather than the jet pulsing frequency and duty-cycle. Therefore, the development time is similar for all pulsed jet cases where the secondary shear-layer is observed.

8.2.3 Penetration

A plot of the penetration vs. time during start-up for each pulsed jet case is provided in Figure 8.11, along with time-averaged data from Chapter 7 for comparison.

In Case I ($\alpha = 0.5, St_\infty = 1/6$), the penetration initially increases rapidly, during the initial pulse $0 < \tau < 3$. At $\tau = 3$, the jet switches off, resulting in the collapse of the barrel shock structure. During the jet-off time period, the continued increase in penetration is due to the expansion of the flow from the initial pulse, behind the lead shock, into the crossflow. However, this rate decreases due to the collapsed barrel shocks and entrainment of free-stream flow. Over subsequent pulsing cycles, the Mach disk height increases due to the continued development of the upstream re-circulation region, as described previously, while the maximum penetration, as measured by the instantaneous stream-line that originates from the centre of the jet orifice, continues to be driven by the expansion of the initial pulse, which has not yet reached the domain outlet. The penetration peaks at the time-averaged value, at $\tau \approx 35$, as the initial jet pulse reaches the domain outlet. By this time, the upstream re-circulation region is sufficiently developed such that the Mach disk and barrel shock structures are quasi-steady. Subsequently, penetration reduces to 75% of the time-averaged value at $\tau = 56$, then returns to the time-averaged value by $\tau = 100$. The variations in penetration at times $\tau > 40$ are due to the instantaneous structure of shocks and vortices, the flow is in a quasi-steady state from $\tau = 40$ onward.

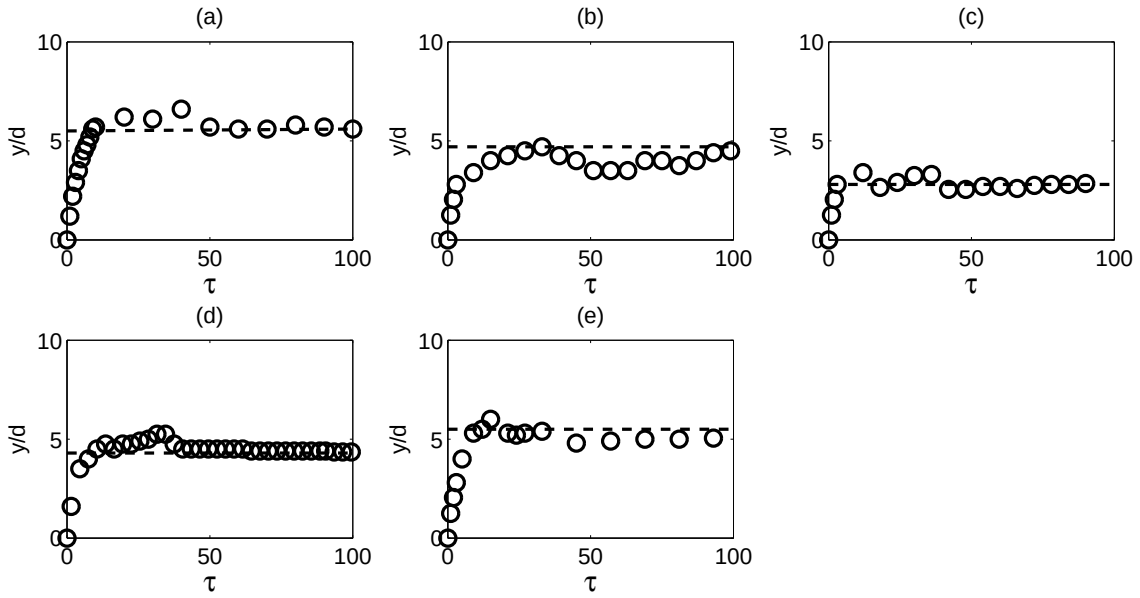

Figure 8.11: Jet penetration vs. time during jet start-up. ∘: Instantaneous penetration, Dash line: time-averaged penetration. (a) Steady jet, (b) Case I ($\alpha = 0.5, St_\infty = 1/6$), (c) Case II ($\alpha = 0.33, St_\infty = 1/6$), (d) Case III ($\alpha = 0.5, St_\infty = 1/3$), and (e) Case IV ($\alpha = 0.75, St_\infty = 1/4$).

Case II ($\alpha = 0.33, St_\infty = 1/6$) has a lower time-averaged penetration than Case I. This reduction in penetration is driven by increased entrainment of free-stream flow, due to the shorter duty-cycle and more significant collapse of the shock structure, as described in Chapter 7. As a result, the time-averaged penetration is reached within the first pulsing period. Once the jet is switched off, the entrainment of free-stream flow causes a down-wash effect, preventing further vertical expansion of the initial jet flow behind the lead shock. Therefore, unlike Case I, the penetration does not continue to increase with the jet off. As the Mach disk and barrel shocks are fully formed within the first pulsing cycle, and the formation of the upstream re-circulation region does not affect these shock structures for subsequent pulsing cycles, the penetration for Case II at times $\tau > 6$ is characterised by variations around the mean value. These variations correspond to the instantaneous shock structure, and entrainment of the free-stream flow. Overshoots of 20% and undershoots of 10% are observed during the period $10 < \tau < 40$. Note that data points in Figure 8.11 show penetration at the end of each pulse, so the undershoots and overshoots correspond to random variations between pulsing cycles, rather than variations within a pulse cycle. At later times, when $\tau > 40$, the downstream flow structure is fully established, and the temporal variations in penetration are reduced.

Case III ($\alpha = 0.5, St_\infty = 1/3$) follows a similar profile to the steady jet. The jet penetration initially increases at a slightly decreasing rate over the period $0 < \tau < 10$. Once the time-averaged penetration is reached, the rate of increasing penetration depth decreases rapidly, near constant penetration is observed over the period $10 < \tau < 30$. A

maximum 22% overshoot is observed at $\tau = 34$. The similarity between Case III and the steady case can be explained by the limited shock collapse and free-stream entrainment, driven by the short jet-off time. However, Case III has reduced penetration compared with the steady case due to the lower duty-cycle.

Finally, Case IV ($\alpha = 0.75, St_\infty = 1/4$) also follows a similar profile to the steady jet, due to limited shock collapse and free-stream entrainment, driven by the short jet-off time. The penetration initially increases rapidly, with shocks forming at a rate consistent with the steady case. Following this, a small overshoot is observed, peaking at 9% above the time-averaged value, at $\tau = 15$. Increased penetration, above the time-averaged value, is maintained during the period $10 < \tau < 40$, corresponding to the continued expansion of the inital jet pulse behind the forming lead shock, as observed in the steady case, and pulsed Cases I and III. Once the downstream shock structure is fully developed, at $\tau \approx 40$, the penetration reduces slightly. In this case, the steady penetration value achieved for $40 < \tau < 100$ is approximately 9% below the time-averaged value. This is due to the timing of each pulse. Figure 8.11 shows the instantaneous penetration when the jet is switched off. For Case IV, with a high duty-cycle, maximum penetration is achieved earlier in the pulse.

8.2.4 Surface Pressure and Jet Force

The surface pressure development during start-up for the pulsed cases is also similar to the steady jet start-up. Figure 8.12 shows instantaneous pressure distributions corresponding to the end of the jet pulse, for consecutive periods. Case I results are shown, animations for other cases are provided in the supplementary material.

The development of the pressure distribution is constrained within the region bounded by the initial lead shock. The low pressure region that forms downstream of the jet orifice is overlaid with periodic high pressure regions, corresponding to lead shocks from subsequent pulses. The deformed bow shock can also be observed wrapping around the jet orifice, corresponding to shear-layer vortex shedding which occurs during each pulsing period. The increase in pressure corresponding to the lead shocks are more clearly observed in the downstream region, where pressure is low, and are difficult to resolve upstream, where pressure is increased due to flow separation within the re-circulation region. As the shock structures have reached a quasi-steady state within $\tau \approx 20$ for Case I and IV, and within $\tau \approx 5$ for Case II and III, the pressure distribution near the jet orifice resembles the fully established cases described in Chapter 7 after these times. The downstream flow development is driven by the initial lead shock, and is independent of the pulsing regime. The downstream region develops over $\tau \approx 40$ for all cases. Similarly, the development of the upstream re-circulation region is driven by the motion of the lead shock within the upstream boundary layer. This occurs over a longer time period, $\tau \approx 60$, for all pulsed cases.

The resulting interaction force, F, is provided in Figure 8.13 for each case, along with the jet thrust T, in coefficient form (C_F and C_T). The behaviour during jet start-

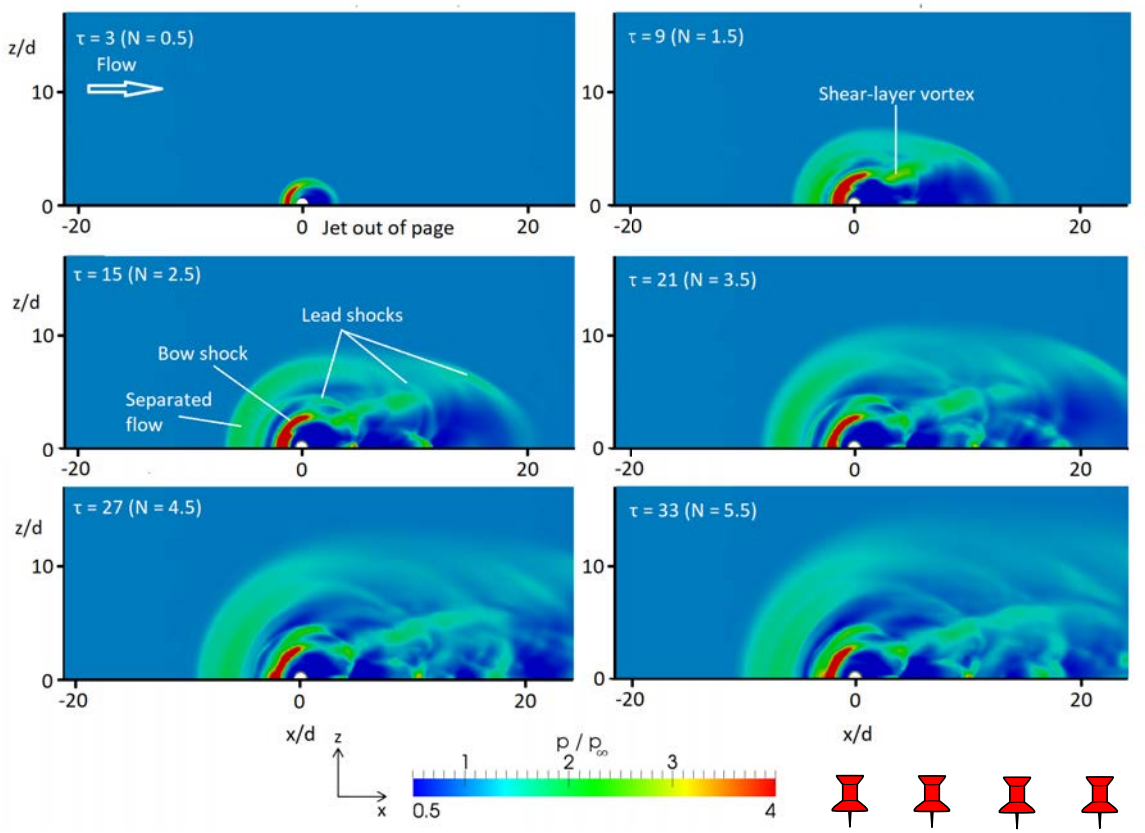

Figure 8.12: Instantaneous surface pressure distribution during jet start-up for pulsed jet Case I ($\alpha = 0.5, St_\infty = 1/6$), at time intervals corresponding to $\tau = 6$ ($\tau = N$).

up appears similar for all cases, including the steady case, with the jet force being established over a period of $\tau = 50$. The interaction force during start-up remains out of phase with the jet thrust, with maximum interaction force occurring when the jet is off.

In the steady case, an 18% overshoot was observed in the jet force. Overshoots of this magnitude are not observed in the pulsed jet cases. Case IV has a small overshoot, of approximately 10%, which occurs during the period $40 \lesssim \tau \lesssim 50$, the same time period as the steady jet overshoot, while Case III has an overshoot of approximately 7% over the same time period. No overshoot is observed in Cases I and II. Therefore, overshoots in jet interaction force are consistent with observed overshoots in jet penetration. In cases where overshoot is observed in the jet interaction force, the magnitude and timing of the overshoot corresponded to the overshoot in jet penetration.

As jet interaction force is primarily driven by the development of the large, low pressure region downstream, the force develops over the same time period for each case, including the steady case, with the fully developed interaction force being reached at $\tau \approx 50$. For $\tau > 50$, periodic fluctuations are observed in each pulsed case. Case I and Case II have peak-to-peak fluctuations of 17% of the time-averaged interaction force, while Case III and Case IV have peak-to-peak fluctuations of 10%. The larger fluctuations observed in Cases I and II correspond to shock collapse observed with longer jet-off times.

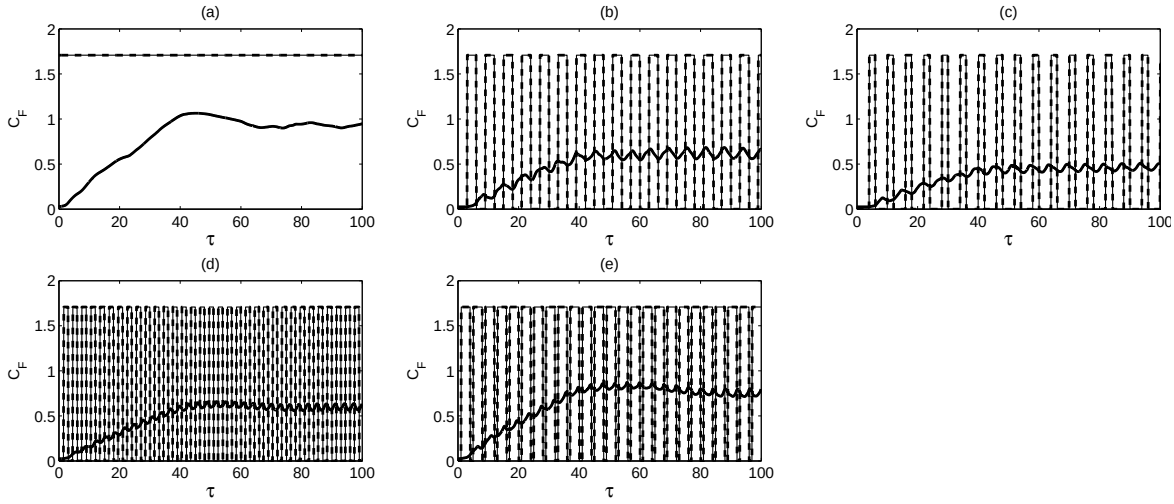

Figure 8.13: Jet thrust coefficient (C_T, Dash line) and interaction force coefficient (C_F, Solid line). (a) Steady jet, (b) Case I ($\alpha = 0.5, St_\infty = 1/6$), (c) Case II ($\alpha = 0.33, St_\infty = 1/6$), (d) Case III ($\alpha = 0.5, St_\infty = 1/3$), and (e) Case IV ($\alpha = 0.75, St_\infty = 1/4$).

Figure 8.14 (a) compares the interaction force for all cases, while Figure 8.14 (b) shows the normalised interaction force. Jet interaction force is a spatially averaged parameter, which depends on jet behaviour over multiple pulsing cycles. As a result, interaction force depends primarily on the pulsing wave-form, with duty-cycle being the most significant factor. Increased duty-cycle results in higher jet interaction force. As described previously, there is a correlation between force overshoot and jet penetration overshoot at $\tau \approx 40$, but this effect is small as it is specific to the initial jet pulse. Recall that penetration overshoots correspond to the expansion of the jet flow behind the initial lead shock. After the start-up period, for $\tau > 50$, jet penetration correlates well with interaction force; cases with higher duty-cycles have deeper penetration and generate higher interaction forces.

Once normalised, the inverse relationship occurs between interaction force and duty-cycle, with larger normalised jet interaction forces observed for lower duty-cycle jets. However, the behaviour during start-up ($\tau < 50$) collapses when the interaction force is normalised, as this is primarily driven by the motion of the initial lead shock, as described previously, which is the same for all cases.

8.3 Conclusions

This chapter has investigated the start-up process of steady and pulsed sonic jets in hypersonic crossflow over a flat plate with a laminar boundary layer at high jet-to-crossflow momentum ratio.

During the start-up period, shear-layer vortex shedding is irregular in the steady jet case, but pulsing the jet ensures that a shear-layer vortex is regularly shed once every pulsing cycle. Shear-layer vortices are developed in counter-rotating pairs during the

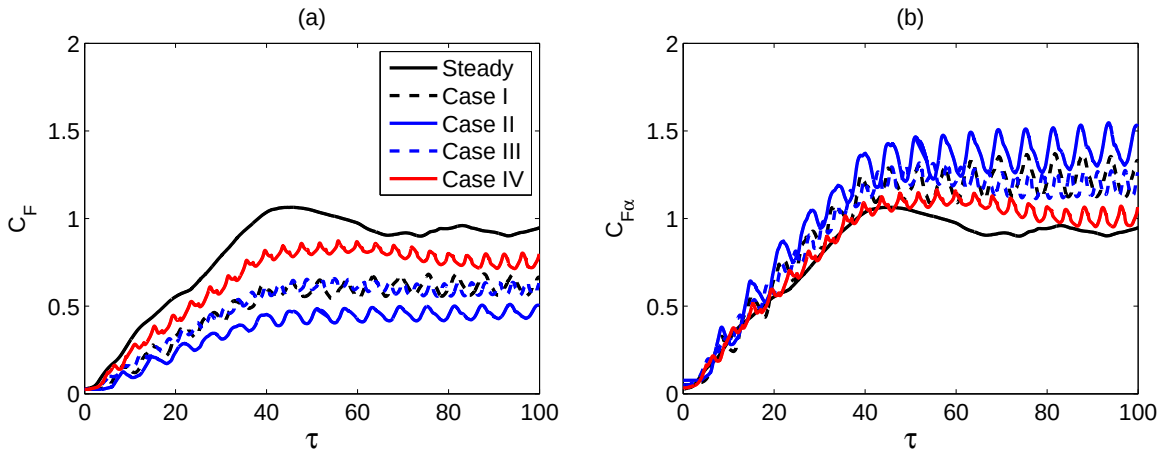

Figure 8.14: Comparison of (a) Jet interaction force coefficient, C_F, and (b) Normalised jet interaction force coefficient, $C_{F\alpha}$. Black line: Steady, Black dash line: Case I ($\alpha = 0.5, St_\infty = 1/6$), Blue line: Case II ($\alpha = 0.33, St_\infty = 1/6$), Blue dash line: Case III ($\alpha = 0.5, St_\infty = 1/3$), and Red line: Case IV ($\alpha = 0.75, St_\infty = 1/4$).

initial start-up for all cases considered. The time period during which counter-rotating shear-layer vortices are observed depends on the Mach disk height. More counter-rotating vortices are observed when the Mach disk forms further from the flat plate. Once the upstream re-circulation region is established, the shear-layer vortex shedding becomes regular, and single vortices are observed for all cases considered in this chapter.

During jet start-up, the interaction force, once normalised for duty-cycle, is driven by the initial lead shock, and is independent of the pulsing regime. The benefits of a reduced duty-cycle in providing a higher interaction force per jet mass flow rate are not observed until the fully developed regime is reached, at $\tau > 50$.

Overall, the interaction force developed during start-up of a steady jet can be characterised as a lightly damped second-order system, with an 18% overshoot, and a settling time of $\tau \approx 60$. Pulsing tends to reduce or eliminate the interaction force overshoot, depending on duty-cycle, without influencing the settling time.

Chapter 9

Air-Breathing Hypersonic Vehicle with Reaction Jet Control

The aim of this chapter is to incorporate reaction control jets into the generic air-breathing hypersonic vehicle model with propulsion-pitch coupling developed in Chapter 3. The closed-loop longitudinal motion is re-assessed using reaction control jets as a supplement to the aerodynamic control surfaces on the full-size vehicle. The ability of the vehicle to maintain stability and control, as measured by military flying qualities criteria, is considered.

The control strategy, with reaction control jets supplementing aerodynamic control surfaces, is outlined in Section 9.1, and the resulting longitudinal motion is described in Section 9.2. Section 9.3 shows the motion of the vehicle when subjected to atmospheric turbulence, while Section 9.4 summarises the effectiveness of reaction control jets as a supplement to aerodynamic control on a generic, propulsion-pitch coupled, air-breathing hypersonic vehicle.

9.1 Control Strategy

Reaction jet control was implemented on the full-size GHAME vehicle described in Chapter 3, as a supplement to the aerodynamic control surfaces. As described in Chapter 3, the GHAME vehicle is controlled by a rudder and two elevons. The elevons function as ailerons using differential movement, and elevators using coordinated movement, according to the following relationships:

$$\delta_a = \frac{\delta v_l - \delta v_r}{2}; \delta_e = \frac{\delta v_l + \delta v_r}{2} \tag{9.1}$$

where δ_a and δ_e refer to the effective elevator and aileron deflections respectively, and δv_l and δv_r refer to the left and right elevon deflections. In the propulsion-pitch coupled vehicle developed in Chapter 3, additional control was provided in the longitudinal axis by the propulsion system, using the throttle, δ_T. The addition of reaction control jets as a supplementary control actuator provides a third means of control, using the jets, δ_j.

To assess the motion of the vehicle, a state-space model was developed in Chapter 3 using linearised equations of motion, based on the small-disturbance theory of Nelson (1989), with modifications to allow for dynamic propulsion-pitch coupling. Here, further modifications are made to incorporate reaction jet control.

The state-space model for the longitudinal motion is as follows:

$$\dot{\mathbf{x}} = \mathbf{A}\mathbf{x} + \mathbf{B}\mathbf{u} \tag{9.2}$$

where $\mathbf{x}$ is the state vector, $\mathbf{u}$ is the input vector, $\mathbf{A}$ is the state matrix, and $\mathbf{B}$ is the input matrix, which includes control inputs from the elevator, $\Delta\delta_e$, the throttle, $\Delta\delta_T$, and the reaction control jets, $\Delta\delta_j$.

$$\underbrace{\begin{bmatrix} \Delta\dot{u} \\ \Delta\dot{w} \\ \Delta\dot{q} \\ \Delta\dot{\theta} \end{bmatrix}}_{\dot{\mathbf{x}}} = \underbrace{\begin{bmatrix} X_u & X_w & 0 & -g \\ Z_u & Z_w & u_0 & 0 \\ M_u + M_{\dot{w}}Z_u & M_w + M_{\dot{w}}Z_w & M_q + M_{\dot{w}}u_0 & 0 \\ 0 & 0 & 1 & 0 \end{bmatrix}}_{\mathbf{A}} \underbrace{\begin{bmatrix} \Delta u \\ \Delta w \\ \Delta q \\ \Delta\theta \end{bmatrix}}_{\mathbf{x}} + \underbrace{\begin{bmatrix} X_{\delta e} & X_{\delta T} & X_{\delta j} \\ Z_{\delta e} & Z_{\delta T} & Z_{\delta j} \\ M_{\delta e} + M_{\dot{w}}Z_{\delta e} & M_{\delta T} + M_{\dot{w}}Z_{\delta T} & M_{\delta j} + M_{\dot{w}}Z_{\delta j} \\ 0 & 0 & 0 \end{bmatrix}}_{\mathbf{B}} \underbrace{\begin{bmatrix} \Delta\delta_e \\ \Delta\delta_T \\ \Delta\delta_j \end{bmatrix}}_{\mathbf{u}} \tag{9.3}$$

The jet control derivatives $X_{\delta j}$, $Z_{\delta j}$, and $M_{\delta j}$ require detailed knowledge regarding the control force developed by the reaction control jets. An estimate of the control force for a steady jet issuing from a flat plate at a single (Mach 5) flight condition, at a single (zero) angle-of-attack, was obtained in Chapter 6 (see Figure 6.38 (a)).

Several assumptions are required to implement longitudinal control over a broad range of flight conditions using reaction control jets. The control force has been derived for a flat plate, and is assumed to be unchanged when the jet issues from the surface of the GHAME vehicle. Further, control force information has only been derived for a single Mach number, at zero angle-of-attack, so variations in these parameters are assumed to not affect the jet thrust or interaction force. As the control force is assumed to be independent of vehicle geometry, airspeed, and angle-of-attack, the $\mathbf{A}$ matrix in Equation 9.3 is independent of the reaction control jets.

When considering longitudinal motion, the thrust direction for the reaction control jet is assumed to be oriented in the vertical direction in the body axis, parallel to the lift force. To maximise the effectiveness of the jet actuators, the jet outlets are placed at the front the vehicle, corresponding to a fixed moment arm of half the vehicle's length, which is 71 m. Therefore, the jet control derivatives are:

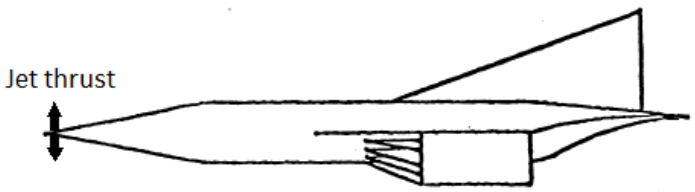

Figure 9.1: Side-view of GHAME vehicle, showing reaction control jet actuator locations.

$$\begin{aligned} X_{\delta j} &= \frac{C_{Dj} Q S}{m} \\ Z_{\delta j} &= \frac{C_{Lj} Q S}{m} \\ M_{\delta j} &= \frac{C_{Mj} Q S c}{I_y} \end{aligned} \tag{9.4}$$

where C_{Lj} is the coefficient of total jet force, F, including jet thrust and interaction force, C_{Dj} is the coefficient of drag produced by the jet, and C_{Mj} is the pitching moment induced by the jet thrust, calculated as:

$$C_{Mj} = \frac{F \times \frac{71}{2}}{QSc} \tag{9.5}$$

Note that the jet force is allowed to take both positive and negative values, corresponding to jet actuators located on both the upper and lower surfaces of the vehicle. With the jets mounted at the nose, a positive (upward) jet force corresponds to a positive (nose-up) pitching moment. A schematic of the GHAME vehicle, showing jet actuator locations, is provided in Figure 9.1. It is also assumed that the jet force can be scaled, without affecting the transient interaction.

Following Chapter 3, the contribution of control actuators to airspeed is neglected (i.e. $X_{\delta e} = X_{\delta j} = 0$). The 30° control deflection limits and 10.5 rad/s (600 deg/s) rate limits applied in Chapter 3 are maintained for the aerodynamic control surfaces.

The maximum jet thrust, T, is scaled to produce 30% of the lift required to trim the vehicle at the Mach 6, 65 000 ft flight condition, which corresponds to approximately 100 kN. The jet area required to achieve a 100 kN jet thrust, using the general thrust equation, can be calculated as follows:

$$\begin{aligned} T &= \dot{m}_j U_j + A_j \left(p_j - p_a\right) \\ &= \left(\rho_j A_j U_j\right) U_j + A_j \left(p_j - p_a\right) \end{aligned} \tag{9.6}$$

Calculating U_j for a sonic jet requires the total temperature of the jet. This depends on the fuel type and specific jet design. The Space Shuttle uses the R-40A Thruster for orbit control. This thruster provides approximately 4 kN of thrust, and uses a

N_2O_4/MMH fuel, which has a combustion temperature of $T_0 = 3385$ K, and a molecular mass of 21.5 (Chazen and Sanscrainte, 1974). Isentropically expanding to Mach 1 gives:

$$\begin{aligned} T_j &= T_{0j}\left(1 + \frac{\gamma - 1}{2} M_j^2\right)^{-1} \\ &= 2821 \text{ K} \end{aligned} \tag{9.7}$$

Therefore, for an ideal gas with $\gamma = 1.4$, the reaction control jet actuator properties are as follows:

$$\begin{aligned} U_j &= 1235 \text{ m/s} \\ \rho_j &= 0.98 \text{ kg/m}^3 \\ A_j &= 0.04 \text{ m}^2 \\ d_j &= 0.22 \text{ m} \end{aligned} \tag{9.8}$$

The calculated jet diameter, d_j, of 22 cm is reasonable when compared with the throat diameter, d_t, of the Space Shuttle R-40A thruster in a 4 kN configuration, $d_t = 15.5$ cm (Chazen and Sanscrainte, 1974).

Bandwidth limits for the reaction control jets are determined by the jet start-up behaviour. The jet thrust coefficient during jet start-up was calculated using LES in Chapter 8, as a function of non-dimensional time, $\tau = t \times U_\infty / d_j$. It was concluded in Chapter 8 that the force during start-up can be characterised as a lightly damped second-order system, with an 18% overshoot, and a settling time of $\tau \approx 60$. This second-order actuator behaviour is included in the reaction control jet model. The second-order actuator has a natural frequency and damping ratio tuned to match the jet start-up overshoot and settling times. The natural frequency and damping ratio required to provide an 18% overshoot, with a settling time of $\tau = 60$, are 1200 rad/s and 0.2 respectively.

In Chapter 8, the steady control force is 47% of the jet thrust, as the jet interaction force acts in the opposite direction to the jet thrust, reducing the overall control force. Therefore, the steady control force in the model corresponds to 47% of the demanded thrust. In addition, the jet thrust in the model ramps up from zero, rather than the idealised square-wave profile considered in Chapter 8.

Figure 9.2 compares the second-order time-dependent jet force corresponding to a 1 N thrust demand, as implemented in the model, with the numerically derived jet start-up force from Chapter 8. Note that this transient response is assumed to be independent of the demanded control force, and the free-stream conditions, as described previously.

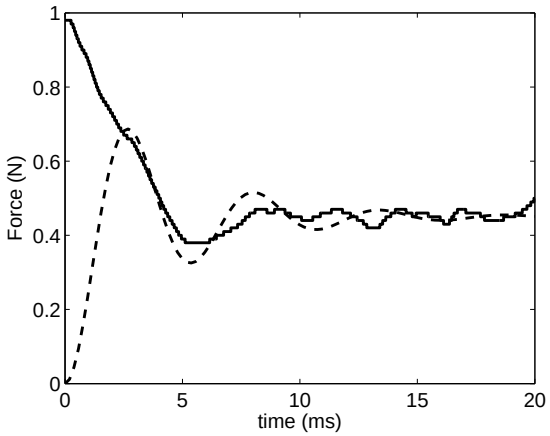

Figure 9.2: Time-dependent reaction control jet force, and assumed actuator response, for a demanded thrust of 1 N, scaled for the full-size GHAME vehicle. Solid line: time-dependent control force derived in Chapter 8, Dotted line: second-order jet actuator response to 1 N thrust demand.

9.2 Closed-Loop Control

Following the same procedure as Chapter 3, a closed-loop control system is implemented to modify the vehicle's flying qualities, using the elevator, throttle, and reaction control jets. If the short-period is excited by a small pitch rate perturbation of 1 deg/s, the control effort required to alter the response such that the vehicle exhibits acceptable flying qualities is shown in Figure 9.3. The full datasets for each of the 11 flight conditions are provided in Appendix B. This is the ideal behaviour, with no deflection and rate limits applied to the actuators. The control deflections are large, both the elevators and jets require inputs greater than their design limits (i.e. $\delta_e > 30°$, $\delta_j > 100$ kN). Note that throttle inputs are not shown in Figure 9.3 − these are small but non-zero.

When the control deflection and rate limits are applied, Figure 9.4 (a) shows that with the addition of jet control, although the actuator behaviour is oscillatory, control is maintained with acceptable flying qualities at several of the supersonic and hypersonic flight conditions. Therefore, even with a simple, single jet configuration, significant benefit is observed over the original vehicle. The results are summarised in Table 9.1, which shows that suitable flying qualities can be achieved at 6 out of 11 flying conditions, compared with 3 out of 11 without reaction jet control. However, the reaction jet control is still unable to maintain control at some low Mach number conditions, due to the coupling between vertical force and pitching moments, and the reduced control authority of the elevators in the transonic regime.

Close inspection of Figure 9.4 (a) shows that, at the Mach 10 flight condition, the rate limit of the aerodynamic control surfaces is slow in comparison to the pitch oscillations of the vehicle. As a result, the elevator deflection exhibits a triangular pattern, and flying qualities are not suitable without supplementation by reaction control jets. The reaction control jet has a higher bandwidth, so the control force

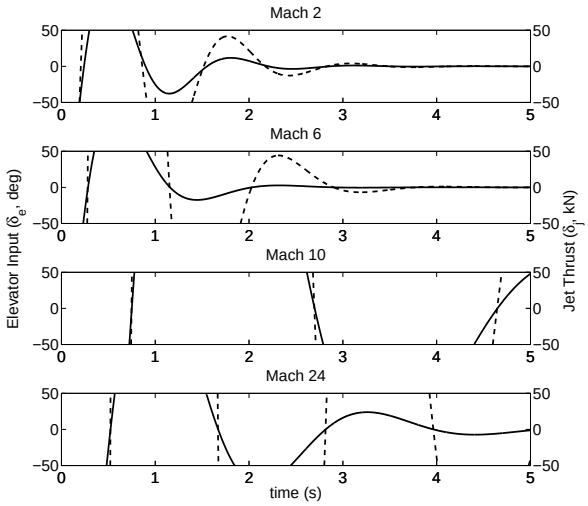

Figure 9.3: Closed-loop control response to 1 deg/s pitch rate perturbation. Solid Line: Elevator deflection (deg); Dash Line: Jet force (kN).

exhibits a square-wave pattern. This is sufficient to damp the high frequency pitching motion, resulting in improved flying qualities. However, the pitching motion is not reduced to zero, so the oscillatory control deflections continue for the time-period considered in Figure 9.4.

To reduce the coupling between vertical force and pitching moment, the jets can be applied in a paired configuration, such that moments can be applied without any coupling to the vertical (translational) motion. This requires an upward jet force at the nose, coupled with a downward jet force at the tail, as shown in Figure 9.5. Results using this simple modified strategy are provided in Figure 9.4 (b). Again, highly oscillatory behaviour is observed at high Mach numbers, but acceptable flying qualities are achieved at 9 out of 11 flight conditions, see Table 9.1, due to the high bandwidth achievable with reaction control jets. The only cases where acceptable flying qualities cannot be achieved is in the subsonic flight regime, where control authority is insufficient.

9.3 Atmospheric Turbulence

Following Chapter 3, the vehicle's response to the Von Karman *severe* turbulence model, with reaction jet control implemented, is provided in Figure 9.6. Recall that without reaction control jets, control was lost in all cases, except at Mach 24. In the single jet configuration (Figure 9.6 (a)) no improvement is observed, control limits are quickly exceeded for the elevator, throttle (not shown), and jets, resulting in unstable flight at all flight conditions except Mach 24. For the twin jet configuration, the Mach 24 flight condition remains stable, while unstable flight is still observed at all other conditions. Therefore, reaction jet control does not provide a significant improvement over aerodynamic control for atmospheric turbulence, for the current conditions.

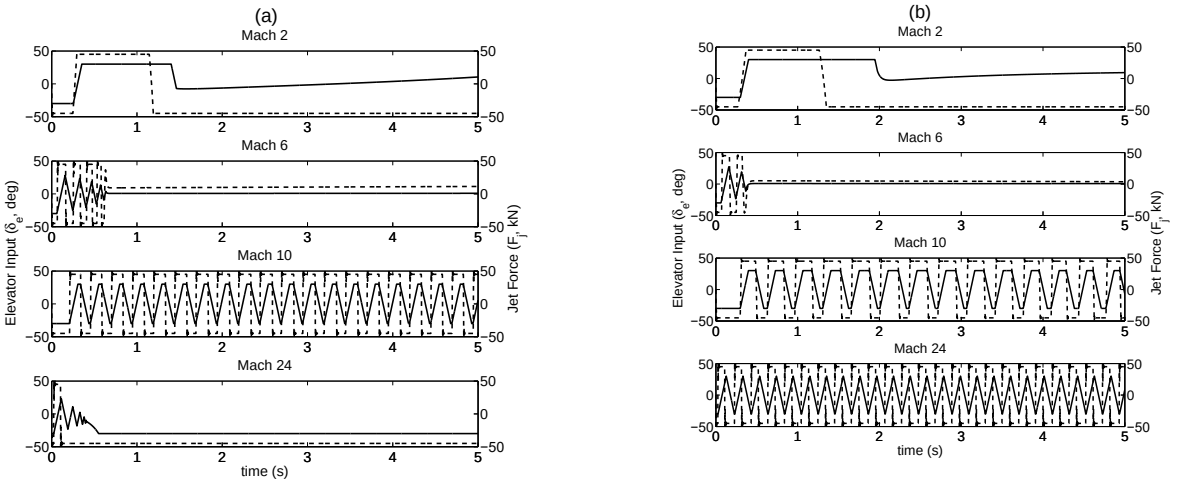

Figure 9.4: Closed-loop control response to 1 deg/s pitch rate perturbation, for (a) Single jet, and (b) Twin jet configuration. Solid Line = Elevator deflection (deg); Dash Line: Jet force (kN).

Table 9.1: Ability to achieve acceptable flying qualities, using pole placement technique with actuator rate and deflection limits applied.

Mach number	Altitude (m)	Aerodynamic	Single Jet	Twin Jet
0.8	305	Not Suitable	Not Suitable	Not Suitable
1.5	6,096	Not Suitable	Not Suitable	Suitable
2.0	15,240	Not Suitable	Suitable	Suitable
6.0	20,000	Not Suitable	Suitable	Suitable
10	33,000	Suitable	Suitable	Suitable
24	33,000	Suitable	Suitable	Suitable
10	30,000	Not Suitable	Suitable	Suitable
6.0	27,500	Not Suitable	Suitable	Suitable
2.5	15,000	Not Suitable	Not Suitable	Suitable
1.5	10,000	Suitable	Not Suitable	Suitable
0.5	0	Not Suitable	Not Suitable	Not Suitable

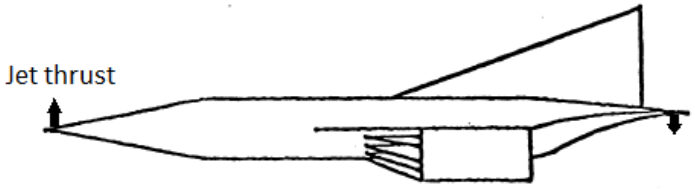

Figure 9.5: Side-view of GHAME vehicle, showing reaction control jet actuator locations for twin jet configuration.

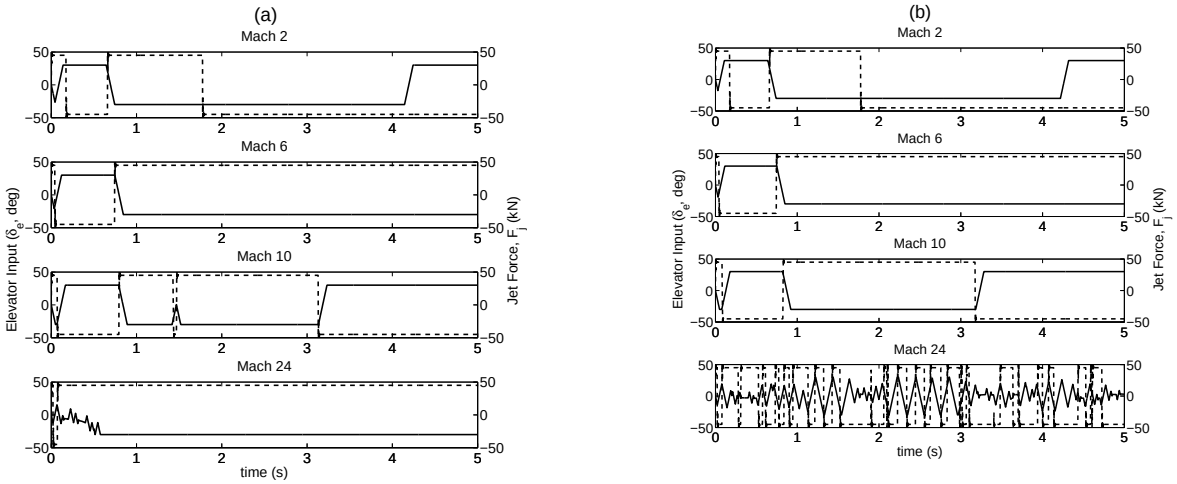

Figure 9.6: Closed-loop control response to *severe* Von Karman turbulence input, for (a) Single jet and (b) Twin jet configuration. Solid Line = Elevator deflection (deg); Dash Line: Jet thrust (kN).

9.4 Conclusions

This chapter has considered the application of reaction control jet actuators on a generic hypersonic vehicle, as a supplement to aerodynamic control. Jet control authority and bandwidth were derived based on the flow physics described in previous chapters.

Some improvement was observed with the implementation of reaction control jets, with a single jet configuration providing acceptable flying qualities over a greater flight envelope than aerodynamic control in isolation. The acceptable flight envelope was further increased using a twin jet configuration, due to the de-coupling of translation and rotation forces in the longitudinal plane. Twin jets also have a higher control authority that a single jet. In the twin jet configuration, stable flight with acceptable flying qualities was observed in 9 out of 11 flight conditions, compared with 6 out of 11 flight conditions for the single jet configuration, and 3 out of 11 flight conditions for the vehicle without reaction control jets. No significant improvement in vehicle stability was observed in the presence of *severe* Von Karman turbulence for either the single jet or twin jet configuration.

Significant simplifications were required to perform the analysis. Time dependent jet force data from Chapters 6 and 7 was used, and it was assumed that jet force is independent of free-stream conditions and vehicle geometry. It was also assumed that jet thrust was able to be scaled between 0 N and 100 kN, without affecting the transient behaviour. As a result, the analysis in this chapter merely serves as an initial indication of the performance improvements that may be achieved by supplementing aerodynamic control surfaces with a high frequency control actuator, such as reaction control jets, for air-breathing hypersonic vehicle applications.

Chapter 10

Conclusions and Future Work

10.1 Conclusions

The aim of this research was to determine the required control bandwidth for a generic air-breathing hypersonic vehicle, and to numerically investigate the unsteady flow physics of steady and pulsed reaction control jets, as a supplementary control actuator.

To address the limited knowledge of propulsion-pitch coupled air-breathing hypersonic vehicle dynamics, a generic rigid-body model was developed. Analysis of this model showed that aerodynamic control authority was low in the transonic region, and that large control surface deflections were required to overcome the pitching moment from the propulsion system at trim, resulting in a low lift-to-drag ratio. A robust control system for the full-size vehicle required a bandwidth of 27 Hz, and 180 Hz was required for a missile-sized vehicle. This far exceeds the bandwidth capability of aerodynamic control surfaces. As a result, acceptable flying qualities were unable to be achieved for both the full-size and the missile-size vehicles at 8 of 11 flight conditions chosen to represent a generic single-stage-to-orbit trajectory. Further, the response to atmospheric turbulence was poor, and the control surfaces quickly saturated, losing control of the vehicle at all conditions except Mach 24. The rate and deflection limits imposed by aerodynamic control prevented successful operation of the vehicle. Therefore, the design of air-breathing hypersonic vehicles may require the consideration of supplementary actuators, such as reaction control jets.

A numerical methodology was developed to investigate the interaction between a reaction control jet and a hypersonic crossflow, using an implicit large-eddy simulation (ILES) approach. The methodology was subjected to an extensive verification and validation process, where results were compared with several canonical unit problems, and the more detailed case of a jet in quiescent atmosphere. The simulations accurately reproduced all physical features of the flow for free-stream Mach numbers up to 10, although small time-steps were required to reduce numerical oscillations in the flow solutions. The numerical methodology was found to be fit for purpose to examine the steady and unsteady flow features of a jet in hypersonic crossflow.

Further verification and validation was achieved through a detailed comparison to

the jet in hypersonic crossflow experiment of Erdem (2011). A mesh resolution study was conducted, and a mesh was chosen to ensure sufficient resolution of unsteady flow structures. The flow solution on this mesh compared well with experimental results, although some differences were observed, due to differences in temperature and physical properties of the flat plate.

A detailed numerical investigation was conducted into the unsteady flow physics of a sonic reaction control jet in hypersonic crossflow. Several new phenomena were observed. The laminar in-flow boundary layer had a significant influence on the structure of the horseshoe and shear-layer vortices. A complex horseshoe vortex structure consisting of 6 individual vortices (2 steady and 2 co-rotating pairs which periodically coalesce) was formed in the large re-circulation region upstream of the jet outlet. Shear-layer vortex shedding was delayed by the thick laminar boundary layer, and as a result, these vortices shed at lower frequency than previously observed. The high free-stream Mach number caused periodic deformation of the bow shock, which was also not previously observed, while other shock structures and wake vortices showed similar behaviour to previous studies, which were conducted at lower Mach numbers, with turbulent in-flow boundary layers. The induced pressure distribution on the flat plate, and the resultant jet interaction force, were described. Interaction force is driven by the steady flow features, such as the bow shock, barrel shocks, and longitudinal vortices. Shear-layer vortex shedding has a small influence, while other unsteady flow features, such as horseshoe vortices and wake vortices, do not significantly influence the interaction force.

Pulsed jets in hypersonic crossflow were numerically investigated at a number of pulsing frequencies and duty-cycles. Pulsing was shown to significantly increase jet penetration depth over steady jets, on a per unit jet mass flow basis. New evidence was provided to support previously reported mechanisms for increased penetration depth, and two new mechanisms were identified, with supporting evidence provided. A maximum 68% increase in penetration was observed, corresponding to a low pulsing frequency ($St_\infty = 1/6$), with a 50% duty-cycle. The collapse of the barrel shocks and entrainment of free-stream flow were found to be key flow features, which depend primarily on the jet-off time. The periodic forcing of lead shocks into the flow resulted in the formation of a secondary shear-layer, and prevented interaction between consecutive shear-layer vortices, allowing penetration increases at higher duty-cycles than is observed in subsonic flows. The presence and structure of longitudinal counter-rotating vortices was influenced by the jet-off time, a phenomenon not previously observed. In cases with a long jet-off time, no clear vortex pair was observed, while for cases with short jet-off time, a clear vortex was observed. Regions of high surface pressure variability were identified, and these differed between pulsing cases. Two additional results were identified: interaction force peaked at the end of the pulsing cycle, when the jet is switched off, and the interaction force per unit jet mass flow rate incresed for reduced duty-cycles, due to the continued presence of the shock structures during the jet-off time.

The start-up of both steady and pulsed jets into hypersonic crossflow were also investigated numerically. Shear-layer vortices were developed in counter-rotating pairs during the initial start-up. The time period during which counter-rotating vortices were observed depends on the Mach disk height. During start-up, the interaction force was driven by the initial lead shock, and was independent of the pulsing regime. The interaction force during start-up was characterised as a lightly damped second-order system, with an 18% overshoot and a settling time of $\tau \approx 60$.

Finally, the second-order model of the reaction control jet actuator was incorporated into the generic air-breathing hypersonic vehicle model, as a supplement to aerodynamic control. Stability and flying qualities showed significant improvement over the baseline, aerodynamic control configuration. Flying qualities improved significantly, and were acceptable at 6 out of 11 flight conditions with a single jet configuration, and 9 out of 11 flight conditions with a twin jet configuration.

10.2 Future Work

Several opportunities for future work have been identified. The relationship between the upstream separated flow region during jet start-up and the development of counter-rotating shear-layer vortices could be further investigated. In Chapter 8 counter-rotating shear-layer vortices were observed, but were limited to the early jet start-up phase, before the upstream separated flow region was fully established. These counter-rotating vortices were observed over a longer period in cases where the Mach disk forms further from the plate. A detailed study of the inlet boundary layer conditions, and jet-to-crossflow momentum ratios corresponding to counter-rotating shear-layer vortex development may provide further insight into the unsteady physics of the jet interaction. If a counter-rotating vortex regime can be identified, it may have significance in terms of jet penetration and control force.

The influence of flow chemistry in the jet fluid may also be of future interest. Flow chemistry was not significant at the flow conditions considered in this work, but is critical to some applications of unsteady jets in hypersonic crossflow, such as scramjet fuel injection. The benefits observed for pulsed jets over steady jets include increased jet penetration, and unique behaviour of longitudinal vortices. These flow characteristics suggest that unsteady sonic injection may be of particular interest to scramjet applications.

Consideration of a broader range of pulsing frequencies and waveforms may allow further optimisation of jet penetration and control force. For example, the pulsed jet cases considered in this work showed that penetration per unit jet mass flow was maximised at low pulsing frequencies. Further reduction in pulsing frequency may increase jet penetration per unit jet mass flow, or may provide other desirable characteristics. Previous research (Karagozian, 2014) has shown that jets in subsonic crossflow are sensitive to pulsing waveform. If this sensitivity is also present in supersonic and hypersonic crossflows, it would provide a significant opportunity for

optimisation of the jet pulsing regime.

The free-stream flow conditions and plate geometry used in this study were focused on the wind-tunnel conditions simulated experimentally by Erdem (2011). The work could be readily extended to real hypersonic vehicle free-stream flow conditions and geometries.

10.3 Summary

Overall, this study has provided additional insight into air-breathing hypersonic vehicle dynamics, and the unsteady flow physics of steady and pulsed sonic jets in hypersonic crossflow. Several new flow phenomena were observed. These results have applications to reaction jet control, which has been the focus of this work, and several other areas, including scramjet fuel injection and supersonic panel flutter.

Appendix A - Dynamics and Control - Full Datasets

Longitudinal Control

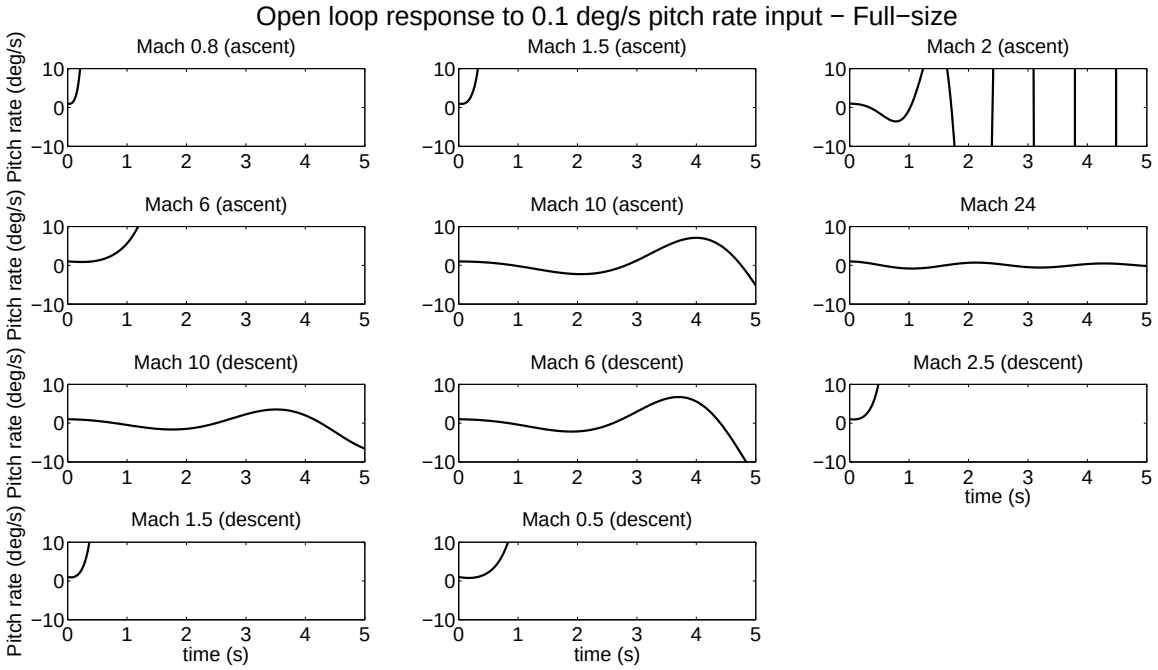

Figure A.1: Open-loop response to 1 deg/s pitch rate perturbation, for the Full-size vehicle

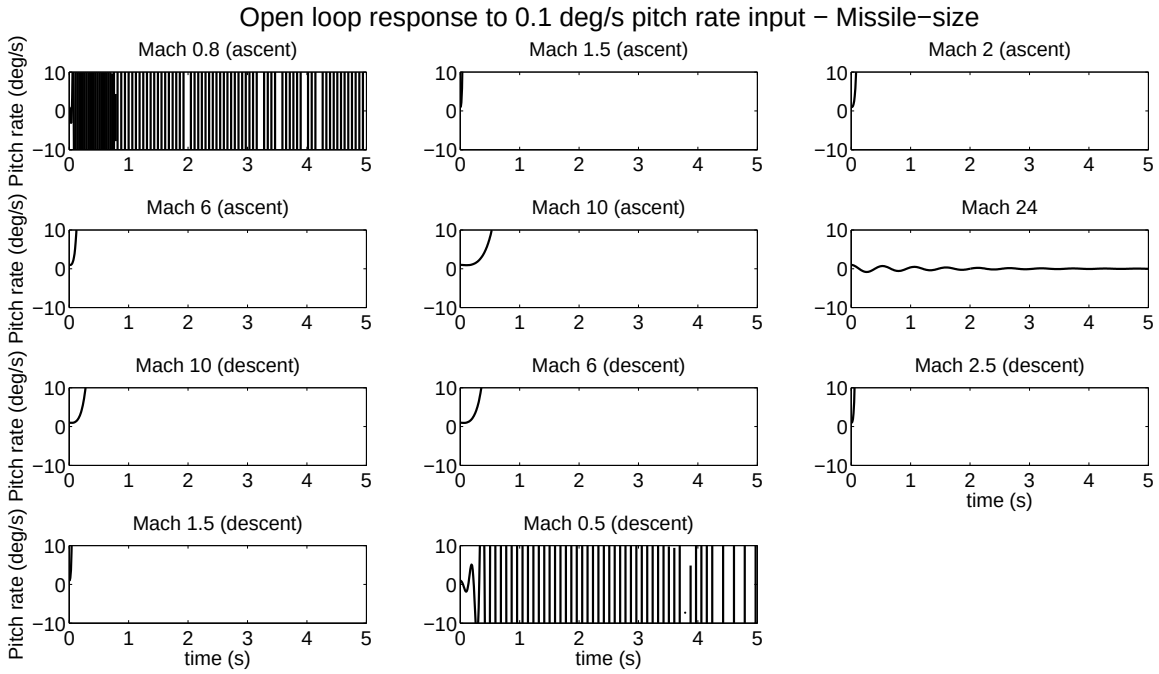

Figure A.2: Open-loop response to 1 deg/s pitch rate perturbation, for the Missile-size vehicle

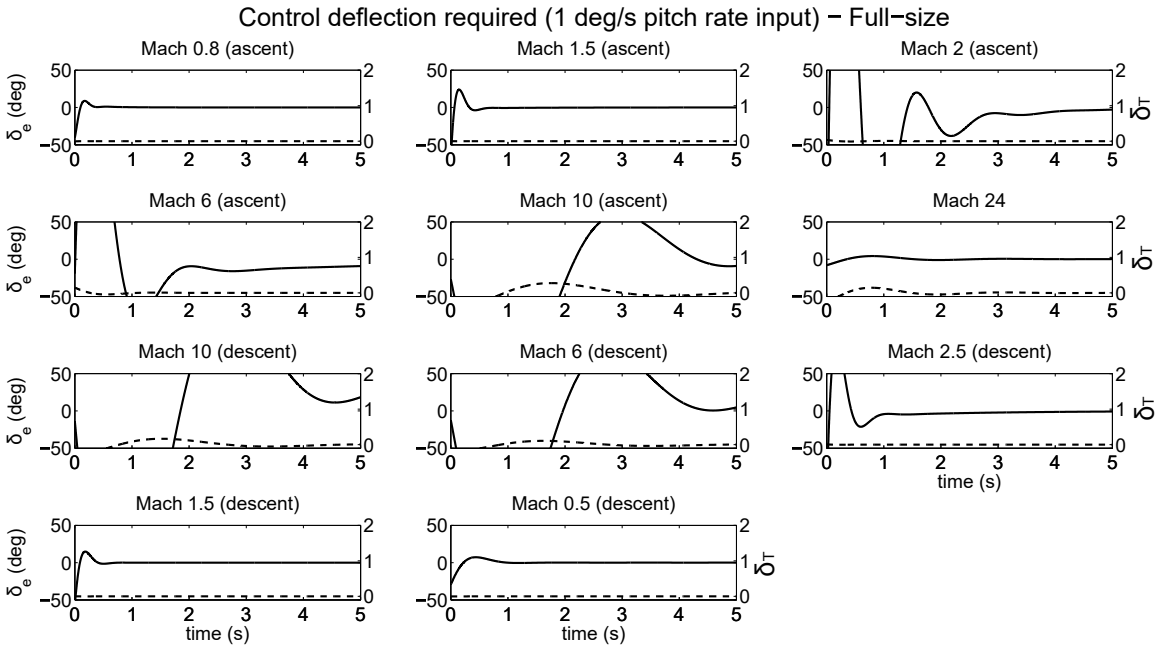

Figure A.3: Closed-loop elevator and throttle response to 1 deg/s pitch rate perturbation, for the Full-size vehicle. Solid Line = Elevator deflection (deg); Dash Line: Throttle position.

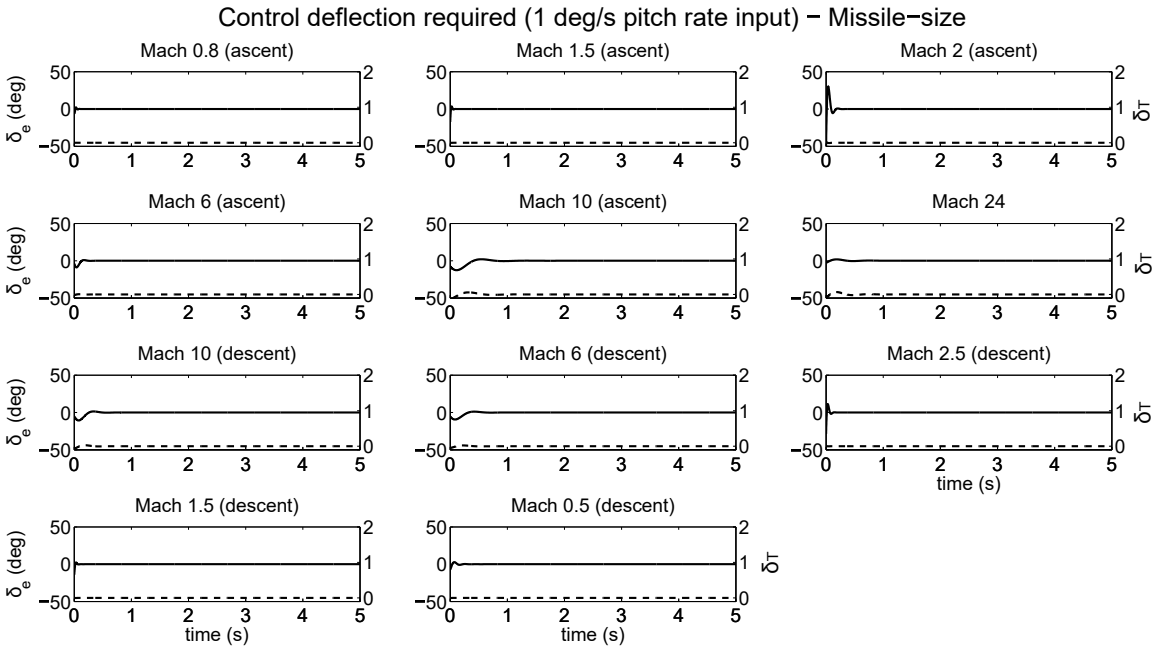

Figure A.4: Closed-loop elevator and throttle response to 1 deg/s pitch rate perturbation, for the Missile-size vehicle. Solid Line = Elevator deflection (deg); Dash Line: Throttle position.

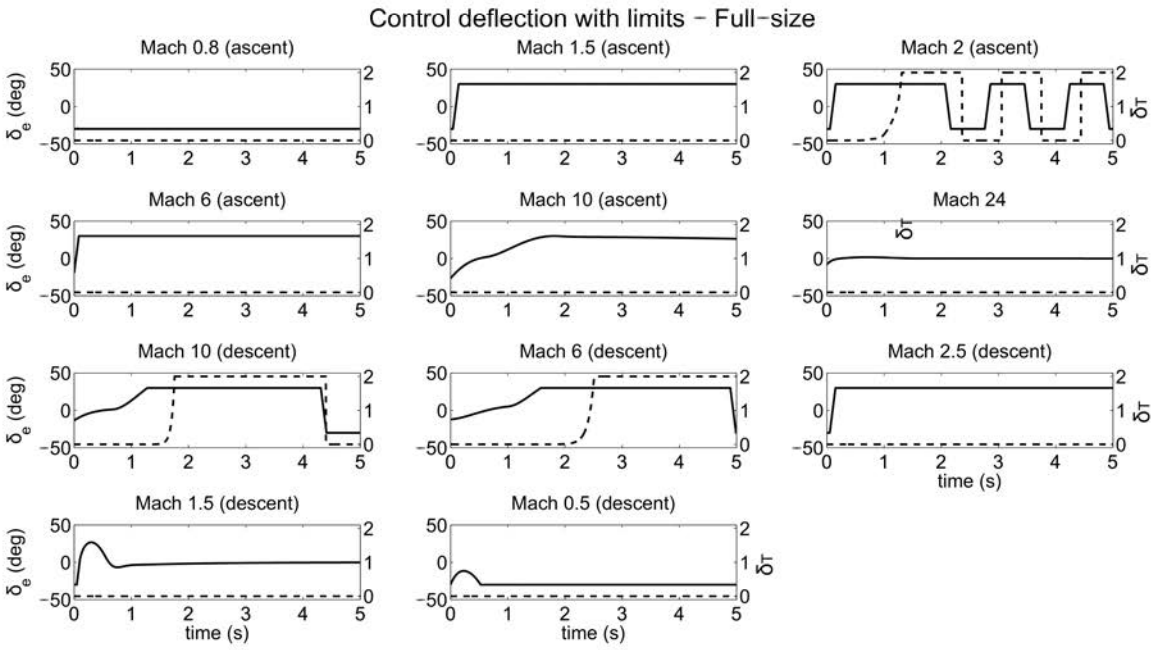

Figure A.5: Closed-loop elevator and throttle response to 1 deg/s pitch rate perturbation, for the Full-size vehicle. Solid Line = Elevator deflection (deg); Dash Line: Throttle position.

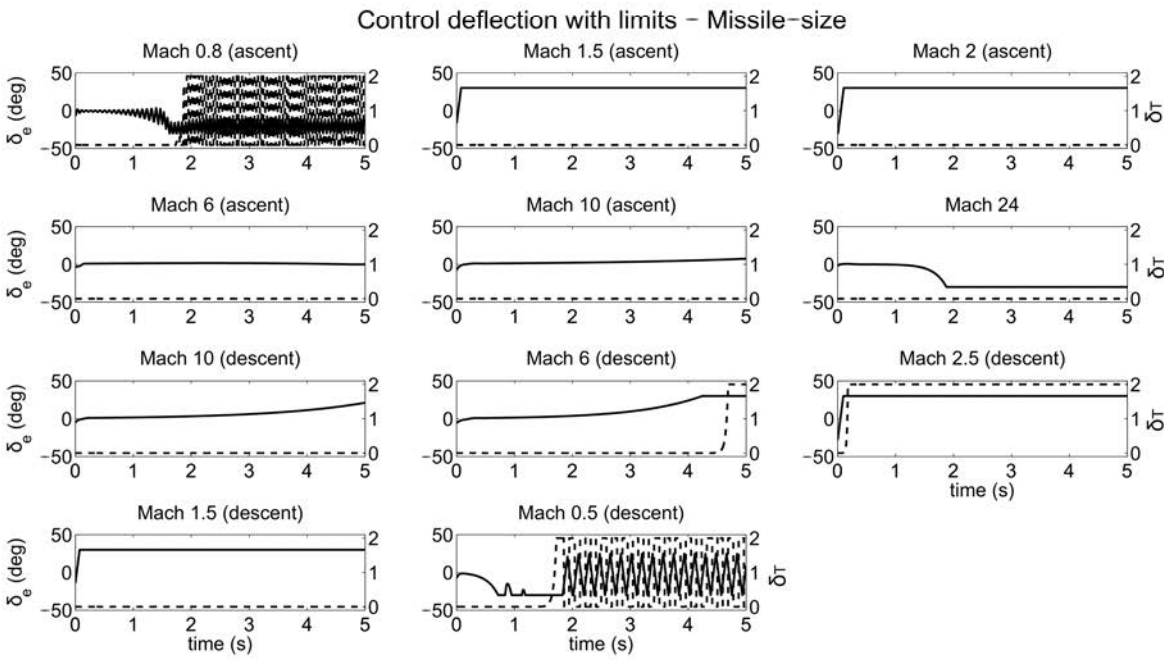

Figure A.6: Closed-loop elevator and throttle response to 1 deg/s pitch rate perturbation, for the Missile-size vehicle. Solid Line = Elevator deflection (deg); Dash Line: Throttle position.

Lateral Control

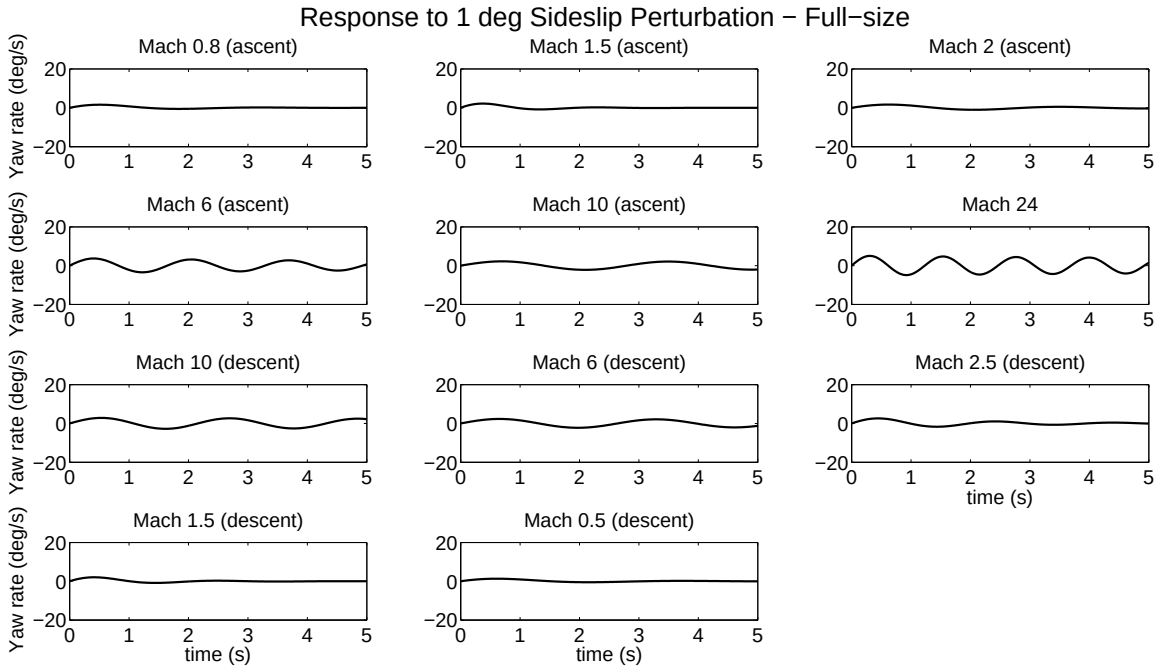

Figure A.7: Open-loop response to 1 deg side-slip perturbation, for the Full-size vehicle.

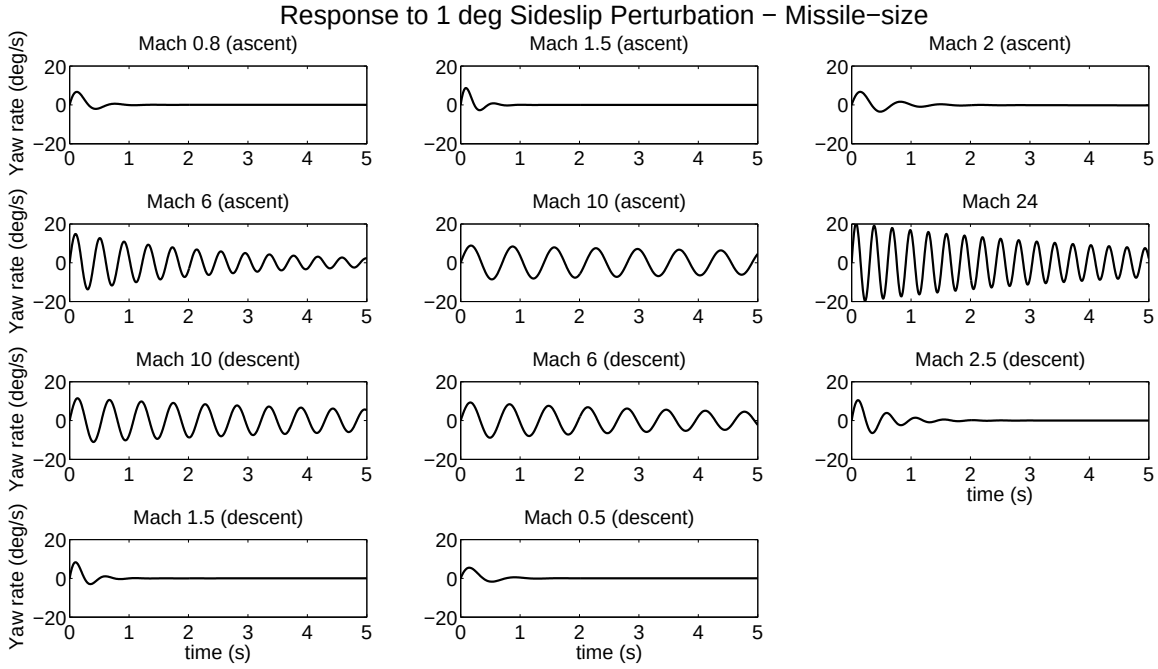

Figure A.8: Open-loop response to 1 deg side-slip perturbation, for the Missile-size vehicle.

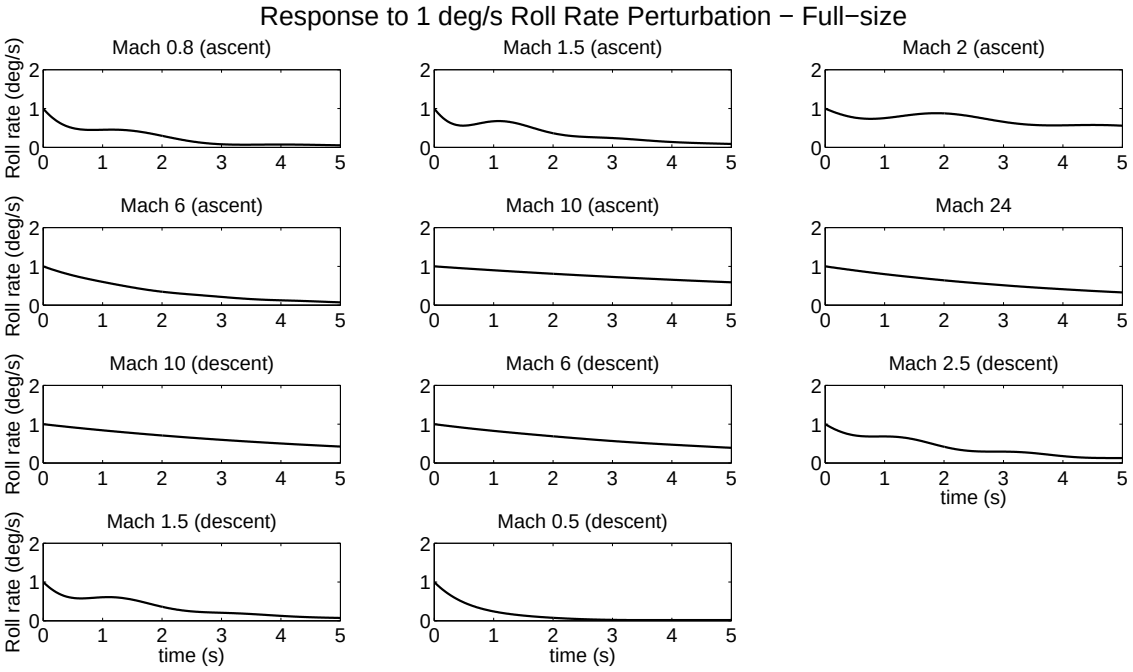

Figure A.9: Open-loop response to 10 deg/s roll rate perturbation, for the Full-size vehicle.

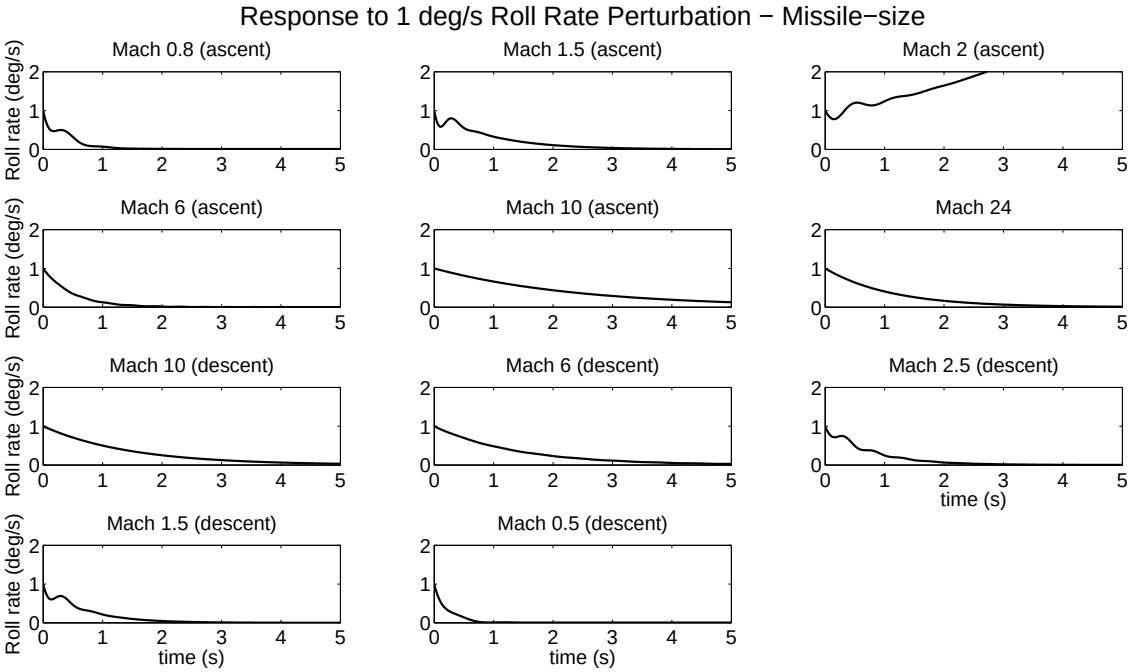

Figure A.10: Open-loop response to 10 deg/s roll rate perturbation, for the Missile-size vehicle.

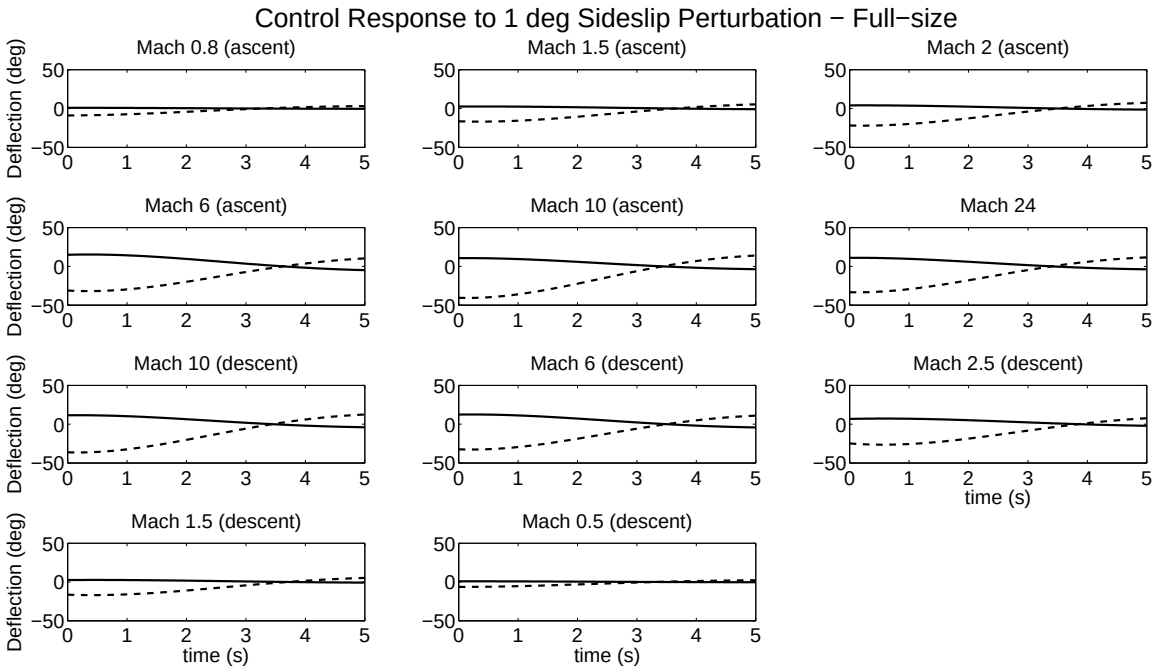

Figure A.11: Closed-loop control surface response to 1 deg side-slip perturbation, for the Full-size vehicle. Solid line: Aileron, Dotted line: Rudder.

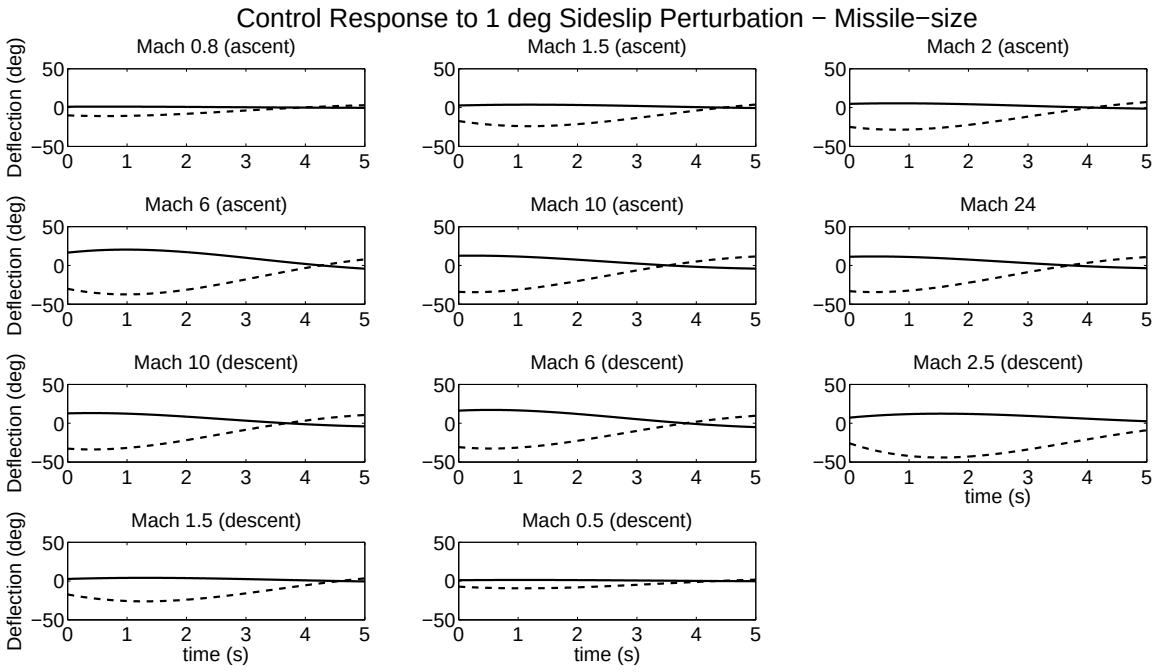

Figure A.12: Closed-loop control surface response to 1 deg side-slip perturbation, for the Missile-size vehicle. Solid line: Aileron, Dotted line: Rudder.

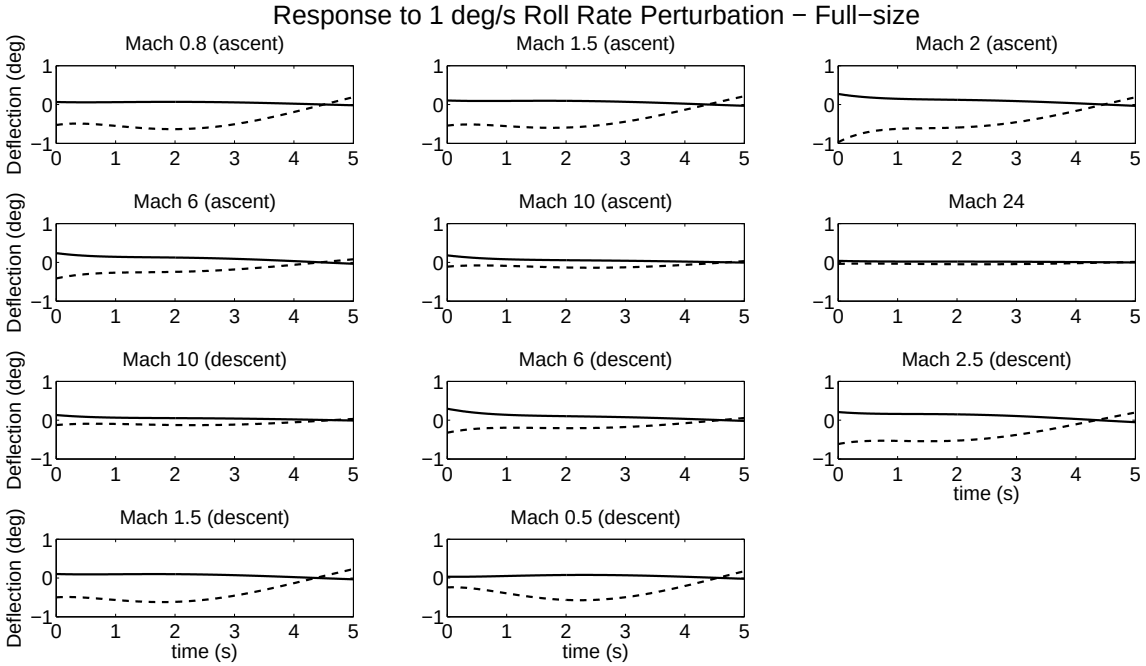

Figure A.13: Closed-loop control surface response to 1 deg/s roll rate perturbation, for the Full-size vehicle. Solid line: Aileron, Dotted line: Rudder.

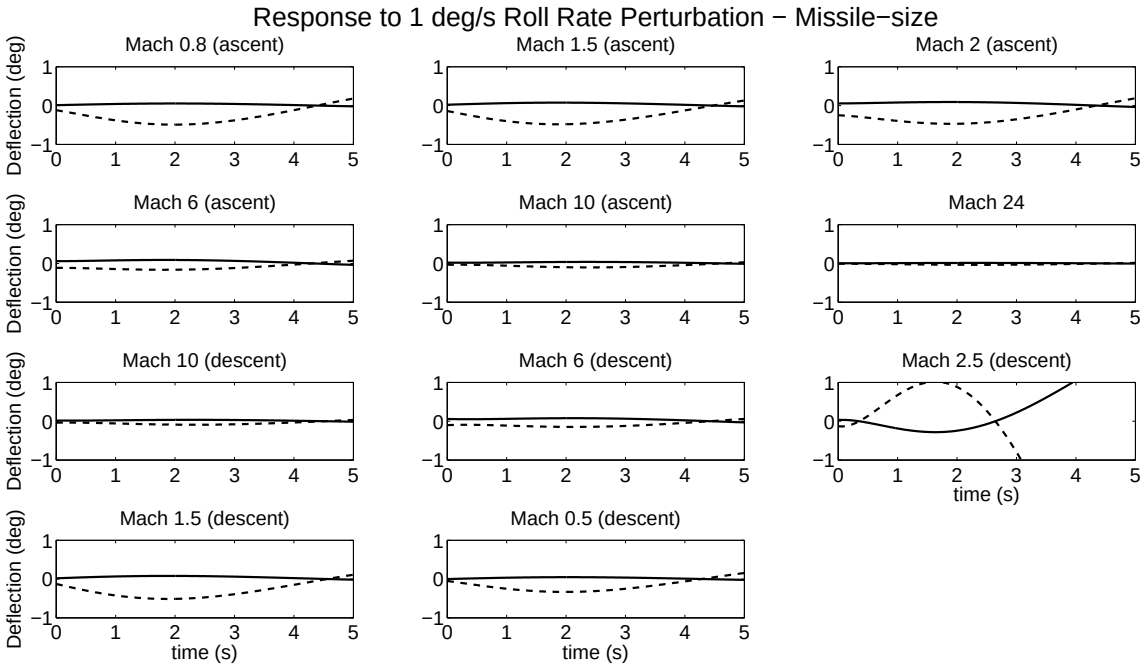

Figure A.14: Closed-loop control surface response to 1 deg/s roll rate perturbation, for the Missile-size vehicle. Solid line: Aileron, Dotted line: Rudder.

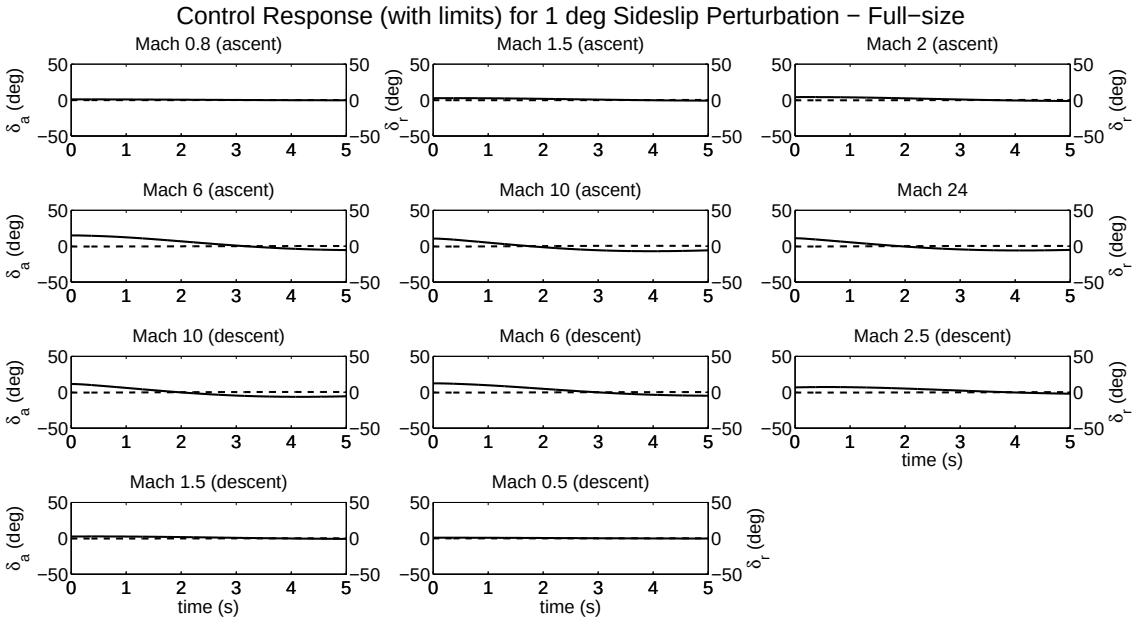

Figure A.15: Closed-loop control surface response to 1 deg side-slip perturbation, for the Full-size vehicle. Solid line: Aileron, Dotted line: Rudder.

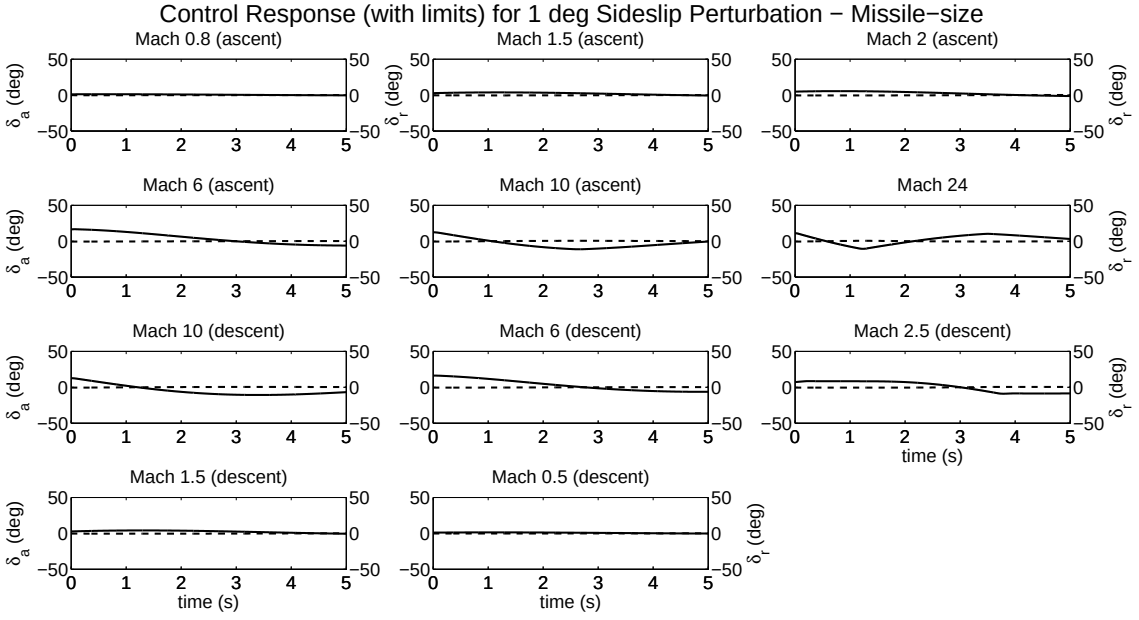

Figure A.16: Closed-loop control surface response to 1 deg side-slip perturbation, for the Missile-size vehicle. Solid line: Aileron, Dotted line: Rudder.

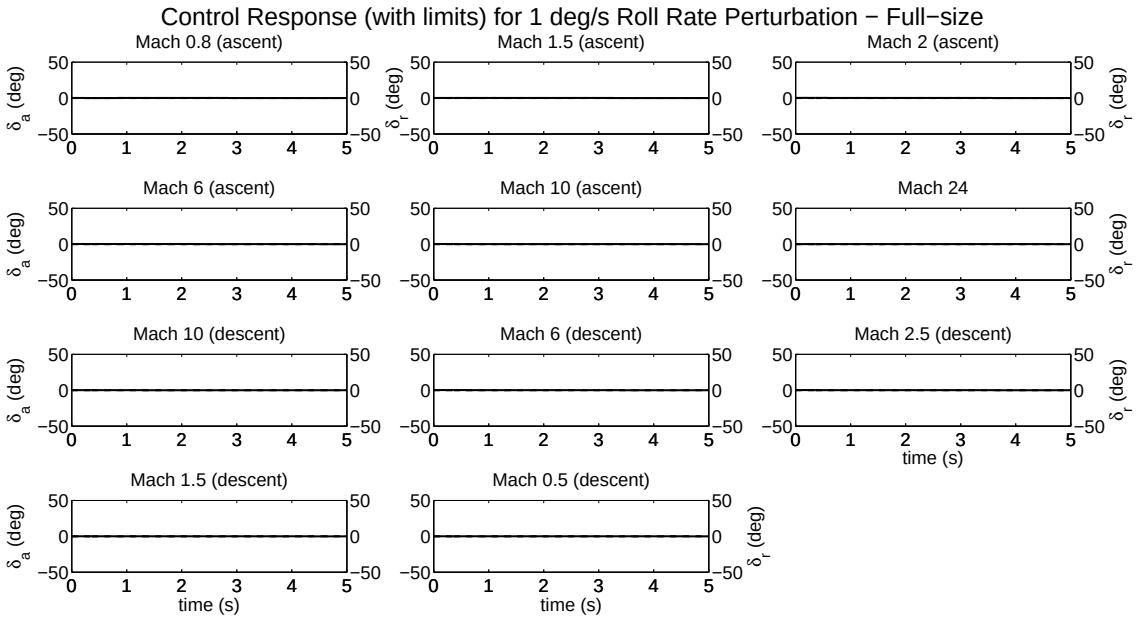

Figure A.17: Closed-loop control surface response to 1 deg/s roll rate perturbation, for the Full-size vehicle. Solid line: Aileron, Dotted line: Rudder.

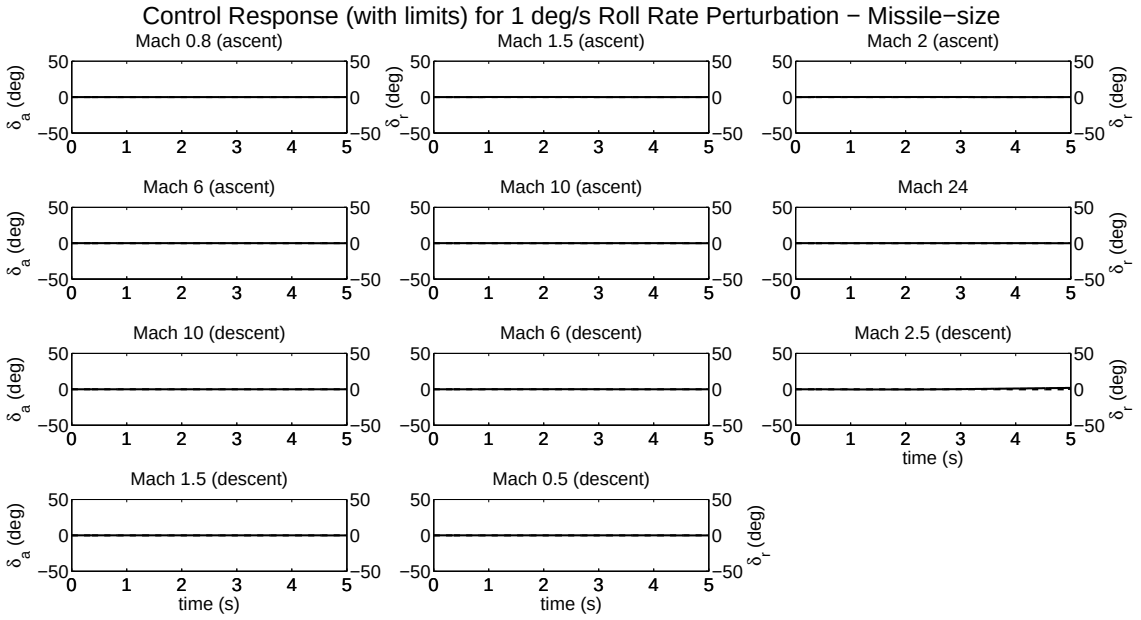

Figure A.18: Closed-loop control surface response to 1 deg/s roll rate perturbation, for the Missile-size vehicle. Solid line: Aileron, Dotted line: Rudder.

Atmospheric Turbulence

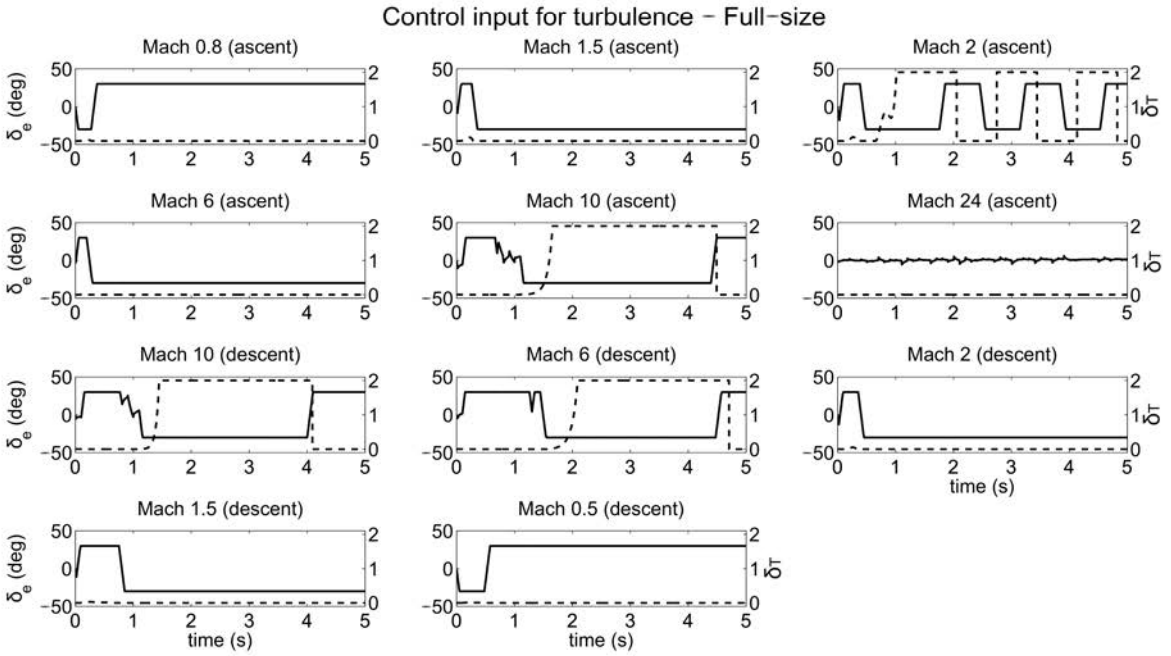

Figure A.19: Closed-loop elevator and throttle response to turbulence, for the Full-size vehicle. Solid line: Elevator deflection (deg); Dash line: Throttle setting.

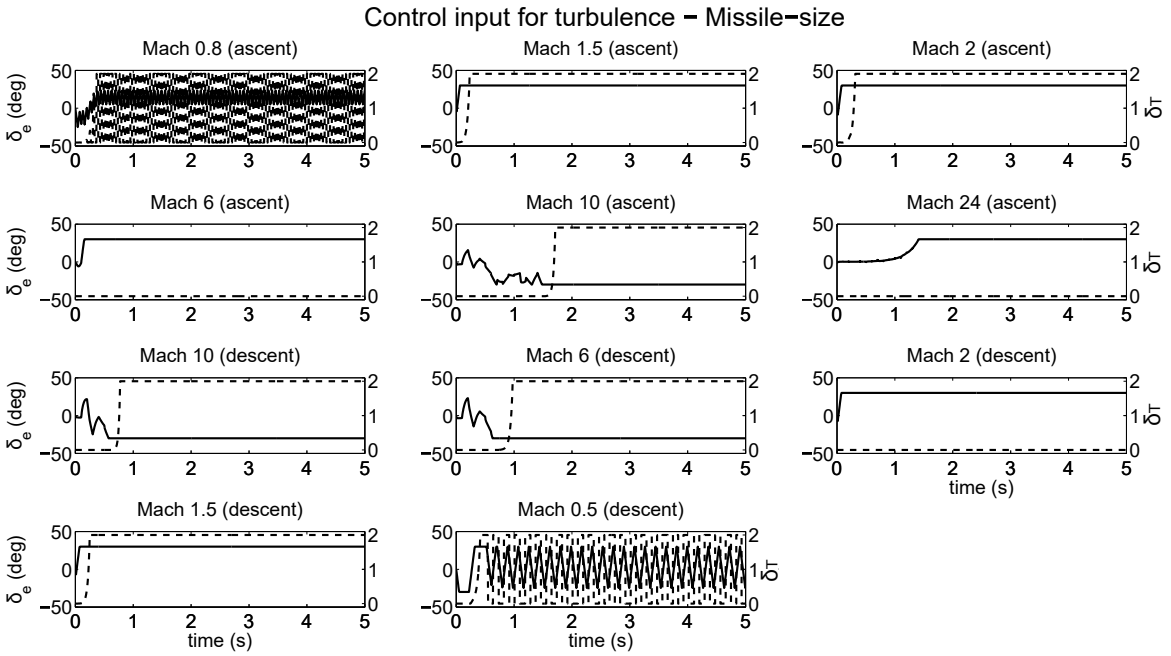

Figure A.20: Closed-loop elevator and throttle response to turbulence, for the Missile-size vehicle. Solid line: Elevator deflection (deg); Dash line: Throttle setting.

Comparison to Uncoupled Vehicle

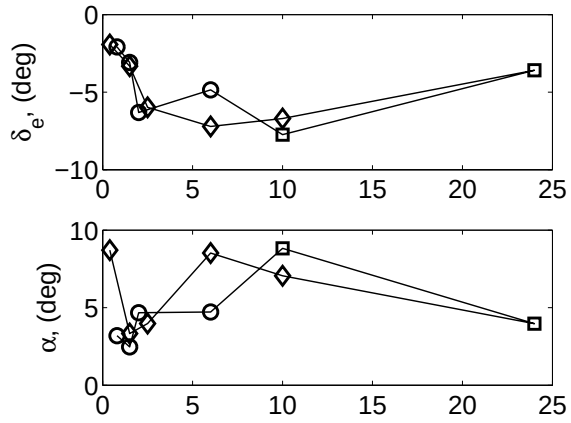

Figure A.21: Trim properties for Uncoupled Full-size vehicle.

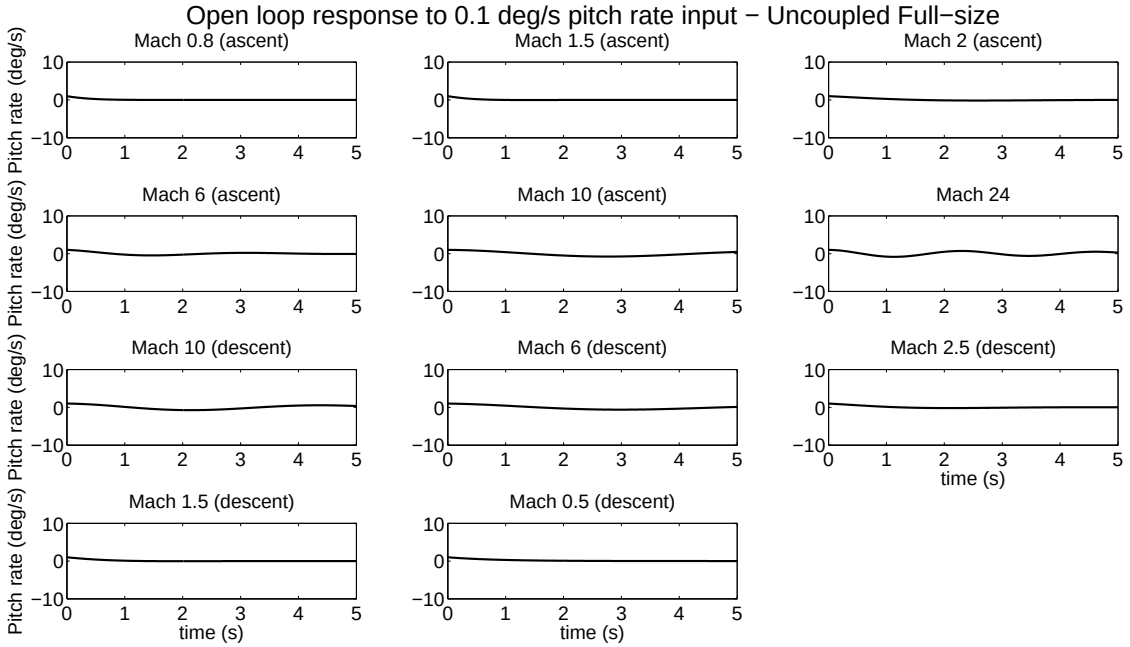

Figure A.22: Open-loop response to 1 deg/s pitch rate perturbation, for the Uncoupled Full-size vehicle.

Table A.1: Poles for longitudinal modes of Uncoupled Full-size vehicle.

Mach number	Altitude (ft)	Mode	Pole (rad/s)
0.8	305	short-period	-2.48 ± 1.02i
		phugoid	-0.026 ± 0.008i
1.5	6 096	short-period	-2.33 ± 1.48i
		phugoid	-0.095, -0.005
2.0	15 240	short-period	-0.65 ± 0.97i
		phugoid	-0.015 ± 0.02i
6.0	20 000	short-period	-0.5 ± 1.92i
		phugoid	-0.018, -0.003
10.0	33 000	short-period	-0.09 ± 1.1i
		phugoid	-0.002 ± 0.0036i
24.0	33 000	short-period	-0.15 ± 2.71i
		phugoid	-0.007, -0.00008
10.0	30 000	short-period	-0.137 ± 1.41i
		phugoid	-0.003 ± 0.003i
6.0	27 500	short-period	-0.16 ± 0.98i
		phugoid	-0.004 ± 0.006i
2.5	15 000	short-period	0.72 ± 1.22i
		phugoid	-0.017 ± 0.011i
1.5	10 000	short-period	-1.4 ± 1.08i
		phugoid	-0.044, -0.016
0.5	0	short-period	-1.2 ± 0.29i
		phugoid	-0.01 ± 0.02i

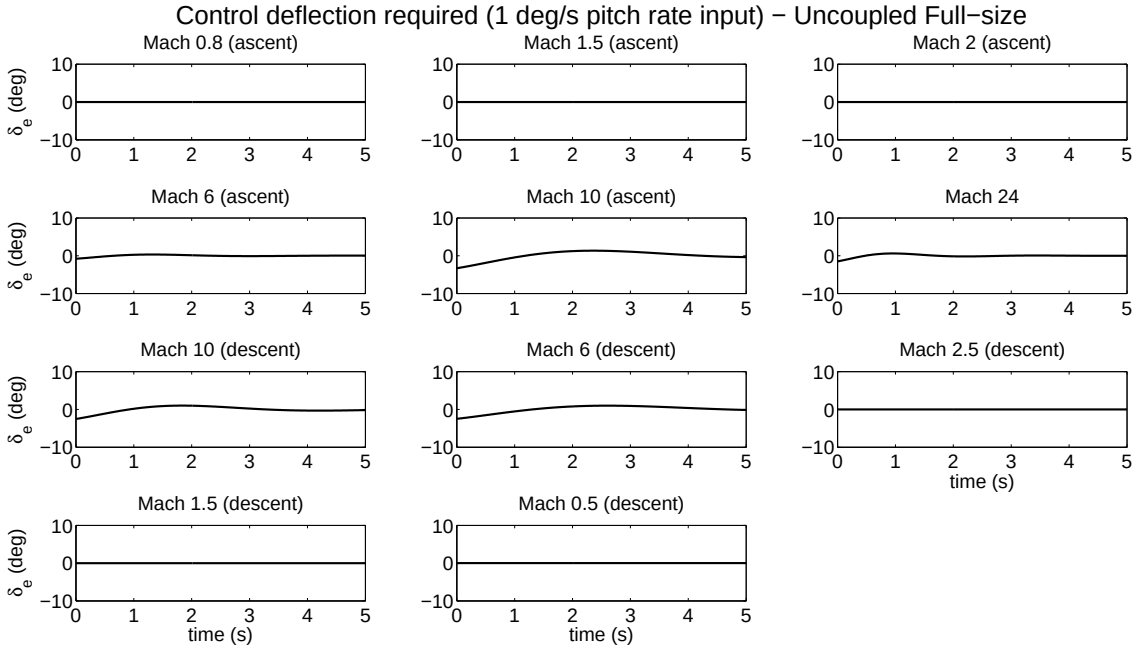

Figure A.23: Closed-loop elevator response to 1 deg/s pitch rate perturbation, for the Uncoupled Full-size vehicle.

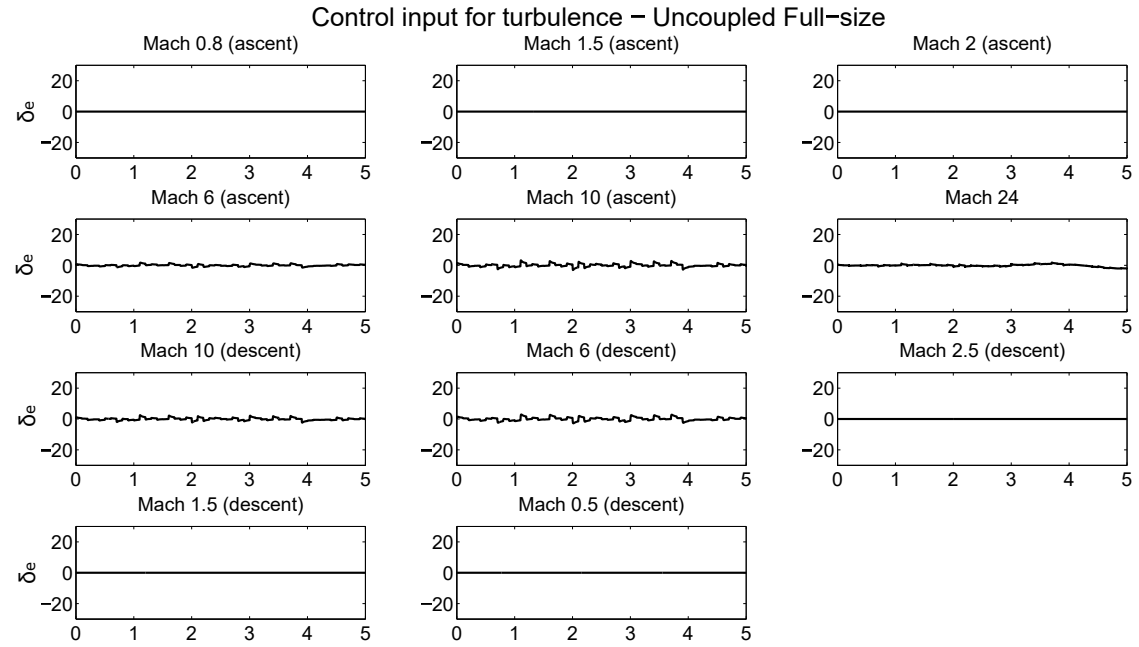

Figure A.24: Closed-loop elevator response to turbulence, for the Uncoupled Full-size vehicle.

Appendix B - Air-Breathing Hypersonic Vehicle with Reaction Jet Control - Full Datasets

Longitudinal Control

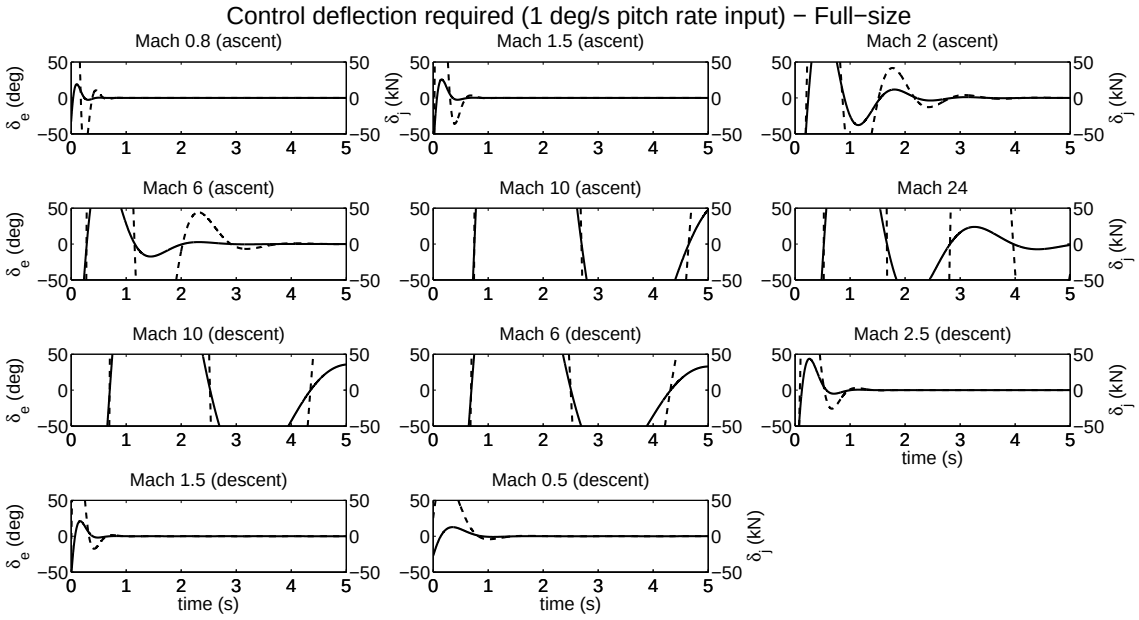

Figure B.1: Closed-loop control response to 1 deg/s pitch rate perturbation, for the Full-size vehicle in the single jet configuration. Solid Line = Elevator deflection (deg); Dash Line: Jet force (kN).

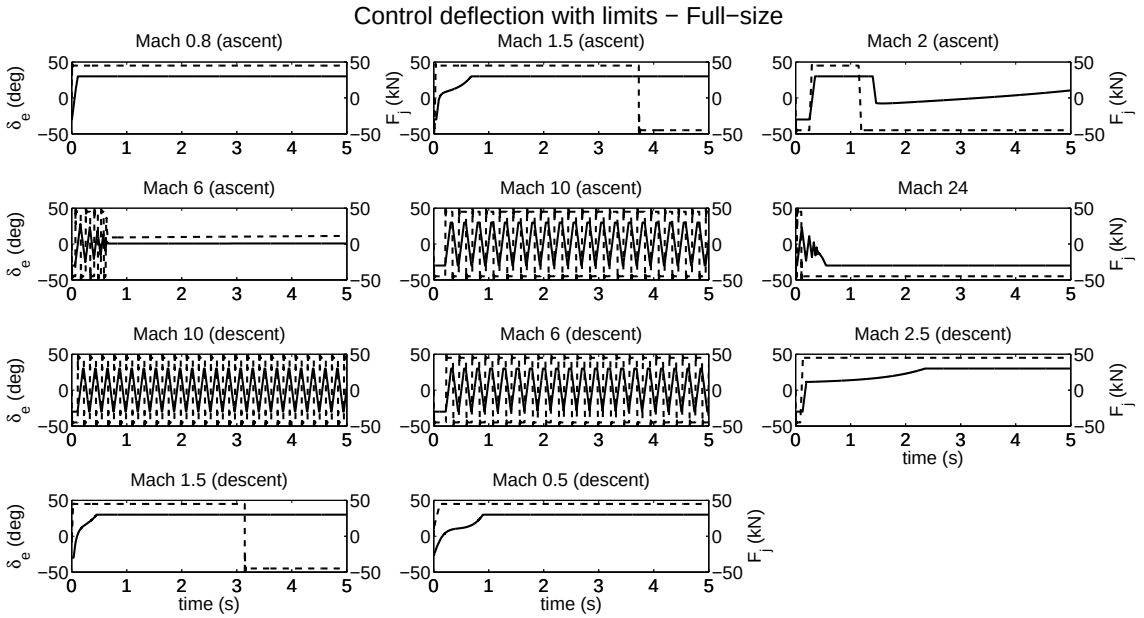

Figure B.2: Closed-loop elevator response to 1 deg/s pitch rate perturbation, for the Full-size vehicle in the single jet configuration. Solid Line = Elevator deflection (deg); Dash Line: Jet force (kN).

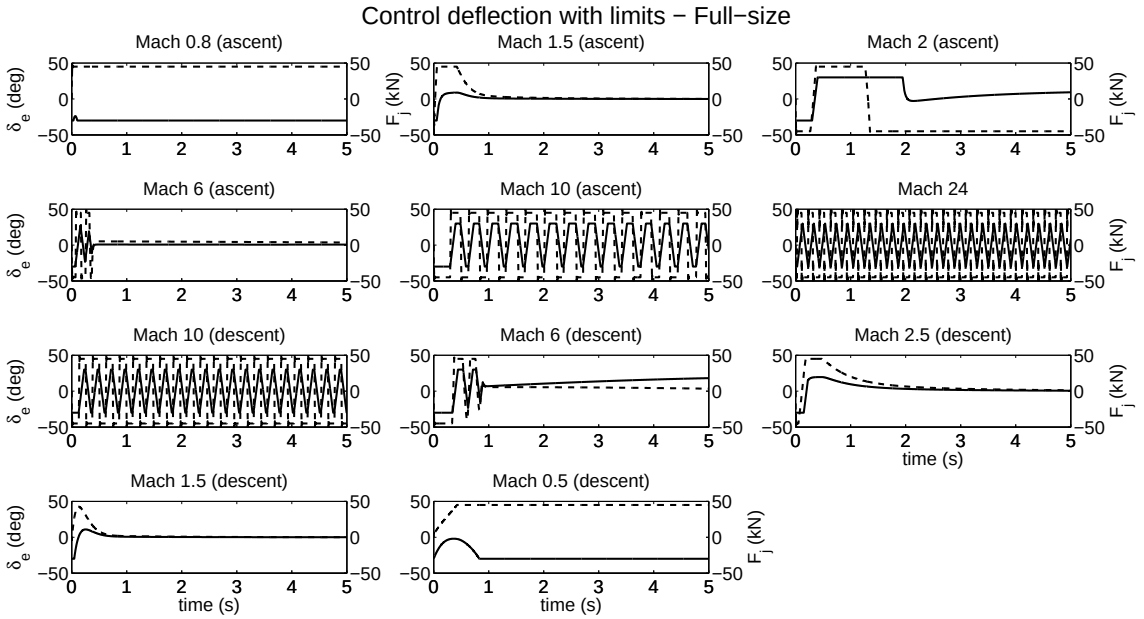

Figure B.3: Closed-loop elevator response to 1 deg/s pitch rate perturbation, for the Full-size vehicle in the twin jet configuration. Solid Line = Elevator deflection (deg); Dash Line: Jet force (kN).

Atmospheric Turbulence

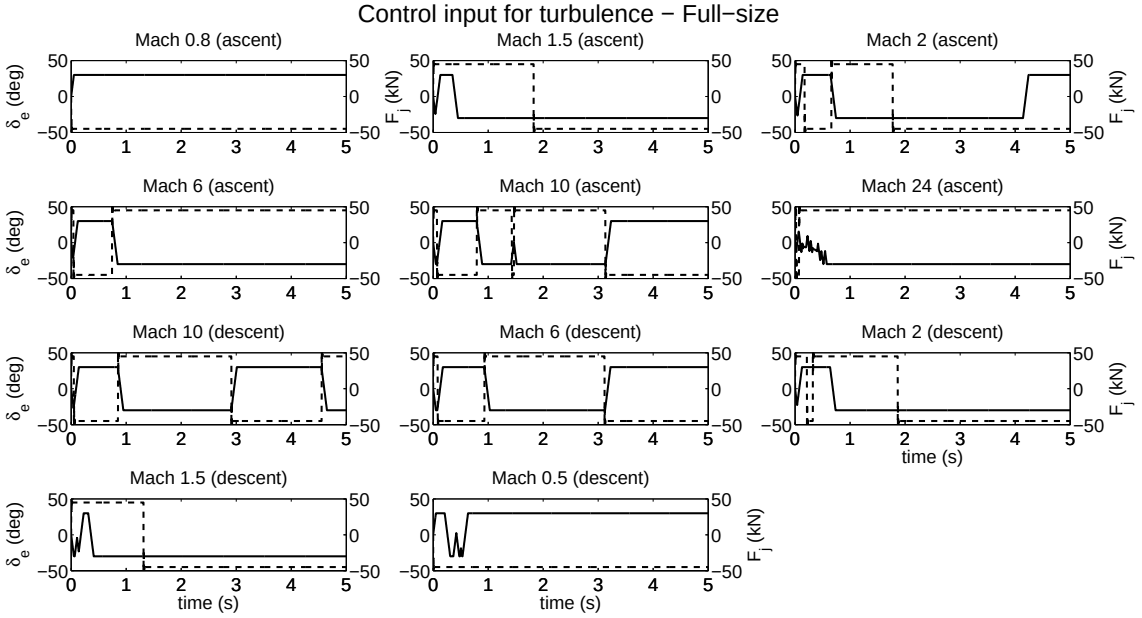

Figure B.4: Closed-loop elevator response to turbulence, for the Full-size vehicle in the single jet configuration. Solid Line = Elevator deflection (deg); Dash Line: Jet force (kN).

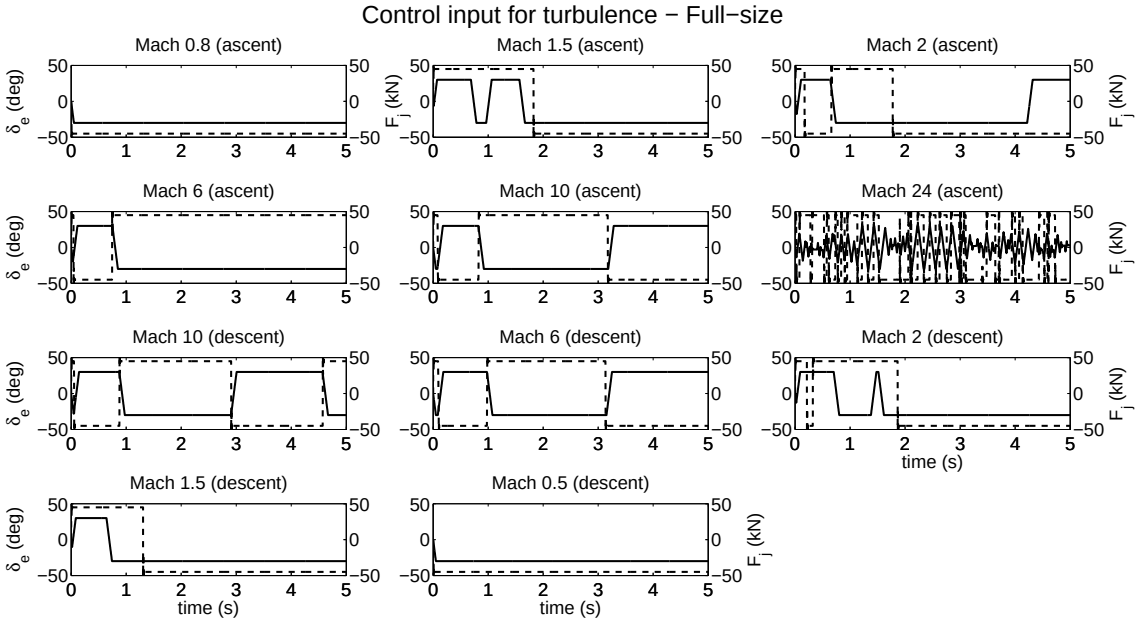

Figure B.5: Closed-loop elevator response to turbulence, for the Full-size vehicle in the twin jet configuration. Solid Line = Elevator deflection (deg); Dash Line: Jet force (kN).

Bibliography

Adamson, T. C. J. and J. A. Nicholls (1959). On the Structure of Jets from Highly Underexpanded Nozzles Into Still Air. *Journal of the Aerospace Sciences 26*(1), 16 – 24.

Ahmad, A., M. R. Saad, A. Che Idris, M. R. A. Rahman, and S. Sujipto (2016). Aerodynamic performance of cruise missile flying above local terrain. *IOP Conf. Series: Materials Science and Engineering 152*, 012006.

Alkandry, H. (2012). *Aerodynamic Interactions of Propulsive Deceleration and Reaction Control System Jets on Mars-Entry Aeroshells*. Ph. D. thesis, Aerospace Engineering and Scientific Computing, The University of Michigan.

Anderson, J. D. (2001). *Fundamentals of Aerodynamics, 3rd ed.* McGraw Hill.

Anderson, J. D. (2004). *Modern Compressible Flow: With Historical Perspective*. McGraw Hill.

Anderson, J. D. (2006). *Hypersonic and High Temperature Gas Dynamics, 2nd ed.* AIAA Education Series.

Anderson, K. V. and D. D. Knight (2012). Plasma Jet for Flight Control. *AIAA Journal 50*(9), 1855 – 1872.

Andre, T., A. Durant, and I. Fedioun (2017). Numerical Study of Supersonic Boundary-Layer Transition due to Sonic Wall Injection. *AIAA Journal 55*(5), 1530 – 1547.

Bahm, C., E. Baumann, J. Martin, D. Bose, R. Beck, and B. Strovers (2005). The X-43A Hyper-X Mach 7 Flight 2 Guidance, Navigation and Control Overview and Flight Test Results. In *AIAA International Space Planes and Hypersonic Systems and Technologies, Capua, Italy*.

Balakumar, P. and A. Chou (2018). Transition Prediction in Hypersonic Boundary Layers Using Receptivity and Freestream Spectra. *AIAA Journal 56*(1), 193 – 208.

Banerjee, S., Z. Wang, B. Baur, F. Holzapfel, J. Che, and C. Cao (2016). L1 Adaptive Control Augmentation for the Longitudinal Dynamics of a Hypersonic Glider. *AIAA Journal of Guidance, Control and Dynamics 39*(2), 275 – 291.

Belavin, V. A., V. V. Golub, I. M. Naboko, and A. M. Opara (1973). Study of the structure of a time-dependent flow created by an emerging stream of shock-heated gas. *Journal of Applied Mechanics and Technical Physics 5*, 34 – 40.

Ben-Yakar, A. (2000). *Experimental Investigation of Mixing and Ignition of Transverse Jets in Supersonic Crossflows*. Ph. D. thesis, Stanford University, Department of Mechanical Engineering.

Ben-Yakar, A., M. G. Mungal, and R. K. Hanson (2006). Time evolution and mixing

characteristics of hydrogen and ethylene transverse jets in supersonic crossflows. *Physics of Fluids 18*, 026101.

Beresh, S. J., J. F. Henfling, R. J. Erven, and R. W. Spillers (2005). Penetration of a Transverse Supersonic Jet into a Subsonic Compressible Crossflow. *AIAA Journal 43*(2), 379 – 389.

Bidan, G. and D. E. Nikitopoulos (2011). Fundamental Study of Modulated Transverse Jets from a Film Cooling Perspective. *AIAA Journal 49*(7), 1498 – 1510.

Bidan, G. and D. E. Nikitopoulos (2013). On Steady and Pulsed Low-Blowing-Ratio Transverse Jets. *Journal of Fluid Mechanics 714*, 393 – 433.

Bilimoria, K. D. and D. K. Schmidt (1995). Integrated Development of the Equations of Motion for Elastic Hypersonic Flight Vehicles. *AIAA Journal of Guidance, Control and Dynamics 18*(1), 73 – 81.

Bogdanoff, D. W. (1994). Advanced Injection and Mixing Techniques for Scramjet Combustors. *AIAA Journal of Propulsion and Power 10*(2), 183 – 190.

Bolender, M. A. and D. B. Doman (2007). Nonlinear Longitudinal Dynamical Model of an Air-breathing Hypersonic Vehicle. *AIAA Journal of Spacecraft and Rockets 44*(2), 374 – 387.

Brandeis, J. and J. Gill (1996). Experimental Investigation of Side Jet Steering for Supersonic and Hypersonic Missiles. *AIAA Journal of Spacecraft and Rockets 33*(3), 346 – 352.

Broadwell, J. E. and R. E. Breidenthal (1984). Structure and mixing of a transverse jet in incompressible flow. *Journal of Fluid Mechanics 148*, 405 – 412.

Brumbaugh, R. W. (1994). Aircraft Model for the AIAA Controls Design Challenge. *AIAA Journal of Guidance, Control and Dynamics 17*(4), 747 – 752.

Buckmaster, J. D. (1964). An investigation of cylindrical starting flows. *AIAA Journal 2*(9), 1649 – 1650.

Cassel, L. A. (2003). Applying Jet Interaction Technology. *AIAA Journal of Spacecraft and Rockets 40*(4), 523 – 537.

Cattafesta, L. N. and M. Sheplak (2011). Actuators for Active Flow Control. *Annual Review of Fluid Mechanics 43*, 247 – 274.

Chai, X., P. S. Iyer, and K. Mahesh (2015). Numerical study of high speed jets in crossflow. *Journal of Fluid Mechanics 785*, 152 – 188.

Chai, X. and K. Mahesh (2011). Simulation of High Speed Turbulent Jets in Crossflows. In *AIAA Aerospace Sciences Meeting, Orlando, FL*.

Chamberlain, R., D. McClure, and A. Dang (2000). CFD Analysis of Lateral Jet Interaction Phenomena for the THAAD Interceptor. In *AIAA Aerospace Sciences Meeting and Exhibit, Reno, NV*.

Chan, S. Y., P. Y. Cheng, D. M. Pitt, T. T. Myers, D. H. Klyde, R. Y. Magdaleno, and D. T. McRuer (1991). Aeroservoelastic Stabilization Techniques for Hypersonic Flight Vehicles, NASA Contractor Report 187614.

Chang, Y. K. and A. D. Vakili (1995). Dynamics of vortex rings in crossflow. *Physics of Fluids 7*, 1583 – 1597.

Chavez, F. R. and D. K. Schmidt (1994a). Analytical Aeropropulsive / Aeroelastic Hypersonic-Vehicle Model with Dynamic Analysis. *AIAA Journal of Guidance, Control and Dynamics 17*(6), 1308 – 1319.

Chavez, F. R. and D. K. Schmidt (1994b). Flight Dynamics and Control of Elastic Hypersonic Vehicles Modeling Uncertainties. *AIAA Paper 3629-94*, 766 – 774.

Chazen, M. L. and W. Sanscrainte (1974). Space Shuttle Bipropellant RCS Engine. *AIAA Journal of Spacecraft 11*(10), 685 – 689.

Chekmarev, S. F. and N. V. Stankus (1984). Gasdynamic model and similarity relations for the starting process in supersonic nozzles and jets. *Soviet Physics - Technical Physics 29*, 920 – 925.

Chen, S. and D. Zhao (2017). Numerical Investigation of Pulsed Fuel Injection for the Hyshot II. In *AIAA International Space Planes and Hypersonic Systems and Technogies Conference, Xiamen, China*.

Chenault, C. F. and P. S. Beran (1998). $k - \epsilon$ and Reynolds Stress Turbulence Model Comparisons for Two-Dimensional Injection Flows. *AIAA Journal 36*(8), 1401 – 1412.

Cockburn, B. and C.-W. Shu (1998). The Runge-Kutta Discontinuous Galerkin Method for Conservation Laws V: Multidimensional Systems. *Journal of Computational Physics 141*, 199 – 224.

Colgren, R., S. Keshmiri, and M. Mirmirani (2009). Nonlinear Ten Degree of Freedom Dynamics Model of a Generic Hypersonic Vehicle. *AIAA Journal of Aircraft 46*(3), 800 – 813.

Corke, T. C., C. Lon Enloe, and S. P. Wilkinson (2010). Dielectric Barrier Discharge Plasma Actuators for Flow Control. *Annual Review of Fluid Mechanics 42*, 505 – 529.

Cortelezzi, L. and A. R. Karagozian (2001). On the formation of the counter-rotating vortex pair in transverse jets. *Journal of Fluid Mechanics 446*, 347 – 373.

Cutler, A. D. and J. P. Drummond (2008). Toward a High-Frequency Pulsed-Detonation Actuator. Technical report, AIAA.

Cutler, A. D., G. C. Harding, and G. S. Diskin (2013). High Frequency Pulsed Injection into a Supersonic Duct Flow. *AIAA Journal 51*(4), 809 – 818.

Dash, S. M., E. R. Perrell, S. Arunajatesan, and C. Kannepalli (2000). Lateral Jet Aerodynamic Interaction Simulations for Dynamic Pressure Loads. In *AIAA Aeroacoustics Conference, Lahaina, HI*.

Dauby, B. H., D. W. Adamczak, J. A. Muse, and M. A. Bolender (2015). HIFiRE 6: Overview and Status Update 2015. In *20th AIAA International Space Planes and Hypersonic Systems and Technologies Conference, Glasgow, Scotland*.

Davidson, J. B., F. J. Lallman, and W. T. Bundick (2001). Real-Time Adaptive Control Allocation applied to a High Performance Aircraft. In *5th SIAM Conference on Control and Its Applications, San Diego, CA*.

de Villiers, E. (2006). *The Potential of Large Eddy Simulation for the Modeling of Wall Bounded Flows*. Ph. D. thesis, Imperial College of Science, Technology and

Medicine, Department of Mechanical Engineering.

DeSpirito, J. (2012). Transient Lateral Jet Interaction Effects on a Generic Fin-Stabilized Projectile. In *AIAA Applied Aerodynamics Conference, New Orleans, LA*.

Dickeson, J. J., A. A. Rodriguez, S. Sridharan, and A. Korad (2010). Elevator Sizing, Placement and Control Relevant Tradeoffs for Hypersonic Vehicles. In *AIAA Guidance, Navigation, and Control Conference, Toronto, Canada*.

Doman, D. B., M. W. Oppenheimer, and M. A. Bolender (2006). Progress in Guidance and Control Research for Space Access and Hypersonic Vehicles. In *45th IEEE Conference on Decision & Control, San Diego, CA*.

Ebrahimi, H. B. (2000). Numerical Simulation of Transient Jet-Interaction Phenomenology in a Supersonic Freestream. *AIAA Journal of Spacecraft and Rockets 37*(6), 713 – 719.

Echols, J. A., K. Puttinnaiah, K. Mondal, and A. A. Rodriguez (2015). Fundamental Control System Design Issues for Scramjet-Powered Hypersonic Vehicles. In *AIAA Guidance, Navigation, and Control Conference, Kissmissee, FL*.

Erdem, E. (2011). *Active Flow Control Studies at Mach 5: Measurement and Computation*. Ph. D. thesis, University of Manchester, School of Mechanical, Aerospace and Civil Engineering.

Erdem, E. and K. Kontis (2009). Non-Plasma and Plasma Transverse Jets in Hypersonic Cross Flow. In *16th AIAA/DLR/DGLR International Space Planes and Hypersonic Systems Technologies Conference, Bremen, Germany*.

Erdem, E. and K. Kontis (2010). Numerical and Experimental Investigation of Transverse Injection Flows. *Shock Waves 20*, 103 – 118.

Eremin, A. V., V. A. Kochnev, A. A. Kulikovskii, and I. M. Naboko (1978). Nonstationary Processes in Starting Strongly Underexpanded Jets. *Journal of Applied Mechanics and Technical Physics 19*, 27 – 31.

Eroglu, A. and R. E. Breidenthal (2001). Structure, Penetration, and Mixing of Pulsed Jets in Crossflow. *AIAA Journal 39*(3), 417 – 423.

FAA (2004). Airplane Flying Handbook. Technical report, Federal Aviation Administration FAA-H-8303-3A.

Falkiewicz, N. J. and C. E. S. Cesnik (2009). A Reduced Order Modeling Framework for Integrated Thermoelastic Analysis of Hypersonic Vehicles. In *AIAA Structures, Structural Dynamics and Materials Conference, Palm Springs, CA*.

Falkiewicz, N. J., C. E. S. Cesnik, M. A. Bolender, and D. B. Doman (2009). Thermoelastic Formulation of a Hypersonic Vehicle Control Surface for Control Oriented Simulation. In *AIAA Guidance, Navigation, and Control Conference, Chicago, IL*.

Falkiewicz, N. J., C. E. S. Cesnik, A. R. Crowell, and J. J. McNamara (2010). Reduced Order Aerothermoelastic Framework for Hypersonic Vehicle Control Simulation. In *AIAA Atmospheric Flight Mechanics Conference, Toronto, Canada*.

Falkiewicz, N. J., S. G. V. Frendries, and C. E. S. Cesnik (2011). Effect of Control

Surface Fuselage Inertial Coupling on Hypersonic Vehicle Flight Dynamics. In *AIAA Atmospheric Flight Mechanics Conference, Portland, OR*.

Ferry, J. W. and J. L. Rovey (2010). Thrust Measurement of Dielectric Barrier Discharge Plasma Actuators and Power Requirements for Aerodynamic Control. In *AIAA Flow Control Conference, Chicago, IL*.

Ferziger, J. H. and M. Peric (2002). *Computational Methods for Fluid Dynamics*. Springer.

Fidan, B., M. Mirmirani, and P. A. Ioannou (2003). Flight Dynamics and Control of Air Breathing Hypersonic Vehicles: Review and New Directions. In *AIAA International Space Planes and Hypersonic Systems and Technologies, Norfolk, VA*.

Fric, T. F. and A. Roshko (1994). Vortical structure in the wake of a transverse jet. *Journal of Fluid Mechanics 279*, 1 – 47.

Fureby, C. (1996). On subgrid scale modeling in large eddy simulation of compressible fluid flow. *Physics of Fluids 8*, 1301 – 1311.

Fureby, C. (2012). Large Eddy Simulation: A Useful Tool for Engineering Fluid Dynamics. In *18th Australasian Fluid Mechanics Conference, Launceston, Australia*.

Garnier, E., N. Adams, and P. Sagaut (2009). *Large Eddy Simulation for Compressible Flows*. Springer.

Getsinger, D. R., L. Gevorkyan, O. I. Smith, and A. R. Karagozian (2014). Structural and stability characteristics of jets in crossflow. *Journal of Fluid Mechanics 760*, 342 – 367.

Gevorkyan, L., T. Shoji, D. R. Getsinger, O. I. Smith, and A. R. Karagozian (2016). Transverse jet mixing characteristics. *Journal of Fluid Mechanics 790*, 237 – 274.

Gharib, M., E. Rambod, and K. Shariff (1998). A universal time scale for vortex ring formation. *Journal of Fluid Mechanics 360*, 121 – 140.

Gosse, R., R. L. Kimmel, and H. B. Johnson (2014). Study of Boundary-Layer Transition on Hypersonic International Flight Research Experimentation 5. *AIAA Journal of Spacecraft and Rockets 51*(1), 151 – 162.

Greenshields, C. J., H. G. Weller, L. Gasparini, and J. M. Reese (2010). Implementation of semi-discrete, non-staggered central schemes in a colocated, polyhedral, finite volume framework for high-speed viscous flows. *International Journal for Numerical Methods in Fluids 63*, 1 – 21.

Grinstein, F. F. and C. Fureby (2007). On Flux-Limiting-Based Implicit Large Eddy Simulation. *Journal of Fluids Engineering 129*, 1483 – 1492.

Grinstein, F. F., C. Fureby, and C. R. DeVore (2005). On MILES based on flux-limiting algorithms. *International Journal for Numerical Methods in Fluids 47*, 1043 – 1051.

Grinstein, F. F., L. Margolin, and W. Rider (2005). *Implicit Large Eddy Simulation: Capturing the Turbulent Flow Dynamics*. Cambridge University Press.

Gruber, M. R., A. S. Nejad, T. H. Chen, and J. C. Dutton (1997). Large structure convection velocity measurements in compressible transverse injection flowfields. *Experiments in Fluids 22*, 397 – 407.

Gutmark, E. and C.-M. Ho (1983). Preferred modes and the spreading rate of jets.

Physics of Fluids 26(10), 2932.

Hank, J. M., J. S. Murphy, and R. C. Mutzman (2008). The X-51A Scramjet Engine Flight Demonstration Program. In *AIAA International Space Planes and Hypersonic Systems and Technologies Conference, Dayton, OH*.

Hassan, B., G. V. Candler, and D. R. Olynick (1993). Thermo-chemical nonequilibrium effects on aerothermodynamics of aerobraking vehicles. *AIAA Journal of Spacecraft and Rockets 30*(6), 647 – 655.

Hasselbrink, E. F. and M. G. Mungal (2001). Transverse jets and jet flames. Part 1. Scaling laws for strong transverse jets. *Journal of Fluid Mechanics 443*, 1 – 25.

Heeg, J., M. G. Gilbert, and A. S. Pototzky (1993). Active Control of Aerothermoelastic Effects for a Conceptual Hypersonic Aircraft. *AIAA Journal of Aircraft 30*(4), 453 – 458.

Hermanson, J. C., A. Wahba, and H. Johari (1998). Duty-Cycle Effects on Penetration of Fully Modulated, Turbulent Jets in Crossflow. *AIAA Journal 36*(10), 1935 – 1937.

Hunt, J. C. R., A. Wray, and P. Moin (1988). Eddies, stream and convergence zones in turbulent flows. Technical report, Center for Turbulence Research Report CTR-S88.

Jackson, K. R., M. R. Gruber, and S. Buccellato (2015). Mach 6 - 8+ Hydrocarbon-Fueled Scramjet Flight Experiment: The HIFiRE Flight 2 Project. *AIAA Journal of Propulsion and Power 31*(1), 36 – 53.

Jasak, H. (1996). *Error Analysis and Estimation for the Finite Volume Method with Applications to Fluid Flows*. Ph. D. thesis, Imperial College of Science, Technology and Medicine, Department of Mechanical Engineering.

Johari, H., M. Pacheco-Tougas, and J. C. Hermanson (1999). Penetration and Mixing of Fully Modulated Turbulent Jets in Crossflow. *AIAA Journal 37*(7), 842 – 850.

Kanipe, D. B. (1983). Plume/Flowfield Jet Interaction Effects on the Space Shuttle Orbiter during Entry. *AIAA Journal of Spacecraft 20*(4), 351 – 355.

Karagozian, A. R. (2014). The jet in crossflow. *Physics of Fluids 26*, 101303.

Karnopp, B. and F. Fischer (1990). On the vibrations of overdamped systems. *Journal of the Franklin Institute 327*, 601 – 609.

Kaufman, L. G., L. Meckler, and S. A. Hartofilis (1965). An Investigation of Flow Separation and Aerodynamic Controls at Hypersonic Speeds. *AIAA Paper 65-753*, 16pp.

Kautsky, J., N. K. Nichols, and P. Van Dooren (1985). Robust Pole Assignment in Linear State Feedback. *International Journal of Control 41*, 1129 – 1155.

Kawai, S. and S. K. Lele (2009). Dynamics and mixing of a sonic jet in a supersonic turbulent crossflow. In *Center for Turbulence Research Annual Research Briefs, pp. 285 - 298, Stanford CA*.

Kawai, S. and S. K. Lele (2010). Large-Eddy Simulation of Jet Mixing in Supersonic Crossflows. *AIAA Journal 48*(9), 2063 – 2083.

Keffer, J. and W. D. Baines (1963). The round turbulent jet in a cross-wind. *Journal of Fluid Mechanics 15*, 481 – 496.

Kelso, R. M., T. T. Lim, and A. E. Perry (1996). An experimental study of round jets in cross-flow. *Journal of Fluid Mechanics 306*, 111–144.

Kimmel, R. L., D. W. Adamczak, T. J. Juliano, and DSTO AVD Brisbane Team (2013). HIFiRE-5 Flight Test Preliminary Results. In *51st AIAA Aerospace Sciences Meeting, Grapevine, TX*.

Kolmogorov, A. N., V. Levin, J. C. R. Hunt, O. M. Phillips, and D. Williams (1991). The local structure of turbulence in incompressible viscous fluid for very large reynolds numbers. *Proceedings of the Royal Society of London. Series A: Mathematical and Physical Sciences 434*.

Kouchi, T., K. Sasaya, J. Watanabe, H. Sibayama, and G. Masuya (2010). Penetration Characteristics of Pulsed Injection into Supersonic Crossflow. In *46th AIAA/ASME/SAE/ASEE Joint Propulsion Conference and Exhibit, Nashville, TN*.

Krothapalli, A., L. Lourenco, and J. M. Buchlin (1990). Separated Flow Upstream of a Jet in a Crossflow. *AIAA Journal 28*(3), 414 – 420.

Kurganov, A., S. Noelle, and G. Petrova (2001). Semidiscrete Central-Upwind Schemes for Hyperbolic Conservation Laws and Hamilton-Jacobi Equations. *SIAM Journal of Scientific Computing 23*(3), 707 – 740.

Kurganov, A. and E. Tadmor (2000). New high-resolution central schemes for nonlinear conservation laws and convection–diffusion equations. *Journal of Computational Physics 160*, 241 – 282.

Li, L., M. Hirota, K. Ouchi, and T. Saito (2017). Evaluation of fluidic thrust vectoring nozzle via thrust pitching angle and thrust pitching moment. *Shock Waves 27*, 53 – 61.

Lim, T. T., T. H. New, and S. C. Lou (2001). On the development of large-scale structures of a jet normal to a cross flow. *Physics of Fluids 13*, 770 – 775.

Lomax, H., T. H. Pulliam, and D. W. Zingg (2001). *Fundamentals of Computational Fluid Dynamics*. Springer.

Mahaffey, R. E., J. A. Schetz, and R. A. Weinraub (1968). Supersonic transverse injection into a supersonic stream. *AIAA Journal 6*(5), 993–994.

Mahesh, K. (2013). The Interaction of Jets with Crossflow. *Annual Review of Fluid Mechanics 45*, 379 – 407.

Marcantoni, L. F., J. P. Tamagno, and S. A. Elaskar (2012). High Speed Flow Simulation using OPENFOAM. *Mecanica Computacional 31*, 2939 – 2959.

Margason, R. J. (1993). Fifty Years of Jet in Cross Flow Research. In *Computational and Experimental Assessment of Jets in Cross Flow, AGARD-CP-534, Advisory Group for Aerospace Research and Development, Winchester, UK*.

Marzouk, Y. M. and A. F. Ghoniem (2007). Vorticity structure and evolution in a transverse jet. *Journal of Fluid Mechanics 575*, 267 – 305.

Maughmer, M., L. Ozoroski, D. Straussfogel, and L. Long (1993). Validation of Engineering Methods for Predicting Hypersonic Vehicle Control Forces and Moments. *AIAA Journal of Guidance, Control and Dynamics 16*(4), 762 – 769.

McDaniel, J. C. and J. Graves (1988). Laser-induced fluorescence visualization of

transverse gaseous injection in a nonreacting supersonic combustor. *AIAA Journal of Propulsion and Power 4*(6), 591 – 597.

M'Closkey, R. T., J. M. King, L. Cortelezzi, and A. R. Karagozian (2002). The active control jet in crossflow. *Journal of Fluid Mechanics 452*, 325 – 335.

Muppidi, S. and K. Mahesh (2005). Study of trajectories of jets in crossflow using direct numerical simulations. *Journal of Fluid Mechanics 530*, 81 – 100.

Murugappan, S. and E. Gutmark (2005). Control of Penetration and Mixing of an Excited Supersonic Jet into a Supersonic Cross-Stream. In *43rd AIAA Aerospace Sciences Meeting, Reno, NV*.

Murugappan, S., E. Gutmark, and C. Carter (2005). Control of penetration and mixing of an excited jet into a supersonic cross stream. *Physics of Fluids 17*, 106101.

Murugappan, S., E. Gutmark, C. Carter, J. Donbar, M. Gruber, and K.-Y. Hsu (2006). Transverse Supersonic Controlled Swirling Jet in a Supersonic Cross Stream. *AIAA Journal 44*(2), 290 – 300.

Naboko, I. M., T. V. Bazhenova, A. I. Opara, and V. A. Belavin (1972). Formation of a jet of shock-heated gas outflowing into evacuated space. *Acta Astronautica 17*, 653 – 658.

Naboko, I. M., V. A. Belavin, and V. V. Golub (1979). Nonstationary wave structure of intermittent supersonic jet. *Acta Astronautica 6*, 885 – 899.

Narayanan, S., P. Barooah, and J. M. Cohen (2003). Dynamics and Control of an Isolated Jet in Crossflow. *AIAA Journal 41*(12), 2316 – 2330.

Naumann, K. W., H. Ende, A. George, and G. Mathieu (1996). Shock Tunnel Experiments on Lateral Jet Interaction Methods and Results. In *AIAA Joint Propulsion Conference and Exhibit, Lake Buena Vista, FL*.

Naumann, K. W., H. Ende, A. George, and G. Mathieu (1998). Stationary and Time Dependent Effects in the Near Interaction of Gaseous Jets in a Supersonic Crossflow. *AIAA Paper-98-2972*, 12pp.

Naumann, K. W., H. Ende, G. Mathieu, and A. George (1993a). Millisecond Aerodynamic Force Measurement with Side-Jet Model in the ISL Shock Tunnel. *AIAA Journal 31*(3), 1068 – 1074.

Naumann, K. W., H. Ende, G. Mathieu, and A. George (1993b). Shock Tunnel Experiments and Approximative Methods on Hypervelocity Side-Jet Control Effectiveness. In *AIAA Joint Propulsion Conference and Exhibit, Monterey, CA*.

Nelson, R. C. (1989). *Flight Stability and Automatic Control*. McGraw Hill.

Ni, Z. Y., N. Cao, and L. Xu (2017). Experimental Investigation of Lateral Pulse Jet Interaction Flowfield Hypersonic Flow. In *AIAA International Space Planes and Hypersonic Systems and Technologies Conference, Xiamen, China*.

Nishihara, M., K. Takashimi, N. Jiang, W. R. Lempert, I. V. Adamovich, J. W. Rich, S. Doraiswamy, and G. V. Candler (2012). Development of a Mach 5 Nonequilibrium-Flow Wind Tunnel. *AIAA Journal 50*(10), 2255 – 2267.

Oberkampf, W. L. and T. G. Trucano (2002). Verification and Validation in Computational Fluid Dynamics. Technical report, Sandia National Laboratories.

Oppenheimer, M. W., T. Skujins, M. A. Bolender, and D. B. Doman (2007). A Flexible Hypersonic Vehicle Model Developed with Piston Theory. In *AIAA Atmospheric Flight Mechanics Conference and Exhibit, Hilton Head, SC*.

Orlik-Ruckeman, K. J. (1966). Stability Derivatives of Sharp Wedges in Viscous Hypersonic Flow. *AIAA Journal 4*(6), 1001 – 1007.

Ortiz, X., A. Hemmatti, D. Rival, and D. Wood (2012). Instantaneous forces and moments on inclined flat plates. In *The Seventh International Colloqium on Bluff Body Aerodynamics and Applications, Shanghai, China*.

Papamoschou, D. and D. G. Hubbard (1993). Visual Observations of Supersonic Transverse Jets. *Experiments in Fluids 14*, 468 – 476.

Papamoschou, D., D. G. Hubbard, and M. Lin (1991). Observations of supersonic transverse jets. Technical report, AIAA Paper 91-1723.

Peebles, C. (2008). *The X-43A Flight Research Program: Lessons Learned on the Road to Mach 10*. AIAA.

Pezzella, G. and A. Viviani (2016). Aerodynamic performance analysis of a winged re-entry vehicle from hypersonic down to subsonic speed. *Aerospace Science and Technology 52*, 129 – 143.

Poinsot, T. J. and S. K. Lele (1992). Boundary conditions for direct simulations of compressible viscous flows. *Journal of Computational Physics 101*, 104 – 129.

Pope, S. B. (2000). *Turbulent Flows*. Cambridge University Press.

Popinski, Z. and C. F. Ehrlich (1966). Development Design Methods for Predicting Hypersonic Dynamic Control Characteristics. Technical report, US Air Force Flight Dynamics Laboratory, AFFDL-TR-66-85.

Portz, R. and C. Segal (2006). Penetration of gaseous jets in supersonic flows. *AIAA Journal 44*(10), 2426 – 2429.

Prime, Z., C. J. Doolan, B. Cazzolato, and L. A. Brooks (2012). Longitudinal Flight Dynamics Modelling and Control of ScramSpace I. In *AIAA Aerospace Sciences Meeting, Nashville, TN*.

Radulescu, M. I. and C. K. Law (2007). The transient start of supersonic jets. *Journal of Fluid Mechanics 575*, 331 – 369.

Rana, Z. A., B. Thornber, and D. Drikakis (2011). Transverse jet injection into a supersonic turbulent cross-flow. *Physics of Fluids 23*, 046103.

Randolph, H., L. Chew, and H. Johari (1994). Pulsed jets in supersonic crossflow. *AIAA Journal of Propulsion and Power 10*(5), 746 – 748.

Raney, D. L., J. D. McMinn, A. S. Pototzky, and C. L. Wooley (1993). Impact of Aeroelasticity on Propulsion and Longitudinal Flight Dynamics on an Air-Breathing Hypersonic Vehicle. *AIAA Paper 93-1367*.

Richardson, L. F. and J. A. Gaunt (1927). The Deferred Approach to the Limit. Part I. The Single Lattice Approach. Part II. Interpenetrating Lattices. *Philosophical Transactions of the Royal Society of London. Series A, Containing Papers of a Mathematical or Physical Character 226*, 299 – 361.

Roache, P. J. (1997). Quantification of Uncertainty in Computational Fluid Dynamics.

Annual Review of Fluid Mechanics 29, 123 – 160.

Rodriguez, A. A., J. J. Dickeson, O. Cifdaloz, R. McCullen, J. Benavides, S. Sridharan, A. Kelkar, J. M. Vogel, and D. Soloway (2008). Modeling and Control of Scramjet-Powered Hypersonic Vehicles: Challenges, Trends and Tradeoffs. In *AIAA Guidance, Navigation and Control Conference and Exhibit, Honolulu, HI.*

Roe, P. L. (1986). Characteristic-Based Schemes for the Euler Equations. *Annual Review of Fluid Mechanics 18*, 337 – 365.

Rogers, R. C. (1971). A study of the mixing of hydrogen injected normal to a supersonic airstream. Technical report, NASA TN D-6114.

Rothstein, A. D. and P. J. Wantuck (1992). A study of the normal injection of hydrogen into a heated supersonic flow using planar laser-induced fluorescence. In *28th SAE, ASME, ASEE Joint Propulsion Conference and Exhibit, Nashville, TN.*

Ruiz, A. M., G. Lacaze, and J. C. Oefelein (2015). Flow topologies and turbulence scales in a jet-in-cross-flow. *Physics of Fluids 27*, 045101.

Ryu, S. and D. Andrisani (2003). Longitudinal Flying Qualities Prediction for Nonlinear Aircraft. *AIAA Journal of Guidance, Control, and Dynamics 26*(3), 474 – 482.

Sachs, G. (2005). Longitudinal Long-Term Modes in Super- And Hyper-Sonic Flight. *AIAA Journal of Guidance, Control, and Dynamics 28*(3), 539 – 541.

Santiago, J. G. and J. C. Dutton (1997). Velocity measurements of a jet injected into a supersonic crossflow. *AIAA Journal of Propulsion and Power 13*(2), 264 – 273.

Sau, R. and K. Mahesh (2008). Dynamics and mixing of vortex rings in crossflow. *Journal of Fluid Mechanics 604*, 389 – 409.

Sau, R. and K. Mahesh (2010). Optimization of pulsed jets in crossflow. *Journal of Fluid Mechanics 653*, 365 – 390.

Schetz, J. A. and F. S. Billig (1966). Penetration of gaseous jets injected into a supersonic stream. *AIAA Journal of Spacecraft and Rockets 3*(11), 1658 – 1665.

Schetz, J. A., P. F. Hawkins, and H. Lehman (1967). Structure of highly underexpanded transverse jets in supersonic stream. *AIAA Journal 5*(5), 882 – 884.

Schmidt, D. K., H. Mamich, and F. Chavez (1991). Dynamics and Control of Hypersonic Vehicles - The Integration Challenge of the 1990's. In *AIAA Third International Aerospace Planes Conference, Orlando, FL.*

Seifert, A. (2007). Closed-Loop Active Flow Control Systems: Actuators. Technical report, School of Mechanical Engineering, Tel-Aviv University.

Shapiro, S. R., J. M. King, R. T. M'Closkey, and A. R. Karagozian (2006). Optimization of Control Jets in Crossflow. *AIAA Journal 44*(6), 1292 – 1298.

Shaughnessy, J. D. and I. M. Gregory (1991). Trim Drag Reduction Concepts for Horizontal Takeoff Single-Stage-To-Orbit Vehicles. Technical report, NASA Langley Research Centre.

Shaughnessy, J. D., S. Z. Pinckney, J. D. McMinn, C. I. Cruz, and M.-L. Kelley (1990). Hypersonic Vehicle Simulation Model: Winged Cone Configuration. Technical report, NASA Langley Research Centre.

Shi, H., G. Wang, X. Lou, J. Yang, and X. Lu (2016). Large-eddy simulation of a pulsed jet into a ssupersonic crossflow. *Computers and Fluids 140*, 320 – 333.

Skujins, T., C. E. S. Cesnik, M. W. Oppenheimer, and D. B. Doman (2008). Applicability of an Analytical Shock/Expansion Solution to the Elevon Control Effectiveness for a 2D Hypersonic Vehicle Configuration. In *AIAA Atmospheric Flight Mechanics Conference, Honolulu, HI*.

Skujins, T., C. E. S. Cesnik, M. W. Oppenheimer, and D. B. Doman (2010). Canard-Elevon Interactions on a Hypersonic Vehicle. *Journal of Spacecraft and Rockets 47*(1), 90 – 100.

Smart, M. (2008). Scramjets. In *Advances on Propulsion Technology for High Speed Aircraft, Neuilly-sur-Seine, France*.

Smith, S. H. and M. G. Mungal (1998). Mixing, structure and scaling of the jet in crossflow. *Journal of Fluid Mechanics 357*, 83 – 122.

Smith, T. R., K. G. Bowcutt, J. R. Selmon, L. Miranda, B. Northrop, R. Mairs, E. R. Unger, K. Y. Lau, T. Silvester, H. Alesi, A. Paull, R. Paull, and D. J. Dolvin (2011). HIFiRE 4: A Low Cost Aerodynamics, Stability and Control Hypersonic Flight Experiment. In *17th AIAA International Space Planes and Hypersonic Systems and Techniologies Conference, San Francisco, CA*.

Spaid, F. W. and E. E. Zukoski (1968). A Study of the Interaction of Gaseous Jets from Transverse Slots with Supersonic External Flows. *AIAA Journal 6*(2), 205 – 212.

Stein, G. (2003). Respect the Unstable. Technical report, IEEE Control Systems Magazine.

Stern, F., R. V. Wilson, H. W. Coleman, and E. G. Paterson (1999). Verification and Validation of CFD Simulations. Technical report, Iowa Institute of Hydraulic Research.

Stevens, B. L. and F. L. Lewis (2003). *Aircraft Control and Simulation*. Wiley.

Sun, M. B. and Z. W. Hu (2018). Generation of upper trailing counter-rotating vortices of a sonic jet in a supersonic crossflow. *AIAA Journal 56*(3), 1047 – 1059.

Sutherland, W. (1893). The viscosity of gases and molecular force. *Philosophical Magazine 5*(36), 507 – 531.

Takahashi, H., G. Masuya, and M. Hirota (2010). Effects of injection and main flow conditions on supersonic turbulent mixing structure. *AIAA Journal 48*(8), 1748 – 1756.

Tennekes, H. and J. L. Lumley (1972). *A First Course in Turbulence*. The MIT Press.

Urzay, J. (2018). Supersonic combustion in air-breathing propulsion systems for hypersonic flight. *Annual Review of Fluid Mechanics 50*, 593 – 627.

USDoD (1980). MIL-F-8785C Military Specification: Flying Qualities of Piloted Airplanes. Technical report, United States Department of Defense.

van Leer, B. (1974). Towards the Ultimate Conservative Difference Scheme II. Monotonicity and Conservation Combined in a Second Order Scheme. *Journal of Computational Physics 14*, 361 – 370.

van Lerberghe, W. M., J. G. Santiago, J. C. Dutton, and R. P. Lucht (2000). Mixing of a sonic transverse jet injected into a supersonic flow. *AIAA Journal 38*(3), 470 – 479.

Versteeg, H. K. and W. Malalasekera (1995). *An Introduction to Computational Fluid Dynamics: The Finite Volume Method*. Longman Scientific and Technical.

Viti, V. (2002). *Numerical studies of the jet interaction flowfield with a main jet and an array of smaller jets.* Ph. D. thesis, Virginia Tech, Department of Aerospace and Ocean Engineering.

Viti, V., R. Neel, and J. A. Schetz (2009). Detailed Flow Physics of the Supersonic Jet Interaction Flow Field. *Physics of Fluids 21*, 046101.

Vlagov, V. V., N. E. Masyakin, and M. N. Polyanskii (1980). Penetration depth of a jet injected into an oncoming supersonic flow. *Fluid Dynamics 15*, 599 – 602.

vonEggers Rudd, L. and D. J. Pines (2000). Integrated Propulsion Effects on Dynamic Stability and Control of Hypersonic Waveriders. In *AIAA Joint Propulsion Conference and Exhibit, Huntsville, AL*.

Vranos, A. and J. J. Nolan (1965). Supersonic mixing of a light gas and air. In *AIAA Joint Propulsion Conference, Colorado Springs, CO*.

Walton, J. (1989). Performance Sensitivity of Hypersonic Vehicles to Changes in Angle of Attack and Dynamic Pressure. In *AIAA Joint Propulsion Conference, Monterey, CA*.

Wang, J., L. Liu, P. Wang, and G. Tang (2016). Guidance and control system design for hypersonic vehicles in dive phase. *Aerospace Science and Technology 53*, 47 – 60.

Watanabe, J., T. Kouchi, K. Takita, and G. Masuya (2012). Large-Eddy Simulation of Jet in Supersonic Crossflow with Different Injectant Species. *AIAA Journal 50*(12), 2765 – 2778.

Watanabe, J., T. Kouchi, K. Takita, and G. Masuya (2013). Characteristics of Hydrogen Jets in Supersonic Crossflow: Large-Eddy Simulation Study. *AIAA Journal of Propulsion and Power 29*(3), 661 – 674.

Weller, H., G. Tabor, H. Jasak, and C. Fureby (1998). A tensorial approach to computational continuum mechanics using object-oriented techniques. *Computers in Physics 12*(6), 620 – 631.

Wendt, J. F. E. (2009). *Computational Fluid Dynamics - An Introduction, 3rd Ed.* Springer.

White, D. A., A. Bowers, K. Illif, and J. Menousek (1992). *Handbook of Intelligent Control: Neural, Fuzzy and Adaptive Approaches*. Van Nostrand Reinhold.

Williams, N. J. and T. M. Moeller (2016). Numerical Investigations of High Frequency Pulsed Fuel Injection into Supersonic Crossflow. In *46th AIAA Fluid Dynamics Conference, Washington D.C., USA*.

Won, S., I. Jeung, B. Parent, and J. Choi (2010). Numerical Investigation of Transverse Hydrogen Jet into Supersonic Crossflow Using Detached-Eddy Simulation. *AIAA Journal 48*(6), 1047 – 1058.

Woodward, P. and P. Colella (1984). The Numerical Simulation of Two-Dimensional

Fluid Flow with String Shocks. *Journal of Computational Physics 54*, 115 – 173.

Woolf, A. F. (2013). Conventional Prompt Global Strike and Long-Range Ballistic Missiles: Background and Issues. Technical report, Congressional Research Service.

York, B. J., N. Sinha, S. M. Dash, A. Hosangadi, D. C. Kenzakowski, and R. A. Lee (1992). Complete Analysis of Steady and Transient Missile Aerodynamic Propulsive Plume Flowfield Interactions. In *AIAA Joint Propulsion Conference and Exhibit, Nashville, TN*.

Yuan, L. L., R. L. Street, and J. H. Ferziger (1999). Large-eddy simulations of a round jet in crossflow. *Journal of Fluid Mechanics 379*, 71 – 104.

Zhang, D., S. Tang, Q. Zhu, and R. Wang (2016). Analysis of dynamic characteristics of the rigid body/elastic body coupling of air-breathing hypersonic vehicles. *Aerospace Science and Technology 48*, 328 – 341.

Zhang, H., Z. Chen, X. Jiang, and Z. Huang (2015). The starting flow structures and evolution of a supersonic planar jet. *Computers and Fluids 114*, 98 – 109.

Zhang, X., W. Yao, and M. Xu (2008). Numerical Investigation of Transient Lateral Jet Interaction in a Supersonic Interceptor Missile. In *International Conference on Simulation and Scientific Computing, China*.

Zipfel, P. (2007). *Modeling and Simulation of Aerospace Vehicle Dynamics*. AIAA Education Series.